Doctorate Dissertation
博士論文

Theoretical Study on the Radial Profile of Pulsar Wind Nebulae

(パルサー星雲放射の空間構造に関する理論的研究)

A Dissertation Submitted for Degree of Doctor of Philosophy

December 2018

平成 30 年 12 月博士(理学)申請

Department of Physics, Graduate School of Science,

The University of Tokyo

東京大学大学院理学系研究科物理学専攻

Wataru Ishizaki

石﨑　涉

Abstract

A rotation-powered pulsar releases its rotation energy as a relativistic pair plasma outflow, called pulsar wind. This relativistic flow interacts with the surrounding interstellar medium and supernova remnant and forms a shock structure. The shocked wind spreads around the pulsar is called the pulsar wind nebula (PWN). In the PWN, there are very high energy electrons and positrons. Such particles emit photons of various energies via synchrotron radiation and inverse Compton scattering, so the PWN is observed in the very wide frequency band from radio to γ-ray.

The X-ray emission of the PWN is emitted by particles with the highest energy in the nebula. In the standard 1–D model constructed by Kennel & Coroniti (hereafter the KC model), the X-ray emitting particles lose their energy quickly by radiative cooling, so the X-ray emission region is smaller than the lower frequency one. As this is consistent with the observational fact that the X-ray image of the Crab Nebula is smaller than the optical or radio ones, so the KC model has been accepted widely.

However, PWNe 3C 58 and G21.5-0.9 show the feature that the extent of the X-ray emission is similar to the extent of the radio emission. This implies that the KC model has a defect as a PWN model, but there are no studies that test whether the KC model reproduces both the volume-integrated spectrum and the radial profile of the surface brightness, simultaneously. In this thesis, we aim to construct a consistent model of the radial profile and emission in PWNe.

First of all, we revisit the KC model and apply it to the Crab nebula, 3C 58 and G21.5-0.9. We conduct a detailed investigation of the parameter dependence of the KC model. As a result, we find that the parameters constrained by the entire spectrum lead to a smaller X-ray nebula than observed one. We also test the case that reproduces only the observations in X and γ-rays, ignoring the radio and optical components. In this case, there are parameter sets that reproduce both the spectrum and emission profile, but the advection time to the edge of the nebula becomes much smaller than the age. Our discussion clarifies that the KC model has severe difficulty to reproduce both the volume-integrated spectrum and the surface brightness simultaneously.

The main assumptions in the KC model are steady state, spherical symmetry and toroidal magnetic field configuration. In order to investigate the validity of the steady-state approximation of the nebula, we solve the time-dependent and spherical symmetric magnetohydrodynamics equations taking into account the effect of the spin-down evolution of the central pulsar and the surrounding supernova remnant. Although the steady KC model ignores the time-dependent effect, it showed a very good agreement on both the fluid structure and the emission calculated in the time-dependent 1-D model.

Next, we consider an effect of a turbulent magnetic field in PWNe. We construct a model that includes the disturbed field as a diffusion process, which is not considered in the KC model in the particle transport process. The previous diffusion models adopted a large diffusion coefficient that makes diffusion more efficient than advection in order to reproduce the large extent of the X-ray. In such a case, the energy and momentum flux due to the diffusion process can no longer be neglected, so a self-consistent model to satisfy the momentum and energy conservation laws is needed. We

present a self-consistent steady 1-D model including the advection, the diffusion, radiative and adiabatic cooling, and the back reaction of the diffusion. We find that the back reaction of the particle diffusion modifies the flow profile. The photon spectrum and the surface brightness profile are different from the model calculations without the back reaction of the particle diffusion. By fitting the spectra of PWNe 3C 58 and G21.5-0.9, we determine the parameter sets and calculate the radial profiles of X-ray surface brightness. For both the objects, obtained profiles of X-ray surface brightness and photon index are well consistent with observations.

The extent of the X-ray emission region is as large as that of the radio in 3C 58 and G21.5-0.9, which can not be explained by KC model. Therefore the spatial diffusion seems indispensable to reproduce the X-ray extent. The time-dependent effect is not important for solving the problem of X-ray extent, but is important for the middle and old aged PWNe due to the interaction between the PWN and the SNR reverse shock. Furthermore, our diffusion model suggests that particles escaped from the nebula significantly contribute to the γ-ray flux. A γ-ray halo, which is similar to observed in the Geminga PWN, larger than the radio nebula has been predicted in our model. The spatially resolved observations are important to constrain the transport of particles and the hydrodynamics of PWNe.

Contents

1 Introduction **1**
- 1.1 Pulsar . . . 3
- 1.2 Pulsar Wind nebula . . . 5
- 1.3 Structure of this thesis . . . 9

2 Theoretical background **11**
- 2.1 Spin-down of Pulsars . . . 11
- 2.2 Pulsar Magnetosphere . . . 12
  - 2.2.1 Unipolar Induction . . . 12
  - 2.2.2 Particle Generation . . . 14
  - 2.2.3 Structure of the Pulsar Magnetosphere; Intuitive Understanding . . . 16
  - 2.2.4 Axisymmetric Magnetosphere . . . 18
  - 2.2.5 Gap Region and Particle Acceleration . . . 24
  - 2.2.6 Emission Mechanism of the Pulsar . . . 26
- 2.3 Pulsar Wind . . . 26
  - 2.3.1 Conservation Laws along the Field Line . . . 27
  - 2.3.2 Bernoulli Equation . . . 28
  - 2.3.3 Magnetic Nozzle . . . 29
  - 2.3.4 Self-collimation and Wind Acceleration . . . 29
- 2.4 Pulsar Wind Nebula . . . 30
  - 2.4.1 General description . . . 30
  - 2.4.2 The Sigma Problem . . . 32

3 Revisiting the Kennel & Coroniti Model **33**
- 3.1 Introduction . . . 33
- 3.2 Model . . . 36
  - 3.2.1 Magnetohydrodynamics of PWNe . . . 36
  - 3.2.2 Broadband emission model of PWNe . . . 38
- 3.3 Parameter Dependence in the model . . . 41
  - 3.3.1 Characteristic frequencies and energies . . . 41
  - 3.3.2 Parameter Dependence: termination shock radius . . . 42
  - 3.3.3 Parameter Dependence: magnetization . . . 45
- 3.4 Application to the Observed Source . . . 47
  - 3.4.1 The Crab Nebula . . . 47
  - 3.4.2 3C 58 and G21.5-0.9 . . . 48
  - 3.4.3 Alternative Model . . . 53
- 3.5 Discussion . . . 53

3.6 Conclusion . . . 54

4 Time-dependent Model 56
4.1 Introduction . . . 56
4.2 Basic Equations . . . 59
4.2.1 Fluid Equations . . . 59
4.2.2 Advection equation . . . 60
4.2.3 Initial and Boundary Conditions . . . 61
4.3 Result . . . 61
4.4 Discussion . . . 66
4.5 Conclusion . . . 68

5 Model with Diffusion and its Back-reaction 69
5.1 Introduction . . . 69
5.2 Pulsar Wind Model with particle diffusion . . . 72
5.2.1 Central Idea . . . 72
5.2.2 Fluid equations . . . 73
5.2.3 Diffusion-Advection equation . . . 75
5.2.4 Spherical steady nebulae . . . 75
5.3 Detailed Calculation Method . . . 77
5.4 Parameter Dependence: diffusion coefficient . . . 77
5.5 Application to the Observed Source . . . 85
5.6 Discussion . . . 90
5.7 Conclusion . . . 91

6 Summary and Future Prospects 92

A Detail Review of a 1–D steady MHD flow 95
A.1 Relativistic MHD Equations . . . 95
A.1.1 Conservation laws in relativistic MHD . . . 95
A.1.2 MHD Systems . . . 96
A.2 Rankine–Hugoniot Condition in Relativistic MHD . . . 96
A.2.1 Assumptions . . . 96
A.2.2 Number Conservation . . . 97
A.2.3 Magnetic Flux Conservation . . . 97
A.2.4 Energy and Momentum Conservation . . . 98
A.2.5 Equation of State . . . 98
A.2.6 Compression Ratio . . . 99
A.2.7 Flow Velocity at the Downstream . . . 100
A.2.8 Downstream Magnetic Field and Number Density . . . 100
A.2.9 Downstream Pressure and Temperature . . . 101
A.2.10 Dependence on σ . . . 101
A.3 Steady Solution to the Relaticistic 1–D MHD equations . . . 103
A.3.1 Basic equations . . . 104
A.3.2 Derivation of 1–D Steady Flow Solution . . . 106
A.3.3 Asymptotic Value . . . 108
A.3.4 Other Quantities . . . 108

B Leptonic Emission **110**
B.1 Synchrotron radiation 110
B.2 Inverse Compton scattering 112

C Particle Acceleration **115**
C.1 Diffusive shock acceleration 115
C.2 DSA in Relativistic shock 116

D Notes on the Ideal MHD Condition in the Diffusion Model **118**

Chapter 1

Introduction

The supernova explosion observed by humankind on July 4, 1054 was the moment of the birth of the neutron star called the Crab pulsar (see Hester, 2008, for review). The Crab pulsar emits the pulsed signal with a period of 33 ms in wide frequency band from the radio band to the γ-ray (Abdo et al., 2010a). Figure 1.1 shows pulse profiles of the Crab pulsar in various band. The Crab pulsar is slowing down its rotation with a rate of 36 ns per year (Lyne et al., 2015). If the Crab pulsar is a typical neutron star, namely which has a mass of 1.4 $M_\odot$ and a radius of 10 km, this rotation energy loss rate is estimated as 5×10^{38} erg s^{-1}, which is about 10^5 times larger than a luminosity of the sun. This energy loss rate is called a spin-down luminosity. The luminosity of the pulsed emission

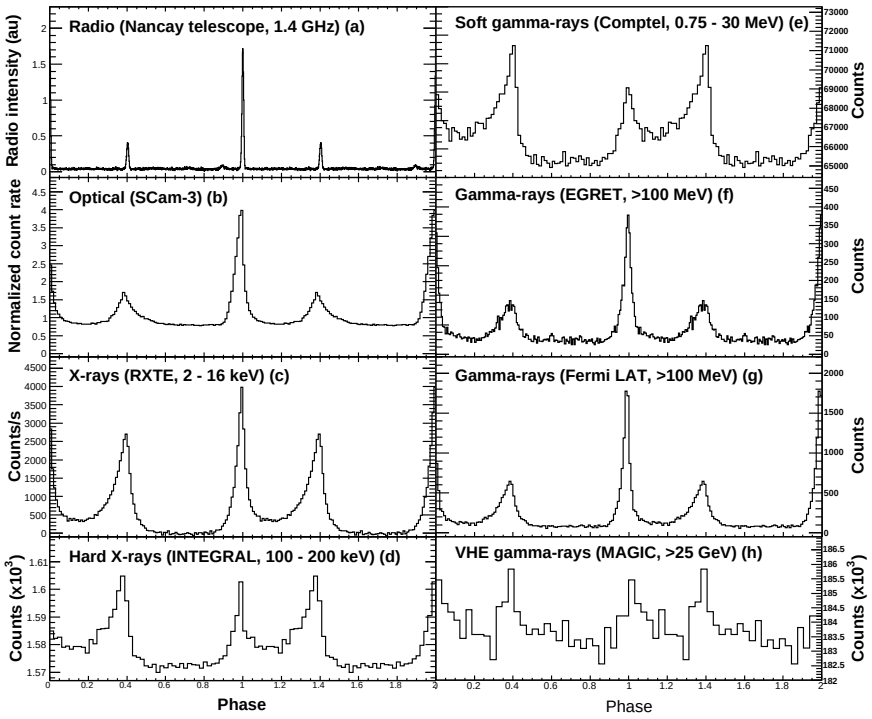

Figure 1.1: Pulse profiles of the Crab pulsar at various frequencies. The horizontal axis is the pulse phase, and light curves for two cycles are shown. The figure from Abdo et al. (2010a). ©AAS. Reproduced with permission.

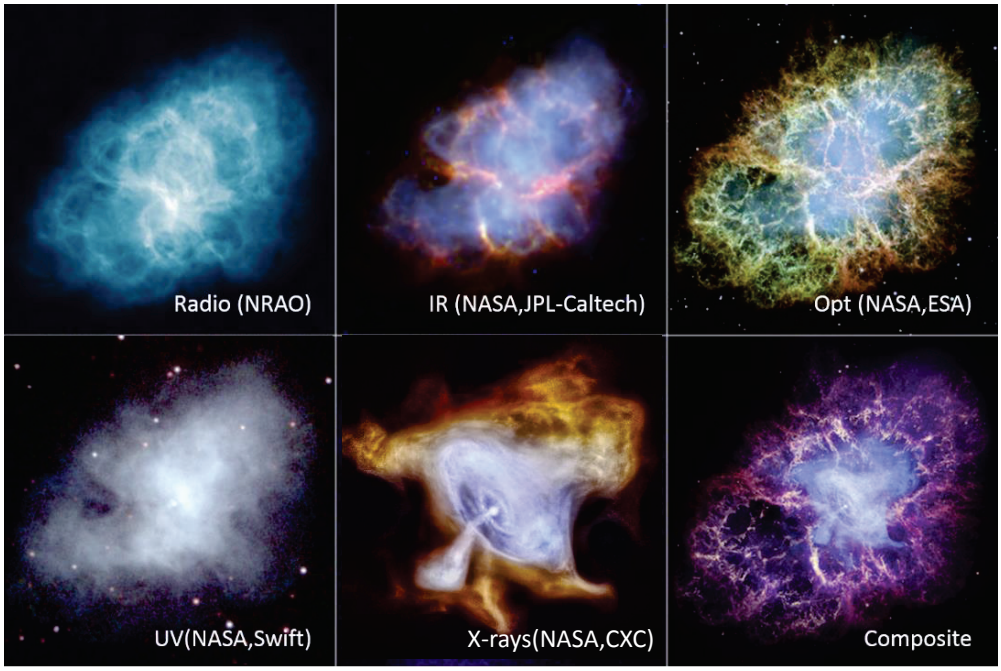

Figure 1.2: The picture of the Crab nebula at various frequencies. The picture denoted "Composite" consists the superposition of three frequency band. The X-ray image is shown in blue, the optical image is shown is in red and yellow and the infrared image is shown in purple. In the X-ray image, a bipolar long slender structure called a "jet" and a structure that surrounds the jet called "torus" are visible. (Credits; Radio:NRAO/AUI and M. Bietenholz; Infrared: NASA/JPL-Caltech/Univ. Minn.; Optical: NASA/ESA/ASU/J.Hester & A.Loll; UV:NASA/Swift/E. Hoversten, PSU; X-ray and composite:NASA/CXC/SAO;)

is only about 1% of the spin-down luminosity, and most of the energy is released in a different way.

Around the Crab pulsar, there is the Crab nebula which extends to about 2 pc and shows a broadband spectrum from radio to γ-ray. Figure 1.2 shows a picture of the Crab nebula at various frequencies. The Crab Nebula has been observed so many times because it is enough bright at all observable wavelength bands. In Figure 1.3, spectra of the Crab Nebula and pulsar are shown as blue and black points, respectively. As seen in the figure, since the luminosity of the Crab nebula is much brighter than the pulsed emission, the spin-down luminosity of the Crab pulsar is thought to be mainly used for forming the Crab nebula (Gold, 1969). In addition, the Crab nebula is expanding at a speed of 2000 km s^{-1} pushing the interstellar matter and supernova ejecta away. Assuming that the surrounding material has a temperature of about 1 keV and a density of about 1 cc^{-1}, the power of expansion is estimated as several 10^{38} erg s^{-1}, which is comparable with the spin-down luminosity. Hence, it is considered that the Crab pulsar converts its rotational energy to the kinetic energy of plasma flow to form the Crab nebula.

The nebula around a pulsar like the Crab nebula is called the pulsar wind nebula. It is known that pulsar wind nebulae contain the very high energy electrons and positrons, which emit the non-thermal emission while propagating in the nebula. In this thesis, we aimed to understand the spatial structure of the nebula and the propagation process of particles by constructing a model that explains not only the emission spectrum of the pulsar wind nebula but also the radial profile of the surface brightness.

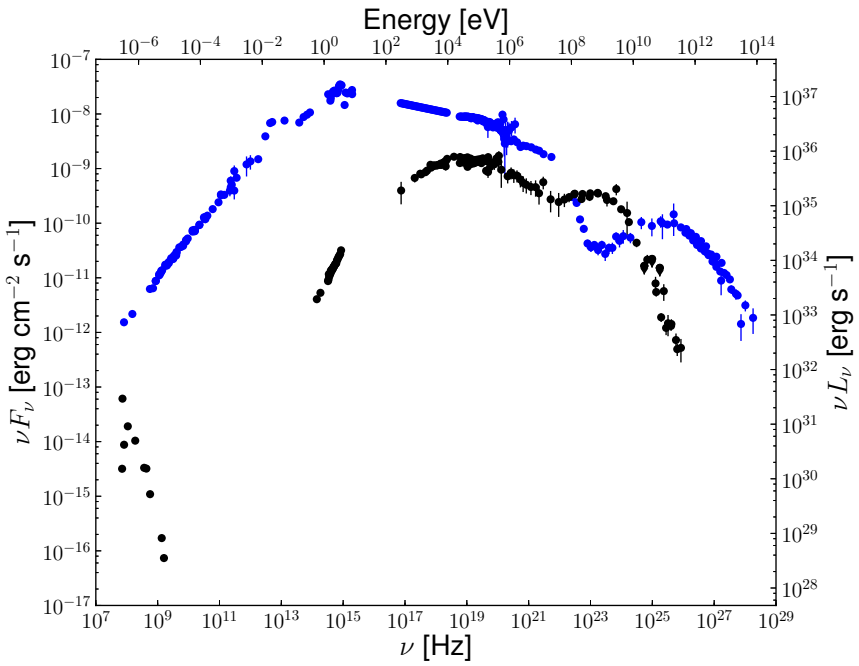

Figure 1.3: The photon spectrum of the Crab nebula (blue) and the Crab pulsar (black). The figure from Bühler & Blandford (2014). The emission of the Crab nebula is thought to be due to inverse Compton scattering for γ-ray and synchrotron radiation from radio to X-rays. The emission of the Crab pulsar is thought to be due to synchrotron radiation from optical to X-rays, and inverse Compton scattering and curvature radiation for γ-rays. Since the spectrum of the radio emission of the Crab pulsar is a clearly separate component, it is thought to be due to the another process (coherent emission). Reproduced with permission by IOP Publishing. All rights reserved.

1.1 Pulsar

Pulsars, which are highly magnetized rotating neutron stars produced after supernova explosions, were first discovered in 1967 as a radio source with extremely precise periodicity (Hewish et al., 1968). The neutron star is extremely dense stars whose density is close to the nuclear density, $\sim 10^{14} g$ cc^{-1}. This periodic signal, which is corresponding to the rotation period, is typically $P \sim 1$ s. Furthermore, since the magnetic flux is compacted by the supernova explosion, neutron stars are expected to have a strong magnetic field (Pacini, 1967). The typical strength of magnetic field on the neutron star surface is estimated as $B_{\rm NS} \sim 10^{12}$G.

Pulsars are classified by the energy source of its emission as follows:

Rotation powered A pulsar converting the rotation energy of the star into the emission. It performs a non-thermal emission in a very wide frequency band.

Accretion powered A pulsar in a binary system. The energy source is the gravitational energy of an accreting matter from a companion star. It mainly emits thermal radiation in X-rays.

Magnetic powered A pulsar that emits X-rays with luminosity that far exceeds the spin-down luminosity of the star. It also called as the "magnetar". It is thought that X-rays are emitted

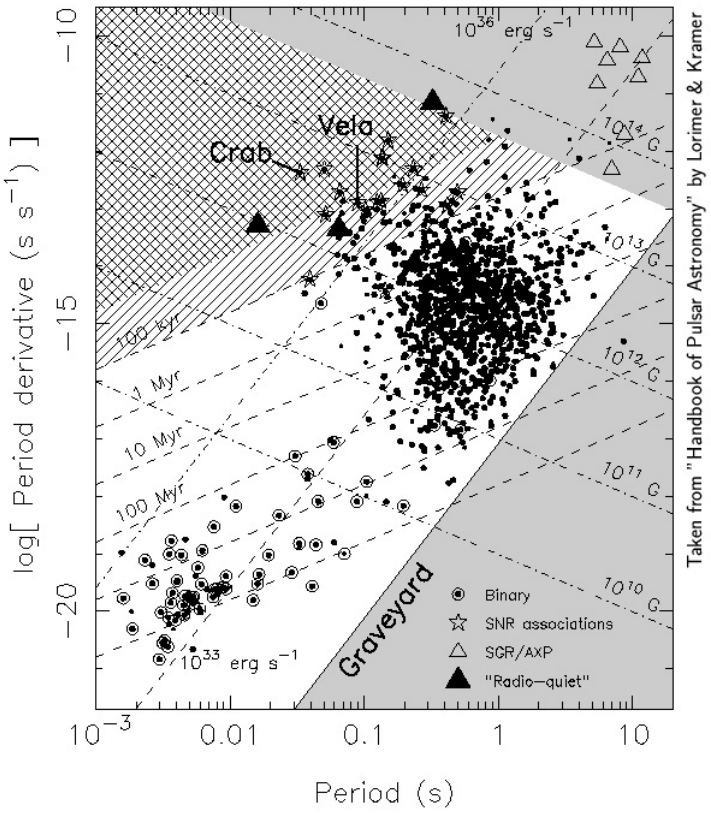

Figure 1.4: The P-$\dot{P}$ diagram from Lorimer & Kramer (2004), which is plotted for each pulsar with the period of the pulsar P on the horizontal axis and the rate of change of the period $\dot{P}$ on the vertical axis. The dashed and dash–dotted lines denote the characteristic age and the surface magnetic field, respectively. The spin-down luminosity, estimated from P and $\dot{P}$, is also shown.

by releasing the energy of the magnetic field via some sort of a dissipative process (e.g., magnetic reconnection).

Thermal powered A pulsar performing an X-ray emission by the thermal energy of the star itself.

For example, the Crab pulsar is classified in the rotation powered pulsar. In this thesis, we discuss only the rotation powered pulsar.

In rotation powered pulsars, not only the rotation period P but also the temporal change of the period (spin-down rate) $\dot{P}$ is measured very accurately. Figure 1.4 is the P-$\dot{P}$ diagram, which is plotted for each pulsar with P as the horizontal axis and $\dot{P}$ as the vertical axis (Lorimer & Kramer, 2004). The fact that the spin-down occurs means that the pulsar releases rotational energy through some kind of processes. A pulsar produces an induced electric field by its own magnetic field and rotation, and generates electron–positron plasma in the magnetosphere (pulsar magnetosphere). Part of this induced electric field is used to accelerate particles, which eventually cause pulsed emission. As mentioned above, in the Crab nebula, the conversion efficiency to radiation is about 1 %, and the majority of the spin-down luminosity is converted to the bulk kinetic energy of the magnetospheric plasma.

The difficulty of the study of pulsars is partially because that the various processes occur in very small region, $\sim 10^{10}$ cm. There are two methods for studying such a phenomena. One is

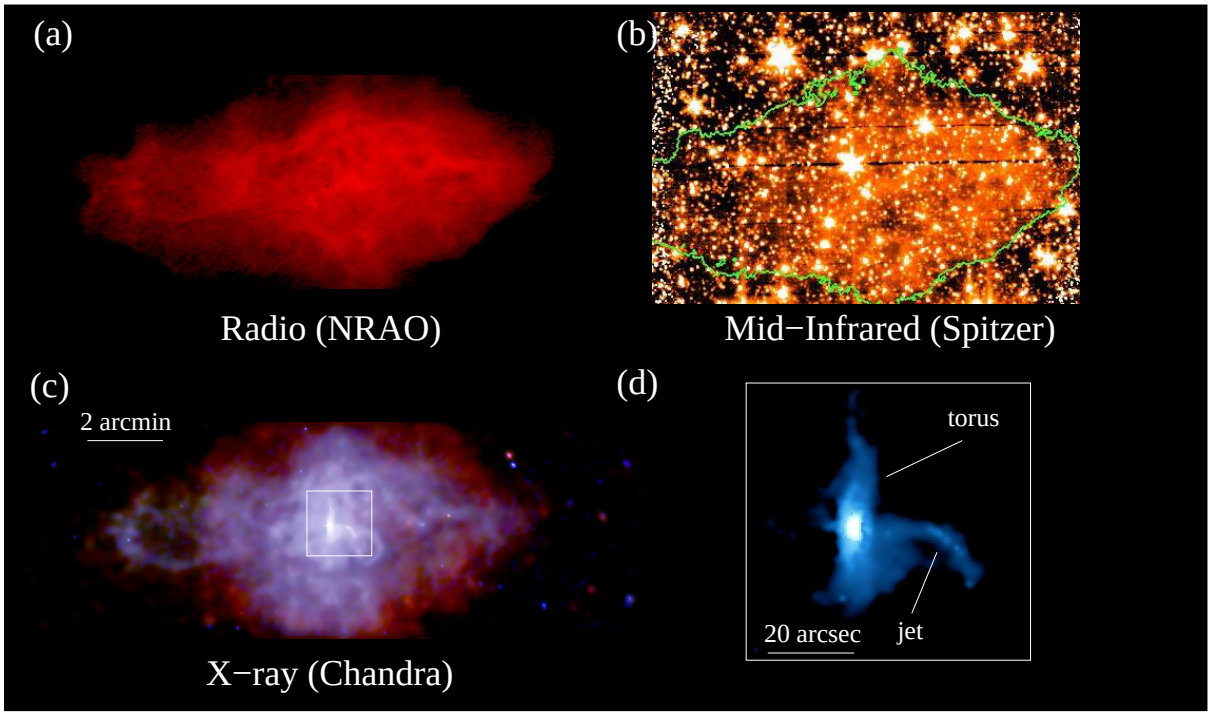

Figure 1.5: Pictures of the pulsar wind nebula 3C 58 seen at various frequencies. The emission region of the X-ray (c) is as large as the emission region of the radio band (a). Picture (b) is an image taken by infrared. In infrared band, the pulsar wind nebula is faint compared to the background starlight. Picture (d) is an enlarged view of the center of Picture (c). Simlar to the Crab nebula, the jet and torus (see Figure 1.2) are also observed in 3C 58. (Radio (VLA) : Reynolds & Aller (1988); Infrared (Spitzer) : Slane et al. (2008); X-ray (Chandra) : Slane et al. (2004);The figure from Gaensler & Slane (2006).)

to investigate pulse shape, spectrum, polarization etc of pulsed emission to uncover the pulsar magnetosphere. For example, the two-peak pulse shape shown in Figure 1.1 has information about the viewing angle and the latitude of the emitting area in the magnetosphere (Bai & Spitkovsky, 2010). The other method is to investigate the pulsar wind nebulae, from which we can obtain bulk properties of the outflowing plasma.

1.2 Pulsar Wind nebula

The nebula formed around the pulsar is ubiquitous. Such a nebula is called a pulsar wind nebula (PWN), and 87 such systems are found at present [1]. Figure 1.5 shows images of one of the PWNe, 3C 58 in radio (Reynolds & Aller, 1988), infrared (Slane et al., 2008), and X-rays (Slane et al., 2004). At the center of this, there is a pulsar called PSR J0205+6449, whose spin-down luminosity is 2.7×10^{37} erg s^{-1} (Murray et al., 2002). PWNe are characterized by a center-filled morphology caused by confinement in a supernova remnant (SNR), which is outflowing ejecta from the progenitor star. PWNe have typically harder radio spectra than the shell-type supernova remnants, which do not accompany pulsars (Weiler & Panagia, 1978). Most PWNe have benn detected as spatially extended

[1] http://www.physics.umanitoba.ca/snr/SNRcat/

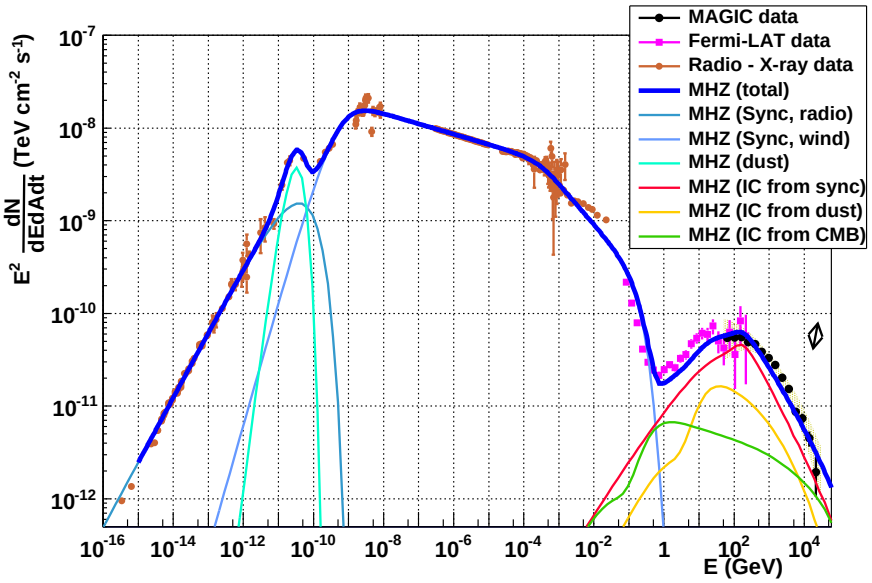

Magnitude	Crab Nebula
Magnetic field	
B (μG)	143
Dust component	
$\ln(N_{\rm dust})$	-29.9
$T_{\rm dust}$ (K)	98
$u_{\rm dust}$(eV cm^{-3})	1.2
Radio electrons	
Spectral index	1.6
$\ln N_r$	119.8
$\gamma_r^{\rm min}$	22
$\gamma_r^{\rm max}$	1.6×10^5
Wind electrons	
Spectral index (low)	3.2
Spectral index (high)	3.8
$\ln N_w$	78.5
$\gamma_w^{\rm min}$	4.0×10^5
$\gamma_w^{\rm break}$	2.9×10^8
$\gamma_w^{\rm max}$	7.2^9

Figure 1.6: The spectrum of the Crab nebula and fitting result (Aleksić et al., 2015). The emission model is given by a mdoel of Meyer et al. (2010) (constant B-field model). Assuming the nebula as a uniform sphere, they fitted the spectrum of the nebula with synchrotron radiation and inverse Compton scattering. The fitting parameters are summarized in the table on the right. Electrons are considered as two species of "radio electrons" emitting the low energy radiation and "wind electrons" emitting the high energy radiation. The total number of the particles is dominated in the particles with the Lorentz factor of $\gamma_r^{\rm min}$ in radio electrons. The total energy of the particles is dominated in the particles with the Lorentz factor of $\gamma_w^{\rm min}$ in wind electrons. Reprinted from Aleksić et al. (2015). Copyright 2019, with permission from Elsevier.

sources in radio and X-rays. While the radio spectral index is almost spatially homogeneous (e.g., Bietenholz et al., 1997; Bietenholz & Bartel, 2008), the X-ray spectral index increases with the distance from the pulsar (e.g., Bocchino & Bykov, 2001; Slane et al., 2004; Schöck et al., 2010). Recently, PWNe are found to be very bright sources in also TeV γ-rays (Kargaltsev et al., 2013). PWNe are the most detected galactic sources in the energy band of TeV γ-rays. Almost all of PWNe which are not detected by Chandra X-ray Observatory were found in H.E.S.S. Galactic plane survey.

Since the photon spectrum of PWNe is non-thermal, it is implies to exist of high energy particles. The emission of the PWN is explained by the synchrotron radiation (Rees & Gunn, 1974) and inverse Compton scattering (de Jager & Harding, 1992) from such high-energy electrons and positrons. Figure 1.6 shows the broadband emission spectrum of the Crab nebula with a model calculated with the parameters in the table on the right of the Figure 1.6, assuming the inside of the nebula is uniform (Aleksić et al., 2015). In the case of the Crab nebula, the resultant magnetic field in the nebula is 143 μG, the typical electron energy is 200 GeV and the maximum energy is 4 PeV. If the nebula is a sphere with a radius of 2 pc, the total energy of the magnetic field is about 10% of the energy of the particles.

In order to take into account the effect of expansion of the nebula, the time-dependent 1-zone model, which treats the nebula as a uniform radiation area with expansion, has been discussed. In such a study, to explain the observed emission spectrum of the Crab nebula, the energy of the magnetic field must be about 0.5 % of the energy of the particle (e.g., Tanaka & Takahara, 2010). Even if the model of the nebula is extended to a one-dimensional (1D) model, where radial structure

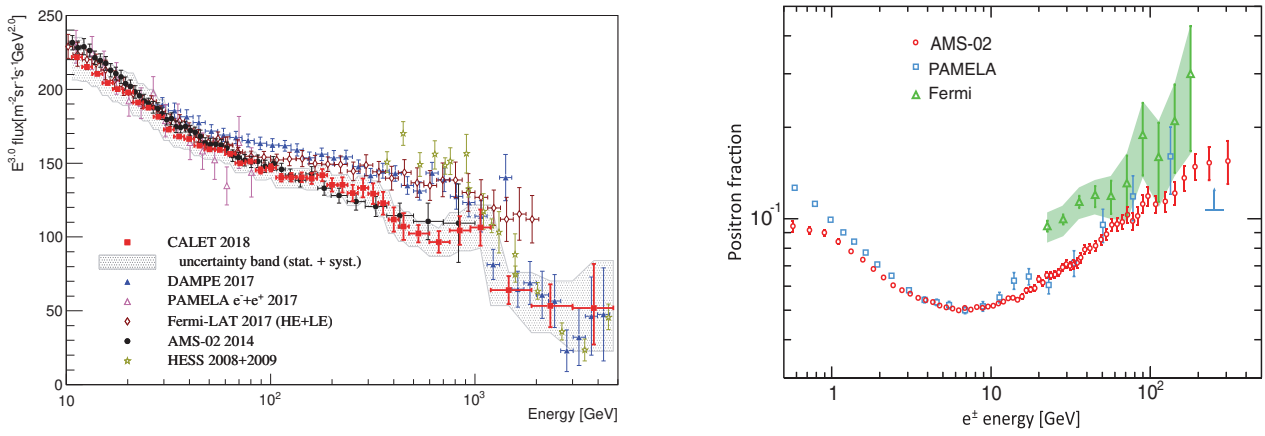

Figure 1.7: (Left) The cosmic-ray energy spectrum of electrons and positrons. (CALET : Adriani et al. (2018a); DAMPE : DAMPE Collaboration et al. (2017); fermi : Abdollahi et al. (2017); Hess : Aharonian et al. (2009); PAMELA : Adriani et al. (2018b)) (Right) The energy dependence of the ratio of the number of positrons to the sum of the number of electrons and positrons. Reprinted figures with permission from Aguilar, M., Alberti, G., Alpat, B., et al., Physical Review Letters, 110, 141102, 2013 (Left) and Adriani, O., Akaike, Y., Asano, K., et al., Physical Review Letters, 120, 261102, 2018a (Right). Copyright 2019 by the American Physical Society.

is considered, a similar magnetic field is derived.

On the other hand, in the pulsar magnetosphere, the magnetic energy largely dominates. It is very difficult to dissipate the magnetic energy to a value the nebula models suggested. This problem is called the sigma problem and is a long standing problem for pulsars and pulsar wind nebulae (see Section 2.4.2). Namely, why can the energy of the magnetic field be converted so efficiently to the kinetic energy of the plasma? This kind of question also appears in context of the acceleration mechanism of relativistic jets in blazar jets, so that this problem is common in various high-energy objects.

PWNe are also very important in considering the origin of leptonic (electrons and positrons) cosmic-rays detected on the earth. Since leptonic cosmic-rays rapidly lose their energy by radiative cooling while propagating in the interstellar space, high-energy electrons should be originated from nearby sources. If the source of cosmic-rays is in nearby the earth, a spectral break or an anisotropy in the arrival direction are detected (e.g., Ioka, 2010). The left panel of Figure 1.7 shows the spectrum of the observed leptonic cosmic-rays. There seems to be a break in the vicinity of 1 TeV in the observed spectrum, and it is actively discussed what it originates from. Adopting the fiducial diffusion coefficient, such TeV electrons/positrons travel a few hundreds pc before they lose their energy via radiative cooling.

Another important observational hint is the energy dependence of the number ratio of positrons to the total leptonic cosmic-rays (Aguilar et al., 2013; Adriani et al., 2018b). Positron cosmic-rays are secondary particles, which generated while a cosmic-ray protons propagating in the interstellar space. In this scenario, the relative amount of positrons to electrons is predicted to decrease with energy (e.g., Moskalenko & Strong, 1998). However, as shown in the right panel of Figure 1.7, the fraction of positrons turns to increase at an energy of above ~ 10 GeV. This suggests that there is another type of sources releasing positrons as primary particles. Promising sources of such positrons are nearby PWNe. Since PWNe are also in the vicinity of 300 pc from the earth, it can contribute

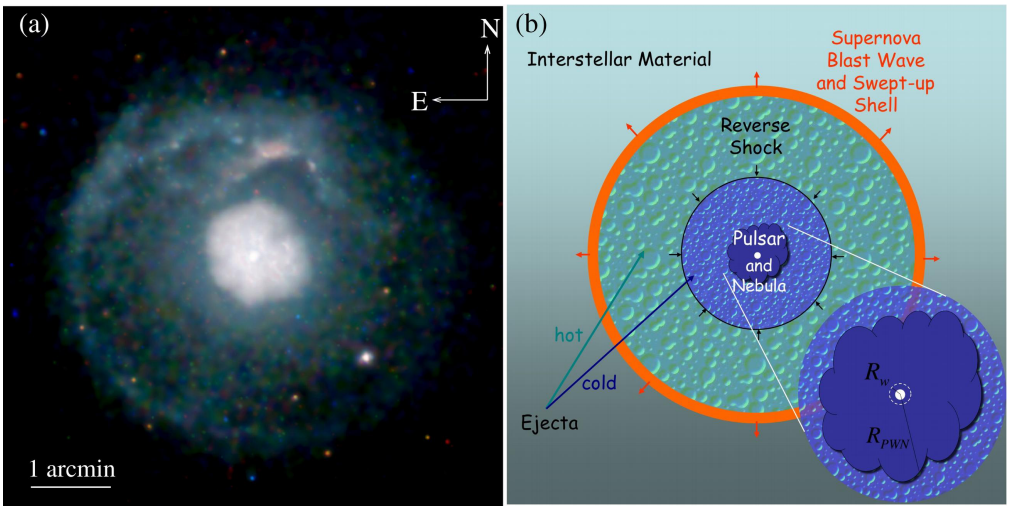

Figure 1.8: (Left) The X-ray image of the pulsar wind nebula G21.5-0.9 taken by Chandra (Matheson & Safi-Harb, 2005). The pulsar wind nebula is a bright part of the center diameter of about 1 arcmin. The halo that spreads faint around the nebula is a shell type supernova remnant (i.e. originated from supernova ejecta). As seen in this picture, a pulsar wind nebula is wrapped in a supernova remnant. Reproduced with permission by IOP Publishing. All rights reserved. (Right) The schematic view of the pulsar wind nebula and supernova remnant. The supernova ejecta propagates as a blast wave in the ISM. On the inside of the blast wave, the reverse shock propagates towards the center, and ejecta is divided into hot and cold before and after the shock. The pulsar wind nebula spreads out while pushing the cold ejecta. As a back-reaction to that, the reverse shock, which is written as a circle with radius R_w in the figure, traveling toward the pulsar wind nebula. The reverse shock balances with the ram pressure of the pulsar wind and becomes a standing shock. Figures taken from Gaensler & Slane (2006).

sufficiently to the flux of leptonic cosmic-rays measured on the earth. Furthermore, since PWNe contain as many positrons as electrons, if nearby PWNe contribute to the leptonic spectrum, the fraction of positrons can be also explained. If it can be shown that such leptonic cosmic-rays flew directly from nearby PWNe, this will give a solution for the first time to the long-standing question: "where is the source of the cosmic-ray?".

However, since PWNe do not release electrons and positrons directly to the interstellar space, such a scenario can not be naively established. Figure 1.8 represents a schematic diagram of a PWN. Since there is a supernova remnant around a PWN, the plasma from the pulsar is confined. Furthermore, since the magnetic field inside the PWN is stronger, electrons and positrons lose their energy due to radiative cooling, and high energy particles can not even reach supernova remnants. Therefore, it is not trivial whether high energy electrons and positrons are released from PWNe.

The hypothesis that electrons and positrons can not reach the edge of the nebula is based on the fact that the X-ray emission region of the Crab nebula is much smaller than the radio and optical emission region (see Figure 1.2). This means that high-energy X-ray emitting particles lose their energy before reaching at the edge. However, as shown in Figure 1.5, in 3C 58, the emission region of the radio and the emission region of X-rays seem to be similar size. Figure 1.9 shows the radial distribution of the surface brightness of 3C 58 at radio and X-rays. The X-ray emission is a synchrotron radiation from the highest energy particles inside the nebula, while radio emission is radiation from a low energy population. As shown in Figure 1.9, the fact that the radio emission

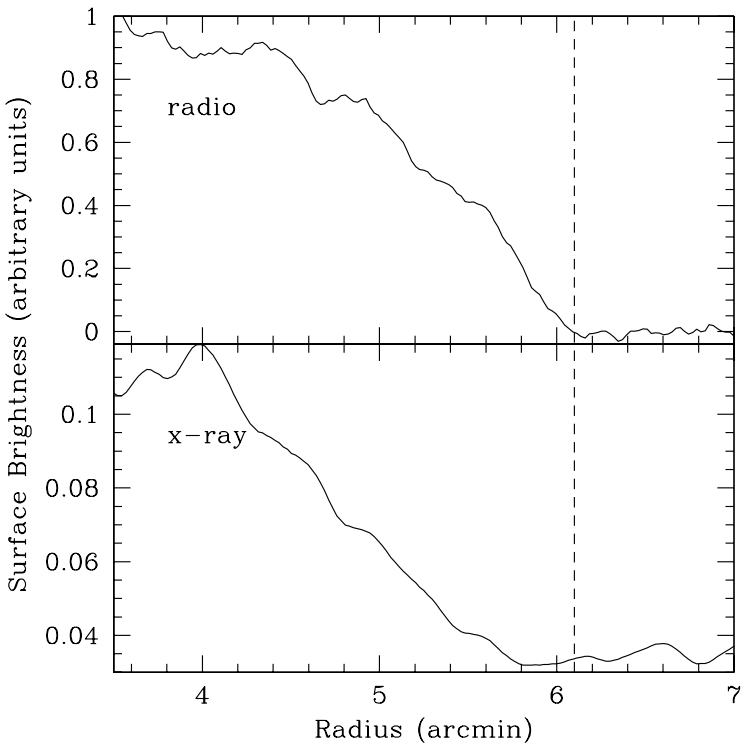

Figure 1.9: The surface brightness of the 3C 58 at the radio band (top) and the X-rays (bottom). The figure from Slane et al. (2004). ©AAS. Reproduced with permission.

region spread to the similar extent as the X-ray emission region suggests that high energy particles are transported without radiative cooling. However, under the magnetic field strength suggested from the spectrum of the nebula, this seems difficult.

1.3 Structure of this thesis

A pulsar wind nebula contains particles with very high energy and radiates in various frequency bands. Since a pulsar wind nebula can be observed spatially resolved in many frequency bands, we can discuss the propagation of such high energy particles with using the spatial information of emission. As we have discussed above, there remain several unsolved problems in the radial profile of PWNe. In this thesis, we try to resolve this problem. We model pulsar wind nebulae in space 1-D to reveal the property of the particle propagation in the nebula.

The most accepted 1-D model of the pulsar wind nebula is the Kennel & Coroniti model (Kennel & Coroniti, 1984a,b, ;hereafter KC model). The X-ray emission of the pulsar wind nebula is emitted by particles with the highest energy in the nebula. If the KC model is valid, the X-ray emitting particles lose energy quickly by the synchrotron cooling, so that the X-ray emission region is smaller than the lower frequency one. This is consistent with the small X-ray emission region of the Crab nebula. The nebula 3C 58 shows the feature that the extent of the X-ray emission is the same as the extent of the radio emission. However, there is no previous study that discuss the photon spectrum and the surface brightness simultaneously. We need to revisit the applicability of the KC model.

The structure of this thesis is as follows. In Chapter 2, we review the standard understanding

for pulsar, pulsar magnetosphere and pulsar wind. In Chapter 3, following my published paper Ishizaki et al. (2017), we test whether the KC model can explain the spatial structure of PWNe or not. There, we find that the KC model can not reproduce the entire spectrum of the nebula and the X-ray surface brightness simultaneously, so that we need to revise the KC model. In Chapter 4, we examine the validity of the steady-state assumption of the KC model using a 1-D time-dependent model. We develop a numerical code to follow the temporal evolution of a relativistic outflow interacting with a supernova ejecta. Our results show that the steady KC model is a good approximation given a boundary condition. Our numerical code is a powerful tool to investigate a long term evolution of PWNe and its emission. However, the effect of temporal evolution does not resolve the extended X-ray emission problem. In Chapter 5, according to our published paper Ishizaki et al. (2018), we take into account the particle diffusion effect with its back-reaction on the flow. We find that the problem of the X-ray extent can be solved, when the diffusion is efficient. We also show that the emission spectrum can be affected by the back-reaction to the flow, if the diffusion is significant. In Chapter 6, we summarize our results and describes future prospects.

In this thesis we use the Gaussian-cgs units, and the signature of the metric $(-,+,+,+)$.

Chapter 2

Theoretical background

2.1 Spin-down of Pulsars

Let us discuss the evolution of pulsar rotation with a simple model. First of all, by using P and $\dot{P}$, a rotational energy loss per unit time (the "spin-down luminosity" $L_{\rm sd}$) can be estimated as follow:

$$L_{sd} = 4\pi^2 I \frac{\dot{P}}{P^3} \sim 3.9 \times 10^{31} \text{ erg s}^{-1} \left(\frac{P}{1 \text{ s}}\right)^{-3} \left(\frac{\dot{P}}{10^{-15} \text{ s s}^{-1}}\right), \tag{2.1}$$

where I is the moment of inertia of the pulsar, and if the pulser is a uniform sphere with a mass of 1.4 $M_\odot$ and a radius of 10 km, it can be found that $I = 10^{45}$ g cm^2. For the rotation frequency $\nu = P^{-1}$ and its change rate $\dot{\nu}$, the following relationship is assumed:

$$\dot{\nu} = -K\nu^n \tag{2.2}$$

where n is a constant, which is called braking index, determined by reflecting the physics of energy loss. For example, in the case where the energy loss is caused by magnetic dipole radiation or a pulsar wind from the aligined rotator (as will be described later), $n = 3$. The braking index can be obtained from observable quantities as $n = \nu\ddot{\nu}/\dot{\nu}^2$, and values such as $n = 1.4 - 2.9$ are obtained (e.g., Livingstone et al., 2007; Lyne et al., 1996; Roy et al., 2012a), but few pulsars are measured.

By integrating the equation (2.2), the temporal evolution of the pulser rotation can be obtained. Substituting $P = 1/\nu$, the equation (2.2) is as follows:

$$\dot{P} = KP^{2-n}. \tag{2.3}$$

Integrating from the birth to the current age $t_{\rm age}$, we obtain the following result as

$$t_{\rm age} = \frac{P}{\dot{P}\,(n-1)} \left(1 - \left(\frac{P_0}{P}\right)^{n-1}\right), \tag{2.4}$$

where P_0 is the rotation period when the pulsar is born. If the period P_0 at birth is sufficiently shorter than the current period P, the age of the pulsar can be estimated by the following expression:

$$t_c = \frac{P}{\dot{P}\,(n-1)} = 1.6 \times 10^7 \text{ yr} \left(\frac{P}{1 \text{ s}}\right) \left(\frac{\dot{P}}{10^{-15} \text{ s s}^{-1}}\right)^{-1}. \tag{2.5}$$

t_c with $n = 3$ is called the "characteristic age" of the pulser and is often used for rough estimate of the age of the pulsar. Furthermore, the time evolution of the period is written as

$$P(t) = P_0 \left(1 + \frac{t}{t_0}\right)^{\frac{1}{n-1}}, \tag{2.6}$$

where t_0 is the characteristic age at the time of birth of the pulsar, namely,

$$t_0 = \frac{P_0}{\dot{P}_0 (n-1)}. \tag{2.7}$$

The time evolution of spin-down luminosity $L_{\rm sd}$ is written as

$$L_{\rm sd} = L_0 \left(1 + \frac{t}{t_0}\right)^{\frac{1+n}{1-n}}, \tag{2.8}$$

where L_0 is the spin-down luminosity at the time of birth of the pulsar. As can be seen from above equation, time dependence of the spin-down luminosity is weak for the young pulsar that satisfies $t_{\rm age} \lesssim t_0$.

2.2 Pulsar Magnetosphere

2.2.1 Unipolar Induction

One may consider that the space outside a pulsar is vacuum. However, surroundings of the neutron star are dominated by electromagnetic force rather than gravity so that, a plasma filled magnetosphere is formed around the pulsar. First of all, in this section, we show that the surroundings of neutron star is not vacuum, by following Goldreich & Julian (1969).

We adopt following assumptions:

- The neutron star is a perfect conductive sphere.
- The magnetic field structure outside the neutron star is dipole.
- The magnetic field structure inside the star is uniform.
- The rotation of axis and the magnetic pole coincide.
- Steady state.
- The surroundings of the neutron star is vacuum. (This is a null hypothesis.)

Here we use the polar coordinate system (r, θ, ϕ), if necessary, the cylindrical coordinate system (ϖ, θ, z) are also used with the direction of the rotation axis as the z axis. The magnetic field is written as:

$$\boldsymbol{B}_{\rm in} = B_0 \boldsymbol{e_z}, \tag{2.9}$$

for inside the star, and

$$\boldsymbol{B}_{\rm out} = B_0 R^3 \left(\frac{\cos\theta}{r^3}\boldsymbol{e_r} + \frac{\sin\theta}{2r^3}\boldsymbol{e_\theta}\right) \tag{2.10}$$

for outside the star, where B_0 is on the surface of the star, R is the radius of the star, $r = \sqrt{\varpi^2 + z^2}$ is the distance to the center of the star, and $\boldsymbol{e_i}$ is an unit vector parallel to the i-th direction.

Let us find the electrostatic potential inside the star. Since the interior of the neutron star is a perfect conductor, namely ideal MHD condition is satisfied, the following relation between the electric and magnetic field holds:

$$\boldsymbol{E}_{\rm in} + \frac{\boldsymbol{\Omega} \times \boldsymbol{r}}{c} \times \boldsymbol{B}_{\rm in} = 0. \tag{2.11}$$

With angular velocity $\boldsymbol{\Omega} = \Omega \boldsymbol{e_r}$ and $\boldsymbol{B_{\rm in}} = B_0 \boldsymbol{e_z}$, we obtain

$$\boldsymbol{E}_{\rm in} = -\frac{B_0 \Omega \varpi}{c} \boldsymbol{e_\varpi}. \tag{2.12}$$

The electrostatic potential $\Phi_{\rm in}$ is obtained by solving following differential equation,

$$\nabla \Phi_{\rm in} = -\boldsymbol{E}_{\rm in} \quad \Longrightarrow \quad \frac{\partial \Phi_{\rm in}}{\partial \varpi} \boldsymbol{e_\varpi} + \frac{1}{\varpi} \frac{\partial \Phi_{\rm in}}{\partial \theta} \boldsymbol{e_\theta} + \frac{\partial \Phi_{\rm in}}{\partial z} \boldsymbol{e_z} = -\left(-\frac{B_0 \Omega \varpi}{c} \boldsymbol{e_\varpi} \right). \tag{2.13}$$

Therefore, we obtain

$$\Phi_{\rm in} = \frac{B_0 \Omega \varpi^2}{2c} + \text{const.} \tag{2.14}$$

Next, we calculate the electrostatic potential outside the star. Since the outside of the star is a vacuum, the potential $\Phi_{\rm out}$ can be obtained by solving the Laplace equation,

$$\Delta \Phi_{\rm out} = 0. \tag{2.15}$$

A general solution to the Laplace equation of an axisymmetric system is written as follows:

$$\Phi_{\rm out} = \sum_{l=0}^{\infty} \left(\alpha_l r^l + \beta_l r^{-(l+1)} \right) P_l \left(\cos\theta \right), \tag{2.16}$$

where P_l is the Legendre polynomial of order l [1]. For this solution to be bounded when $r \to \infty$, we have to be $\alpha_l = 0$ for all l. Thus the external solution is written as:

$$\Phi_{\rm out} = \sum_{l=0}^{\infty} \frac{\beta_l}{r^{l+1}} P_l \left(\cos\theta \right). \tag{2.17}$$

Let us find the coefficient β_l so that the potential is continuous on the surface of the star $r = R$. In polar coordinates, equation (2.14) is written as:

$$\Phi_{\rm in} = -\frac{B_0 \Omega}{3c} r^2 P_2 \left(\cos\theta \right) + \frac{B_0 \Omega}{6c} r^2 + \text{const.} \tag{2.18}$$

By adjusting the integral constant, we obtain the following simple form

$$\Phi_{\rm in} \left(R, \theta \right) = -\frac{B_0 \Omega}{3c} R^2 P_2 \left(\cos\theta \right), \tag{2.19}$$

at the surface of the star. Imposing the $\Phi_{\rm in} = \Phi_{\rm out}$ at $r = R$, we finally obtain

$$\Phi_{\rm out} \left(r, \theta \right) = -\frac{B_0 \Omega R^5}{3cr^3} P_2 \left(\cos\theta \right). \tag{2.20}$$

[1] Legendre polynomials are generated by Rodrigues' formula, $P_n(x) = \frac{1}{2^n n!} \frac{d^n}{dx^n} \left[\left(x^2 - 1 \right)^n \right]$. For example, $P_0(x) = 1, P_1(x) = x, P_2(x) = (3x^2 - 1)/2 \cdots$.

By using the obtained electrostatic potential, we evaluate the magnitude of the electric field parallel to the magnetic field line on the neutron star surface. Since the external electric field is

$$\boldsymbol{E}_{\rm out} = \frac{B_0 \Omega R^5}{2cr^4}\left(3\cos^2\theta - 1\right)\boldsymbol{e_r} - \frac{B_0 \Omega R^5}{2cr^4}\sin 2\theta \boldsymbol{e_\theta}, \tag{2.21}$$

$\boldsymbol{E}\cdot\boldsymbol{B}$ is calculated as

$$\boldsymbol{E}_{\rm out}\cdot\boldsymbol{B}_{\rm out} = -\frac{R\Omega}{c}\left(\frac{R}{r}\right)^7 B_0^2\cos^3\theta. \tag{2.22}$$

Thus, the electric field along the magnetic field line on the surface of the star is

$$\boldsymbol{E}_{\rm out}\left(R,\theta\right)\cdot\frac{\boldsymbol{B}_{\rm out}\left(R,\theta\right)}{B_0} = -\frac{R\Omega}{c}B_0\cos^3\theta. \tag{2.23}$$

A phenomenon in which a potential difference is generated when a conductor sphere rotates in a magnetic field is called a unipolar induction.

Let us compare gravity and electric force acting on an electron at $r = R$ and $\theta = 0$. The ratio of the electric field to the gravity is estimated as,

$$\frac{\text{(electric force)}}{\text{(gravity)}} \sim 6\times 10^{11}\ \left(\frac{B_0}{10^{12}\ \text{G}}\right)\left(\frac{R}{10\ \text{km}}\right)^3\left(\frac{P}{1\ \text{s}}\right)^{-1}\left(\frac{M_{\rm NS}}{1.4\ \ M_\odot}\right)^{-1}, \tag{2.24}$$

where $M_{\rm NS}$ is the mass of the neutron star. Consequently, electrons on the surface of neutron stars are drawn from the stars and distributed around the stars. In other words, the surroundings of the neutron star can not keep being vacuum.

2.2.2 Particle Generation

In the vacuum magnetosphere discussed in the previous section, charged particles around the neutron stars are immediately accelerated by the electric field due to the unipolar induction and emit γ-rays. Under a strong magnetic field, electron and positron are generated by the process of $\gamma + B \rightarrow e^+ + e^- + B$. In this section, following (Beskin, 1999), we briefly review the particle generation process around the neutron star.

Electrons drawn from neutron stars immediately lose momentum perpendicular to the magnetic field by radiative cooling by synchrotron radiation under a strong magnetic field due to the neutron star. An electron moves along the field line while being accelerated by an electric field by unipolar induction. Since the field lines near the magnetic pole of the neutron star have curvature, electrons emits the photon via the curvature radiation. A typical frequency of the curvature radiation is written as,

$$\omega_{\rm cur} = 0.44\frac{c}{R_c}\gamma^3, \tag{2.25}$$

where R_c is the curvature radius of the magnetic field and γ is the Lorentz factor of the electron. The emitted energy per unit time per particle is written as (e.g., Rybicki & Lightman, 1979):

$$P_{\rm cur} = \frac{2ce^2}{3R_c^2}\gamma^4. \tag{2.26}$$

The maximum energy of the particle is estimated as the energy where the acceleration due to the electric field is equal to the loss due to the radiation ($P_{\rm cur} \sim eE_\parallel c$), the following is obtained.

$$\gamma_{\rm max} \sim 2.8\times 10^7\ \xi^{\frac{1}{2}}\left(\frac{R}{10\ \text{km}}\right)^{\frac{3}{4}}\left(\frac{P}{1\ \text{s}}\right)^{-\frac{1}{4}}\left(\frac{B_0}{10^{12}\ \text{G}}\right)^{\frac{1}{4}}, \tag{2.27}$$

where $\xi = R_c/R$ is the ratio of the curvature radius R_c to the star radius R. The corresponding typical energy $\epsilon_{\rm ph}$ of the photon which is emitted by the particle with such energy is,

$$\epsilon_{\rm ph} \sim 200 \text{ GeV } \xi^{\frac{1}{2}} \left(\frac{R}{10 \text{ km}}\right)^{\frac{5}{4}} \left(\frac{P}{1 \text{ s}}\right)^{-\frac{3}{4}} \left(\frac{B_0}{10^{12} \text{ G}}\right)^{\frac{3}{4}}. \tag{2.28}$$

Such a high energy γ-ray creates secondary electron-positron pair via the magnetic pair creation. The probability per unit propagation distance, in which a γ-ray with an energy $\epsilon_{\rm ph} \gg m_e c^2$ propagating at angle θ to the magnetic field are converted into pairs, can be written as (Berestetskii et al., 1982):

$$\alpha_{B\gamma} = \frac{3\sqrt{3}}{16\sqrt{2}} \alpha_{\rm EM}^2 \left(\frac{B \sin\theta}{B_\hbar}\right) \frac{1}{r_e} \exp\left[-\frac{8}{3} \frac{B_\hbar}{B \sin\theta} \frac{m_e c^2}{\epsilon_{\rm ph}}\right] \tag{2.29}$$

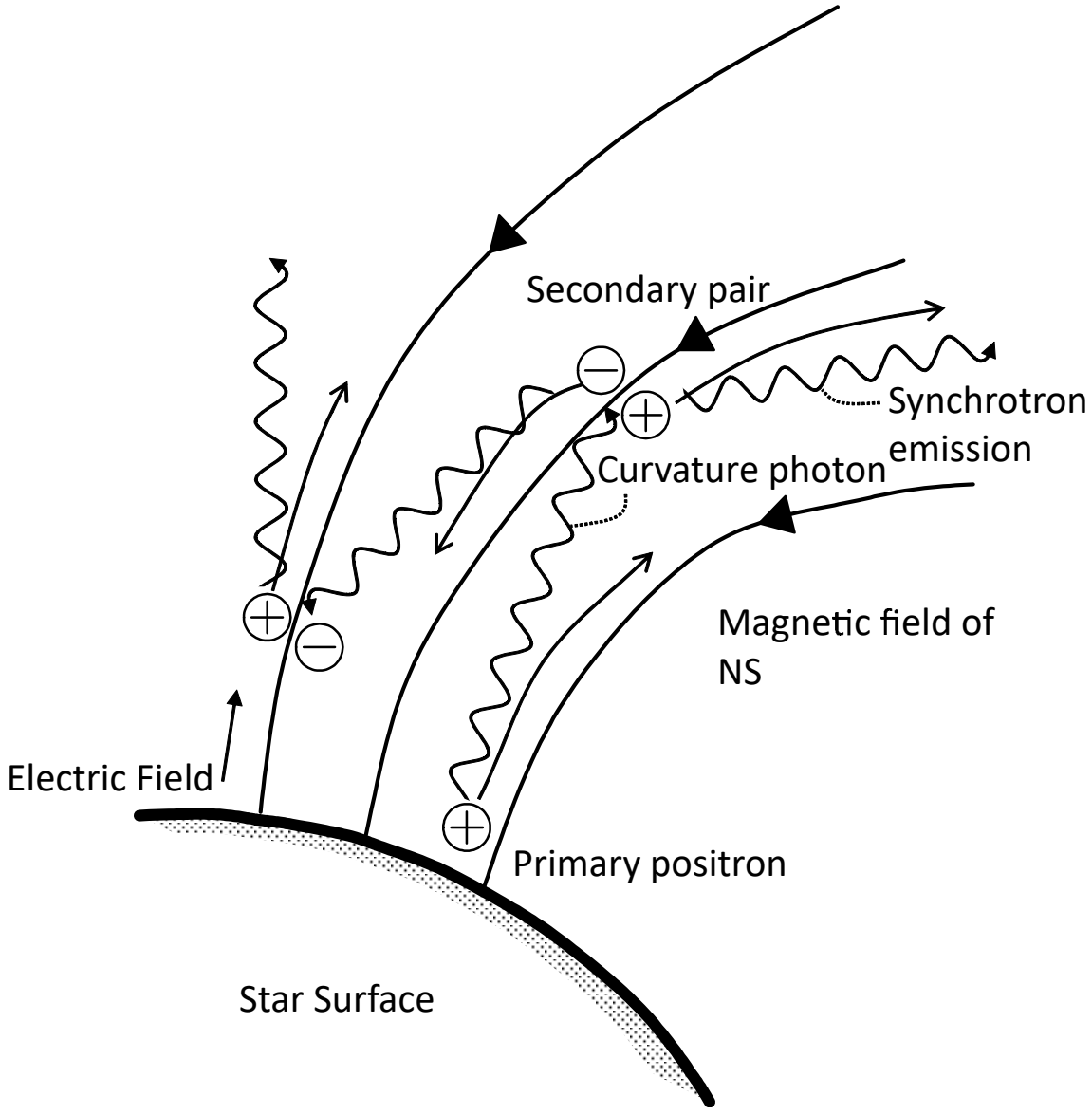

Figure 2.1: A schematic view of the particle generation at the polar region of the pulsar.

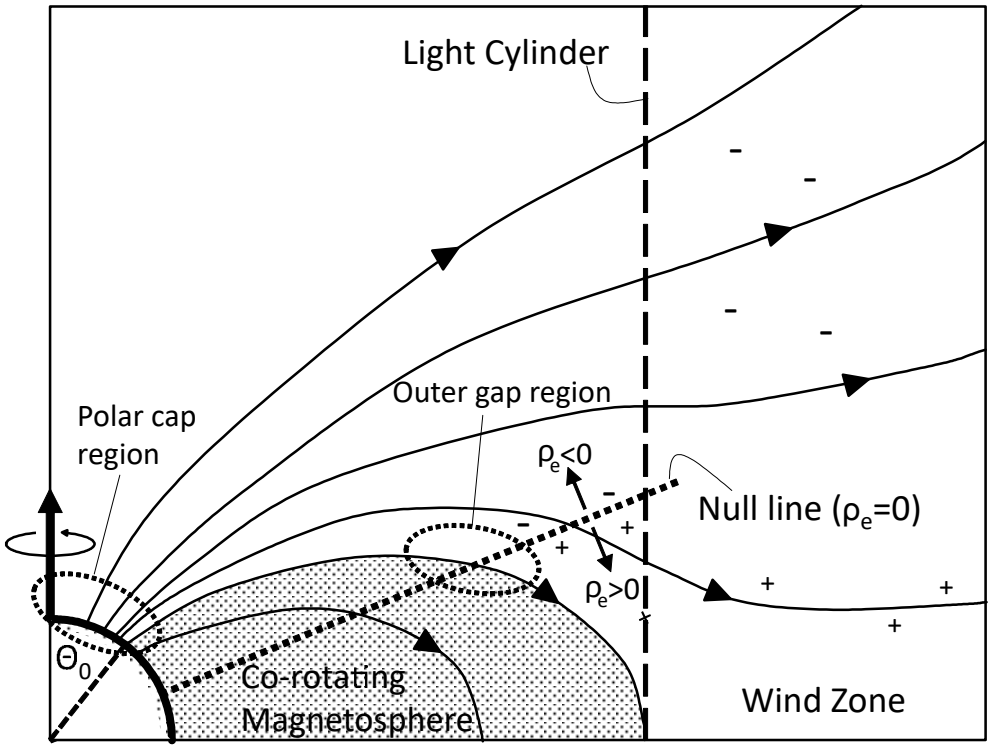

Figure 2.2: Schematic view of the pulsar magnetosphere. The lower left quadrant circle represents the pulsar and the solid lines represent the magnetic field lines extending from the pulsar. Field lines and plasmas that can co-rotate are limited to those shown in shaded areas.

where $B_\hbar$ is the critical field, which is the strength of the magnetic field where the nonlinearity of the quantum electrodynamics becomes important (Schwinger limit), and is written as

$$B_\hbar = \frac{m_e c^3}{e\hbar}, \tag{2.30}$$

$\alpha_{\rm EM} = e^2/\hbar c$ is the fine structure constant and $r_e = e^2/m_e c^2$ is the classical electron radius. The electrons and positrons generated in this process are accelerated again as long as there is an electric field along the magnetic field, and emit γ-rays, which also makes pairs (Sturrock, 1971). This process continues in a chain until the electric field along the magnetic field is screened (see Figure 2.1). Through these processes, a pulsar magnetosphere filled with pair plasma is formed around the pulsar.

2.2.3 Structure of the Pulsar Magnetosphere; Intuitive Understanding

As discussed in the previous section, around the pulsar, it is thought that the charged particles are distributed so as to screen the electric field along the magnetic field. In such a case, since equation (2.11) holds both inside and outside the star, the electric field outside the pulser can be written as follows:

$$\boldsymbol{E} = -\frac{\boldsymbol{\Omega} \times \boldsymbol{r}}{c} \times \boldsymbol{B}. \tag{2.31}$$

The charge density is obtained as follows using Gauss' law (see Section 2.2.4 for details):

$$\rho_e = -\frac{\boldsymbol{\Omega}\cdot\boldsymbol{B}}{2\pi c}\frac{1}{1-(\Omega r/c)^2\sin^2\theta}. \tag{2.32}$$

Assuming that this charge distribution is given by a completely charge separated plasma, the particle number density of the magnetosphere can be estimated as follows:

$$n_{\rm GJ} = \frac{\boldsymbol{\Omega}\cdot\boldsymbol{B}}{2\pi ce} \sim 7\times10^{10}\ {\rm cc}^{-1}\left(\frac{B}{10^{12}\ {\rm G}}\right)\left(\frac{P}{1\ {\rm s}}\right)^{-1}. \tag{2.33}$$

This is called the Goldreich-Julian density and represents the minimum number density necessary to screen the electric field along the magnetic field lines.

Next, we discuss the motion of the plasma in the pulsar magnetosphere (c.f. Ruderman & Sutherland, 1975). Figure 2.2 shows the structure of the pulsar magnetosphere proposed by Goldreich & Julian (1969). Since the particles in the magnetosphere are secondary products to the electromagnetic field, the energy density of the magnetic field would be larger than the energy density of the particles. Under such circumstances, the force-free approximation is justified. As a consequence, charged particles in the magnetosphere are known to co-rotate with the pulsar and its field lines (see Section 2.2.4 for details). However, particles can not co-rotate beyond the speed of light. The light cylinder $\varpi_{\rm lc}$ is the radius at which the co-rotational speed is equal to the speed of light and can be written as follows:

$$\varpi_{\rm LC} = \frac{c}{\Omega} \sim 4.7\times10^{9}\ {\rm cm}\left(\frac{P}{1{\rm s}}\right). \tag{2.34}$$

A magnetic field line that closes inside the light cylinder is called a closed field line, that extends beyond the light cylinder is called an open field line, and that is boundary between them is called a last open field line (Figure 2.2). Magnetic lines of force that originate from the polar side of θ_0 on the surface of the star can not form a closed co-rotating magnetosphere, and will produce a pulsar wind flowing out from the light cylinder.

Let us estimate the angle at which the last open field line appears at the surface of the star, assuming the magnetic field within the light cylinder as a dipole field. In the dipole magnetic field, since $\sin^2\theta/r = {\rm const}$ holds, the angle of the last open field line respect to the magnetic pole at the surface of the star is estimated as:

$$\theta_0 \sim \left(\frac{R\Omega}{c}\right)^{1/2}. \tag{2.35}$$

The area where the base of the open magnetic field lines defines on the star surface is called polar cap. The radius r_p of polar cap can be written as follows:

$$r_p = \sqrt{\frac{\Omega R^3}{c}} \sim 1.4\times10^{4}\ {\rm cm}\left(\frac{R}{10{\rm km}}\right)^{3/2}\left(\frac{P}{1{\rm s}}\right)^{-1/2}. \tag{2.36}$$

Charged particles on the open field lines can flow out along the field line, so that a relativistic plasma wind would be emitted from the light cylinder and called the pulsar wind. This brings out the rotational energy of the pulser as kinetic energy to the outside. Let us estimate the energy loss rate due to the pulsar wind. The potential difference ΔV, which is caused by unipolar induction, between the edge of the polar cap and the magnetic pole is written as:

$$\Delta V \sim \Phi_{\rm in}(R,\theta_0) - \Phi_{\rm in}(R,\theta=0) = \frac{B_0R^3\Omega^2}{2c^2} \sim 6.6\times10^{12}\ V\left(\frac{B_0}{10^{12}{\rm G}}\right)\left(\frac{R}{10{\rm km}}\right)^{3}\left(\frac{P}{1{\rm s}}\right)^{-2}. \tag{2.37}$$

Here, we used equation (2.14). Note that the equation (2.37) also means the maximum of the potential difference that can be used to accelerate the particle among the potential differences generated by the pulser in the unipolar induction. If the current is estimated assuming that charged particles of Goldreich-Julian density flow out at the speed of light from the polar cap region, the energy that pulsar wind brings per unit time can be calculated as follows:

$$L_{pw} \sim \Delta V \times \left(2 \times \pi r_p^2 \times c \times e n_{\rm GJ}\right) = \frac{B_0^2 \Omega^4 R^6}{4c^3} \sim 2.8 \times 10^{31}\ {\rm erg/s} \left(\frac{B_0}{10^{12}{\rm G}}\right)^2 \left(\frac{R}{10{\rm km}}\right)^6 \left(\frac{P}{1{\rm s}}\right)^{-4}. \tag{2.38}$$

Here, since the polar cap region exists at two magnetic poles, the energy loss rate is doubled. If this is equal to the spin-down luminosity, $\dot{\Omega} \propto \Omega^3$ is obtained. This corresponds to breaking index $n = 3$.

2.2.4 Axisymmetric Magnetosphere

In this section, we explain the theory of the structure of the pulsar magnetosphere in more detail following Beskin (2009). Unless otherwise noted, steady state and axisymmetry, and coincidence of the axis of the magnetic field and the axis of rotation are assumed.

Force-free Approximation

The conservation law of energy and momentum on matter ($T_M^{\mu\nu}$) and electromagnetic field ($T_{\rm EM}^{\mu\nu}$) is given by

$$\partial_\nu \left(T_M^{\mu\nu} + T_{EM}^{\mu\nu}\right) = 0. \tag{2.39}$$

Assuming that the energy density of matter is much smaller than that of an electromagnetic field, we have

$$\partial_\nu T_{\rm EM}^{\mu\nu} = 0, \tag{2.40}$$

which is called the force-free approximation. The energy–momentum tensor of the electromagnetic field is explicitly written as follows:

$$T_{\rm EM}^{\mu\nu} = \begin{pmatrix} \frac{E^2+B^2}{8\pi} & \frac{1}{4\pi}\left(\boldsymbol{E}\times\boldsymbol{B}\right) \\ \frac{1}{4\pi}\left(\boldsymbol{E}\times\boldsymbol{B}\right) & -\frac{1}{4\pi}\left(\boldsymbol{E}\otimes\boldsymbol{E}+\boldsymbol{B}\otimes\boldsymbol{B}\right) + \frac{E^2+B^2}{8\pi}\overleftrightarrow{I} \end{pmatrix}. \tag{2.41}$$

Assuming a steady state and using the Maxwell equation, we obtain

$$\boldsymbol{j}\cdot\boldsymbol{E} = 0 \tag{2.42}$$

from the time component, and

$$\rho_e \boldsymbol{E} + \frac{\boldsymbol{j}}{c}\times\boldsymbol{B} = 0 \tag{2.43}$$

from the spatial component.

Magnetic Flux Function

Let us introduce the magnetic flux function, which is important in description of axisymmetric MHD. We take the cylindrical coordinate system (ϖ, ϕ, z) and assume the axisymmetry $\partial_\phi = 0$ and the steady state $\partial_t = 0$. Hereafter, the components in the meridian of the physical quantity are

represented by the subscript subscript p (poloidal) and the azimuth component by the subscript subscript t (toroidal). For example, the magnetic field is written as:

$$\boldsymbol{B} = \boldsymbol{B_p} + \boldsymbol{B_t}. \tag{2.44}$$

The plasma velocity is

$$\boldsymbol{v} = \boldsymbol{v_p} + \boldsymbol{v_t}. \tag{2.45}$$

Since the magnetic field can be written as $\boldsymbol{B} = \nabla \times \boldsymbol{A}$ by introducing the vector potential $\boldsymbol{A}$, we have

$$\boldsymbol{B} = \nabla \times \boldsymbol{A} = \left[-\frac{1}{\varpi}\frac{\partial\left(\varpi A_\phi\right)}{\partial z}\boldsymbol{e_\varpi} + \frac{1}{\varpi}\frac{\partial\left(\varpi A_\phi\right)}{\partial \varpi}\boldsymbol{e_z} \right] + \left(\frac{\partial A_z}{\partial \varpi} - \frac{\partial A_\varpi}{\partial z} \right) \boldsymbol{e_\phi}. \tag{2.46}$$

As can be seem from this result, the poloidal field can be written with one variable A_ϕ. Therefore, we define the function $\Psi(\varpi, \phi)$ as follows:

$$\Psi = 2\pi\varpi A_\phi = \int_0^\varpi 2\pi\varpi B_z d\varpi. \tag{2.47}$$

With using Ψ, poloidal component of equation (2.46) is written as

$$\boldsymbol{B_p} = \frac{1}{2\pi\varpi}\nabla\Psi \times \boldsymbol{e_\phi}. \tag{2.48}$$

Since Ψ is the magnetic flux within the radius of ϖ from the polar axis, it is called the magnetic flux function. Furthermore, using the function $I(\varpi, \phi)$, we write the troidal magnetic field as

$$B_t = -\frac{2I}{c\varpi}, \tag{2.49}$$

where I corresponds to the total current flowing out within the radius ϖ from the polar axis. Therefore, the magnetic field $\boldsymbol{B}$ is written as

$$\boldsymbol{B} = \frac{1}{2\pi\varpi}\nabla\Psi \times \boldsymbol{e_\phi} - \frac{2I}{c\varpi}\boldsymbol{e_\phi}. \tag{2.50}$$

Note that $\nabla \cdot \boldsymbol{B} = 0$ is automatically satisfied under such expression. This is consistent with the fact that $\boldsymbol{B}$ is represented by two variables, I and Ψ.

Multiplying $\boldsymbol{e_\phi}$ as an outer product on both sides of equation (2.48), we have

$$\nabla\Psi = 2\pi\varpi\boldsymbol{e_\phi} \times \boldsymbol{B_p}. \tag{2.51}$$

Hence, we obtain

$$\boldsymbol{B} \cdot \nabla\Psi = \boldsymbol{B_p} \cdot \nabla\Psi = 0 \tag{2.52}$$

This means that Ψ is constant along the field line. In other words, since Ψ relates to the magnetic field line in a one-to-one correspondence, it can be used as coordinates for specifying magnetic field line.

From $\nabla \times \boldsymbol{B} = 4\pi\boldsymbol{j}/c$, we have

$$\boldsymbol{j_p} = -\frac{1}{2\pi\varpi}\nabla I \times \boldsymbol{e_\phi}. \tag{2.53}$$

In the same way as equation (2.52), we obtain

$$\boldsymbol{j} \cdot \nabla I = \boldsymbol{j_p} \cdot \nabla I = 0. \tag{2.54}$$

Note that the equation of charge continuity $\nabla \cdot \boldsymbol{j} = 0$ is automatically satisfied.

Co-rotating Magnetosphere

Here we start from the ideal MHD condition, which means that the electric field is vanished in the fluid rest frame, and it can be written as

$$\boldsymbol{E} + \frac{\boldsymbol{v}}{c} \times \boldsymbol{B} = 0. \tag{2.55}$$

Note that this implies $\boldsymbol{E} \cdot \boldsymbol{B} = 0$.

In steady state, $\nabla \times \boldsymbol{E} = 0$ from Faraday's law. Therefore, by introducing electrostatic potential Φ_e, $\boldsymbol{E}$ can be written as

$$\boldsymbol{E} = -\nabla \Phi_e. \tag{2.56}$$

Since $\partial_\phi = 0$, we have

$$E_t = \boldsymbol{E} \cdot \boldsymbol{e_\phi} = -\frac{1}{\varpi} \frac{\partial \Phi_e}{\partial \phi} = 0. \tag{2.57}$$

That is, in the steady and axisymmetric MHD, the troidal electric field can not exist. Since the electric field has only the poloidal component, we obtain

$$\boldsymbol{E} \cdot \boldsymbol{B} = \boldsymbol{E_p} \cdot \boldsymbol{B_p} = 0. \tag{2.58}$$

This indicates that the electric field and the magnetic field are orthogonal in the meridional plane. Furthermore, multiplying $\boldsymbol{B_p}$ on both sides of $\boldsymbol{E_p} = -\nabla \Phi_e$ as an inner product, we obtain

$$\boldsymbol{B_p} \cdot \nabla \Phi_e = 0. \tag{2.59}$$

This implies that the electric potential is constant along the field line. In other words, as long as a particle moves along a field line, it is not accelerated by the electric field. Since the electrostatic potential Φ_e corresponds one-to-one to the field line, Φ_e can be written as a function of only Ψ (i.e. $\Phi_e = \Phi_e(\Psi)$). Therefore, using the magnetic flux function, the electric field $\boldsymbol{E}$ is written as

$$\boldsymbol{E} = -\nabla \Phi_e = -\frac{\varpi \Omega(\Psi)}{c} \boldsymbol{e_\phi} \times \boldsymbol{B_p} = -\frac{\Omega}{2\pi c} \nabla \Psi, \tag{2.60}$$

where Ω is a scalar function of only Ψ and written as

$$\Omega = 2\pi c \frac{d\Phi_e}{d\Psi}. \tag{2.61}$$

The toroidal component of the equation (2.55) is

$$\boldsymbol{v_p} \times \boldsymbol{B_p} = 0. \tag{2.62}$$

Therefore, using a scalar function κ, the poloidal velocity can be written as

$$\boldsymbol{v_p} = \kappa \boldsymbol{B_p}. \tag{2.63}$$

The poloidal component of the equation (2.55) is

$$\boldsymbol{E_p} + \frac{1}{c} (\boldsymbol{v_t} \times \boldsymbol{B_p} + \boldsymbol{v_p} \times \boldsymbol{B_t}) = 0. \tag{2.64}$$

Substituting equation (2.63) and taking the cross product with B_p, we obtain:

$$\boldsymbol{E_p} \times \boldsymbol{B_p} + \frac{B_p^2}{c} (\kappa \boldsymbol{B_t} - \boldsymbol{v_t}) = 0. \tag{2.65}$$

Since $\boldsymbol{E_p} \perp \boldsymbol{B_p}$ (see equation (2.58)), we can solve eqation (2.65) for v_t and obtain the following result:

$$v_t = \kappa B_t + \frac{c\,[\boldsymbol{E_p} \times \boldsymbol{B_p}]_t}{B_p^2}. \tag{2.66}$$

Substituting this to equation (2.65), we have

$$\boldsymbol{E_p} \times \boldsymbol{B_p} = \frac{\varpi\Omega}{c} B_p^2 \boldsymbol{e_\phi}. \tag{2.67}$$

Combining above results, we obtain

$$\boldsymbol{v} = \kappa \boldsymbol{B} + \varpi\Omega \boldsymbol{e_\phi}. \tag{2.68}$$

As can be seen in this equation, Ω means the angular velocity, if the magnetic field has no toroidal component. Since the Ω is constant along the filed line, the second term of equation (2.68) implies that the plasma co-rotates with the star (as known as the Ferarro's isorotation law (Ferraro, 1937)). In particular, where there is no toroidal field, the plasma co-rotates completely with the central star. The co-rotaion of the plasma is interpreted as the $E \times B$ drift motion.

Goldreich–Julian Density

Let us calculate the charge density from the electric field $\boldsymbol{E}$. By substituting equation (2.60) to the Gauss' law $\nabla \cdot \boldsymbol{E} = 4\pi\rho_e$, we get:

$$\rho_e = \frac{1}{4\pi}\nabla \cdot \boldsymbol{E} = -\frac{1}{4\pi c}\nabla \cdot \left[\varpi\Omega \left(B_z \boldsymbol{e_\varpi} - B_\varpi \boldsymbol{e_z}\right)\right]. \tag{2.69}$$

If Ω is a constant, this equation can be written as

$$\rho_e = -\frac{\Omega}{4\pi c}\left(2B_z - \frac{4\pi\varpi}{c} j_\phi\right). \tag{2.70}$$

Furthermore, if we assume that the current is only due to co-rotating motion of charged particles (i.e. $\boldsymbol{j} = \rho_e \varpi\Omega \boldsymbol{e_\phi}$), we obtain:

$$\rho_e = -\frac{\Omega B_z}{2\pi c} \frac{1}{1 - \left(\frac{\varpi}{\varpi_{\rm LC}}\right)^2}. \tag{2.71}$$

This is the Goldreich–Julian density seen in Section 2.2.3. Equation (2.71) fails at $\varpi \to \varpi_{\rm LC}$ is due to the assumption that the current is only co-rotational current. In the actual magnetosphere, there are poloidal current flows along the open-field line. A toroidal magnetic field is generated by that currents, so that the flow deviates from the complete co-rotation.

Trans-field Equation

Let us derive an equation describing the shape of the field lines in the magnetosphere from equation (2.43). Since $E_t = 0$, the troidal component of equation (2.43) is

$$\boldsymbol{j_p} \times \boldsymbol{B_p} = 0. \tag{2.72}$$

Substituting equation (2.50) and (2.53), we obtain

$$\nabla I \times \nabla \Psi = 0. \tag{2.73}$$

Using equation (2.51), we obtain

$$\boldsymbol{B} \cdot \nabla I = 0. \tag{2.74}$$

Therefore, I is constant along the field line, so that we can write I as the function of Ψ, namely $I = I(\Psi)$.

The poloidal component of equation (2.43) can be written as

$$\rho_e \boldsymbol{E_p} + \frac{1}{c}\left(\boldsymbol{j_t} \times \boldsymbol{B_p} + \boldsymbol{j_p} \times \boldsymbol{B_t}\right) = 0. \tag{2.75}$$

The cross product of $\boldsymbol{j}$ and $\boldsymbol{B}$ can be calculated as follows:

$$\boldsymbol{j_t} \times \boldsymbol{B_p} = \frac{j_t}{2\pi\varpi}\nabla\Psi \tag{2.76}$$

and

$$\boldsymbol{j_p} \times \boldsymbol{B_t} = -\frac{I\nabla I}{\pi\varpi^2} = -\frac{1}{\pi\varpi^2} I \frac{dI}{d\Psi}\nabla\Psi. \tag{2.77}$$

Therefore, equation (2.75) can be written as

$$\left(-\frac{\nabla\cdot\boldsymbol{E}}{4\pi}\frac{\Omega}{2\pi c} - \frac{1}{\pi\varpi^2} I\frac{dI}{d\Psi} + \frac{j_t}{2\pi\varpi}\right)\nabla\Psi = 0. \tag{2.78}$$

j_t is obtained from $\nabla\cdot\boldsymbol{B} = 4\pi\boldsymbol{j}/c$ as follows:

$$j_t = -\frac{c}{8\pi^2\varpi}\left[\nabla^2\Psi - \frac{2}{\varpi}\frac{\partial\Psi}{\partial\varpi}\right]. \tag{2.79}$$

By substituting equation (2.60) and (2.79) into equation (2.78), we have:

$$\left(1 - \frac{\Omega^2\varpi^2}{c^2}\right)\nabla^2\Psi - \frac{2}{\varpi}\frac{\partial\Psi}{\partial\varpi} + \frac{16\pi^2}{c^2} I\frac{dI}{d\Psi} = 0. \tag{2.80}$$

This equation is called Grad–Shafranov equation (Shafranov, 1958; Grad, 1960). As can be seen in equation (2.75), this equation means the balance of forces in the direction perpendicular to the field lines applied to the test particles on the field line.

Force-free Magnetosphere and Further Models

There are many studies to solve the structure of the magnetosphere by solving Force-free Grad-Shafranov equation (see Venter, 2016, and references therein). It is technically very difficult to solve (even numerically) the Grad-Shafranov equation because it is a nonlinear equation and because the type of the equation changes from elliptical to hyperbolic in the light cylinder. Contopoulos et al. (1999) succeeded for the first time in obtaining the structure of the magnetosphere by simultaneously solving the Grad-Shafranov equation (i.e. equation (2.80)) inside and outside the light cylinder. Figure 2.3 shows their calculation results. They found that the inside of the light cylinder is almost dipole field, and the outside is almost radial shape.

Motivated by the formation of the Y–point near the light cylinder of the equatorial plane, the calculation to solve the dissipative force-free equation is being conducted by many authors (e.g., Li et al., 2012). Calculations taking into account of the effects of general relativity (e.g., Pétri, 2016), and calculations taking into account of the multipole magnetic field on the star are also performed (e.g., Akgün et al., 2018). In addition, there are studies that investigate oblique rotator by time-dependent 3–D calculation (e.g., Spitkovsky, 2006).

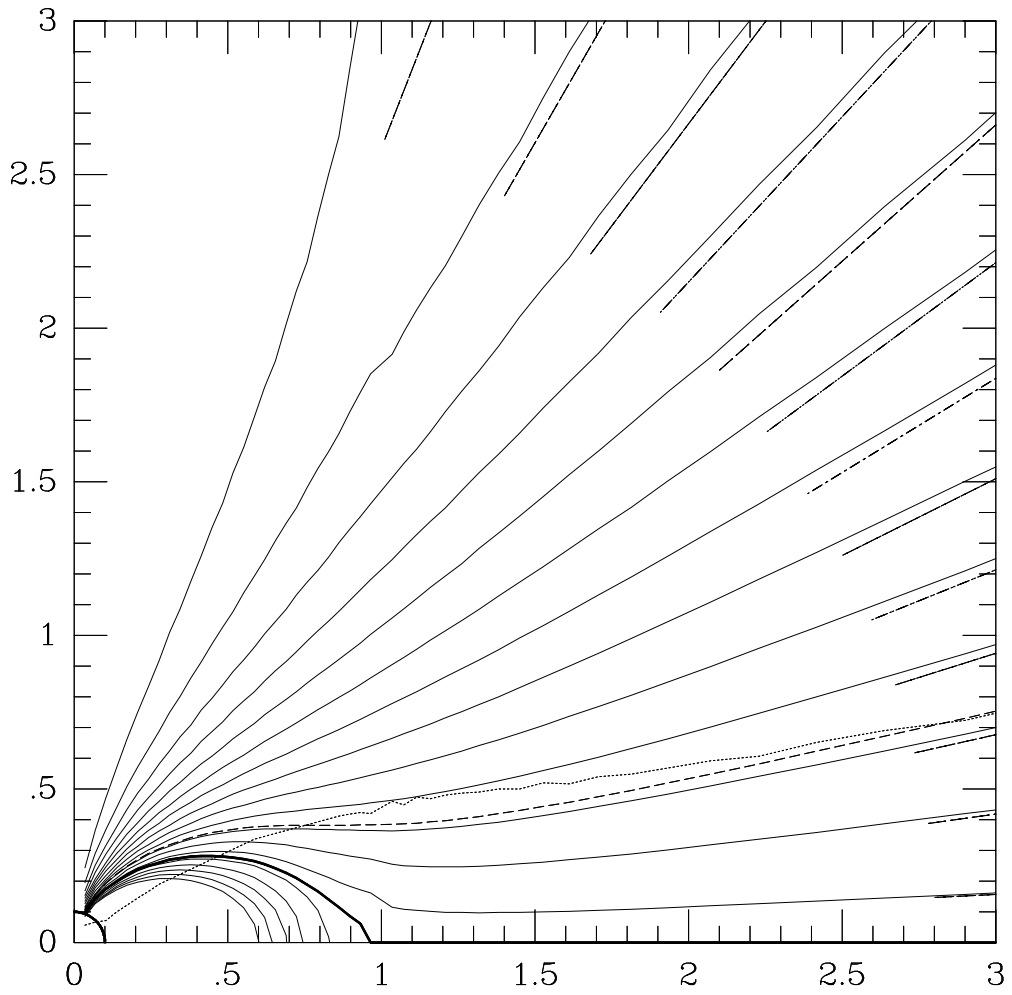

Figure 2.3: Calculation result of the force-free magnetosphere by Contopoulos et al. (1999). The thin solid line shows magnetic field lines in interval of 0.1 $\Psi_{\rm pc}$, where $\Psi_{\rm pc}$ is the flux function at the radius of the classical polar cap as determined by equation (2.35). The thick solid line represents the last open field line, which is $\Psi = 1.36\Psi_{\rm pc}$. The dashed line represents a field line that is the boundary where the direction of the bulk current changes, and it is $\Psi = 1.08\Psi_{\rm pc}$. The dotted line indicates a null line (i.e., $\rho_{\rm GJ} = 0$). The figure is from Contopoulos et al. (1999). ©AAS. Reproduced with permission.

As an advanced calculation than the force-free equations, a simulation with MHD equations considering plasma inertia is also performed. Interestingly, Komissarov (2006) found that the solution of the time-dependent MHD equation shows a structure very similar to the solution of Contopoulos et al. (1999) at steady state. Furthermore, as a calculation close to the first principle calculation, there are studies to calculate using particle-in-cell (PIC) simulation. Recently, Philippov & Spitkovsky (2018) performed a global PIC simulation of the oblique rotator, including the general relativistic effect, pair production, ion extraction from the surface, and radiation (Figure 2.4).

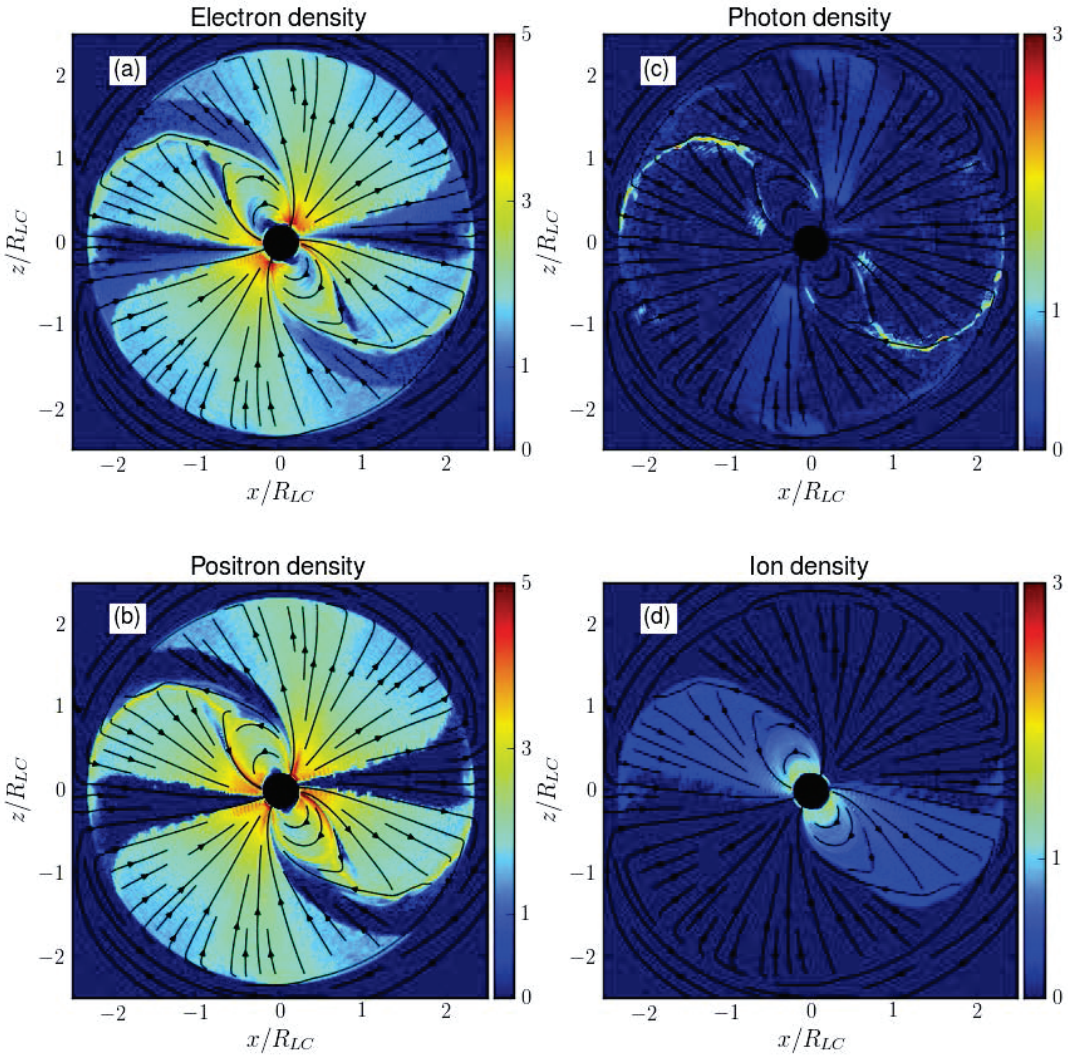

Figure 2.4: The calculation result for the 60 deg inclined pulsar magnetosphere by Philippov & Spitkovsky (2018). The figure shows the number density normalized by the GJ density on the plane that contains the magnetic pole and the rotation axis. (a): electrons, (b): positrons, (c): photons, (d): ions extracted from the star surface. A solid black line represents the field line. ©AAS. Reproduced with permission.

2.2.5 Gap Region and Particle Acceleration

In the pulsar magnetosphere where particles are sufficiently generated, there is no electric field parallel to the field lines, so that the particle acceleration process does not occur. However, actual pulsars emit at various wavelengths from radio to γ-rays. In the actual pulsar magnetosphere, there

is a region called a "gap" where the electric field pararell to the field line is not screened, because of the displacement from the Goldreich–Julian charge density, and the particle acceleration should be realized in such regions.

A promising candidate for the place where the gap exists is the magnetic poles of the pulsar. Since particles are flowing out along open field lines, particles can be deficient at the surface of the star. It is expected that the electric field exists above the polar cap with a thickness of about the mean free path of the magnetic pair creation. A model in which particles are accelerated by such an electric field formed near the magnetic pole is called a polar cap model. The mean free path of the typical γ-ray to the magnetic pair creation provides the thickness of the gap (Ruderman & Sutherland, 1975) as:

$$h_{\rm RS} \sim 5 \times 10^3 \text{ cm } \xi^{\frac{2}{7}} \left(\frac{R}{10 \text{ km}}\right)^{\frac{2}{7}} \left(\frac{P}{1 \text{ s}}\right)^{\frac{3}{7}} \left(\frac{B_0}{10^{12} \text{ G}}\right)^{-\frac{4}{7}}. \tag{2.81}$$

Another promising candidate is the area where the last open field line intersects the null line (i.e., $\rho_{\rm GJ} = 0$). As shown in Figure 2.5, when electrons flow out to the leftward along the open field line, the vicinity of the left side of the null line is charged to positive. Then, the positron on the right side of the null line receives the electrostatic force and moves to the rightward. As a result, the vicinity of the right side of the null line is charged to negative and an electric field along the magnetic field is formed. The model to consider acceleration of particles in this area is called the outer gap model and was proposed by Cheng et al. (1986). Unlikely the polar cap region, the magnetic field is weak around the outer gap region, so that the magnetic pair creation is inefficient. Photons are converted into pairs with a collision with the soft photons such as X-rays from the NS surface and X-rays from the outer gap region on the opposite side.

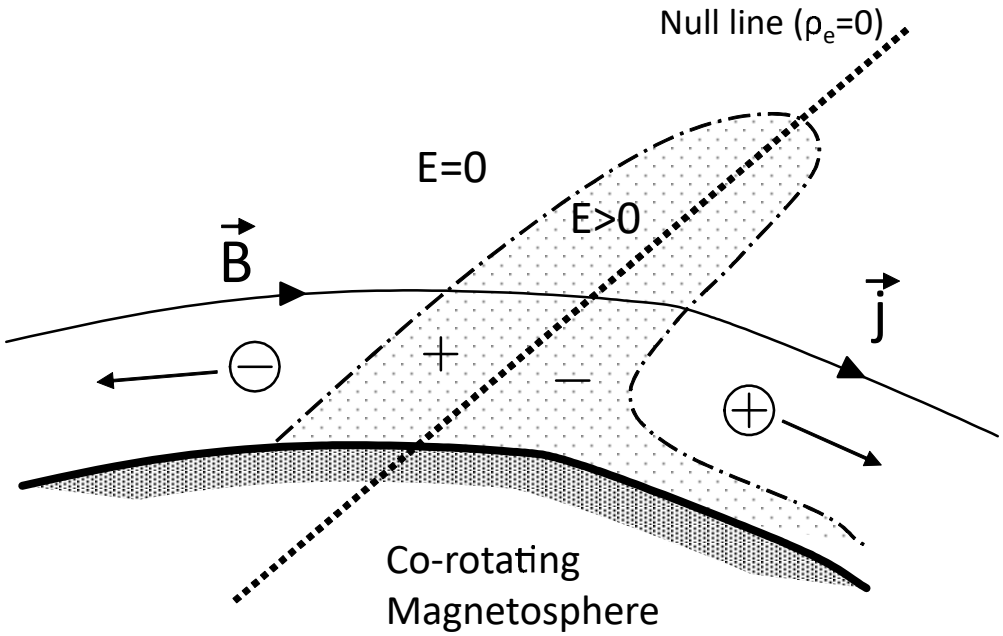

Figure 2.5: Schematic diagram of outer gap region. The shaded area below is the co-rotation region. The area where the electric field exists is indicated by dotted-dash line. The null line (i.e., $\rho_{\rm GJ} = 0$) is indicated by dashed line. As the electrons flow out from the null line along the magnetic field, the outer gap region grows (see text for details).

With increasing the energy of the photon, the cross section of the magnetic pair creation rapidly increases. In the polar cap model, this appears as super exponential cutoff in the pulsar radiation spectrum (Daugherty & Harding, 1996). On the other hand, in the outer gap model, the cross section of the pair creation is approximately the Thomson cross section and hardly depends on energy. As a result, the emission spectrum shows exponential or hard cutoff. Since the radiation spectrum of γ-ray pulsars detected by Fermi supports exponential cutoff (e.g., Abdo et al., 2010b,c; Leung et al., 2014), γ-ray is considered to be emitted from outer gap. The radio emission is considered to be from the polar cap because of the narrow pulse width and the fact that the phase of the pulse is different from γ-ray for most of the γ-ray pulsar.

The number κ of secondary particles that one (primary) particle can generate with pair creation is called multiplicity. The particle generation with the polar cap model is about $\kappa \sim 10^5$ with very optimistic parameters (Timokhin & Harding, 2015), but this is still smaller than the value required for the radiation model of pulsar wind nebulae (e.g., Bucciantini et al., 2011; Tanaka & Takahara, 2013a). In outer gap model, it is thought that it is about $\kappa \sim 10^4$ (e.g., Hirotani, 2006), and it can not be explained with this model. This is an unresolved issue, and is still discussed in both the model of the magnetosphere and the model of the nebula (e.g., Olmi et al., 2014; Timokhin & Harding, 2018).

2.2.6 Emission Mechanism of the Pulsar

Since the gap region can not be observed directly, the emission mechanism of the pulsar has been investigated indirectly by using the pulse shape, the polarization degree / spectrum for each pulse phase. In order to calculate the pulse shape, it is necessary not only to calculate the particle acceleration in the gap region and the structure of the magnetosphere, but also a geometrical consideration taking into account the direction of the observer.

The radiation mechanisms of X-ray and γ-ray are the curvature radiation from the primary particles directly accelerated at the gap and the synchrotron radiation and the inverse Compton scattering from secondary particles. For example, using the outer gap model, Takata & Chang (2007) calculated the spectrum, polarization degree and pulse shape. They reproduced the properties of the pulsed emission from Crab pulsar and PSR B0540-69, considering the curvature radiation from primary particles and the synchrotron radiation and inverse Compton scattering from secondary particles. The Philippov & Spitkovsky (2018), which introduced in Section 2.2.4, calculated not only the magnetosphere structure but also the photon emission from particles and its propagation and absorption. The theoretical understanding of the radio emission of the pulsar has not advanced much (e.g., Melrose & Rafat, 2017). Radio emission from the pulsar has a very high brightness temperature $T \sim 10^{24}$, suggesting a coherent radiation process (Pietka et al., 2015). Application of a model of radiation from the bunched plasma, which has been studied in the context of the solar burst, has been discussed, however consensus has not yet been obtained (see Eilek & Hankins, 2016, for review)

Although the pulsar emission model is still under discussion, observationally, it turns out that the conversion efficiency from the spin-down luminosity to the pulse emission is $\sim 10\%$ or less (Szary et al., 2014). Most of the spin-down luminosity is emitted as the kinetic luminosity of the pulsar wind described in next section.

2.3 Pulsar Wind

As mentioned in Section 2.2.3, the wind blows along the open field line in the pulsar magnetosphere. In order to correctly describe the motion of the pulsar wind, it is necessary to consider the inertia

of the flow, so that the force-free approximation equation is not appropriate. In this section, we derive an equation taking into account the inertia of the flow and explain the condition for pulsar wind to be accelerated. The following discussion is in line with Toma & Takahara (2013).

2.3.1 Conservation Laws along the Field Line

In steady and axisymmetric MHD equations, there are several constants of motion along the field lines. The conservation law of particle number in the steady state is

$$\nabla \cdot (n\gamma \boldsymbol{v_p}) = 0, \tag{2.82}$$

where n is a number density measured in the rest frame of the fluid. Since $\nabla \cdot \boldsymbol{B_p} = 0$ and $\boldsymbol{v_p} = \kappa \boldsymbol{B_p}$, we obtain

$$\boldsymbol{B_p} \cdot \nabla (n\gamma\kappa) = 0. \tag{2.83}$$

The mass flux per unit magnetic flux η is constant along the field line and written as:

$$\eta(\Psi) \equiv 4\pi m_e n \gamma \kappa. \tag{2.84}$$

The energy–momentum conservation law is already given as equation (2.39). From the time component, we obtain

$$\nabla \cdot \left[(\epsilon + p)\gamma^2 \boldsymbol{v_p} + \frac{c}{4\pi} [\boldsymbol{E} \times \boldsymbol{B}]_p \right] = 0 \tag{2.85}$$

Using equation (2.63), (2.60) and $[\boldsymbol{E} \times \boldsymbol{B}]_p = \boldsymbol{E_p} \times \boldsymbol{B_t}$, we have

$$\boldsymbol{B_p} \cdot \nabla \left[(\epsilon + p)\gamma^2 \kappa - \frac{\varpi\Omega}{4\pi} B_t \right] = 0. \tag{2.86}$$

The energy flux per unit rest energy flux $\mathcal{E}$ is constant along the field line and written as:

$$\mathcal{E}(\Psi) \equiv \left(\frac{\mu}{m_e c^2} \right) \gamma - \frac{\varpi \Omega B_t}{\eta c^2}, \tag{2.87}$$

where $\mu = (\epsilon + p)/n$ is the enthalpy per particle. The ratio of the Poynting flux to the kinetic energy flux σ is written as:

$$\sigma = -\frac{m_e \varpi \Omega B_t}{\eta \mu \gamma} = \frac{\mathcal{E} - \gamma}{\gamma}. \tag{2.88}$$

The toroidal component of equation (2.39) is written as

$$\boldsymbol{B_p} \cdot \nabla \left[(\epsilon + p)\varpi\gamma^2 v_t \kappa - \frac{\varpi\Omega}{4\pi} \varpi B_t \right] = 0. \tag{2.89}$$

The angular momentum flux per unit mass flux $\mathcal{L}$ is constant along the field line and written as:

$$\mathcal{L}(\Psi) \equiv \left(\frac{\mu}{m_e c^2} \right) \varpi \gamma v_t - \frac{\varpi B_t}{\eta}. \tag{2.90}$$

Furthermore, Ω in equation (2.66) is also the constant of motion along the field line, namely

$$\Omega(\Psi) = \frac{v_t - \kappa B_t}{\varpi}. \tag{2.91}$$

2.3.2 Bernoulli Equation

Here, we consider a situation where the functional form of $\boldsymbol{B_p}$ is given. By using equation(2.63), (2.60) and the equation of state, the unknown variables of the physical quantity of flow are four, namely n, v_t, κ, and B_t. As we introduced in Section 2.3.1, there are four constants of motion equations (2.84), (2.87), (2.90) and (2.91), so that four unknown quantities can be expressed by these constants of motion. After some algebra, we obtain

$$v_t = \frac{1}{\varpi}\frac{c^2\left(M^2\mathcal{L} - \varpi^2\Omega\mathcal{E}\right) + \varpi^2\Omega^2\mathcal{L}}{c^2\left(M^2-1\right)\mathcal{E} + \Omega\mathcal{L}}, \tag{2.92}$$

$$B_t = -\frac{\eta}{\varpi}\frac{\varpi^2\Omega\mathcal{E} - \mathcal{L}}{\left(M^2-1\right) + \varpi^2\Omega^2/c^2}, \tag{2.93}$$

$$\kappa = \frac{v_p}{B_p} = \frac{M^2}{\eta}\frac{c^2\left(M^2-1\right) + r^2\Omega^2}{c^2\left(M^2-1\right)\mathcal{E} + \mathcal{L}\Omega}, \tag{2.94}$$

and

$$\left(\frac{\mu}{m_e c^2}\right)\gamma = \frac{c^2\left(M^2-1\right)\mathcal{E} + \mathcal{L}\Omega}{c^2\left(M^2-1\right) + \varpi^2\Omega^2}, \tag{2.95}$$

where M is the Alfvén Mach number

$$M = \frac{\gamma v_p}{v_A} = \sqrt{\eta\kappa\gamma\left(\frac{\mu}{m_e c^2}\right)} = \sqrt{\frac{\gamma v_p \eta}{B_p}\frac{\mu}{m_e c^2}}, \tag{2.96}$$

and v_A is the Alfvén velocity

$$v_A \equiv \frac{B_p c}{\sqrt{4\pi\mu n}}. \tag{2.97}$$

The radius at which the denominator of equations (2.92)-(2.95) becomes 0 is called the Alfvén point and can be written as follows:

$$\varpi_A = \sqrt{\frac{\mathcal{L}}{\mathcal{E}\Omega}}. \tag{2.98}$$

In order for equations (2.92)-(2.95) to be regular at Alfvén point, the Mach number M_A in $\varpi = \varpi_A$ is

$$M_A^2 = 1 - \frac{\varpi_A^2}{\varpi_{\rm LC}^2}. \tag{2.99}$$

Since $M_A^2 > 0$, it is generally found that $\varpi_A < \varpi_{\rm LC}$. In other words, the flow which reaches far enough always passes through the Alfvén point. Using $x = \varpi/\varpi_{\rm LC}$ and $\gamma^2\left(v_p^2 + v_t^2\right) = c^2$, after some algebra, we obtain

$$1 + (\gamma v_p)^2 = \left(\frac{\mathcal{E}mc^2}{\mu}\right)^2 \frac{x^2\left(1 - x_A^2 - M^2\right)^2 - \left(x^2\left(1 - x_A^2\right) - x_A^2 M^2\right)^2}{x^2\left(1 - x^2 - M^2\right)^2}, \tag{2.100}$$

where $x_A = \varpi_{\rm A}/\varpi_{\rm LC} = \sqrt{\Omega\mathcal{L}/\mathcal{E}c^2}$ is the radius of the Alfven point normalized by $\varpi_{\rm LC}$. Additionally, from equation (2.84) and (2.97), we have

$$\frac{\mu}{nmc^2} = \frac{4\pi m M^2}{\eta^2}. \tag{2.101}$$

If μ can be written as $\mu = \mu(n)$ using the equation of state, equation (2.101) gives an relation between n and M. Since $M^2 = \eta\mu\left(\gamma v_p\right)/B_p m_e c^2$, equation (2.100) is an equation with only γv_p.

2.3.3 Magnetic Nozzle

Let us derive the differential equations of v_p in $\varpi \gg \varpi_{\rm LC}$, assuming that the flow is cold ($\mu \sim mc^2$). Since $\varpi\Omega \gg c \geq v_t$, from equation (2.91), we obtain

$$-\frac{B_t}{B_p} = \frac{\varpi\Omega - v_t}{v_p} \sim \frac{\varpi\Omega}{v_p}. \tag{2.102}$$

Substituting this to equation (2.87) and eliminating B_t, we have

$$\mathcal{E} \sim \gamma + \frac{\Omega^2}{\eta c^2}\frac{\mathcal{S}}{v_p}, \tag{2.103}$$

where $\mathcal{S} = \varpi^2 B_p$. Differentiating the logarithm of equation (2.103), we have

$$\frac{-d\gamma}{\mathcal{E}-\gamma} = \frac{d\mathcal{S}}{\mathcal{S}} - \frac{dv_p}{v_p}. \tag{2.104}$$

Assuming $v \sim v_p \sim c$, we can write the dv_p as $dv_p \sim c\gamma^{-3}d\gamma$. Therefore, we have

$$\left(\frac{1}{\mathcal{E}-\gamma} - \frac{1}{\gamma^3}\right)d\gamma = -\frac{d\mathcal{S}}{\mathcal{S}}. \tag{2.105}$$

The meaning of this equation can be interpreted in analogy with de Laval nozzle by considering $1/\mathcal{S}$ as an effective cross section (Begelman & Li, 1994). For the wind that satisfies $\gamma > (\mathcal{E}-\gamma)^{1/3}$, γ is increasing with decreasing S. This is similar to the fact that the supersonic flow through de Laval nozzle accelerates as the nozzle cross section increases. This is explained in the context of electrodynamics as follows. As can be seen from equation (2.49), the region where $\mathcal{S} = B_p\varpi^2 \sim B_t\varpi$ decreases is a region where the poloidal current flowing out within the radius ϖ from the polar axis decreases. This means that the current traverses poloidal field lines, so that it is said that the wind is accelerating by the $\boldsymbol{j} \times \boldsymbol{B}$ force.

2.3.4 Self-collimation and Wind Acceleration

The condition for accelerating the pulsar wind is that $\mathcal{S}$ decreases. This corresponds to a structure in which the field lines spread faster than a split monopole configuration (i.e. radial configuration). The model of pulsar wind nebulae requires that a pulsar wind is accelerating to $\gamma \sim 10^6$ just before the termination shock (to be described later). Takahashi & Shibata (1998) showed that such acceleration can be realized if $\mathcal{S} \propto \varpi^{-0.4}$. However, it is unknown whether a magnetic field that spreads faster than split monopole will form around the pulsar. For the non-relativistic wind, if the magnetic field of the central star is the split monopole structure, the field lines are collimated in the axial direction at the large distance, and so that the efficient acceleration of the wind at the equatorial plane is realized (Sakurai, 1985). In contrast, for the relativistic case, the mechanism of the self-collimation is very weak (Bogovalov, 2001). Figure 2.6 shows the resultant magnetic field structure for each cases. For the relativistic case, since the electrostatic force (is $\mathcal{O}(v^2/c^2)$ so negligible for the non-relativistic case) can be balanced to the Lorentz force, the wind is not always accelerated. Some studies argue that acceleration of wind can occur in more general magnetic field configuration (e.g., Vlahakis, 2004; Okamoto & Sigalo, 2006), and this problem is still an unsolved. This is the sigma problem (to be described later) seen from the aspect of the model of the pulsar wind.

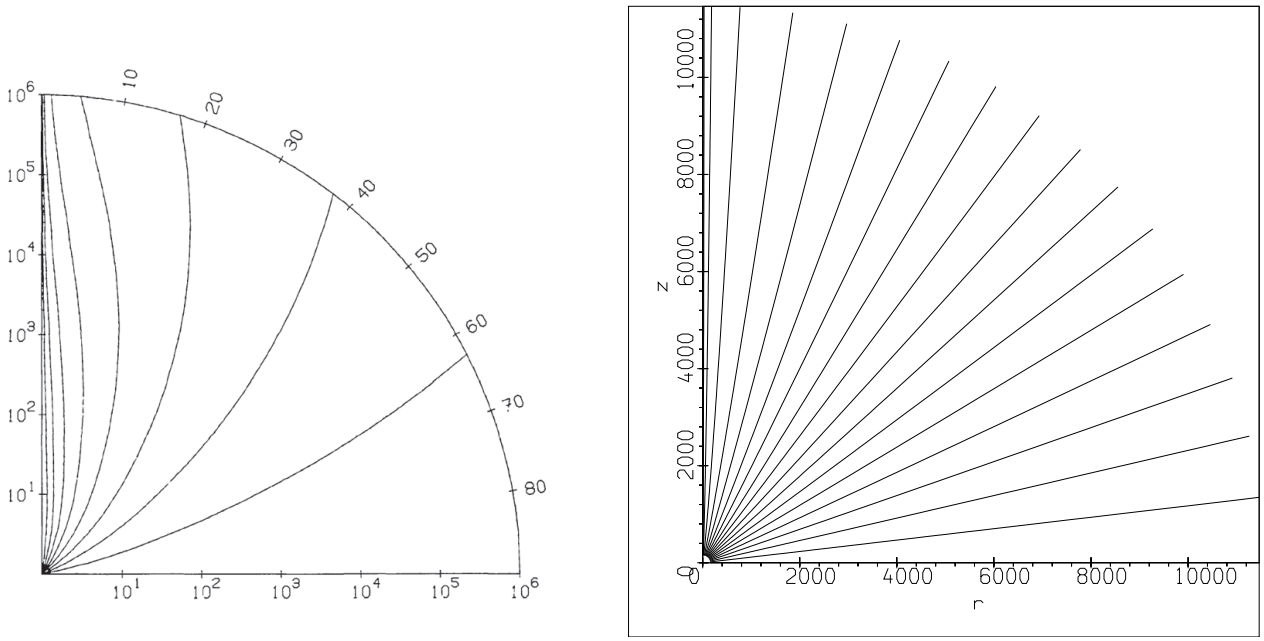

Figure 2.6: The structure of the poloidal field at large distance. The left panel shows for the non-relativistic case calculated by Sakurai (1985). A unit of the distance is the Alfvén radius. The right panel shows for the relativistic case calculated by Bogovalov (2001). In the right plot, a unit of the distance is the light cylinder rather than the Alfvén point. Credit (Left): Sakurai, A&A, 152, 121, 1985, reproduced with permission ©ESO. Credit (Right): Bogovalov, A&A, 371, 1155, 2001, reproduced with permission ©ESO.

2.4 Pulsar Wind Nebula

2.4.1 General description

The Pulsar wind that blows into the interstellar space (or surrounding SNR) with super sonic velocity forms a shock structure with the surrounding medium. The shocked pulsar wind obtains the entropy and spreads through interstellar space while synchrotron radiation (Rees & Gunn, 1974). Such a shocked wind spread around the pulsar is called the pulsar wind nebula. The theoretical model of the pulsar wind nebula will be explained in more detail in Section 3, so we will focus on a brief overview.

Figure 2.7 is the schematic view of the structure of the pulsar wind nebula. Since a formation of a pulsar is accompanied by a supernova, the pulsar is surrounded by an SNR (at least in enough young stage). Thus, the wind interacts with the SNR to form the shock structure, namely the termination shock, the contact discontinuity and the forward shock. At the termination shock, particles are isotropized in momentum space, and the bulk flow is decelerated to the sub-sonic velocity. At this time, it is thought that non-thermal particle distribution is formed by the particle acceleration process in the termination shock (see Appendix C). The particle energy distribution is usually expressed by a power-law as high as $\sim 10^{15}$ eV. The average energy of the particle $\sim 10^{11}$ eV is a significantly relativistic value so that the relaticistic equation of state $p = \epsilon/3$ holds.

The shocked wind expands while maintaining the pressure equilibrium with the surrounding SNR in the contact discontinuity. In the contact discontinuity, the Rayleigh-Taylor instability grows due to the mass density difference between the SNR material and the wind material, and sometimes

appears as a columnar structure called a filament. If the velocity of the shocked wind is faster than the speed of matter of the SNR, the forward shock develops.

The emission spectrum of pulsar wind nebulae is well explained by the synchrotron radiation and inverse Compton scattering from the electron and positron (see Figure 1.6). The spectrum from radio to X-rays is synchrotron radiation component, and γ-ray is mainly inverse Compton scattering component (de Jager & Harding, 1992; Atoyan & Aharonian, 1996). Synchrotron radiation is due to the interaction with the magnetic field associated with the pulsar wind itself. In a steady outflow the poloidal component of the magnetic field can be neglected at a large distance from the light cylinder, so that only the toroidal component is considered in many PWN models. This magnetic field is compressed as the shocked wind decelerates, and is strengthened until equipartition between the magnetic pressure and the plasma pressure is achieved (Rees & Gunn, 1974). The seed photons of the inverse Compton scattering are mainly photons from the interstellar dust and CMB, and synchrotron photons in the nebula itself (Tanaka & Takahara, 2011). The optical photons from star light is also important, but the inverse Compton scattering with such a photon is suppressed by the Klein–Nishina effect in many cases. The bremsstrahlung hardly contribute to the spectrum because the number density of pairs in the nebula is considered to be small (Atoyan & Aharonian, 1996).

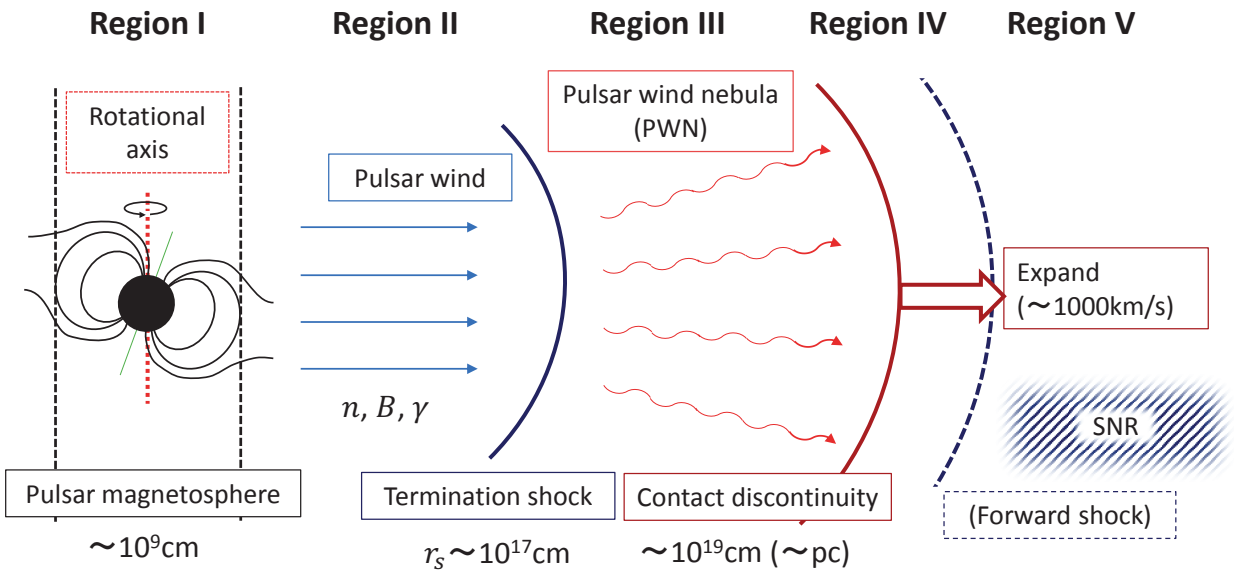

Figure 2.7: Schematic of the pulsar wind nebula. Region I is the pulsar magnetosphere. Region II is the place where the pulsar wind is blowing at a ultra-relativistic velocity. Region III is the place where the pulsar wind is isotropized and decelerated through the termination shock. The part emitting as the pulsar wind nebula is this region III. The pulsar wind reaches the contact discontinuity, and the outside of this is a material from a supernova explosion. Region IV is a place where the supernova remnants is compressesed and heated by the pulsar wind. Region V is a supernova remnant that expands with kinetic energy of supernova explosion. It propagates as a blast wave towards the external interstellar medium.

2.4.2 The Sigma Problem

The longstanding problem of pulsar wind nebulae is the σ problem. This was presented in the model of the Crab nebula by Kennel & Coroniti (1984a). The pulsar wind blows almost at the speed of light just before the termination shock. On the other hand, the expansion velocity of the Crab nebula is approximately 2000 kms^{-1}, which is much slower than the light speed. Kennel & Coroniti (1984a) constructed a 1-D MHD model and investigated conditions for decelerating. In order to decelerate the flow, σ must be much smaller than 1. They quantitatively discussed this and obtained the value $\sigma \sim 0.003$, which is also roughly consistent with the magnetic field obtained from the spectral model fitting (e.g., Tanaka & Takahara, 2010). In addition, Kennel & Coroniti (1984b) constructed the emission model, and found that $\gamma \sim 10^6$ just before the termination shock. These results means that the magnetic energy of the pulsar wind is very efficiently converted into the wind kinetic energy. However, as mentioned in Section 2.3.4, such an efficient acceleration is difficult from the model of pulsar wind. This discrepancy is called the σ problem and is not solved yet.

Porth et al. (2014) showed that there is a solution in which the flow is sufficiently decelerated even if $\sigma \sim 1$ by 3-D MHD simulation. In their calculations, due to the kink instability, the nebula is filled with a turbulent magnetic field. As a result, the magnetic pressure is effectively weakened so that the flow can be decelerated. Recently, Tanaka et al. (2018) constructed a 1D model that takes into account the conversion from an ordered field to a turbulent field phenomenologically. They also showed that flow can be sufficiently slowed even if σ is large. However, they did not discuss the broadband emission model. When the magnetic field is strong, the efficiency of synchrotron radiation would change significantly. Thus, such a solution to the σ problem needs to consider simultaneously the emission model, and is still incomplete.

Chapter 3

Revisiting the Kennel & Coroniti Model

3.1 Introduction

Kennel & Coroniti (1984a,b, hereafter KC84s) constructed a steady-state and 1-D magnetohydrodynamic model (KC model) of the Crab Nebula. Their study is motivated that the speed of the nebula expansion is much slower than the un-shocked wind ($v \sim c$). As mentioned in Section 2.4, this can be explained well if it is $\sigma \ll 1$ upstream of the termination shock. Also, assuming the particle acceleration at the termination shock, they calculated the evolution of non-thermal pairs

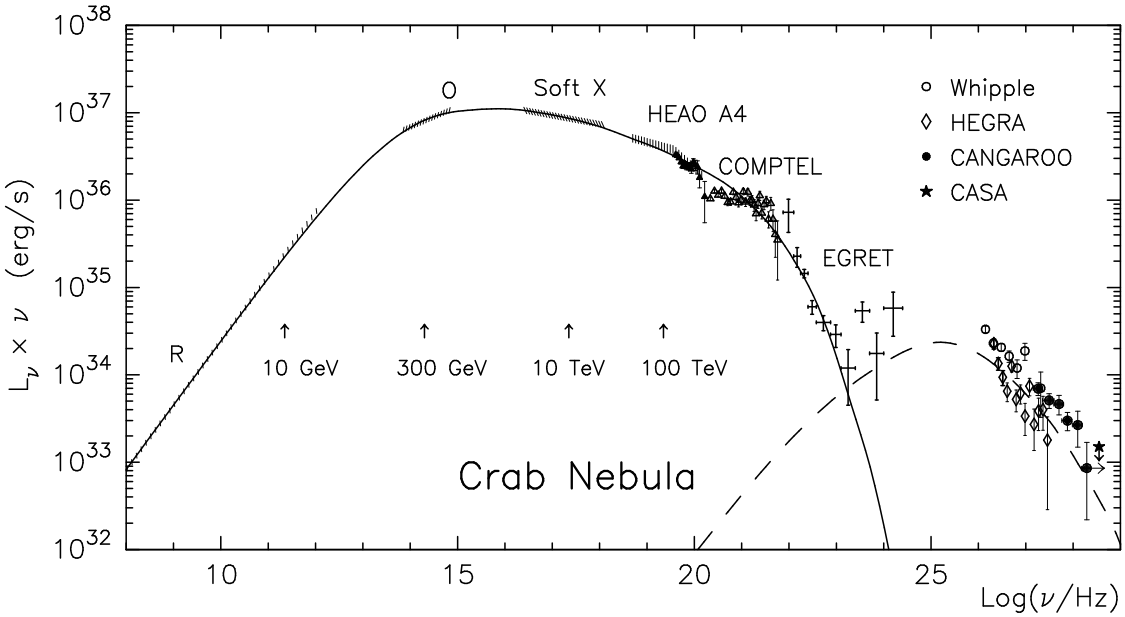

Figure 3.1: The entire spectrum of the Crab nebula and the model curve obtained Atoyan & Aharonian (1996). The solid line represents the synchrotron emission from non-thermal pairs. The dashed line represents the inverse Compton scattering. Credit: Atoyan & Aharonian, A&AS, 120, 453, 1996, reproduced with permission ©ESO.

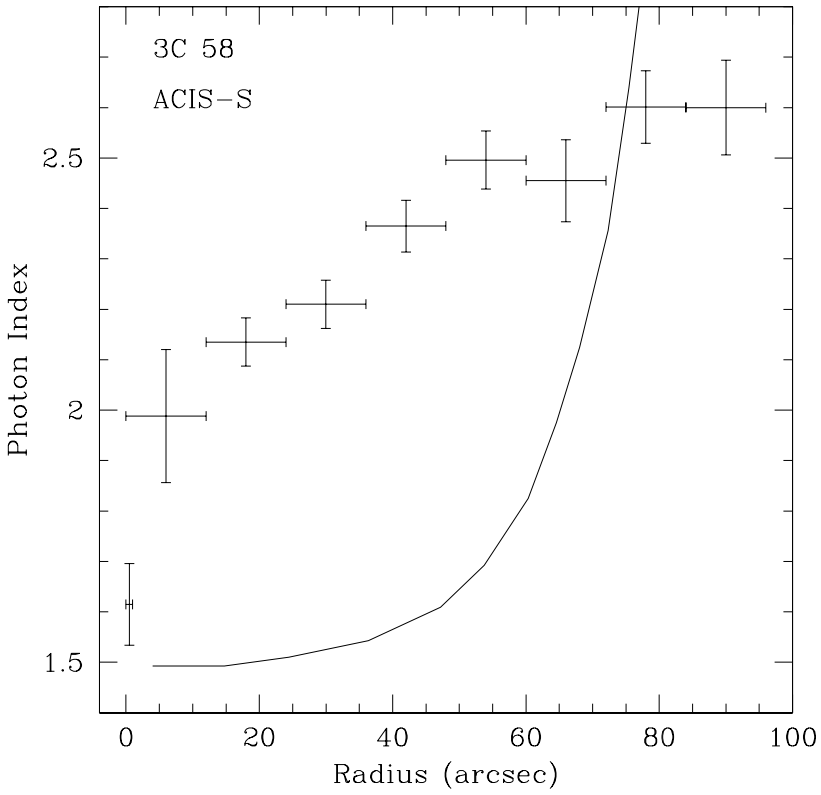

Figure 3.2: The radial profile of the X-ray photon index for 3C 58. The black solid line is the predicted profile based on the KC model. The figure from Slane et al. (2004). ©AAS. Reproduced with permission.

along the flow and the synchrotron emission from advected particles. Adopting the KC model, Atoyan & Aharonian (1996) succeeded in reproducing the entire photon spectrum including the inverse Compton component. Figure 3.1 shows their result for the Crab Nebula. Thus, the KC model has been thought to be the standard model as it explains both the radiation spectrum of the nebula and the expansion speed well.

X-ray space telescopes including the Chandra X-ray Observatory in the 2000's, have achieved abundant observational results on the pulsar wind nebula other than the Crab Nebula. The KC model was subjected to more stringent verification, and as a result the problem of the model was found out. Reynolds (2003) suggested that it is unclear whether KC84s can apply to general PWNe other than the Crab Nebula. Moreover, Slane et al. (2004) showed that the KC84s model disagrees with the observed radial profile of the X-ray spectral index in 3C 58. They suggested that the radial profile of the X-ray spectral index in the model should change more rapidly (see Figure 3.2), and the X-ray nebula size becomes more compact than the observation. Note that the entire photon spectrum was not taken into account as a model constraint in Slane et al. (2004).

As a emission model of the pulsar wind nebula, calculations to reproduce the broadband spectra of entire nebulae by 1-zone models have been successful (e.g., Bednarek & Bartosik, 2003; Chevalier, 2005; Tanaka & Takahara, 2010; Bucciantini et al., 2011; Vorster et al., 2013b). However, as shown in Figure 3.3, the 1-zone models can not describe the spatial distribution of the emission (e.g., Amato et al., 2000), thus it is indispensable to invest a model which includes the spatial structure

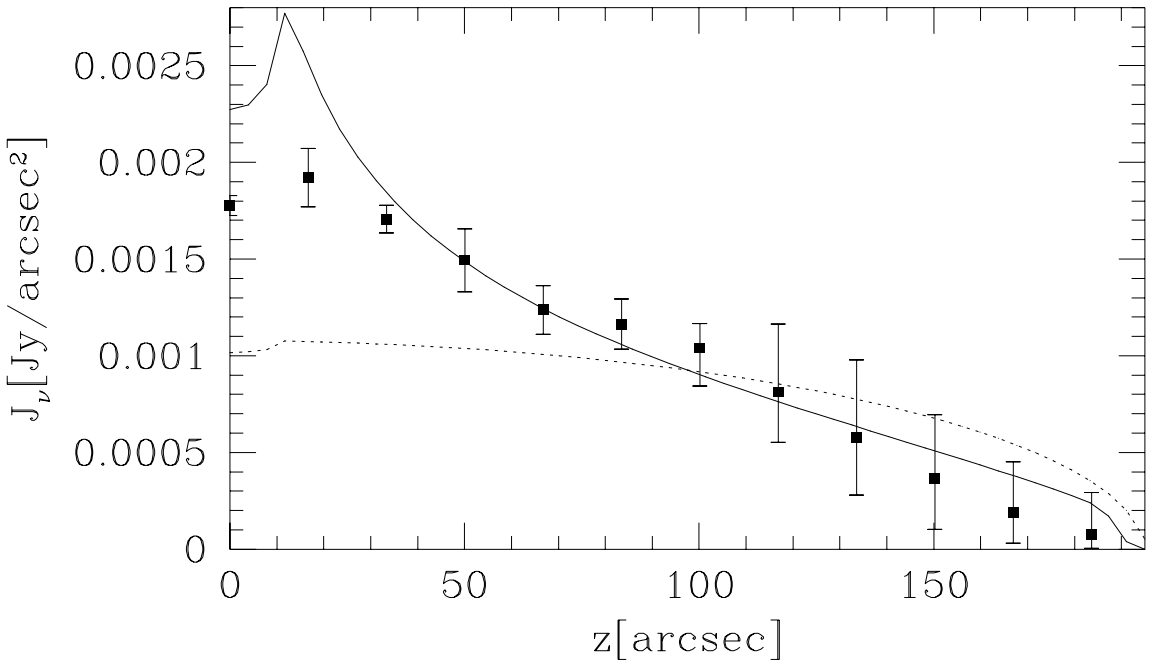

Figure 3.3: Comparison with the radio surface brightness of the KC model (solid line) and the 1-zone model (dotted line), where a sphere with a uniform emissivity is assumed. The radio data points are obtained by the technique called "data spherization", which is averaged radial profile, developed by Amato et al. (2000). The error bars contains the uncertainties caused by this procedure. Credit: Amato et al., A&A, 359, 1107, 2000, reproduced with permission ©ESO.

of nebulae.

Observed facts showing the deviation from the KC model ignited the revision of KC84s. Tang & Chevalier (2012) introduced the effect of the spatial diffusion of the particles, and reproduced the X-ray radial profile. Porth et al. (2016) supported this idea via 3D magnetohydrodynamic and test-particle simulations. In each of the studies, simultaneous verification of the entire spectrum and the spatial profile of the emission is not discussed, thus there is no consensus on the spatial structure in PWN models so far. In order to advance the study, it is essential to clarify controversial points in the simple steady 1-D model before introducing nontrivial effects such as the particle diffusion.

We choose two objects, 3C 58 and G21.5-0.9, to examine the 1-D steady model. Both of the PWNe show the feature that the extent of the X-ray emission is the same as the radio one (see Figure 1.5 and 3.4), in contrast to the Crab Nebula, in which the observed size shrinks with increasing frequency. Moreover, the 1-D steady model has been never applied to those two PWNe. Our purpose is to make the validity of the 1-D steady model clear for general PWNe, so that those two PWNe are suitable targets for testing.

In this chapter, we revisit the 1-D steady model and calculate the photon spectrum and its radial profile numerically. In Section 3.2, we review the 1-D steady model of PWNe based on KC84s. The parameter dependence of this model is investigated in Section 3.3. The application to the two observed sources (3C 58 and G21.5-0.9) is presented in Section 3.4. Section 3.5 summarizes our results and discusses about the 1-D steady modeling.

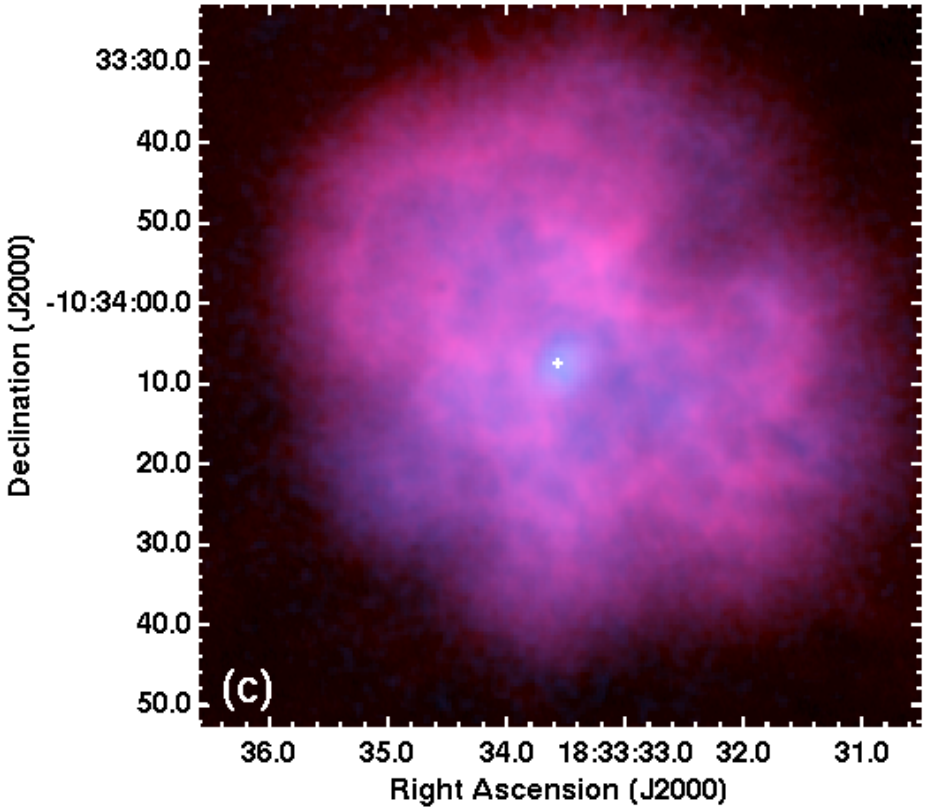

Figure 3.4: The image of G21.5-0.9 in 4.75 GHz radio band obtained by Bietenholz & Bartel (2008) (red) and 0.2-10 keV X-rays obtained by Matheson & Safi-Harb (2010) (blue). The extent in the X-ray is comparable with the one in the radio band. ©AAS. Reproduced with permission.

3.2 Model

3.2.1 Magnetohydrodynamics of PWNe

Here, we assume that the PWN is a steady and spherical system with a radius $r_{\rm N}$. The relativistic magnetized wind emitted from the central pulsar forms a strong termination shock at a radius $r_{\rm s}$. We also assume that the gas pressure of the pre-shock wind is negligible, so that the wind property is regulated by three quantities, the comoving number density n, bulk Lorentz factor γ, and magnetic field in the lab frame B at the shock front. Almost all of the pulsar spin-down luminosity $L_{\rm sd}$ is converted to the wind luminosity as

$$L_{\rm sd} = 4\pi r_{\rm s}^2 n_{\rm u} u_{\rm u} \gamma_{\rm u} m_{\rm e} c^3 \left(1+\sigma\right), \tag{3.1}$$

where $u \equiv \sqrt{\gamma^2 - 1}$, the subscript u denotes values at just upstream of the shock, and σ is the ratio of the magnetic energy flux to the particle energy flux at the upstream of the shock,

$$\sigma \equiv \frac{B_{\rm u}^2/4\pi}{n_{\rm u} u_{\rm u} \gamma_{\rm u} m_{\rm e} c^2}. \tag{3.2}$$

Since the scale of the termination shock is much larger than the scale of the light-cylinder, the magnetic field at the shock is almost purely toroidal field (e.g., Goldreich & Julian, 1969). The

upstream plasma is highly relativistic ($u_{\rm u}/\gamma_{\rm u} \simeq 1$), which means the downstream temperature is relativistic (adiabatic index 4/3). The physical quantities in the downstream is given by the Rankine-Hugoniot conditions (KC84s, see Appendix A.2 for details) as

$$n_{\rm d} = \frac{n_{\rm u} u_{\rm u}}{u_{\rm d}}, \tag{3.3}$$

$$u_{\rm d}^2 = \frac{8\sigma^2 + 10\sigma + 1 + \sqrt{64\sigma^2(\sigma+1)^2 + 20\sigma(\sigma+1) + 1}}{16(\sigma+1)}, \tag{3.4}$$

$$P_{\rm d} = \frac{n_{\rm u} m c^2 u_{\rm u}^2}{4\gamma_{\rm d} u_{\rm d}} \left[1 + \sigma\left(1 - \frac{\gamma_{\rm d}}{u_{\rm d}}\right)\right], \tag{3.5}$$

$$B_{\rm d} = B_{\rm u}\frac{\gamma_{\rm d}}{u_{\rm d}}, \tag{3.6}$$

where the subscript d denotes the values at just downstream of the shock, and P is the gas pressure.

Adopting Equations (3.3)–(3.6) as boundary conditions at the radius $r = r_{\rm s}$, we can solve the steady state and spherical symmetric MHD equations. Under the toroidal field approximation and the adiabatic assumption, the MHD equations are integrable. After some algebra with introducing $\delta \equiv u_{\rm d}/(\sigma u_{\rm u})$, we obtain (KC84s, see Appendix A.3 for details)

$$\sqrt{1+u^2(r)}\left(\delta + \frac{(u_{\rm d}^2/\sigma) - \frac{1}{2}}{u_{\rm d}^2 + \frac{1}{4}}\left(\frac{u(r)r^2}{u_{\rm d} r_{\rm s}^2}\right)^{-\frac{1}{3}} + \frac{u_{\rm d}}{u(r)}\right) = \gamma_{\rm d}\left(\delta + \frac{(u_{\rm d}^2/\sigma) - \frac{1}{2}}{u_{\rm d}^2 + \frac{1}{4}} + 1\right), \tag{3.7}$$

from which we obtain the radial profile of the four velocity $u(r)$. In the case of the strong shock, $u_{\rm d}$ is a function of only σ as shown in Equation (3.4). If $\delta \ll 1$ is hold, the parameter of the flow equation (3.7) becomes only σ and does not depend on $n_{\rm u}$ and $u_{\rm u}$. We calculate $u(r)$ numerically as a function of the radius, whereas KC84s neglected δ and adopted $\gamma_{\rm d} \simeq 1$ in the downstream. Then, the MHD conservation laws provide the other quantities as follows:

$$n_{\rm tot}(r) = n_{\rm d}\frac{u_{\rm d} r_{\rm s}^2}{u(r) r^2}, \tag{3.8}$$

$$B(r) = B_{\rm d}\frac{\gamma(r)}{\gamma_{\rm d}}\frac{u_{\rm d} r_{\rm s}}{u(r) r}, \tag{3.9}$$

$$P(r) = P_{\rm d}\left(\frac{u_{\rm d} r_{\rm s}^2}{u(r) r^2}\right)^{4/3}, \tag{3.10}$$

where $n_{\rm tot}(r)$ is the number density in the wind measured in the co-moving frame.

In Figure 3.5, the radial dependence of $u(r)$ and $B(r)$ in our test calculations are shown for $\sigma = 10^{-6}$, 10^{-5}, 10^{-4}, 10^{-3} and 10^{-2}. Since $\delta \ll 1$ for all the cases, the results are similar to KC84s. For $\sigma \ll 1$, at a small radius, the pressure ratio $\beta_{\rm pl} \equiv B^2/8\pi P$ ($\ll 1$ at $r = r_{\rm s}$) gradually increases with radius as $\beta_{\rm pl} \propto r^2$. In that regime, the flow decelerate as $u \propto r^{-2}$ (equivalently $n_{\rm tot} \propto r^0$), $B \propto r$ and $P \propto r^0$. At the radius

$$r \simeq r_{\rm eq} \equiv r_{\rm s}/\sqrt{3\sigma}, \tag{3.11}$$

$\beta_{\rm pl}$ becomes $\mathcal{O}(1)$, namely the magnetic pressure starts to dominate. Outside $r_{\rm eq}$, $u(r)$ is almost constant, $B \propto r^{-1}$ and $P \propto r^{-8/3}$. Thus, the magnetic field has a maximum value at $r \simeq r_{\rm eq}$ as shown in Figure 3.5.

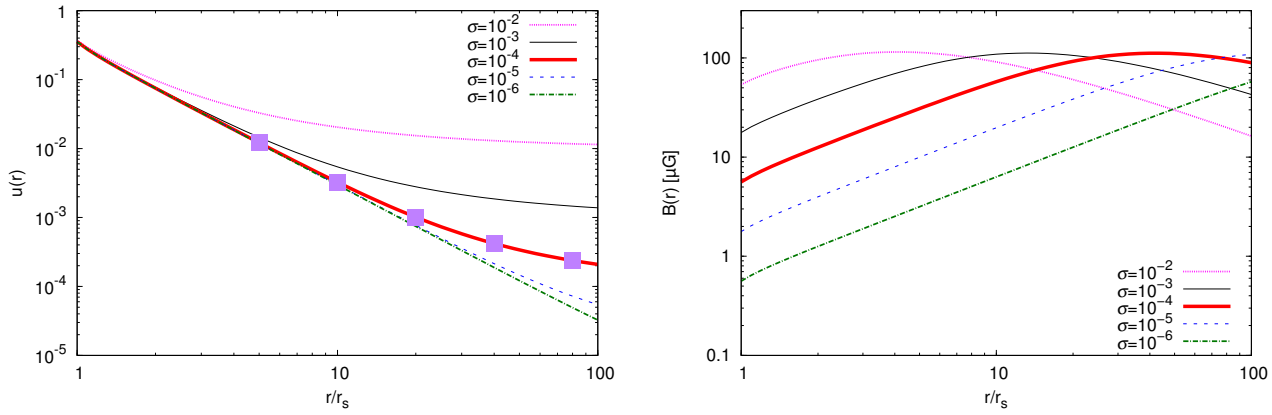

Figure 3.5: Test calculations of u (left) and B (right) with $u_{\rm u} = 10^6$, $L_{\rm sd} = 10^{38}$erg s^{-1}, and $r_{\rm s} = 0.1$ pc for various σ. The squares mark values of the four velocity at the edge of the nebula for $r_{\rm N}/r_{\rm s} = 5$, 10, 20, 40 and 80.

3.2.2 Broadband emission model of PWNe

The energy spectrum $n(E, r)$ of electron–positron pairs is calculated consistently with the MHD model,

$$n_{\rm tot}(r) = \int n(E, r) dE. \tag{3.12}$$

At the termination shock $r = r_{\rm s}$, $n(E, r_{\rm s})$ is assumed to have a broken power-law shape at injection as following:

$$n(E, r_{\rm s}) = \begin{cases} \dfrac{n_0}{E_{\rm b}} \left(\dfrac{E}{E_{\rm b}} \right)^{-p_1} & (E_{\rm min} < E < E_{\rm b}) \\ \dfrac{n_0}{E_{\rm b}} \left(\dfrac{E}{E_{\rm b}} \right)^{-p_2} & (E_{\rm b} < E < E_{\rm max}) \end{cases}, \tag{3.13}$$

where the parameters are the break energy $E_{\rm b}$, minimum energy $E_{\rm min}$, maximum energy $E_{\rm max}$, and two power-law indices p_1 and p_2 for low and high energy parts, respectively. The normalization constant $n_0 = C_1 n_{\rm d}$ is determined by Equation (3.12) as

$$C_1 \equiv \left[\frac{1}{p_1 - 1} \left\{ \left(\frac{E_{\rm min}}{E_{\rm b}} \right)^{1-p_1} - 1 \right\} + \frac{1}{p_2 - 1} \left\{ 1 - \left(\frac{E_{\rm max}}{E_{\rm b}} \right)^{1-p_2} \right\} \right]^{-1}. \tag{3.14}$$

While the origin of the radio spectral component may be different from that for the X-ray and optical components as discussed in KC84s, in this calculation, we use a broken power-law distribution that has been adopted by the 1-zone studies (e.g., Tanaka & Takahara, 2010).

The index p_1 is almost uniquely given by the observed radio spectral index, which is generally lower than 2 (e.g., Salter et al., 1989). In this case, the particles with energies $\sim E_{\rm min}$ dominate the particle number. For simplicity, we fix the minimum energy as $E_{\rm min} = 10 m_{\rm e} c^2$ and leave the pair multiplicity problem (c.f. Tanaka & Takahara, 2013b). The particles above $E_{\rm b}$ may be produced via the shock acceleration (Spitkovsky, 2008) (see Appendix C). The maximum energy $E_{\rm max}$ is determined by the "size-limited" method (same as KC84s); the energy at which a gyro radius is

equal to the termination shock radius provides

$$E_{\rm max} = eB_{\rm u}r_{\rm s} = \sqrt{\frac{e^2}{c}\frac{L_{\rm sd}\sigma}{1+\sigma}}. \tag{3.15}$$

The pressure calculated by integrate $n(E, r_{\rm s})$,

$$P_{\rm d} = \frac{1}{3}\int En(E, r_{\rm s})dE, \tag{3.16}$$

should satisfy Equation (3.5). Thus, we get

$$n_{\rm d} = \frac{3L_{\rm sd}}{16\pi r_{\rm s}^2 c u_{\rm d}\gamma_{\rm d}E_{\rm b}\,(1+\sigma)}\frac{C_2}{C_1}\left[1+\sigma\left(1-\frac{\gamma_{\rm d}}{u_{\rm d}}\right)\right], \tag{3.17}$$

where

$$C_2 = \left[\frac{1}{2-p_1}\left\{1-\left(\frac{E_{\rm min}}{E_{\rm b}}\right)^{2-p_1}\right\} + \frac{1}{p_2-2}\left\{1-\left(\frac{E_{\rm max}}{E_{\rm b}}\right)^{2-p_2}\right\}\right]^{-1}. \tag{3.18}$$

Notify that $\gamma_{\rm d}$ or $u_{\rm d}$ is already given as a function of only σ (see Equation (3.4)), so that the quantities in the upstream are written with the six parameters $L_{\rm sd}$, σ, $r_{\rm s}$, $E_{\rm b}$, p_1, and p_2 as

$$\gamma_{\rm u} = \frac{4}{3}\frac{E_{\rm b}}{mc^2}\gamma_{\rm d}\frac{C_1}{C_2}\left[1+\sigma\left(1-\frac{\gamma_{\rm d}}{u_{\rm d}}\right)\right]^{-1}, \tag{3.19}$$

$$B_{\rm u} = \left[\frac{L_{\rm sd}}{cr_{\rm s}^2}\frac{\sigma}{1+\sigma}\right]^{1/2}, \tag{3.20}$$

and

$$n_{\rm u} = \frac{9L_{\rm sd}}{64\pi r_{\rm s}^2 c\gamma_{\rm d}^2 m_{\rm e}c^2\,(1+\sigma)}\left(\frac{C_2}{C_1}\frac{m_{\rm e}c^2}{E_{\rm b}}\right)^2\left[1+\sigma\left(1-\frac{\gamma_{\rm d}}{u_{\rm d}}\right)\right]^2. \tag{3.21}$$

From these relations, the initial spectrum described by equation (3.13) is also written by these six parameters.

In this 1-D model, there is a unique parameter $r_{\rm s}$, which is not in the 1-zone models, and $r_{\rm s}$ significantly affects the results as will be shown in Section 3.3. The advection time is provided by the solution to the Bernoulli equation (3.7),

$$t_{\rm adv} = \int_{r_{\rm s}}^{r_{\rm N}}\frac{dr}{cu(r)}. \tag{3.22}$$

In the 1-zone time-dependent models, the age of the PWN is an important parameter (e.g., Tanaka & Takahara, 2010). As the counterpart of this in our steady model, the parameter $r_{\rm s}$ adjusts the advection time, which may be close to the age of the PWN.

The radial evolution of $n(E, r)$ and photon emission are calculated with the numerical code used in Sasaki et al. (2015), which are based on the time-dependent code in Asano & Mészáros (2011) (see also Asano & Mészáros, 2012). We take into the calculation code account the Klein-Nishina effect on the inverse Compton (IC) cooling, and follow the temporal evolution of the energy distribution along the stream. Using the Lagrangian method (transforming the elapsed time into advected

radius as $dr = cu(r)dt$), we solve the steady transport equation (e.g. Parker (1965); Ginzburg & Syrovatskii (1964))

$$u(r)\frac{\partial n(E,r)}{\partial r} = \frac{\partial}{\partial E}\left[\left(\dot{E}_{\rm syn} + \dot{E}_{\rm IC}\right) n(E,r)\right] + \frac{\partial}{\partial E}\left[\frac{cEn(E,r)}{3r^2}\frac{d}{dr}\left(r^2 u(r)\right)\right] - \frac{c}{r^2} n(E,r)\frac{d}{dr}\left(r^2 u(r)\right), \tag{3.23}$$

where $\dot{E}_{\rm syn}$ and $\dot{E}_{\rm IC}$ are the energy loss rates due to synchrotron radiation and IC scattering, respectively. The three terms of the right hand side of Equation () represent the effects of the radiative cooling, adiabatic cooling and dilution, respectively.

Here we used the solution of $u(r)$ in adiabatic approximation. In other words, it is assumed that radiative cooling does not affect flow dynamics. This approximation is valid when the particle cooling time of $E \sim E_{\rm b}$ is longer than the advection time (KC84s). Most of the results shown in this chapter safely satisfy this condition.

The spectral emissivity per unit volume $j_\nu(r)$ is calculated consistently with pair energy spectrum $n(E,r)$, magnetic field distribution $B(r)$, and interstitial radiation field (ISRF) with the Klein–Nishina effect (see Appendix B). The model of ISRF is taken from GALPROP v54.1 (Vladimirov et al., 2011, and the references therein), and the result of Porter & Strong (2005) is adopted as shown in Figure 3.6. We assume that the ISRF is uniform and isotropic in nebula, and ignore synchrotron self-Compton (SSC). The SSC contributes only in limited case like the Crab Nebula (Torres et al., 2013; Tanaka & Takahara, 2011). Furthermore, since the density of pairs is sufficiently low, the contribution of bremsstrahlung is also ignored (Atoyan & Aharonian, 1996).

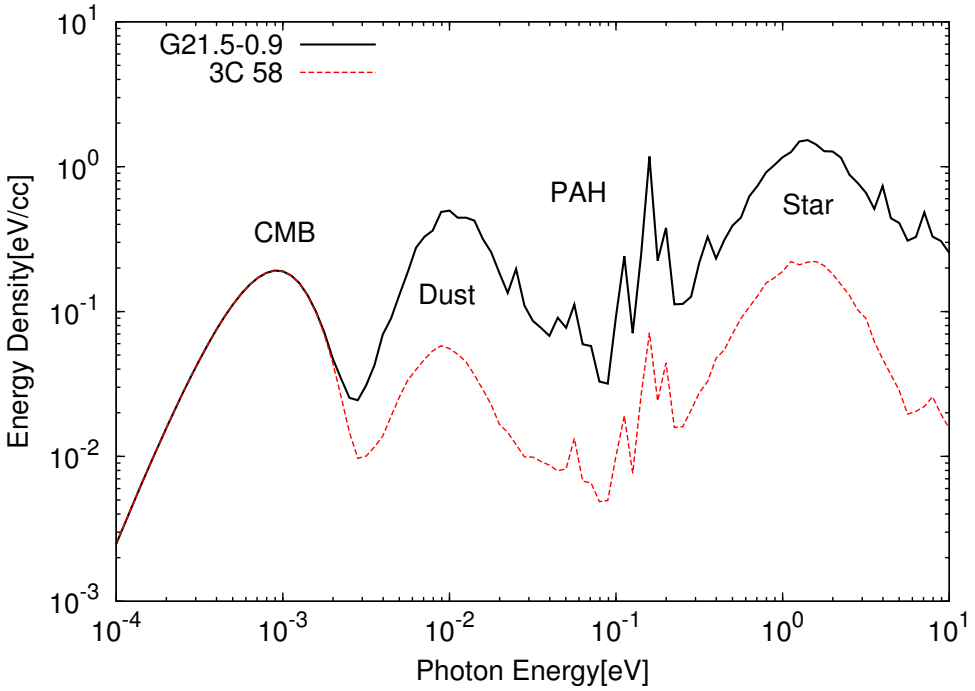

Figure 3.6: The spectra of the interstellar radiation field taken from GALPROP v54.1. The black solid line is one adopted for G21.5-0.9, which is located at $R = 4$ kpc and $z = 0$ kpc. The red dashed line is for 3C 58, which is located at $R = 9.4$ kpc and $z = 0.5$ kpc.

Neglecting the emission from the up-stream wind, we obtain the photon spectrum of the entire

nebula F_ν,

$$F_\nu = \frac{1}{D^2}\int_{r_s}^{r_N} j_\nu(r)\, r^2 dr, \tag{3.24}$$

where D is the distance to the PWN from us. The radial profile of the surface brightness B_ν is given by

$$B_\nu(s) = 2\int_{\max(r_s,s)}^{r_N} \frac{j_\nu(r)\, r dr}{\sqrt{r^2-s^2}}, \tag{3.25}$$

where s is the distance perpendicular to the line of sight from the central pulsar.

3.3 Parameter Dependence in the model

In this section, we discuss how the entire spectrum $L_\nu \equiv 4\pi D^2 F_\nu$ and the surface brightness B_ν depend on the parameters in this 1-D steady model. There are some previous studies that discussed the parameter dependence of the 1-D model. KC84s have already discussed how the parameters u_u and σ change the total synchrotron luminosity $\int L_\nu d\nu$ (not the spectral distribution). While Schöck et al. (2010) have studied the X-ray spatial profile for different r_s assuming that the flow velocity decreases as a power-law of r independently of σ, we investigate the parameter dependence consistently with the MHD flow solution. We focus on the dependence on the parameters r_s and σ, which largely affect the spatial structure of the emission. In this section, the nebula size $r_N = 2.0$ pc is fixed. The external photon field is taken from the model for G21.5-0.9 in Figure 3.6. For four parameters out of the six parameters in our model, we adopt a parameter set as $L_{sd} = 10^{38}$ erg s^{-1}, $E_b = 10^5 m_e c^2$, $p_1 = 1.1$, and $p_2 = 2.5$, and change r_s or σ below.

3.3.1 Characteristic frequencies and energies

First, we introduce some typical particle energies and their corresponding photon frequencies, and discuss their dependence on model parameters. In this subsection, discussions are limited to the "imcompressive" cases, namely $r_N < r_{eq}$ (i.e., $r_N/r_s < (3\sigma)^{-1/2}$). In this case, the magnetic field has a maximum value $3B_u r_N/r_s$ at the edge of the nebula. The cooling effect for pairs with energies $E = E_b$ is also found to be negligible. We find the first typical frequency, which corresponds to the intrinsic break frequency,

$$\begin{aligned}\nu_b &= \frac{3eB(r_N)}{4\pi m_e c}\left(\frac{E_b}{m_e c^2}\right)^2 \\ &\simeq 4.7\times10^{12}\ \mathrm{Hz}\left(\frac{L_{sd}}{10^{38}\mathrm{erg\ s^{-1}}}\right)^{\frac{1}{2}}\left(\frac{\sigma}{10^{-4}}\right)^{\frac{1}{2}}\left(\frac{E_b}{10^5 m_e c^2}\right)^2\left(\frac{r_s}{0.1\ \mathrm{pc}}\right)^{-2}\left(\frac{r_N}{2\ \mathrm{pc}}\right).\end{aligned} \tag{3.26}$$

In the case of $B \propto r$ or equivalently $u \propto r^{-2}$, the energy of pairs injected with $E = E_{max}$ decreases with r via the synchrotron cooling as

$$E_{cut}(r) = \frac{E_{max}}{1+\frac{1}{5}\frac{E_{max}}{E_{bof}}\left((\frac{r}{r_s})^5-1\right)}, \tag{3.27}$$

where the burn-off energy

$$\begin{aligned}E_{bof} &\equiv \frac{9m_e^4c^8u_d}{4e^4B_d^2r_s} \simeq \frac{m_e^4c^9r_s}{8\sqrt{2}e^4L_{sd}\sigma} \\ &\simeq 4.3\times10^{17}\mathrm{eV}\left(\frac{L_{sd}}{10^{38}\mathrm{erg\ s^{-1}}}\right)^{-1}\left(\frac{\sigma}{10^{-4}}\right)^{-1}\left(\frac{r_s}{0.1\ \mathrm{pc}}\right),\end{aligned} \tag{3.28}$$

(KC84s). At $r = r_{\rm N}$, the maximum energy is given by $E_{\rm cut}(r_{\rm N}) \simeq 5E_{\rm bof}(r_{\rm s}/r_{\rm N})^5$. Then, the cooling frequency at the outer boundary is given by

$$\begin{aligned}\nu_{\rm c} &= \frac{3eB(r_{\rm N})}{4\pi m_{\rm e}c}\left(\frac{E_{\rm cut}(r_{\rm N})}{m_{\rm e}c^2}\right)^2 \\ &\simeq 8.2\times10^{14}\ {\rm Hz}\left(\frac{L_{\rm sd}}{10^{38}{\rm erg\ s^{-1}}}\right)^{-\frac{3}{2}}\left(\frac{\sigma}{10^{-4}}\right)^{-\frac{3}{2}}\left(\frac{r_{\rm s}}{0.1\ {\rm pc}}\right)^{10}\left(\frac{r_{\rm N}}{2\ {\rm pc}}\right)^{-9}. \end{aligned} \tag{3.29}$$

Above $\nu_{\rm c}$, the entire spectrum should show the softening behavior.

The maximum particle energy decreases following Equation (3.27), while the magnetic field increases as $B(r) = 3B_{\rm u}(r/r_{\rm s})$. The typical synchrotron frequency $\propto B(r)E_{\rm cut}(r)^2$ peaks at

$$\begin{aligned} r \simeq r_{\rm pk} &\equiv \left(\frac{5E_{\rm bof}}{9E_{\rm max}}\right)^{1/5} r_{\rm s} \\ &\simeq 0.14{\rm pc}\left(\frac{L_{\rm sd}}{10^{38}{\rm erg\ s^{-1}}}\right)^{-3/10}\left(\frac{\sigma}{10^{-4}}\right)^{-3/10}\left(\frac{r_{\rm s}}{0.1\ {\rm pc}}\right)^{6/5}, \end{aligned} \tag{3.30}$$

where we have assumed $E_{\rm max} \ll 5E_{\rm bof}$. With $r_{\rm pk}$, the cut-off frequency in the synchrotron spectrum is calculated as

$$\begin{aligned}\nu_{\rm cut} &= \frac{3eB(r_{\rm pk})}{4\pi m_{\rm e}c}\left(\frac{E_{\rm cut}(r_{\rm pk})}{m_{\rm e}c^2}\right)^2 \\ &\simeq \frac{729e}{400\pi m_{\rm e}c}\sqrt{\frac{L_{\rm sd}\sigma}{cr_{\rm s}^2}}\left(\frac{5E_{\rm bof}}{9E_{\rm max}}\right)^{1/5}\left(\frac{E_{\rm max}}{m_{\rm e}c^2}\right)^2 \\ &\simeq 9.3\times10^{18}\ {\rm Hz}\left(\frac{L_{\rm sd}}{10^{38}{\rm erg\ s^{-1}}}\right)^{11/10}\left(\frac{\sigma}{10^{-4}}\right)^{11/10}\left(\frac{r_{\rm s}}{0.1\ {\rm pc}}\right)^{-4/5}, \end{aligned} \tag{3.31}$$

above which the flux decreases exponentially.

3.3.2 Parameter Dependence: termination shock radius

The termination shock radius is not included as a parameter of the one-zone model. In the 1-D model, the value $r_{\rm s}$ is a characteristic parameter. In most of PWNe, the termination shock radii are not observationally measured well. As an example of the limited PWNe in which this has been constrained, for the Crab Nebula (Schweizer et al., 2013), Vela (Helfand et al., 2001), and MSH 15-52 (Yatsu et al., 2009), a possible shock structure (inner ring) is detected with X-ray observations. In Figure 3.7, we show the $r_{\rm s}$-dependences of the entire spectrum L_ν and the X-ray surface brightness with $\sigma = 10^{-4}$. Emission below 10^{20} Hz ($\sim$ 400 keV) is synchrotron radiation, and γ-ray is IC component. Note that in the case for $r_{\rm s} = 0.05$ pc, $E_{\rm cut}(r) < E_{\rm b}$ beyond $r \gtrsim 1.5$ pc , i.e., the adiabatic approximation is invalid. In Table 3.1, for various $r_{\rm s}$, we summarize the advection time, the volume-averaged magnetic field $B_{\rm av}$ as,

$$\frac{B_{\rm av}^2}{8\pi} = \int_{r_{\rm s}}^{r_{\rm N}} \frac{B(r)^2}{8\pi} 4\pi r^2 dr \Big/ \int_{r_{\rm s}}^{r_{\rm N}} 4\pi r^2 dr, \tag{3.32}$$

and the maximum magnetic field $B_{\rm max} = B(r_{\rm N})$ because we have $r_{\rm eq} > r_{\rm N}$ from Equation (3.11) with $\sigma = 10^{-4}$.

First, let us explain the case of $r_{\rm s} = 0.1$ pc (red solid line in Figure 3.7) as a benchmark case. In this case, $r_{\rm eq} = 5.7$ pc. There are two breaks in the synchrotron spectrum: the intrinsic break

Radius of termination shock (pc)	0.05	0.1	0.2	0.4
Total number of pairs (10^{50})	9.5	3.4	0.97	0.25
Advection time (yr)	6800	2400	690	180
Total pressure at $r = r_{\rm N}$ (10^{-10}dyn cm^{-2})	36	16	5.4	1.5
Maximum magnetic field (μG)	250	100	32	8.7
Averaged magnetic field (μG)	240	88	26	6.8
$r_{\rm eq}/r_{\rm N}$	1.4	2.9	5.8	12

Table 3.1: Obtained parameters for the test calculation with $\sigma = 10^{-4}$ shown in Fig. 3.7. See Fig. 3.7 for the other parameters. In these parameter sets, the magnetic field always reaches its maximum at $r = r_{\rm N}$

at $\nu_{\rm b} \sim 2.2 \times 10^{12}$ Hz corresponding to $E_{\rm b}$ and the cooling break at $\nu_{\rm c} \sim 3.6 \times 10^{14}$ Hz. Estimating with the advection time and the average magnetic field, the cooling break energy of pairs is

$$E_{\rm c}^{\rm (av)} \simeq \frac{6\pi m_{\rm e}^2 c^3}{\sigma_{\rm T} B_{\rm av}^2 t_{\rm adv}} \simeq 670 \ {\rm GeV} \left(\frac{B_{\rm av}}{88\mu{\rm G}}\right)^{-2} \left(\frac{t_{\rm adv}}{2400{\rm yr}}\right)^{-1}. \tag{3.33}$$

The corresponding cooling break frequency is

$$\begin{aligned} \nu_{\rm c}^{\rm (av)} &= \frac{3eB_{\rm av}}{4\pi m_{\rm e} c} \left(\frac{E_{\rm c}^{\rm (av)}}{m_{\rm e}c^2}\right)^2 \\ &\simeq 6.4 \times 10^{14} \ {\rm Hz} \left(\frac{B_{\rm av}}{88\mu{\rm G}}\right)^{-3} \left(\frac{t_{\rm adv}}{2400{\rm yr}}\right)^{-2}. \end{aligned} \tag{3.34}$$

The above values obtained in the one-zone model like treatment are roughly in agreement with our results.

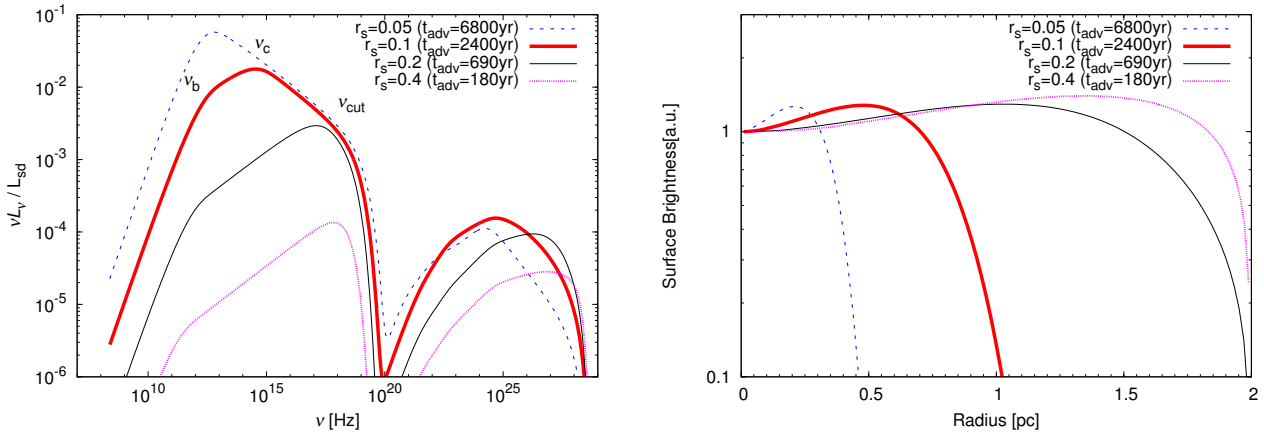

Figure 3.7: Test calculations to see the shock radius dependence. The parameters are $L_{\rm sd} = 10^{38}$ erg s^{-1}, $E_{\rm b} = 10^5 m_{\rm e}c^2$, $\sigma = 10^{-4}$, $p_1 = 1.1$, and $p_2 = 2.5$. (Left) The entire spectrum calculated for various values of $r_{\rm s}$ (see Table 3.1). (Right) The radial profile of the X-ray surface brightness for 0.5-10 keV range. The nebula radius $r_{\rm N}$ is 2 pc.

The analytical expressions of the spectral indices α ($F_\nu \propto \nu^{-\alpha}$) are $(p_1-1)/2$ below $\nu_{\rm b}$, and $(p_2-1)/2$ for $\nu_{\rm b} < \nu < \nu_{\rm c}$. The calculated spectrum agrees with those values. In 1-zone models, the index above $\nu_{\rm c}$ steepened by 1/2, which is well known as the "cooling break". However, in the 1-D models following $B \propto r$ and $u \propto r^{-2}$, the spectral change $\Delta = (p+7)/18$ is slightly different from 1/2 (Kennel & Coroniti, 1984b; Reynolds, 2009), which also agrees with our result.

Let us focus the flux of entire spectrum at $\nu = \nu_{\rm cut}$. When the synchrotron cooling is efficient for particles of $E = E_{\rm max}$, almost all of those energies are released by photon emission until $r = r_{\rm pk}$. Since the energy density of non-thermal electrons and positrons, which have an energy $E = E_{\rm max}$ at $r = r_{\rm s}$, is estimated as $L_{\rm sd}(E_{\rm max}/E_{\rm b})^{2-p_2}$, the synchrotron luminosity at $\nu \sim \nu_{\rm cut}$ is calculated as $\nu_{\rm cut}L_{\nu_{\rm cut}} \sim 1.7\times10^{-2}L_{\rm sd}$ for $\sigma = 10^{-4}$ and $p_2 = 2.5$, which seems to roughly agree with the flux in Figure 3.7. The above estimate does not depend on $r_{\rm s}$, which agrees with the results for $r_{\rm s} \leq 0.2$ pc, where $\nu_{\rm c} < \nu_{\rm cut}$.

A particle of energy E emits synchrotron photons of frequency $\nu \propto E^2B$, and power $p_{\rm syn} \propto E^2B^2$, then the spectral emissivity j_ν is proportional to $n(E)E^2B^2(dE/\nu)$. When we can assume $\sigma \ll 1$ and $n_{\rm tot} \propto r^0$, $j_\nu \propto n_0 E_{\rm b}^{p-1}\nu^{-(p-1)/2}B(r)^{(p+1)/2}$ (p is index of the pair energy spectrum) at the energy range where the cooling effect is not significant. The "imcompressive" regime implies that the magnetic field behaves as $B \sim B_{\rm d}r/r_{\rm s} \propto L_{\rm sd}^{1/2}r_{\rm s}^{-2}\sigma^{1/2}r$. Since C_2 can be regarded as a constant for $p_1 < 2 < p_2$ and $E_{\rm min} \ll E_{\rm b} \ll E_{\rm max}$, we obtain $n_0 \propto L_{\rm sd}r_{\rm s}^{-2}E_{\rm b}^{-1}$. Finally, we obtain the entire specific luminosity ($L_\nu \sim 4\pi\int_{r_{\rm s}}^{r_{\rm N}} dr r^2 j_\nu$) as

$$\nu L_\nu \propto L_{\rm sd}^{(p+5)/4}E_{\rm b}^{p-2}\sigma^{(p+1)/4}r_{\rm s}^{-(p+3)}r_{\rm N}^{(p+7)/2}\nu^{-(p-3)/2}, \tag{3.35}$$

where p is p_1 for $\nu < \nu_{\rm b}$, and p_2 for $\nu_{\rm b} < \nu < \nu_{\rm c}$. At $\nu = \nu_{\rm b} \propto L_{\rm sd}^{1/2}\sigma^{1/2}E_{\rm b}^2r_{\rm s}^{-2}r_{\rm N}$ (Equation (3.26)),

$$\frac{\nu_{\rm b}L_{\nu_{\rm b}}}{L_{\rm sd}} \simeq 7\times10^{-3}\left(\frac{L_{\rm sd}}{10^{38}{\rm erg\ s^{-1}}}\right)\left(\frac{\sigma}{10^{-4}}\right)\left(\frac{E_{\rm b}}{10^5 m_{\rm e}c^2}\right)\left(\frac{r_{\rm s}}{0.1\ {\rm pc}}\right)^{-6}\left(\frac{r_{\rm N}}{2\ {\rm pc}}\right)^{5}. \tag{3.36}$$

where the absolute value, which is difficult to evaluate analytically, is adopted from our numerical results. Above $\nu = \nu_{\rm c} \propto L_{\rm sd}^{-3/2}\sigma^{-3/2}r_{\rm s}^{10}r_{\rm N}^{-9}$ (Equation (3.29)), using the above formula, the spectrum behaves as $\nu L_\nu \sim \nu_{\rm c}L_{\nu_{\rm c}}(\nu/\nu_{\rm c})^{-5(p_2-2)/9}$ so that

$$\nu L_\nu \propto L_{\rm sd}^{(p_2+4)/6}E_{\rm b}^{p_2-2}\sigma^{(p_2-2)/6}r_{\rm s}^{-4(p_2-2)/9}\nu^{-5(p_2-2)/9}, \tag{3.37}$$

for $\nu_{\rm c} < \nu < \nu_{\rm cut}$. These expressions are in good agreement with our numerical results.

The cooling frequency depends very strongly on $r_{\rm s}$. The frequencies $\nu_{\rm b}$ and $\nu_{\rm c}$ have similar values for $r_{\rm s} = 0.05$ pc, while $\nu_{\rm c}$ and $\nu_{\rm cut}$ merge for $r_{\rm s} = 0.2$ pc. For $r_{\rm s} = 0.4$ pc, $\nu_{\rm c}$ becomes higher than $\nu_{\rm cut}$. That is, in this case both the radiative cooling effect and the adiabatic cooling effect are negligible. This results the flux at $\nu = \nu_{\rm cut}$ for $r_{\rm s} = 0.4$ pc is lower than the fluxes for smaller $r_{\rm s}$.

The value of $E_{\rm cut}(r_{\rm N})$ increases with $r_{\rm s}$, because the synchrotron cooling becomes less effective. Reflecting this, the IC spectra show a soft-to-hard evolution with $r_{\rm s}$. The high-energy cut-off of the IC component is determined by the maximum energy of pairs. Electron-positron pairs spend only a fraction of their energy on the emission of the IC. In the example of Figure 3.7, since $L_{\rm sd}$ and $E_{\rm b}$ are the same value, the IC flux at low energy range ($10^{20} - 10^{22}$Hz) is essentially proportional to the total number of corresponding low energy particles in the nebula. As shown in the left panel in Figure 3.5, a flow with a small ratio of $r_{\rm N}/r_{\rm s}$ reaches the edge of the nebula before significant deceleration. Consequently, the advection time becomes shorter for a smaller $r_{\rm N}/r_{\rm s}$ as shown in Table 3.1. If we can neglect the cooling effect, the total particle number $\propto t_{\rm adv}L_{\rm sd}E_{\rm b}^{p_1-2}$ decreases with $r_{\rm s}$. This effect is seen as the flux growth with increasing $t_{\rm adv}$ below $\sim 10^{22}$ Hz. For $r_{\rm s} = 0.05$

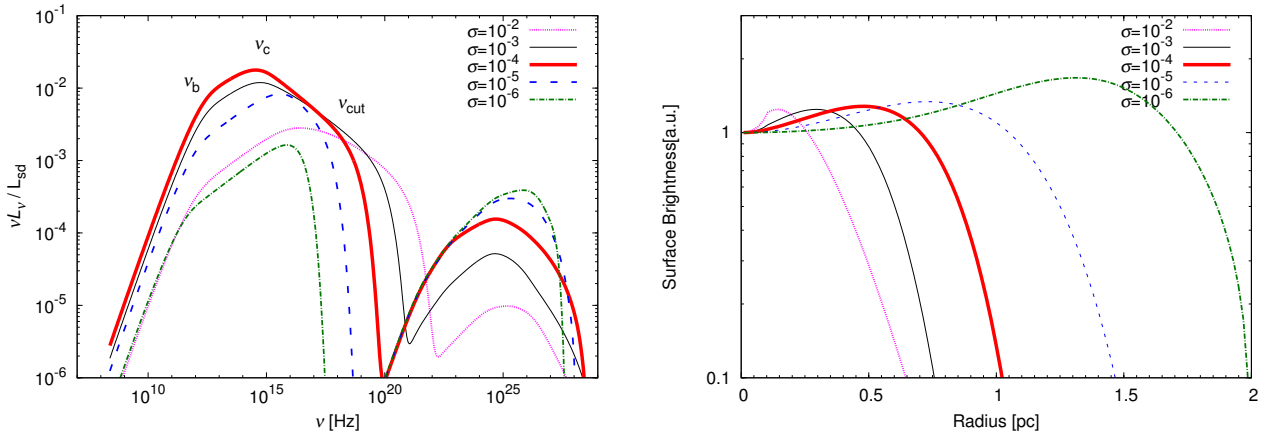

Figure 3.8: Test calculations to see σ dependence. The parameters are the same as those in Fig. 3.7 except for σ and $r_{\rm s} = 0.1$ pc. (Left) The entire spectrum calculated for various values of σ (see Table 3.2). (Right) The radial profile of the X-ray surface brightness for 0.5-10 keV range.

pc, the synchrotron cooling is significant ($E_{\rm cut}(0.7r_{\rm N}) \lesssim E_{\rm b}$), which practically reduces the particle number above $E_{\rm b}$ in the nebula. Therefore, the IC flux in this case does not follow the above trend.

The X-ray surface brightness (see the right panel of Figure 3.7) is regulated by the synchrotron cooling. In the smaller $r_{\rm s}$, the stronger magnetic field leads to a compact X-ray profile. The $r_{\rm s}$-dependence of the X-ray extent is $r_{\rm s}^{10/9}$ for $r_{\rm s} \leq 0.2$ pc as explained as follows. When the cooling effect is significant, $E_{\rm cut} \propto E_{\rm bof}(r_{\rm s}/r)^5 \propto \sigma^{-1} r_{\rm s}^6 r^{-5}$, while the magnetic field behaves as $B \propto \sigma^{1/2} r_{\rm s}^{-2} r$. For a given frequency $\nu \propto BE^2$, the maximum radius to emit photons with frequency ν is proportional to $\sigma^{-1/6} r_{\rm s}^{10/9}$. This is consistent with the $r_{\rm s}$-dependence of the X-ray extent $r_{\rm s}^{10/9}$ for the case that the cooling effect is significant. For $r_{\rm s} = 0.4$ pc, the synchrotron cooling hardly affects the X-ray profile. In order to reconcile the fact that the X-ray extent is comparable to the radio nebula, a large $r_{\rm s}$ is preferable, though the synchrotron component becomes very hard and dim in this case.

As shown in Table 3.1, the total pressure $P_{\rm tot} \equiv 4Pu^2 + P + B^2/8\pi$ at the outer boundary, which may balance with the pressure outside the nebula, decreases with $r_{\rm s}$ by roughly an order of magnitude. Since the uncertainty of the current observation of the outside pressure is larger than this variance, it may be difficult to constrain the value of $r_{\rm s}$ directly.

3.3.3 Parameter Dependence: magnetization

Figure 3.8 shows the σ dependences of the entire spectrum and the X-ray surface brightness. The radius of the termination shock is fixed at $r_{\rm s} = 0.1$ pc and the other parameters are the same as in the previous subsection, but the value of σ changes from 10^{-6} to 10^{-2}. As is shown in the figure, a complicated behavior appears in the spectral shape as σ increasing. The change of σ modifies the profiles of the emission through two processes: the strength of magnetic field (see Equation (3.20)) and the deceleration profile as shown in Fig. 3.5. The magnetic field strength affects the typical synchrotron frequency and the cooling efficiency. The flow velocity profile adjusts the radius $r_{\rm eq}$, where the magnetic field becomes maximum, and the advection time, which controls the total energy in the nebula and the cooling efficiency (the ratio of the cooling time to the advection time).

For $\sigma \leq 10^{-4}$, the radius $r_{\rm eq}$ is outside $r_{\rm N}$ (see Table 3.2, note that $r_{\rm N}/r_{\rm s}$ corresponds to 20 in

Magnetization Parameter	10^{-2}	10^{-3}	10^{-4}	10^{-5}	10^{-6}
Total number of pairs (10^{50})	0.37	1.6	3.4	4.0	4.2
Advection time (yr)	280	1200	2400	2900	2900
Total pressure at $r = r_{\rm N}$ (10^{-10}erg cm^{-3})	2.3	8.9	16	21	23
Maximum magnetic field (μG)	130	130	100	43	14
Magnetic field at $r = r_{\rm N}$ (μG)	69	120	100	43	14
Averaged magnetic field (μG)	86	120	87	34	11
$r_{\rm eq}/r_{\rm N}$	0.29	0.91	2.89	9.13	28.9

Table 3.2: Obtained parameters for the test calculation with $r_{\rm s} = 0.1$ pc shown in Fig. 3.8. See Fig. 3.7 for the other parameters.

Figure 3.5), so that the behaviors of the characteristic frequencies are well explained by Equations (3.26), (3.29), and (3.31) as $\nu_{\rm b} \propto \sigma^{1/2}$, $\nu_{\rm c} \propto \sigma^{-3/2}$, and $\nu_{\rm cut} \propto \sigma^{11/10}$. In the case of $\sigma = 10^{-6}$, since the average magnetic field in the nebula is weak, the frequency $\nu_{\rm c}$ is much higher than $\nu_{\rm cut}$, so that the power-law portion for $\nu_{\rm c} < \nu < \nu_{\rm cut}$ is absent. Below $\nu_{\rm cut}$, the spectral behavior for $\sigma \leq 10^{-4}$ is well represented by the formulae of Equations (3.35) and (3.36) In the frequency range of $\nu_{\rm c} < \nu < \nu_{\rm cut}$, the spectrum practically follows Equation (3.37) for the cases of $\sigma = 10^{-5}$ and 10^{-4}. As σ increases, the stronger magnetic field results in greater efficiency of emission during advection time. The peak of the synchrotron flux at $\nu = \nu_{\rm c}$ grows with σ^{p_2-2} (see Equations (3.29) and (3.35)) for $\sigma \leq 10^{-4}$, accompanying the shift of $\nu_{\rm c}$ to a lower frequency.

For $\sigma \geq 10^{-3}$, the behavior of the entire spectrum is different from the above trend . This is because the radial evolution of the magnetic field can be no longer approximated by $B \propto r$. As shown in Table 3.2, the radius $r_{\rm eq}$ is inside the nebula radius $r_{\rm N}$ in this parameter region unlike the discussion in Section 3.3.1. In this case, the magnetic field prevents the flow deceleration at $r > r_{\rm eq}$, and the adiabatic cooling become efficient. Furthermore, the decline of the advection time (see Table 3.2) leads to the reduction of the total energy in the nebula. As a result, above $\sigma = 10^{-4}$, the synchrotron peak flux turns into decreasing and the cooling frequency turns into increasing. Therefore, unlike the 1-zone model, we can not make $\nu_{\rm c}$ extremely low in the 1-D steady model.

In the case of $r_{\rm eq} < r_{\rm N}$, the entire spectrum is mainly contributed by radiation from non-thermal pairs at $r < r_{\rm eq}$. At $r > r_{\rm eq}$, electrons/positrons lose their energies via adiabatic cooling as $E \propto (r/r_{\rm eq})^{-2/3}$ and the magnetic field decays as $\propto r^{-1}$. Thus, the energy loss rate rapidly decreases as $r^{-10/3}$. Since this is a more rapid decrease than the increase in volume r^2, the emission beyond $r = r_{\rm eq}$ is almost negligible. From Equation (3.27), assuming $E_{\rm max} \gg E_{\rm bof}$, we obtain $E_{\rm cut}(r_{\rm eq}) \simeq 5E_{\rm bof}(r_{\rm s}/r_{\rm eq})^5 \simeq 5E_{\rm bof}(3\sigma)^{5/2}$. In this case, the cooling frequency for enough large σ that $r_{\rm eq}$ is smaller than $r_{\rm N}$ may be estimated with $E_{\rm cut}$ at $r = r_{\rm eq}$ as

$$\begin{aligned} \nu_{\rm c}^{\rm (eq)} &= \frac{3eB(r_{\rm eq})}{4\pi m_{\rm e}c}\left(\frac{E_{\rm cut}(r_{\rm eq})}{m_{\rm e}c^2}\right)^2 \\ &\simeq 5.9\times10^{16}\ {\rm Hz}\left(\frac{L_{\rm sd}}{10^{38}{\rm erg\ s^{-1}}}\right)^{-\frac{3}{2}}\left(\frac{\sigma}{10^{-2}}\right)^3\left(\frac{r_{\rm s}}{0.1\ {\rm pc}}\right). \end{aligned} \tag{3.38}$$

Since the case for $\sigma = 10^{-2}, 10^{-3}$ are in a marginal situation ($r_{\rm eq} \sim r_{\rm N}$), the estimated dependence on σ (equation (3.38)) is a little bit strong. However, at least, it is certain that the cooling frequency for $\sigma > 10^{-4}$ ($r_{\rm eq} < r_{\rm N}$) becomes large with increasing σ.

The intrinsic break frequency for the case of $r_{\rm eq} < r_{\rm N}$ is estimated as the typical synchrotron

frequency of the pairs with energy $E_{\rm b}$ at the radius $r = r_{\rm eq}$. We obtain,

$$\begin{aligned}\nu_{\rm b}^{\rm (eq)} &= \frac{3}{4\pi}\frac{eB\left(r_{\rm eq}\right)}{mc}\left(\frac{E_{\rm b}}{mc^2}\right)^2 \\ &\simeq 1.4\times10^{13}\ {\rm Hz}\left(\frac{L_{\rm sd}}{10^{38}{\rm erg\ s^{-1}}}\right)^{\frac{1}{2}}\left(\frac{E_{\rm b}}{10^5 m_{\rm e}c^2}\right)^2\left(\frac{r_{\rm s}}{0.1\ {\rm pc}}\right)^{-1}. \end{aligned} \tag{3.39}$$

Note that the intrinsic break hardly depends on σ in the case of $r_{\rm eq} < r_{\rm N}$. This is because the radiation near the frequency $\nu_{\rm b}^{\rm (eq)}$ is due to the radiation from the pairs at the radius where the equipartition of the magnetic pressure and the gas pressure is held.

In the frequency range of $\nu_{\rm c}^{\rm (eq)} < \nu < \nu_{\rm cut}$ for a larger σ, the spectrum is harder than the analytical estimate $\alpha = (5p_2 - 1)/9$ for $r_{\rm eq} < r_{\rm N}$. On the other hand, since $r_{\rm pk} \sim r_{\rm s}$, the frequency $\nu_{\rm cut}$ well agrees with the analytical estimate of Equation (3.31) even for a larger σ. For $\sigma \geq 10^{-4}$, as we have mentioned in the previous subsection, the luminosity around $\nu_{\rm cut}$ is almost independent of σ, while the peak luminosity at $\nu = \nu_{\rm c}$ decreases with increasing σ following the reduction of the total energy in the nebula. Those complicated effects lead to the spectral hardening between $\nu_{\rm c}$ and $\nu_{\rm cut}$.

With increasing σ, the peak flux of the IC component declines monotonically. Below the spectral break frequency 10^{23} Hz, which corresponds to the photon energy emitted by particles of $E_{\rm b}$ interacting with dust photons, all the model curves for $\sigma \leq 10^{-4}$ almost overlap each other. In this range of σ, the flow profiles are almost the same, so that the IC emission, which does not directly depend on the strength of the magnetic field, is almost the same value for each result with σ. On the other hand, above 10^{23} Hz, the softening of the photon spectrum with increasing σ is seen. Although $E_{\rm max}$ is higher for a larger σ, the cut-off energy $E_{\rm cut}(r_{\rm N})$ at the edge of the nebula is reduced by the severe synchrotron cooling. Above $\sigma = 10^{-4}$, the short advection time leads to the reduction of the IC flux. The spectral hardening of the IC component is caused by the drop of the cooling efficiency due to the short advection time. While the flux decrease of the synchrotron component due to the reduction of the advection time is mitigated by the magnetic field growth, the IC component more rapidly falls with σ than the synchrotron one.

In the right panel of Figure 3.8 represents the surface brightness profile in X-rays. With increasing σ, the extent of the X-ray nebula becomes small. The analytical expression of the dependence $\sigma^{-1/6}$ obtained in the previous subsection is consistent with this results.

3.4 Application to the Observed Source

3.4.1 The Crab Nebula

In order to check our model, we calculate the entire spectrum and the X-ray profile of the Crab Nebula and compare the result with Atoyan & Aharonian (1996) (hereafter AA96). Assuming that synchrotron photons exist homogeneously in the nebula, we calculate the SSC approximately. In other words, the soft photons used to calculate the IC are CMB photons and SSC photons as described above. Other differences in our model from AA96 are as follows. In our model, low energy particles that corresponds to the radio emission are supplied from the pulsar wind, while AA96 considered them as another components. In AA96, the maximum energy of the pair $E_{\rm max}$ was treated as a parameter of the model (for our model, see the Equation (3.15)). Finally, in AA96, the correction factor κ was introduced. This is a parameter for adjusting the ratio of synchrotron flux to SSC flux. The parameter κ (cf. AA96 adopted $\kappa \sim 0.5$) may represent the effects of deviation from the spherical symmetry or inhomogeneity inside the PWN.

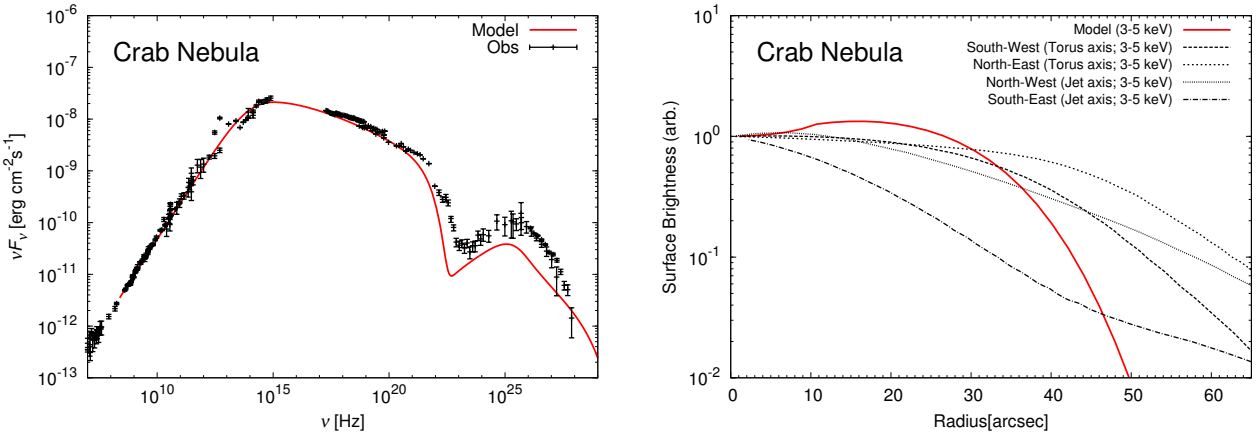

Figure 3.9: An entire photon spectrum (left panel) and a radial profile of surface brightness in 3.0-5.0 keV range (right panel) for the Crab Nebula. The data points of the spectral energy density are taken from Baars et al. (1977) (radio), Macías-Pérez et al. (2010) (radio, optical), Grasdalen (1979); Temim et al. (2006); Ney & Stein (1968) (IR), Kuiper et al. (2001) (X-ray, γ-ray), and Aharonian et al. (2004, 2006); Abdo et al. (2010a) (very high energy γ-ray). The data points of the X-ray surface brightness are taken from Madsen et al. (2015).

In Figure 3.9, the entire photon spectrum and the X-ray radial profile for the Crab Nebula are shown. All the parameters to calculate the spectrum for the Crab Nebula are same as AA96 without "Obtained parameter", and are summarized in Table 3.3. The flux of the inverse Compton is slightly smaller than the value observed and calculated with AA96. The difference in the SSC flux is due to the additional parameters κ and $E_{\rm max}$ in AA96. Even if we take smaller σ to increase the SSC flux, the maximum energy of synchrotron emission becomes much lower than the cut-off energy of observed spectrum (see Equation (3.31)). Within our conservative model assumption for the maximum energy of the particle, it is not possible to fit the spectrum near the cutoff of the spectrum.

The right panel of Figure 3.9 shows the radial profile of surface brightness in 3.0-5.0 keV range. The extent of X-ray nebulae calculated by our model roughly agree with observation. As we will see later, comparing with the cases of 3C 58 and G21.5-0.9, there is not much motivation to improve the 1-D steady model in the case of the Crab nebula.

3.4.2 3C 58 and G21.5-0.9

Here we apply our model to observed sources 3C 58 and G21.5-0.9, where enough data sets are available to constrain the model parameters. Furthermore, in both of the two PWNe, the X-ray nebula size is comparable to the radio band. We discuss both the entire spectrum and the spatial profile of those objects.

3C 58 is a object located $D = 2$kpc away (Kothes, 2013). The images of 3C 58 were obtained in the radio wavelengths (e.g., Reynolds & Aller, 1988) and X-ray band (e.g Slane et al., 2004). The radial profile of photon index in the X-ray band was also obtained. Since the extent of radio and X-rays emission is $\sim 5' \times 9'$, $r_{\rm N}$ is set to 2pc. The spin period and its time derivative for the central pulsar of 3C 58 (PSR J0205+6449) are 65.7 ms (Murray et al., 2002; Camilo et al., 2002) and 1.94×10^{-13} s s^{-1} (Livingstone et al., 2009), respectively. The spin-down luminosity is estimated as 2.7×10^{37} erg s^{-1}, assuming 10^{45} g cm^2 for the moment inertia of the pulsar.

Given parameters [a]	Symbol	Crab
Spin-down luminosity (erg s^{-1})	L_{sd}	5×10^{38}
Distance (kpc)	D	2.0
Radius of the nebula (pc)	r_N	1.8
Fitting parameters [a]		
Break energy (eV)	E_b	2.5×10^{11}
Low energy power-law index	p_1	1.6
High energy power-law index	p_2	2.4
Radius of the termination shock (pc)	r_s	0.1
Magnetization parameter	σ	5.0×10^{-3}
Obtained parameters		
Initial bulk Lorentz factor	γ_u	3.2×10^3
Pre-shock density (cm^{-3})	n_u	1.7×10^{-9}
Pre-shock magnetic field (μG)	B_u	30
Maximum Energy (eV)	E_{max}	2.7×10^{15}
Advection time (yr)	t_{adv}	380
Averaged magnetic field (μG)	B_{av}	234
Total pressure at $r = r_N$ (erg cm^{-3})	P_{tot}	2.0×10^{-9}
r_{eq}/r_N		0.45

[a] The parameters denoted with "Given parameter" and "Fitting parameter" are adopted the same value as AA96.

Table 3.3: Parameters in the calculations for the Crab Nebula.

G21.5-0.9 is a PWN that locates 4.8kpc away (Tian & Leahy, 2008). G21.5-0.9 shows spherical structures in the radio (Bietenholz & Bartel, 2008) and X-ray (Matheson & Safi-Harb, 2005, 2010; Camilo et al., 2006) images. The radio and X-ray sizes of the PWN ($\sim 40''$ in radius) are almost the same again. Since its angular diameter is approximately $40''$, r_N is set to 0.9pc. PSR J1833-1034, the central object of G21.5-0.9, has a spin period 61.9 ms (Gupta et al., 2005) and its derivative 2.02×10^{-13} s s^{-1} (Roy et al., 2012b), from which we obtain the spin-down luminosity $L_{sd} = 3.5 \times 10^{37}$ erg s^{-1}.

The parameters for fitting the spectra of the two PWNe are summarized in Table 5.1. See Figure 3.6 for the ISRFs taken from GALPROP v54.1 for the two cases. First, we discuss the parameter sets denoted with "broadband" in the Table 5.1 (hereafter we call them broadband model). Figure 3.10 shows the resultant radial profiles of $u(r)$ and $B(r)$. In both the two PWNe, r_{eq} is outside the nebula radius r_N in our parameter sets. The particle spectra in Figure 3.11 show the evolution of E_{cut} as discussed in Section 3.3.1.

The volume-integrated photon spectra for the two PWNe are shown in Figure 3.12. Our models roughly reproduce the entire structures of the spectra. In 3C 58, the data points obtained with *Fermi* (Abdo et al., 2013) may contain large systematic errors due to the emission from the central pulsar so that we treat those data as upper limits. The model spectrum of the X-ray band is clearly softer than the observed X-ray data in 3C 58 due to the cooling effect. As discussed in Section 3.3.3, ν_c can be higher than the X-ray energy range by adopting a larger σ or conversely lower σ. In such cases, the model spectrum of the X-ray may be as hard as observed. However, when we adopt a lower σ to make ν_c above the X-ray frequency, the synchrotron component does not extend to the X-ray energy as Equation (3.31) indicates. We also do not find a consistent high-ν_c model with a very large σ or a slightly large r_s, for which the radio and X-ray fluxes are hard to be reproduced

		3C 58		G21.5-0.9	
Given parameters	Symbol	broadband	alternative	broadband	alternative
Spin-down luminosity (erg s^{-1})	L_{sd}	3.0×10^{37}		3.5×10^{37}	
Distance (kpc)	D	2.0[a]		4.8[b]	
Radius of the nebula (pc)	r_N	2.0		0.9	
Fitting parameters					
Break energy (eV)	E_b	4.1×10^{10}	1.1×10^{11}	2.6×10^{10}	3.1×10^{12}
Low energy power-law index	p_1	1.26		1.1	
High energy power-law index	p_2	3.0	3.2	2.3	3.0
Radius of the termination shock (pc)	r_s	0.13	0.26	0.05	0.1
Magnetization parameter	σ	1.0×10^{-4}	1.0×10^{-3}	2.0×10^{-4}	3.0×10^{-2}
Obtained parameters					
Initial bulk Lorentz factor	γ_u	7.3×10^{3}	5.5×10^{5}	2.1×10^{4}	1.8×10^{7}
Pre-shock density (cm^{-3})	n_u	1.1×10^{-11}	5.1×10^{-16}	1.1×10^{-11}	3.5×10^{-18}
Pre-shock magnetic field (μG)	B_u	0.79	1.2	3.1	19
Maximum Energy (eV)	E_{max}	9.5×10^{13}	3.0×10^{14}	1.4×10^{14}	1.7×10^{15}
Advection time (yr)	t_{adv}	1500	330	800	38
Averaged magnetic field (μG)	B_{av}	31	21	120	61
Total pressure at $r = r_N$ (erg cm^{-3})	P_{tot}	3.7×10^{-10}	8.3×10^{-11}	2.1×10^{-9}	1.2×10^{-10}
r_{eq}/r_N		3.8	2.4	2.3	0.37

[a] Kothes (2013); [b] Tian & Leahy (2008).

Table 3.4: Parameters in our calculations.

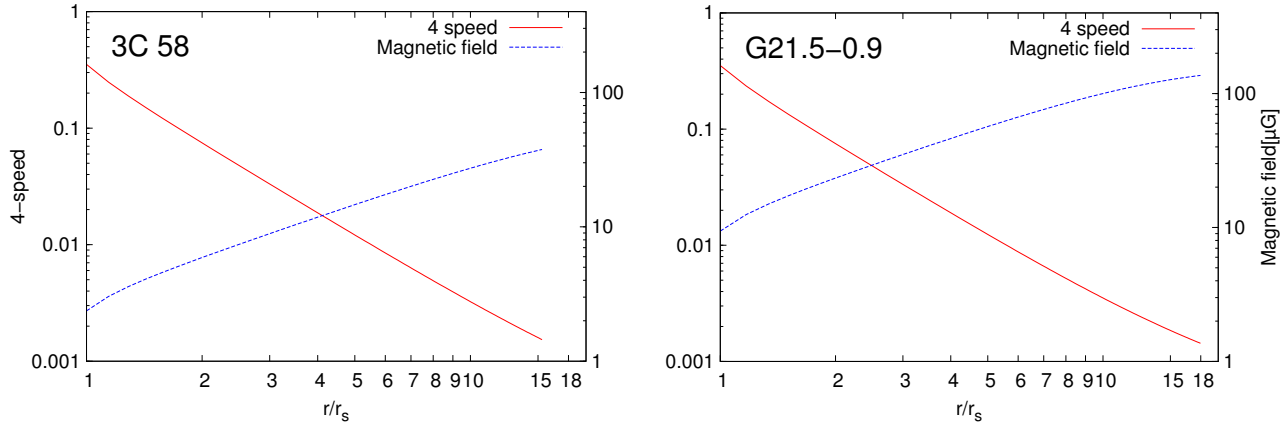

Figure 3.10: Radial profiles of the four-speed $u(r)$ (left axis) and the magnetic field $B(r)$ (right axis) in the broadband model (see Table 3.4) for 3C 58 (left panel) and G21.5-0.9 (right panel).

simultaneously. One may suppose that a smaller p_2 can agree with the observed X-ray spectral index, even if ν_c is below the X-ray frequency. The extrapolation from the X-ray data requires $\nu_c < 10^{14}$ Hz to make ν_b above the radio data points. As shown in 3.3.3 and Figure 3.8, due to the ν_c-turnover, such a low ν_c is hard to be realized in our model. Therefore, our model spectra cannot be reconciled with the X-ray spectral index.

A similar problem as in 3C 58 also occurs in the X-ray spectrum of G21.5-0.9. When we adopt

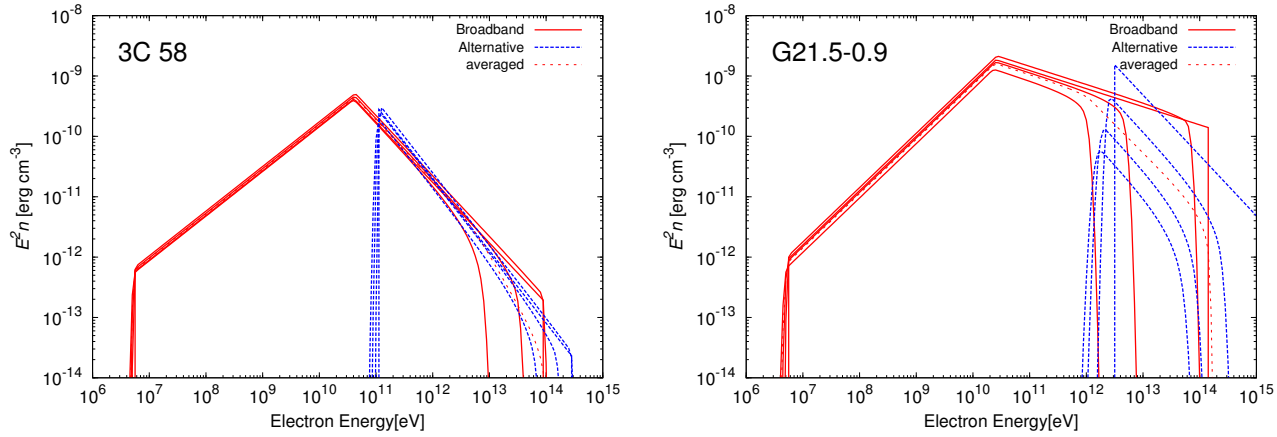

Figure 3.11: Evolutions of the particle spectra for 3C 58 (left panel) and G21.5-0.9 (right panel) in the broadband (red solid) and alternative (blue dashed) models. The different lines correspond to $r = r_{\rm s}$, $5r_{\rm s}$, $10r_{\rm s}$, $r_{\rm N} \simeq 15r_{\rm s}$ for 3C 58, and $r = r_{\rm s}$, $6r_{\rm s}$, $12r_{\rm s}$, $r_{\rm N} = 18r_{\rm s}$ for G21.5-0.9 (right to left). The thin dashed lines represent the volume-averaged spectra in the broadband models.

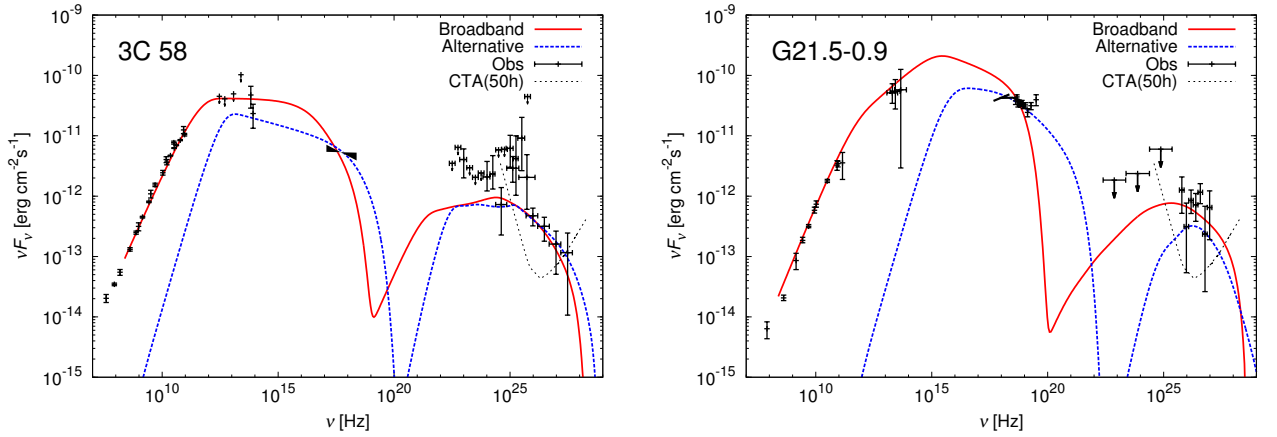

Figure 3.12: Entire photon spectra for 3C 58 (left panel) and G21.5-0.9 (right panel). The data points are taken from Weiland et al. (2011) (radio), Green (1994), Slane et al. (2008) (IR), Torii et al. (2000) (X), Abdo et al. (2013) (GeV), and Aleksić et al. (2014) (TeV) for 3C 58, and Salter et al. (1989) (Radio), Gallant & Tuffs (1998) (IR), Tsujimoto et al. (2011), Nynka et al. (2014), de Rosa et al. (2009) (X), Ackermann et al. (2011) (GeV), and Djannati-Ataï et al. (2008) (TeV) for G21.5-0.9. While the red solid lines represent the broadband models, the blue dashed lines represent the alternative models (see text), in which the radio/IR data are disregarded.

the model with $p_2 = 2$ to reproduce a flat spectrum ($\nu L_\nu \propto \nu^0$) above $\nu_{\rm c}$, a much lower σ is required to adjust the X-ray flux. For such a low σ, $\nu_{\rm cut}$ becomes lower than the X-ray band.

For these two objects, $\nu_{\rm c}$ is forced under the X-ray band. As a result, the X-ray spectra show softer shapes than the observed ones. The X-ray extents are more compact than the radio images (Figure 3.13). The radial profiles of photon indices in 0.5-10.0 keV range (Figure 3.14) is also different from the observation data. However, the contradiction of 3C 58 is less noticeable than

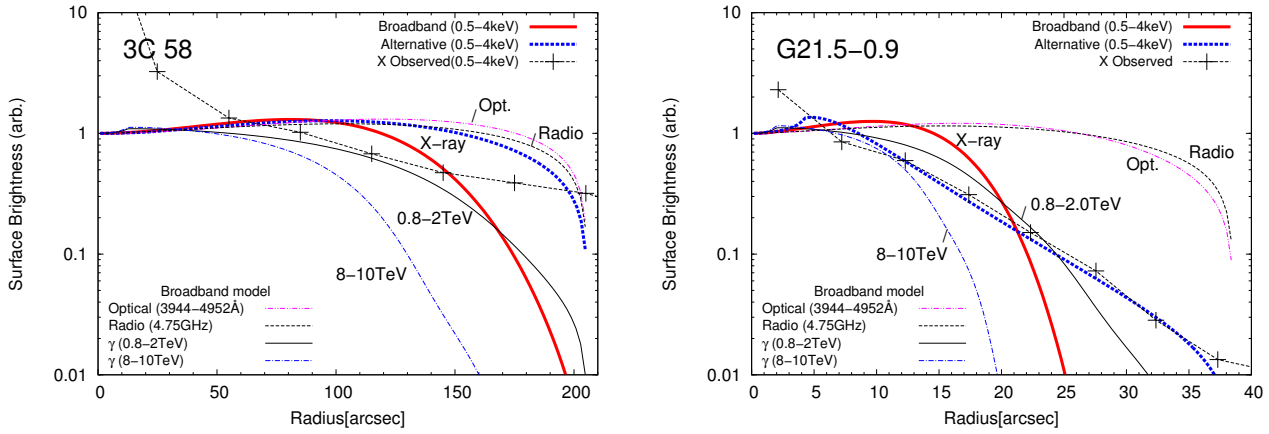

Figure 3.13: Radial profiles of the surface brightness in various frequencies for 3C 58 (left panel) and G21.5-0.9 (right panel). The X-ray data points are taken from Slane et al. (2004) and Matheson & Safi-Harb (2005) for 3C 58 and G21.5-0.9, respectively. The thick lines are the X-ray surface brightnesses for the broadband (red solid) and alternative (blue dashed) models.

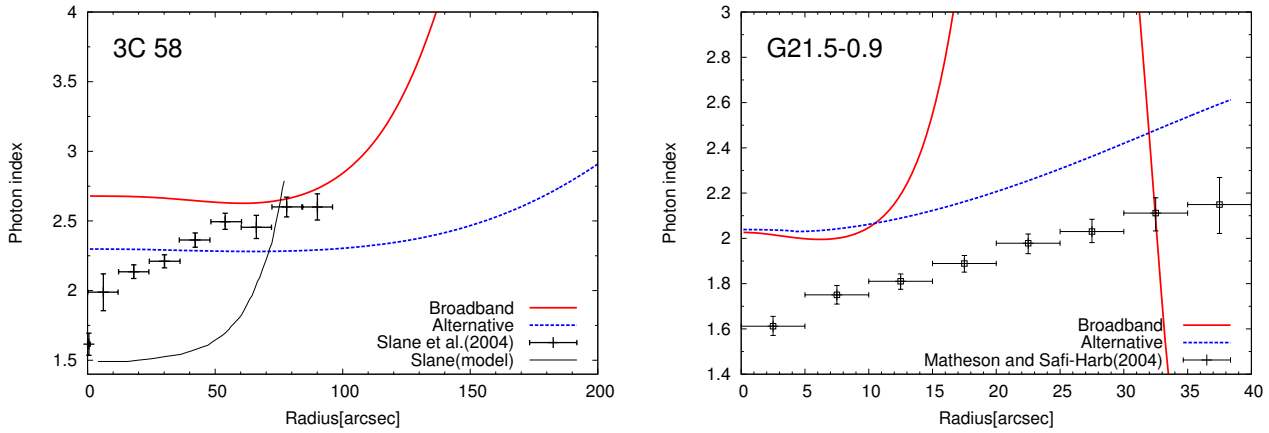

Figure 3.14: Radial profiles of photon indices in 0.5-10.0 keV range for 3C 58 (left panel) and G21.5-0.9 (right panel) in the broadband (red solid) and alternative (blue dashed) models. The model and data points in Slane et al. (2004) are also plotted for 3C 58. The data points for G21.5-0.9 are taken from Matheson & Safi-Harb (2005).

the model curve by Slane et al. (2004) based on Reynolds (2003). Note that the radial profiles of photon indices in optical (3944-4952$\AA$) and radio (4.75 GHz) band for two objects do not depend on angular distance from the pulsar. Since ν_c is higher than the frequencies of these bands in the parameters of the broadband model, the pairs can emit radio and optical photons anywhere in the nebula without radiative cooling effect. Thus the spectral indices at such bands are hardly depends on the radius.

The advection time of G21.5-0.9 well agrees with the age 870 yr (Bietenholz & Bartel, 2008). However, Wang et al. (2006) argued that this object associates with BC48 guest star and its age is thus about 2000 yr. In this case, $t_{\rm adv}$ in the broadband model becomes less than half of the age.

In 3C 58, if this object associates with SN 1181 (Stephenson, 1971), $t_{\rm adv}$ is about 2 times larger than the age. The characteristic ages of these objects are 5370 yr for 3C 58 and 4850 yr for G21.5-0.9, respectively. Notify that the characteristic age tends to be longer than the actual pulsar age, especially for young pulsars. Meanwhile, the previous 1-zone time dependent models have obtained the ages. For G21.5-0.9, $t_{\rm age}$ was estimated to be 1000yr (Tanaka & Takahara, 2011) or 870 yr (Vorster et al., 2013b; Torres et al., 2014) in 1-zone models. Those are close to our calculated $t_{\rm adv}$. This results encourages our 1-D model. On the other hand, for 3C 58, Bucciantini et al. (2011), Torres et al. (2013) and Tanaka & Takahara (2013a) obtained $t_{\rm age} \sim 2000$ yr, which is comparable with $t_{\rm adv}$ in our broadband model. However, Bucciantini et al. (2011) and Torres et al. (2014) adopted the different value of the distance to the object, and these three studies did not include the data of Aleksić et al. (2014). In this case, a direct comparison of the age with our advection times does not seem meaningful so much.

3.4.3 Alternative Model

Next, we explain the case where the radio/IR/optical emission can be considered as an additional component. In the broken power-law spectrum for the pair injection, the low-energy portion dominates the number. In the case of the Crab Nebula, the required particle number to reconcile the radio flux is much larger than the theoretically expected value (See Section 2.2.5, Tanaka & Takahara, 2010, 2011). is much larger than the theoretically expected value (Tanaka & Takahara, 2010, 2011). Atoyan & Aharonian (1996) and Olmi et al. (2015) treated the low-energy component as a different component from the wind particles in their calculations. Therefore, as an alternative model, we assume that the low energy particle component responsible for radio/IR radiation has a different origin than the high energy component. The alternative model ignores such a low-energy pairs and incorporates only high energy particles above $E_{\rm b}$.

Blue dashed lines in Figure 3.12-3.14 are for the alternative models, whose model parameters are summarized in Table 3.4. We adopt a slightly large $r_{\rm s}$ and large σ, which lead to X-ray extents consistent with observation as shown in Figure 3.13. The difference of the X-ray profiles in the two PWNe is attributed to the effect of the adiabatic cooling in G21.5-0.9 as shown in Figure 3.11. A signature of adiabatic cooling appears, because we have adopted a larger σ enough to establish $r_{\rm eq} < r_{\rm N}$ for G21.5-0.9. These models seem to reproduce the observed X-ray surface brightness and X-γ flux, however the obtained advection time is extremely short (see Table 3.4).

3.5 Discussion

As shown in Section 3.4, we have fitted the entire spectra of 3C 58 and G21.5-0.9. The resultant $r_{\rm s}$ by fitting the entire spectrum of nebula in the broadband models is similar to the value of the Crab Nebula, but the resultant σ about 10 times smaller than the conceivable value in the Crab Nebula. Our 1-D model has difficulty to reproduce both of the hard spectra and the extent of X-ray nebula. As discussed in Section 3.4, to avoid the spectral softening due to the cooling effect in X-ray range is hard to be avoid. As a result, the X-ray nebula size becomes more compact than the observed extents. The 1-D model should be improved by introduction of possible physical processes, such as the spatial diffusion of high energy particles, re-acceleration by turbulences, and amplification/dissipation of the magnetic field.

The 1-D model tends to lead a lower σ than the values derived from 1-zone models. Time-dependent one-zone models resulted in $\sigma \sim 0.03$–0.5 (Bucciantini et al., 2011; Torres et al., 2013; Tanaka & Takahara, 2013a) and 0.01–0.2 (Tanaka & Takahara, 2011; Vorster et al., 2013b; Torres et al., 2014) for 3C 58 and G21.5-0.9, respectively, while the value in our calculation is $\sigma \sim 10^{-4}$.

On the other hand, since the magnetic field increases with radius in the 1-D model, the resultant average magnetic field $B_{\rm av}$ is consistent with the previous 1-zone models (see also Equations (3.33) and (3.34)). In contrast to the cooling break $\nu_{\rm c}$, $\nu_{\rm cut}$ is determined by the magnetic field near the shock rather than $B_{\rm av}$. Thus, the one-zone model tends to overestimate the maximum synchrotron frequency about $B_{\rm av}/B_{\rm d}$ times higher than the 1-D model.

The fitted shock radius $r_{\rm s}$ of 3C 58 is twice as large as that of G21.5-0.9. The total pressures at $r = r_{\rm N}$ in our models are $P_{\rm tot,3C\ 58} \sim 3.7 \times 10^{-10}$ erg cm^{-3} and $P_{\rm tot,G21.5} \sim 2.1 \times 10^{-9}$ erg cm^{-3}. From the pressure balance, the large $p_{\rm tot}$ implies the large plasma pressure of the surrounding supernova ejecta. For 3C 58, Slane et al. (2004) obtained $kT_e \sim 0.23$ keV and $n_{\rm SNR} \sim 0.38$ cc^{-1} and then its pressure $\sim 1.4 \times 10^{-10}$ erg cm^{-3}. For G21.5-0.9, Matheson & Safi-Harb (2010) obtained $kT_e \sim 0.3$ keV and $n_{\rm SNR} \sim 0.63$ cm^{-3} and then its pressure $\sim 3.0 \times 10^{-10}$ erg cm^{-3}. While the pressure values may be not so robust, this indicates that the surrounding SNR of G21.5-0.9 has higher pressure than 3C 58. In addition, the fact that the bright shell-like SNR is clearly seen in G21.5-0.9 also supports that the pressure for G21.5-0.9 would be higher than that for 3C 58.

In the broadband model, the flux level of the entire spectrum is well reproduced, but the X-ray spectral index does not fit the observed value. We also discuss alternative models, in which the emission in radio and optical is assumed to be different from the direct emission from the pulsar wind (Atoyan & Aharonian, 1996; Olmi et al., 2014, 2015). As shown in Table 3.4, the σ obtained by the alternative model tends to be larger than the value of the broadband model. This trend is similar to several one-zone models (Torres et al., 2013; Vorster et al., 2013b). The time-dependent model of Torres et al. (2013) introduced an order of magnitude larger energy density of the ISRF (i.e., a larger magnetic field strength) than ours in order to reproduce the X-ray spectral index of 3C 58. In the model of Vorster et al. (2013b), the X-ray spectrum of G21.5-0.9 was also reproduced by a strong magnetic field (230μG),and hard spectral index ($p_2 = 2.0$). Note that their predicted GeV flux seems to be above the *Fermi* upper-limit (Ackermann et al., 2011). In those models, the cooling break was set far below the keV range. However, as discussed in Section 3.3.3, it is hard to set such a low $\nu_{\rm c}$ in 1-D steady model. The temporal evolution of the magnetic field in one-zone models causes the gradual hardening of the particle spectrum (see also Tanaka & Takahara, 2010), which is favorable to fit the X-ray data differently from our steady model.

In the alternative models, since a larger σ is required, the resultant short advection time prevents high-energy particles from radiative cooling before reaching the edge of the nebula. However, such a short advection time may contradict the age of the PWNe. In order to validate $t_{\rm age} \gg t_{\rm adv}$, it should be required that the particles escape from the nebula efficiently. For 3C 58 and G21.5-0.9, the large amount of the escaped high-energy particles should emit photons outside the PWNe, such a signature outside PWNe has not been claimed. For example, the model of Holler et al. (2012), in which the radial profile of flow velocity is artificially tuned, also implies ~ 100 yr for the advection time in G0.9+0.1, though the characteristic age is more than kyr. We should carefully note the advection time in modeling the outflow property (see Equation (3.22)). If outer supernova ejecta effectively confine PWN, the fast plasma flow implied by the high σ model should be decelerated near the edge of the PWN and should induce the turbulence in the PWN. As a result, the wind material may be efficiently mixed inside the PWN (e.g., Porth et al., 2014). In this case, the 1-zone approximation may be rather adequate.

3.6 Conclusion

We have revisited the 1-D steady model, and applied to the pulsar wind nebulae, in order to find a parameter set consistent with both the entire photon spectrum and surface brightness profile. It is

still controversial whether the simple 1-D model reproduces observed properties of the PWNe other than the Crab Nebula or not. As we have shown in Section 3.3, both the entire photon spectrum and surface brightness profile largely depend on the parameters, the uncertain shock radius $r_{\rm s}$ and the magnetization parameter σ. The flux of inverse Compton component becomes dim with increasing σ. In contrast, the synchrotron component is not a monotonic function of σ. For the dependence on $r_{\rm s}$, while the synchrotron component becomes dim with increasing with $r_{\rm s}$, the IC component shows complicated behaviors. The X-ray size of a PWN becomes large with increasing $r_{\rm s}$ and decreasing σ.

We have fitted the entire spectrum of two observed sources 3C 58 and G21.5-0.9. Calculating the radial profile of the surface brightness for those models, we show that the obtained X-ray extents are significantly smaller than the observed sizes. Moreover, we have performed another parameter set called "alternative" model, where we treat the radio and optical emissions as extra components. The alternative models successfully reproduce the observed X-ray surface brightness and the X-ray and γ-ray fluxes. However, those models imply too short advection time. In summary, the 1-D model constructed by KC84s has severe difficulty to reproduce both the spectrum and spatial emission profile of PWNe consistently. The model should be improved by taking some possible physical processes into consideration, such as spatial diffusion of non-thermal particles, reacceleration by turbulences.

Chapter 4

Time-dependent Model

4.1 Introduction

As we have seen in Chapter 3, the KC model can not reproduce the entire spectrum and the X-ray surface brightness simultaneously. The main assumption in the KC model is steady-state, spherically symmetric and toroidal magnetic field configuration. In this chapter, we examine how the time dependence affects the emission of the nebula.

The effect of the temporal evolution of the pulsar wind nebula is well studied by using 1-zone models, which treats the nebula as a uniform region. Figure 4.1 shows the result of applying 1-zone model by Tanaka & Takahara (2010) to the Crab nebula. In their model, the time evolution of the spin-sown luminosity as represented by equation (2.8), and radiative cooling and adiabatic cooling are considered. In Tanaka & Takahara (2010), the expansion speed of the nebula is assumed as a constant 1800km s^{-1}.

Torres et al. (2014) also calculated the emission spectra of various pulsar wind nebulae, taking into account the more detailed expansion evolution of the nebula and the escape of particles from the nebula. Figure 4.2 shows the results of their calculation. The results for the old nebula show

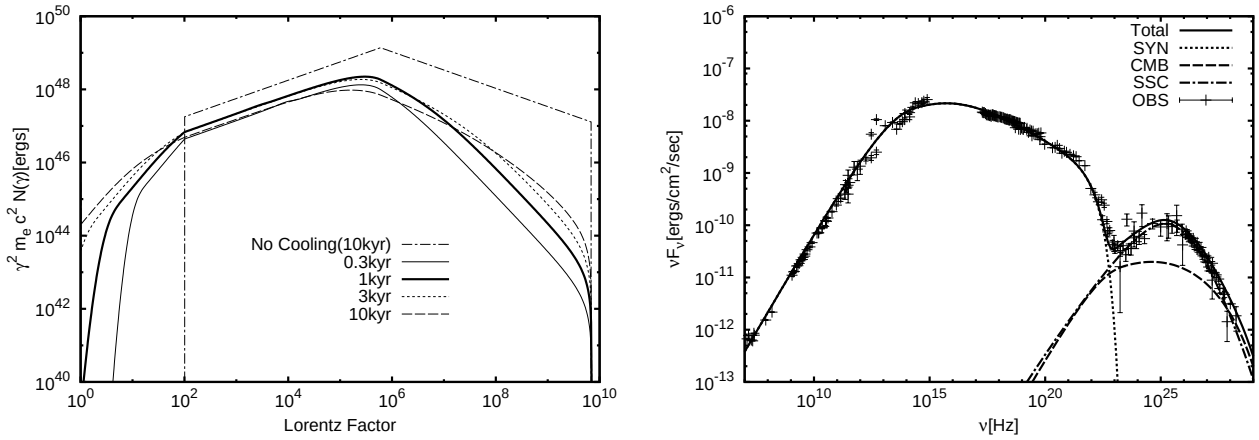

Figure 4.1: Calculation result of the 1-zone model for the Crab nebula by Tanaka & Takahara (2010). The left panel represents the energy spectrum of the pairs for various age of the nebula. The right panel shows the calculated entire spectrum of the Crab nebula at the present day. Figures from Tanaka & Takahara (2010). ©AAS. Reproduced with permission.

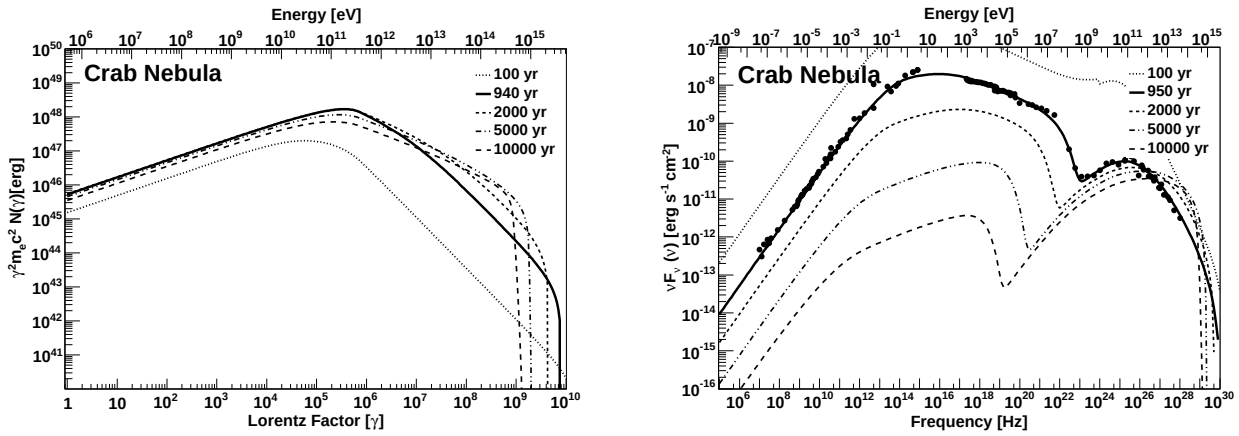

Figure 4.2: Calculation result of the 1-zone model constructed by Torres et al. (2014) for the Crab nebula. (Left) The energy spectrum of the pairs for various age of the nebula. (Right) The entire spectrum of the current Crab nebula (solid lines). Other lines such as the dotted line, the dash line and so on represent the entire spectrum of Crab nebula at various ages. Reprinted from Torres et al. (2014), Copyright 2019, with permission from Elsevier.

significant differences between Tanaka & Takahara (2010) and Torres et al. (2014). This is due to the essential problem that in the 1-zone model, namely the evolution of the energy density of the magnetic field can not be calculated self-consistently. Actually, the phenomenological models of the evolution of the magnetic field used in each models are different in Tanaka & Takahara (2010) and Torres et al. (2014). Furthermore, as mentioned in Section 3.1, 1-zone model can not reproduce the surface brightness of the nebula (e.g., Amato et al., 2000).

van der Swaluw et al. (2001) solved the 1-D non-relativistic and pure hydrodynamic (HD) equations and discussed the structure of PWNe. They showed that by simultaneously solving the surrounding SNR and the PWN, the expansion law of the PWN is strongly influenced by the SNR. However, in their calculations, the emission from the PWN was not discussed because they did not calculate the magnetic field. Vorster et al. (2013a) calculated the magnetic field by solving the induction equation by a post-process method on the pure-HD calculation. As we saw in Section 3.4, the magnetic pressure becomes as strong as the gas pressure, so their approximation is invalid.

Bucciantini et al. (2003) solved the 1-D and time-dependent MHD equation for the first time, considering the surrounding SNR. The left panel of Figure 4.3 shows the pressure profile for $\sigma = 3 \times 10^{-3}$ in Bucciantini et al. (2003). In this calculation, the termination shock can not be resolved, so there is no guarantee that the structure inside the nebula evolution was calculated correctly. In their next paper, Bucciantini et al. (2004) performed more accurate calculations so as to resolve the termination shock. The right panel of Figure 4.3 represents the temporal evolution of the radius of the termination shock and the contact discontinuity. They showed that the radius of the termination shock decreases with increasing σ, and the radius of the contact discontinuity does not depend on σ. Furthermore, they showed that it is necessary to be $\sigma \sim 0.001$ in order to reproduce the observed ratio of the radius of the termination shock to the radius of the termination shock of the Crab nebula. However, these studies discussed only the dynamical structure of PWNe, and did not calculate the radiation.

Lu et al. (2017) performed the emission from PWNe based on the calculation results of the time-dependent 1-D MHD model. They incorporated the time-dependent effect using fitting formulae given in Bucciantini et al. (2004) of the time evolution of the contact discontinuity and the

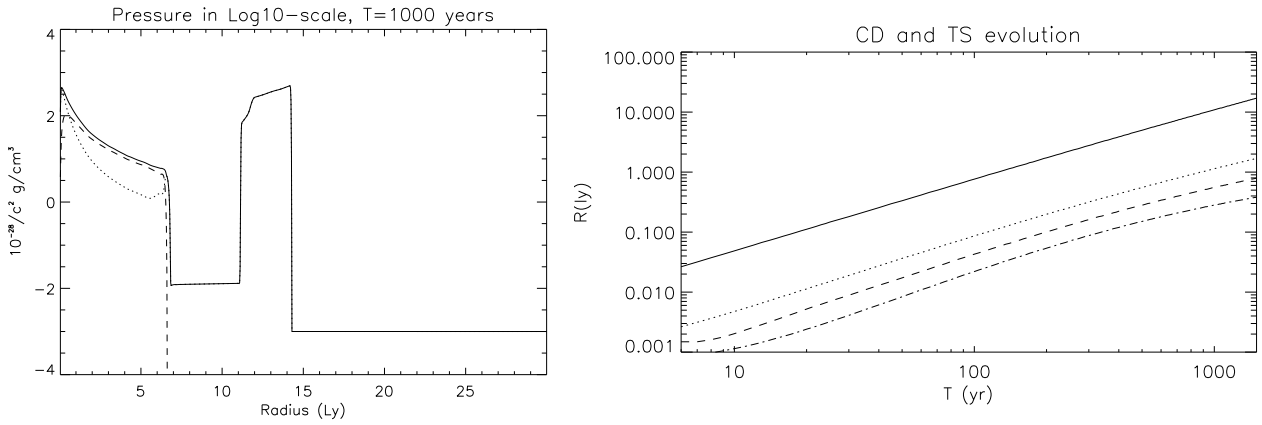

Figure 4.3: (Left) The total pressure profile of the PWN–SNR system for $\sigma = 3.0 \times 10^{-3}$. The dotted line represents the plasma gas pressure. The dashed line represents the magnetic pressure. Credit: Bucciantini et al., A&A, 405, 617, 2003, reproduced with permission ©ESO. (Right) The temporal evolution of the radius of the contact discontinuity (solid line) and termination shock for $\sigma = 0$ (dotted line), $\sigma = 0.0016$ (dashed line) and $\sigma = 0.003$ (dash–dotted line). Credit: Bucciantini et al., A&A, 422, 609, 2004, reproduced with permission ©ESO.

termination shock. They also obtained the internal structure of the nebula by scaling the solution of the steady KC model with the radius of the termination shock calculated from the fitting formulae. As the particle transport process, they considered not only the advection like the KC model but also the Bohm diffusion. In Figure 4.4 shows the magnetic field strengths, which used for their calculation, and the resultant diffusion coefficients. Since they did not solve the MHD equations, they used a phenomenological model similar to Torres et al. (2014) to obtain the absolute value of the energy density of the magnetic field. Figure 4.5 shows the result of applying their model to 3C 58. Although they reproduced both the entire spectrum and the radial profile of the photon index, they do not clarify which of time-dependence or diffusion is important for leading such a result.

In this chapter, the effect of the time-dependence of the 1-D model is investigated. We solve the time-dependent 1-D MHD equation taking into account the spin-down evolution of the central pulsar and the evolution of the supernova remnant outside the nebula. Furthermore, the temporal evolution of the energy distribution of pairs is calculated taking into consideration the radiative cooling and adiabatic cooling, and the emission from of the nebula is calculated. Since the uncertainty of the radius of the termination shock greatly affects the emission spectrum (see section 3.3), we calculate for the case of the Crab Nebula in which the termination shock is well measured. In Section 4.2, the MHD equation solved in this chapter and the equation describing the time evolution of the energy spectrum of the particle are shown. Section 4.3 shows results of the time-dependent model and describes the result of comparison with the KC model. We discuss the results in Section 4.4, and summarize the results in Section 4.5.

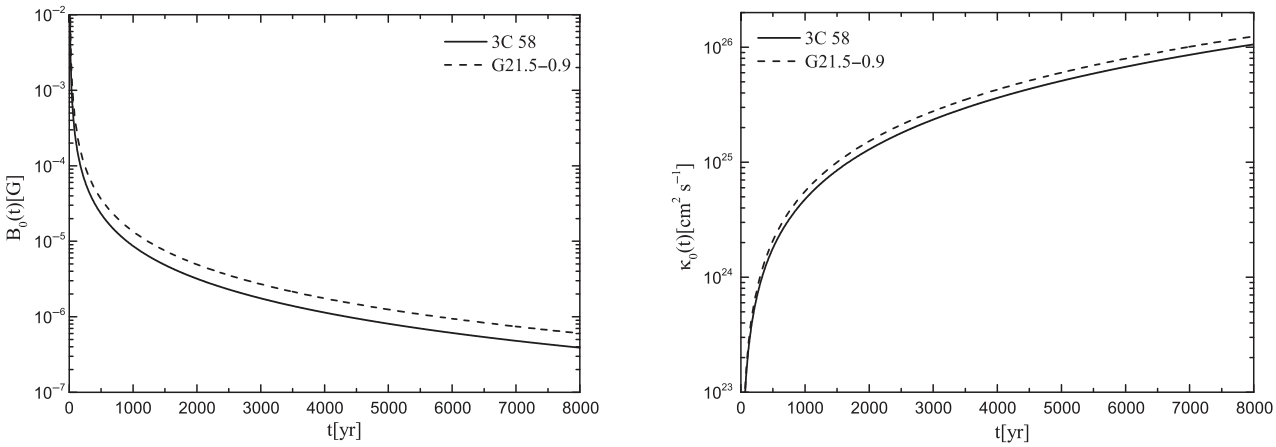

Figure 4.4: Temporal evolution of the magnetic field (left) used in the calculation of Lu et al. (2017) and the resultant diffusion coefficient (right) for a particle with energy 1 TeV. Since the diffusion process is assumed as Bohm diffusion, the diffusion coefficient is a function of the energy and magnetic field only. Figures from Lu et al. (2017). Credit: Lu et al., MNRAS, 60, 4135, 2017, reproduced with permission ©OUP.

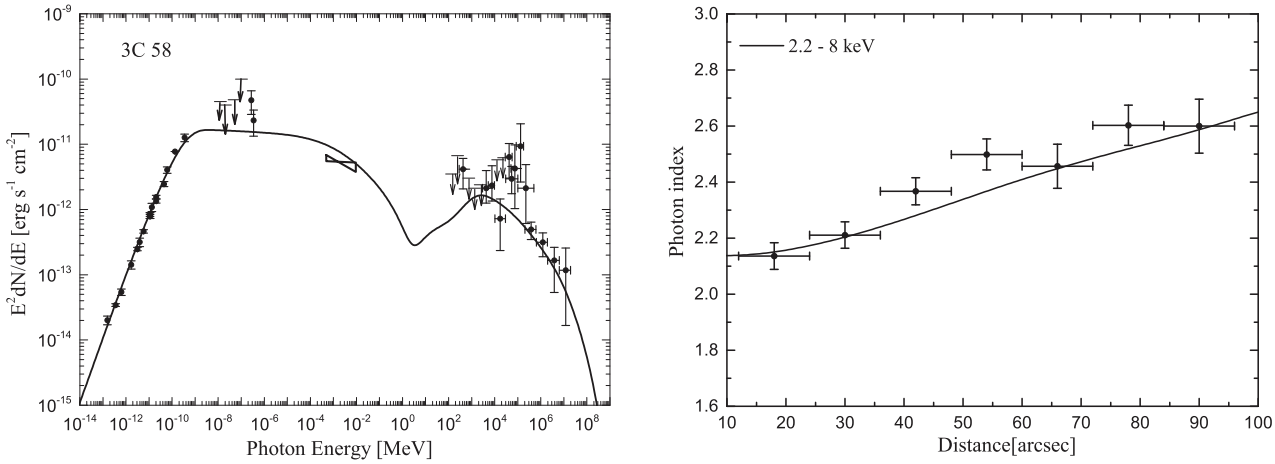

Figure 4.5: Calculation results of the entire spectrum and the radial profile of X-ray photon index for 3C 58 by the model of Lu et al. (2017). Figures from Lu et al. (2017). Credit: Lu et al., MNRAS, 60, 4135, 2017, reproduced with permission ©OUP.

4.2 Basic Equations

4.2.1 Fluid Equations

As shown in Appendix A.1, MHD equations imposing the spherical symmetry, toroidal magnetic field, ideal MHD condition and perfect fluid are written as follows: The mass conservation law is

$$\frac{1}{c}\frac{\partial}{\partial t}(\gamma\rho) + \frac{1}{r^2}\frac{\partial}{\partial r}\left[r^2\rho\gamma v\right] = 0. \tag{4.1}$$

The conservation law of the magnetic flux is

$$\frac{1}{c}\frac{\partial}{\partial t}\left[\left(\frac{h}{r}\right)\gamma\right]+\frac{1}{r^2}\frac{\partial}{\partial r}\left[r^2\left(\frac{h}{r}\right)\gamma v\right]=0, \tag{4.2}$$

where $h = B_0/\sqrt{4\pi}$ and B_0 is the magnetic field measured at the fluid rest frame. The energy conservation law is

$$\frac{1}{c}\frac{\partial}{\partial t}\left[\left(w+h^2\right)\gamma^2-\left(P+\frac{h^2}{2}\right)\right]+\frac{1}{r^2}\frac{\partial}{\partial r}\left[r^2\left(w+h^2\right)\gamma^2 v\right]=0, \tag{4.3}$$

where $w = \epsilon + P$ is the enthalpy density. The momentum conservation law is

$$\frac{1}{c}\frac{\partial}{\partial t}\left[\left(w+h^2\right)\gamma^2 v\right]+\frac{1}{r^2}\frac{\partial}{\partial r}\left\{r^2\left[\left(w+h^2\right)\gamma^2+\left(P+\frac{h^2}{2}\right)\right]\right\}=\frac{2P}{r}. \tag{4.4}$$

In order to describe the difference of the thermodynamical properties between the pulsar wind and the super nova remnant, we solve an additional equation

$$\frac{1}{c}\frac{\partial}{\partial t}\left(\gamma\rho\phi\right)+\frac{1}{r^2}\frac{\partial}{\partial r}\left[r^2\rho\gamma v\phi\right]=0, \tag{4.5}$$

where ϕ is the quantity that represents the species of the matter. Note that this equation is also written as $D\phi/Dt = 0$. The equation of state is

$$P=\left(\Gamma(\phi)-1\right)\left(\epsilon-\rho c^2\right), \tag{4.6}$$

where $\Gamma(\phi)$ is obtained from

$$\frac{1}{\Gamma(\phi)-1}=\frac{1}{\Gamma_2-1}\frac{\phi-\phi_1}{\phi_2-\phi_1}-\frac{1}{\Gamma_1-1}\frac{\phi-\phi_2}{\phi_2-\phi_1}, \tag{4.7}$$

where $\Gamma_1 = 4/3$ and $\Gamma_2 = 5/3$ are the adiabatic ratio of the relativistic (PWN) matter and the non-relativistic matter (SNR), respectively. The above equation is solved using HLL method and the 3rd-order MUSCL reconstruction.

4.2.2 Advection equation

The equation describing the time evolution of the energy spectrum of electrons and positrons is written as:

$$\frac{\partial n}{\partial t}+\frac{1}{r^2}\frac{\partial}{\partial r}\left[r^2 u(r,t)n(E,r)\right]=\frac{\partial}{\partial E}\left[\dot{E}_{\rm syn}(r,t)n(E,r)\right]+\frac{\partial}{\partial E}\left[\frac{cEn(E,r)}{3r^2}\frac{d}{dr}\left(r^2u(r,t)\right)\right]. \tag{4.8}$$

In this chapter, we solve this equation between the termination shock and contact discontinuity in the following Lagrangian method. Since the number of particles is conserved, the following equation holds,

$$n\left(E,r,t\right)dEdV=n\left(E_0,r_0,t_0\right)dE_0dV_0, \tag{4.9}$$

where $dV = d(1/n_{\rm tot})$ is the volume element and the subscript 0 denotes the physical quantity at the moment when the particle is injected into the nebula at the termination shock. The relation between E and E_0 is obtained by solving the following equation describing the evolution of energy per particle:

$$\frac{DE}{Dt}=\frac{E}{3}\frac{Dn}{Dt}-Q_{\rm syn}, \tag{4.10}$$

where $D/Dt = \gamma\left(\partial_t + v\partial_r\right)$ is the Lagrangian derivative.

4.2.3 Initial and Boundary Conditions

Since the MHD equations are hyperbolic system, both initial conditions and boundary conditions are required. For the boundary condition at the inner boundary, we set the Dirichlet condition to be consistent with the time-dependent spin-down luminosity according to equation (2.8). At the outer boundary, we set the free boundary condition. The initial conditions are as follows. Owing to the numerically stability, we set the outer boundary of the SNR, $r_{\rm SNR}^{(0)} = 0.2$ pc and inner boundary of the SNR is $r_{\rm PW}^{(0)} = 0.1$ pc inside which un-shocked pulsar wind flows. Inside the radius $r_{\rm PW}^{(0)}$, we set the steady solution of a cold ($\frac{p}{\rho} \sim 10^{-5} \ll 1$) supersonic flow, in which γ is constant, $\rho \propto r^{-2}$, $B \propto r^{-1}$ and the adiabatic index is 4/3. In the region satisfying $r_{\rm PW}^{(0)} < r < r_{\rm SNR}^{(0)}$, we set the ejecta whose adiabatic ratio 5/3 with homologous expansion, where $v \propto r$, $\rho \propto r^0$. We adopt the ejecta mass $M_{\rm ej} = 8.5\ M_\odot$ (e.g., Nomoto et al., 1982; Owen & Barlow, 2015), and a typical value of supernova explosion $E_{\rm KN} = 5.0 \times 10^{50}$ erg as the kinetic energy of ejecta to reproduce the size of the nebula at present. The absolute values of v and ρ are determined from the following equations:

$$M_{\rm ej} = \int_{r_{\rm PW}^{(0)}}^{r_{\rm SNR}^{(0)}} 4\pi\rho r^2 dr, \tag{4.11}$$

and

$$E_{\rm KN} = \int_{r_{\rm PW}^{(0)}}^{r_{\rm SNR}^{(0)}} \frac{\rho v^2}{2} 4\pi r^2 dr. \tag{4.12}$$

Outside $r_{\rm SNR}^{(0)}$, we set the uniform interstellar matter profile.

4.3 Result

In this section, the result for the Crab nebula calculated with the parameters in Table 4.1 is shown. The parameter for the supernova ejecta and magnetization are chosen to reproduce the size of the Crab nebula at present (950 yr) $r_{\rm N} \sim 2.0$ pc and $r_{\rm s} \sim 0.1$ pc. Figure 4.6 shows the spatial structure of the pressure in the nebula at 950 yr. The termination shock is a discontinuity in ~ 0.1 pc. Around the discontinuity at 2.1 pc, the contact discontinuity and the forward shock formed between the PWN and the SNR are located. Due to a numerical instability, an artificial oscillation is seen, but this does not significantly affect the expansion law of the nebula and most of the internal structure of the nebula. Between $r_{\rm N}$ and 2.7 pc, supernova ejecta The structure inside 3.1 pc is the SNR in the free expansion phase. The forward shock formed propagating in the ISM locates at ~ 3.1 pc. The reverse shock in the ejecta locates at ~ 2.7 pc. The temporal evolution of the position of the discontinuities is shown in the left panel of Figure 4.7. At 1800 yr, the trend of the evolution of the termination shock and the contact discontinuity changes, which corresponds to the time when the PWN starts interaction with the reverse shock in the ejecta. The right panel of the Figure 4.7 shows the spatial structure of total pressure at various times. As seen in this figure, at the 1800 yr, the reverse shock from the SNR is not so developed. In this parameter, the change in the expansion law of the nebula seen in the left panel of Figure 4.7 is due to the fact that the expansion of the nebula is rather fast and catches up with the reverse shock.

The radius of the termination shock continues to increase until 1800 yr. Before interaction with the reverse shock, the nebula continues to expand quickly, so the average pressure within the nebula decreases with time. As a result, the radius at which the pulsar wind ram pressure and the pressure inside the nebula are balanced, which corresponds to the termination shock, increases. Conversely, after 1800 yr, the expansion of the nebula is suppressed by the SNR, so that the decrease of the

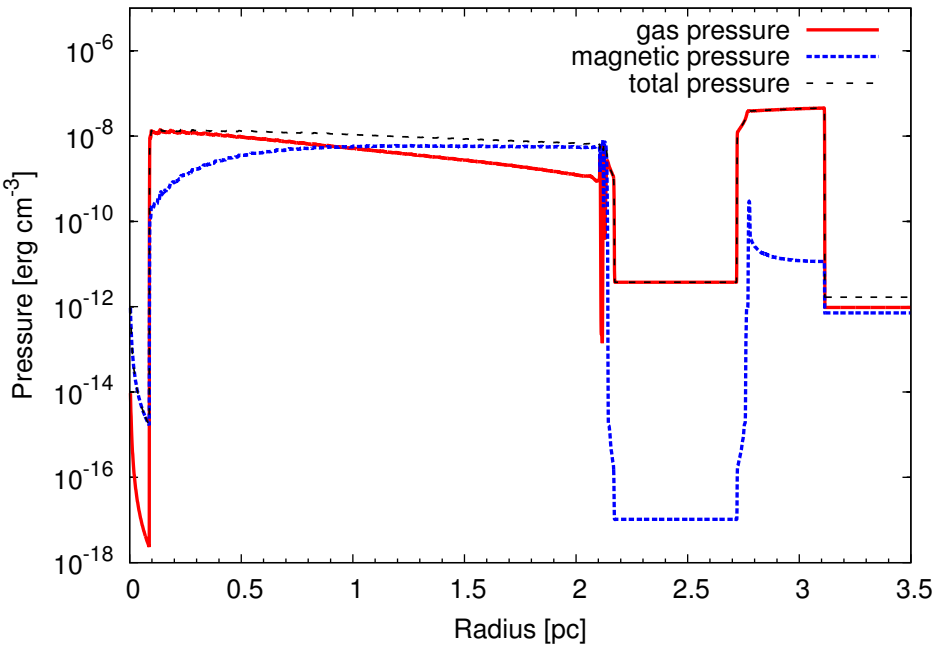

Figure 4.6: The pressure profile when the age of the nebula is 950 yr. The red solid line represents the plasma gas pressure, the blue dotted line represents the magnetic pressure, and the dashed line is sum of them.

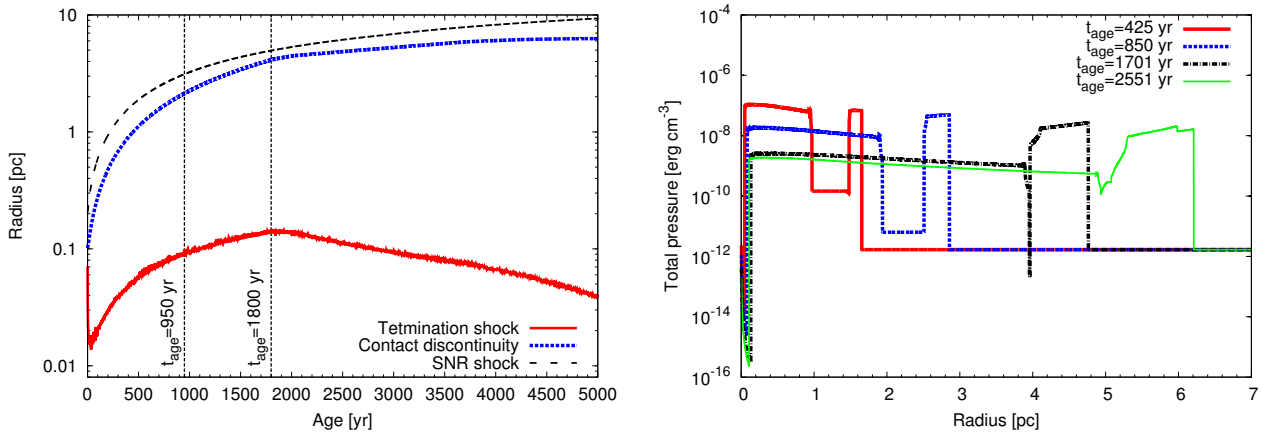

Figure 4.7: (Left) The temporal evolution of the radius of the termination shock $r_{\rm s}$ (red solid line), the radius of the contact discontinuity $r_{\rm N}$ (blue dotted line), and the radius of the SNR shock (black dashed line). The left vertical dashed line represents the current age of the Crab nebula. The right vertical dashed line represents the time when the nebula begin interacting with the SNR reverse shock. (Right) The total pressure (i.e. sum of the gas and magnetic pressure) profile at the various age of the nebula.

pressure in the nebula is drastically diminished. By comparing the result of 1701 yr and 2551 yr in the right panel of the figure 4.7, we find that the pressure inside the nebula is practically not

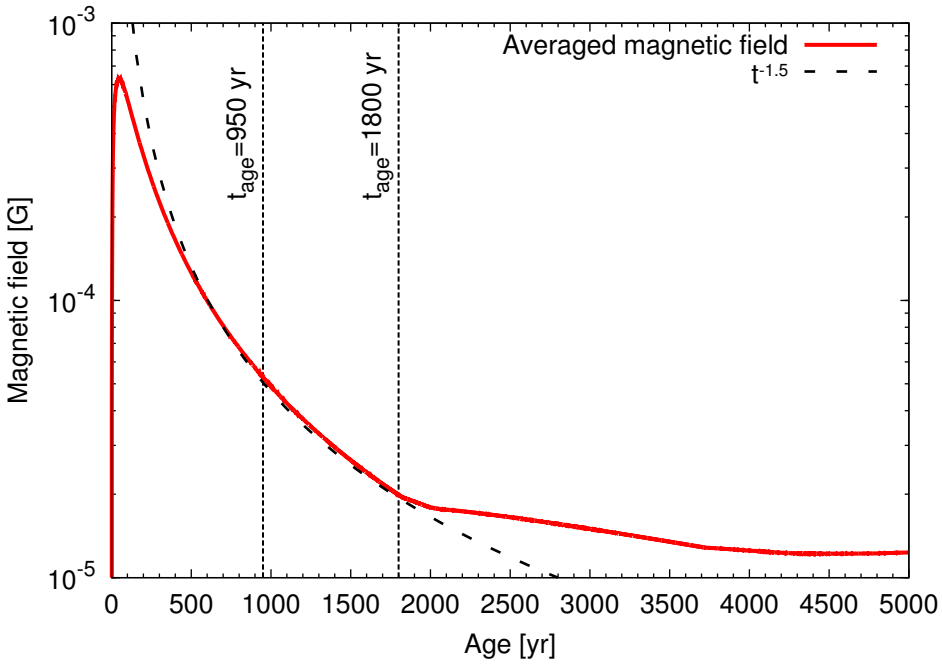

Figure 4.8: The temporal evolution of the volume averaged magnetic field. The black dashed line is a curve proportional to $t^{-1.5}$, which is derived from the phenomenological treatment by Tanaka & Takahara (2010). The vertical dashed lines are same as the left panel of Figure 4.7.

decreased. Since $t > t_0$ holds at 1800 yr, the spin-down luminosity of the pulser goes down in time. As a result, the termination shock propagates inward.

The temporal evolution of the averaged magnetic field in the nebula obtained from equation (3.32) is shown in Figure 4.8. After $t > t_0$, the magnetic field in the nebula shows time evolution proportional to $t^{-1.5}$. This behavior is consistent with the treatment of the magnetic field used in Tanaka & Takahara (2010). They derived the equation describing the temporal evolution of the magnetic field with assuming that the total energy of the magnetic field injected inside the nebula is conserved. After 1800 yr, it deviates from $t^{-1.5}$, but this does not necessarily represent a deviation from their model. This is because the expansion law of the nebula changes as shown in Figure 4.7 (cf. Tanaka & Takahara (2010) was considering a constant velocity expansion). In order to discuss the accuracy of the phenomenological model of the magnetic field, further consideration taking into account the difference in the expansion law is necessary.

In order to investigate the effect of time-dependence, we also perform the calculation with the steady KC model using the radius of termination shock r_s and the spin-down luminosity at 950 yr. Figure 4.9 is a comparison of the gas pressure (top), the velocity (bottom left) and the magnetic field (bottom right). Given the boundary condition, the profile of the pressure and the magnetic field calculated by the steady KC model are in very good agreement. It can be said that the steady state approximation well represents the hydrodynamical structure of the nebula. Due to the numerical oscillation is severe in the velocity field, it shows the time averaged result over 30 years. The velocity field with the steady KC model is in good agreement with the time-dependent result in the range of $r < 0.5$ pc, however for the $r > 0.5$ pc the deviation is seen. This may be due to the fact that the steady KC model does not consider the effect of the external medium (i.e. SNR).

Figure 4.10 represents the temporal evolution of the energy distribution of electrons and positrons

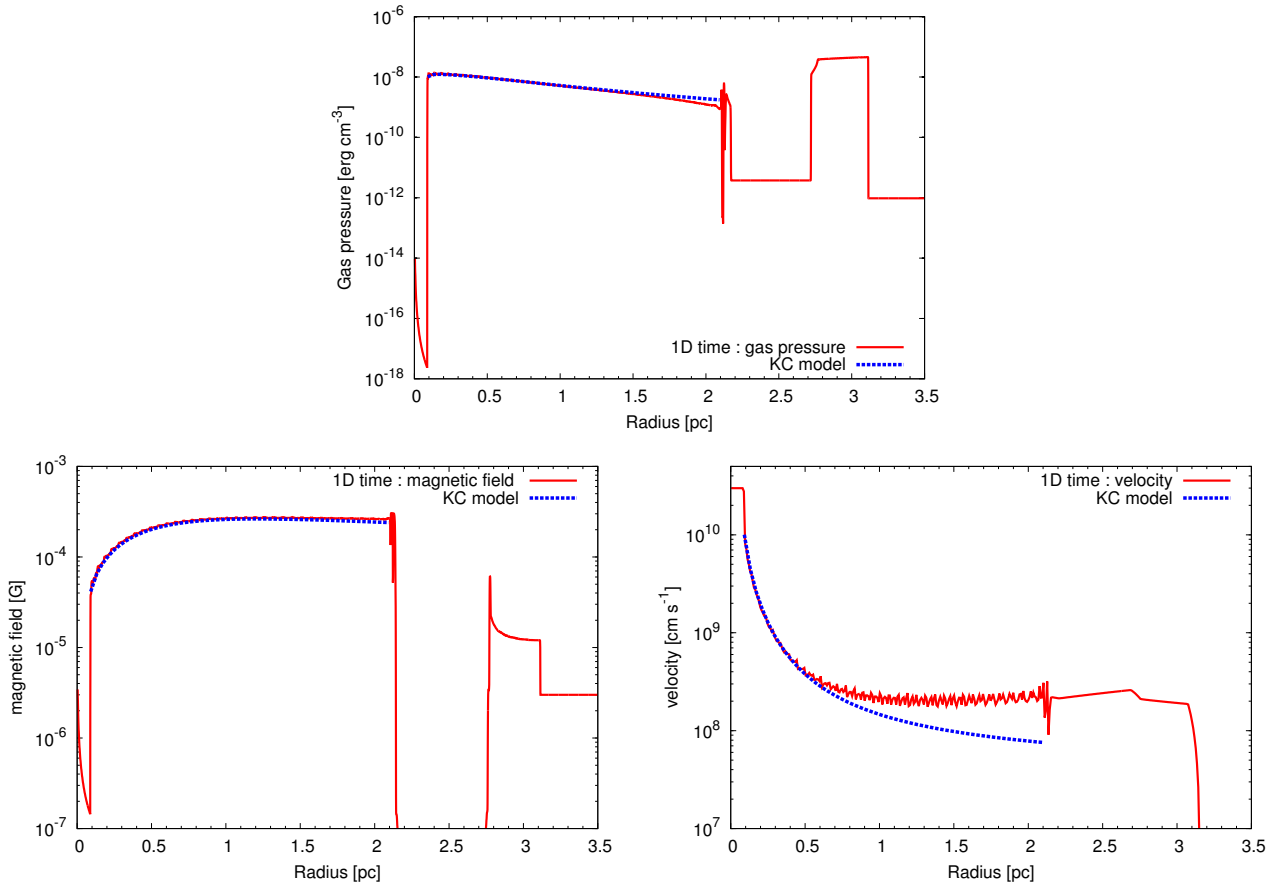

Figure 4.9: The comparison between the steady KC model and our time-dependent model at 950 yr. (Top) The gas pressure. (Bottom Left) The magnetic field. (Bottom Right) The velocity field.

calculated using the time-dependent results of 950 yr. The entire spectrum of the nebula and the surface brightness of the X-ray calculated in the same way as 3.4.1 are shown in Figure 4.11. Not only the hydrodynamic structure but also the emission spectrum and the surface brightness are found to coincide very well with the steady KC model.

In Figure 4.12, the temporal evolution of the entire spectrum and the X-ray surface brightness profile is shown. The flux of the synchrotron component of the entire spectrum decreases with time as expected from Figure 4.8. However, after 1800 yr, the decrease of the magnetic field and the expansion of the nebula are suppressed, so that the diminishment of the flux becomes slow. The temporal evolution of the X-ray surface brightness is not monotonous. While the nebula is in the free expansion phase (i.e. before 1800 yr), the emission region of X-rays spreads with the nebula expansion as age increases. However, when the expansion of the nebula is suppressed (i.e. after 1800 yr), the emission region turns to contraction. This can be understood from the fact that the expansion of the nebula, which induces the effect of broadening the emission region, is slowed down, whereas the radiative cooling, which leads to contract the emission region, continues.

Pulsar parameters [a]	Symbol	Crab
Distance (kpc)	D	2.0
Age (yr)	$t_{\rm age}$	950
Initial Spin-down luminosity (erg s^{-1})	L_0	3.4×10^{39}
Initial Spin-down time (yr)	t_0	700
Braking index	n	2.51
Pulsar Wind parameters [a]		
Magnetization	σ	1.0×10^{-3}
Initial Radius (pc)	$r_{\rm PW}^{(0)}$	0.1
Minimum Energy (eV)	$E_{\rm min}$	5.1×10^{7}
Break Energy (eV)	$E_{\rm b}$	3.1×10^{11}
Maximum Energy (eV)	$E_{\rm max}$	7.0×10^{15}
Low-energy index	p_1	1.3
High-energy index	p_2	2.35
Supernova Remnant parameters [a]		
Ejecta Mass ($M_\odot$)	$M_{\rm ej}$	8.5
Kinetic Energy of the Ejecta (erg)	$E_{\rm KN}$	5.0×10^{50}
Initial Radius (pc)	$r_{\rm SNR}^{(0)}$	0.2
Interstellar Medium parameters [a]		
Ambient Mass Density (g cc^{-1})	$\rho_{\rm ISM}$	1.0×10^{-24}
Magnetic Field (μG)	$B_{\rm ISM}$	3.0
Temperature (eV)	$T_{\rm ISM}$	1.0
Obtained parameters		
Current Radius of the termination shock (pc)	$r_{\rm N}$	0.92
Current Radius of the nebula (pc)	$r_{\rm s}$	2.1
Current spin-down luminosity (erg s^{-1})	$L_{\rm sd}$	4.6×10^{38}
Bulk Lorentz factor	$\gamma_{\rm u}$	8.4×10^{4}
Pre-shock density (cm^{-3})	$n_{\rm u}$	2.7×10^{-12}

Table 4.1: Parameters in the time-dependent calculations for the Crab Nebula.

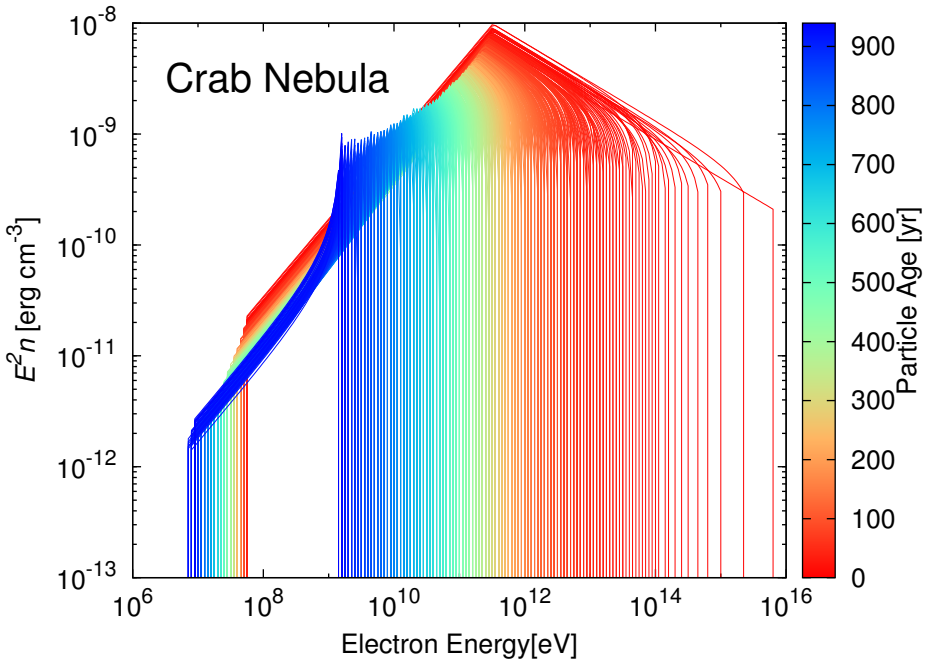

Figure 4.10: The energy spectra of electrons and positrons for various particle age, which is the elapsed time since injection into the nebula. The color contour represents the particle age.

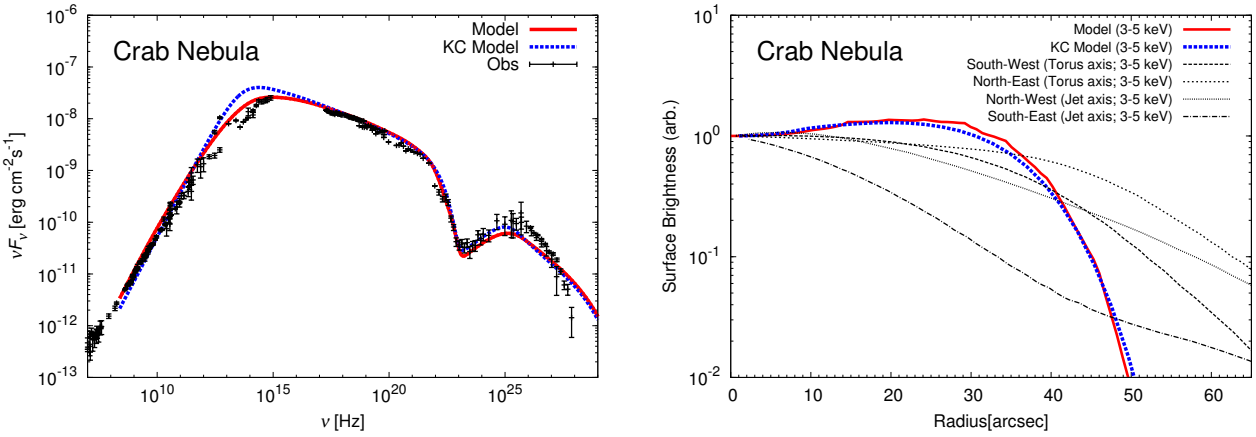

Figure 4.11: (Left) The entire spectrum calculated by the time-dependent 1-D model (red solid line) and the steady KC model (blue dotted line). (Right) The profiles of the X-ray surface brightness for the time-dependent 1-D model (red solid line) and the steady KC model (blue dotted line). The data points and curves are the same as Figure 3.9.

4.4 Discussion

As seen in Section 4.3, the steady-state approximation is a very accurate approximation in the model of PWNe. The main time-dependent effects neglected in the steady KC model are associated with the expansion of the nebula and the spin-down evolution of the central pulsar. In fact, time

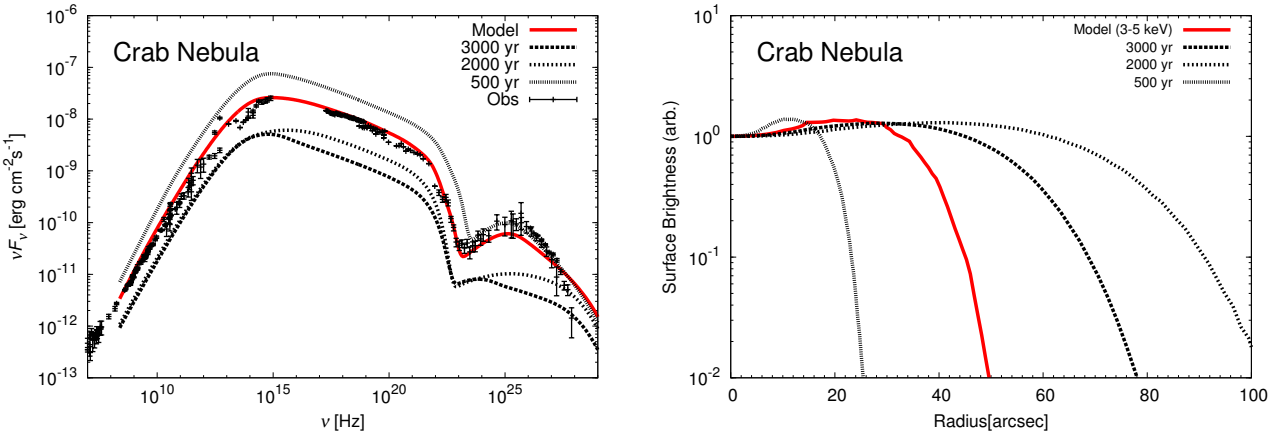

Figure 4.12: (Left) Entire spectra of the Crab nebula for various ages. (Right) Profiles of X-ray surface brightness for various ages.

scales of these are much longer than the time that it takes for the sound speed to traverse inside the nebula ($\sim$ 10 yr). The most notable difference between the time-dependent model and the steady KC model is the velocity field (see Figure 4.9). The resultant advection time calculated by the steady KC model (see equation (3.22)) is about 1.5 times longer than the actual age of the nebula 950 yr. The expansion velocity of the nebula is determined by the pressure equilibrium of the nebula and the surrounding SNR rather than the velocity of the fluid. Since the steady KC model does not consider the existence of external materials, such inconsistency may be seen. Nevertheless, the pressure and the magnetic field profile in the steady KC model are still good approximations because the ram pressure can be ignored against the gas pressure and magnetic pressure.

We also tried to calculate the case where σ is larger. However, due to the fast inward move of the termination shock, the numerical resolution was insufficient. As pointed out by Bucciantini et al. (2004), the termination shock $r_{\rm s}$ becomes small with σ increases. On the other hand, the size of the contact discontinuity $r_{\rm N}$ depends only on the total amount of spin-down energy injected by the pulser, and hardly depends on σ. Therefore, σ is very constrained by $r_{\rm s}$ and $r_{\rm N}$. The required value of $\sigma = 10^{-3}$ in this calculation reconfirms the sigma problem in terms of pressure equilibrium (not expanding speed). In Porth et al. (2014) and Tanaka et al. (2018), by considering the difference in magnetic configuration, they tried to solve the problem of the pulsar wind deceleration. It is important to investigate whether their models can reconcile the sigma problem also from the viewpoint of pressure equilibrium. Although Porth et al. (2014) calculated the time evolution of the nebula only about 100 yr despite placing $r_{\rm s}$ at a large radius $\sim$ 0.3 pc as an initial condition, so that it is unclear whether pressure equilibrium was realized for such a short period. Tanaka et al. (2018) modeled phenomenologically taking into account the turbulence effects. Their model is a steady model ignoring the external medium, and only explains the expansion velocity. By improving the model of Tanaka et al. (2018) in consideration of the external medium and spin-down effect and calculating with our method, we can investigate whether the effect of the turbulent magnetic field can really solve the sigma problem or not.

4.5 Conclusion

In order to investigate the validity of the steady state assumption in the KC model, we solved the time-dependent and spherical symmetric MHD equations taking into account the effect of the spin-down evolution of the central pulsar and the surrounding SNR. Furthermore, the evolution of the energy spectrum of non-thermal particles in the nebula was consistently calculated considering radiative and adiabatic cooling, and the emission from the nebula was calculated. We found that the steady state assumption in PWNe is a very good approximation in terms of both the hydrodynamic structure and the emission model.

As mentioned in Chapter 1, PWNe are the most detected source on TeV γ-rays. Currently under construction CTA (Cherenkov Telescope Array Acharya et al., 2013, underconstructing ground-based gamma-ray observatory) is expected to discover more than 10 times sources with sensitivity increases. It is expected that old PWNe which was not seen due to dim until now can be found. In the emission model of the old PWNe, it is essential to calculate the interaction with the SNR, our model can calculate such a situation. Furthermore, the angular resolution is also improved in CTA. Then, it will be possible to discuss the relations between TeV γ-ray extent, X-ray extent and the nebula age. In order to interpret such observational information to the physical quantity of the nebula (e.g., the age of the nebula), a model considering both space and time dependence is necessary. In other words, our model is useful not only for the purpose of investigating the validity of the steady-state approximation but also for translating the information on spatially resolved observations of PWNe to the physical quantities in future. It is necessary to further deepen the knowledge of this time-dependent 1-D model by conducting calculations in various parameters.

Chapter 5

Model with Diffusion and its Back-reaction

5.1 Introduction

Although the KC model has been accepted as a standard model of PWNe, some problems in the KC model have been raised by morphology researches with high angular resolution observations in X-ray (see Chapter 3). In Chapter 3, we applied the KC model to G21.5-0.9 and 3C 58, and showed that the KC model has severe difficulty to reproduce both the entire spectrum and the surface brightness profile simultaneously.

Since the problems in the KC model have been claimed, several authors have discussed improve-

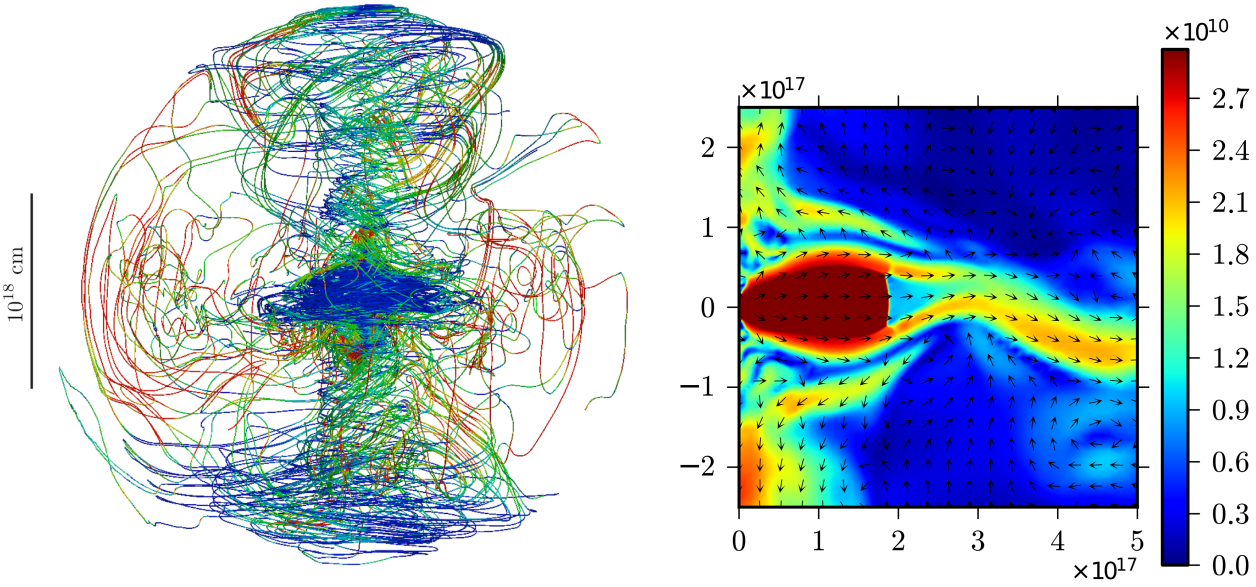

Figure 5.1: (Left) The sampled magnetic field lines of the 3–D MHD simulation performed by Porth et al. (2014). The color indicates the ratio of the strength of the poloidal field to the strength of the troidal field. Blue means toroidal, and red means poloidal. (Right) The velocity magnitude (contour) and direction (arrows). Credit: Porth et al., MNRAS, 431, L48, 2013, reproduced with permission ©OUP.

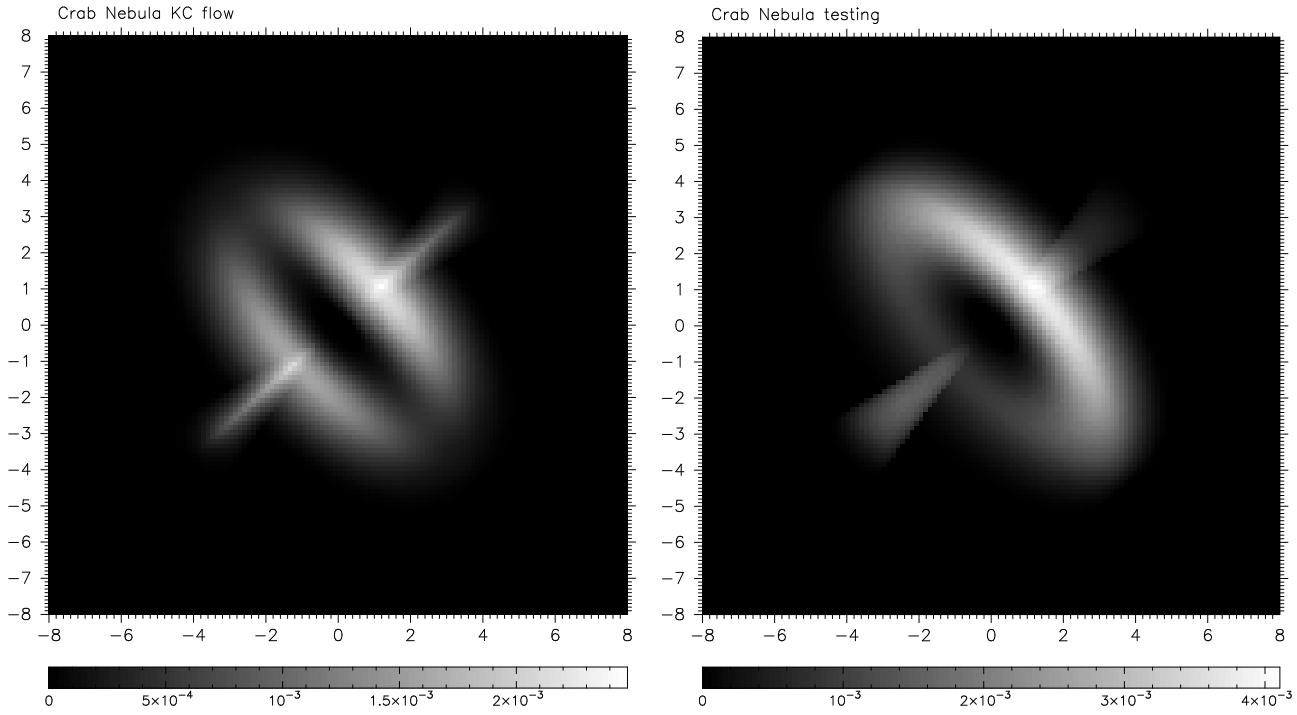

Figure 5.2: (Left) The calculated X-ray image with assumption that the magnetic field is purely toroidal. (Right) The calculated X-ray image with assumption of an existence of the disturbed field. Figures from Shibata et al. (2003). Credit: Shibata et al., MNRAS, 346, 841, 2003, reproduced with permission ©OUP.

ment of the KC model. In the KC model, particles are simply advected with the spherical wind. However, Porth et al. (2014) performed a three-dimensional full MHD simulation and showed that PWNe are in very disturbed state (Figure 5.1). Shibata et al. (2003) suggested the existence of turbulent magnetic field in the nebula by using a semi-analytic method. The left panel of Figure 5.2 represents the X-ray image calculated by Shibata et al. (2003) with assumption that the magnetic field is purely toroidal. As seen in this result, they pointed out that it can not be reproduced the torus-like structure of the X-ray image of the Crab nebula shown in Figure 1.2 by the model with only the ordered field. Moreover, they indicated that if there is a disturbed field with an amplitude as large as the ordered field, a torus-like X-ray image can be obtained as shown in the right panel of Figure 5.2.

In such disturbed plasma, the particle diffusion can be an important process. Tang & Chevalier (2012) preformed the test-particle simulation taking into account particle diffusion in the background fluid and synchrotron cooling, and showed that the model reproduces the radial profiles of the photon index in 3C 58 and G21.5-0.9 (Figure 5.3). Porth et al. (2016) also performed the test-particle simulation to obtain the diffusion coefficient based on the 3–D MHD simulation by Porth et al. (2014). Their 1–D steady diffusion model with the obtained diffusion coefficient, can explain the radial profile of the surface brightness and the photon index of 3C 58, G21.5-0.9 and the Vela (Figure 5.4).

The recent confirmation of the largely extended γ-ray halo around the Geminga pulsar by HAWC (Abeysekara et al., 2017a) also supports the idea of the particle diffusion (Abeysekara et al., 2017b). The extended gamma-ray would be emitted by electron–positron pairs diffusively escaped from the

nebula (Figure 5.5). On the other hand, in Vela, which is one of the neighboring pulsar wind nebula, if electrons/positrons of pulsar wind is not confined efficiently in the nebula, the expected flux of the cosmic-ray contradicts the observation (Huang et al., 2018). Thus, the diffusion process in the pulsar wind nebula is an important theme not only in the model of the nebula but also in the cosmic-ray physics.

Although the consideration of the diffusion process in pulsar wind nebulae is very important, its models are still in the developing stage. Tang & Chevalier (2012) and Porth et al. (2016), which adopt the test-particle approximation, did not discuss the emission spectrum. A model consistent with both the spectrum and radial profile is desired (Ishizaki et al., 2017).

In most of other astronomical phenomena, the spatial diffusion is considered for energetically sub-dominant component with respect to the motion of the background fluid. However, even energetically dominating particles are required to diffuse in order to reconcile the observed X-ray profile in PWNe. Although we have a consensus that a diffusion coefficient of about 10^{27} cm^2 s^{-1} is required to reproduce the observed X-ray profile of PWNe (e.g., Tang & Chevalier, 2012; Porth et al., 2016), this value implies that the energy flux carried by the diffusion is comparable to or larger than that carried by the advection with fluid. In such cases, the test-particle approximation is not appropriate.

If we simply apply the particle diffusion fixing the velocity profile of the background fluid, the energy and momentum conservations along the fluid are not assured. We need to take into account the back reaction of the particle diffusion on the background fluid. Moreover, the idea of the particle diffusion in PWNe is ambiguous. The pulsar wind consists of only non-thermal particles, which themselves are subject for the diffusion process, so that the definition of the background fluid is not straightforward. Namely, the method to distinguish the diffusive component from the background fluid is not apparent.

In this chapter, we aim mainly to reproduce both the entire spectrum and X-ray radial profile of 3C 58 and G21.5-0.9 by improving the KC model with the diffusion effect. In Chapter 4, we have already shown that the steady-state approximation is significant given the inner and outer boundaries. In this chapter, we neglect the temporal evolution effect and assume steady state. In Section 5.2, we explicitly define the background fluid and derive fluid equations satisfying the

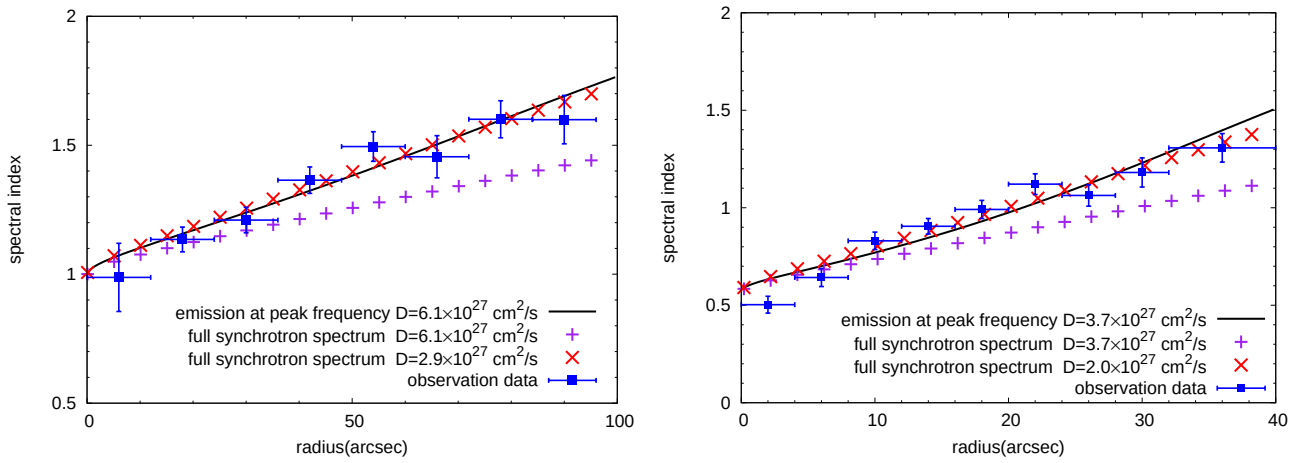

Figure 5.3: The radial profile of the X-ray spectral index with the pure diffusion model of Tang & Chevalier (2012). The left panel and right panel represent results for 3C 58 and G21.5-0.9, respectively. ©AAS. Reproduced with permission.

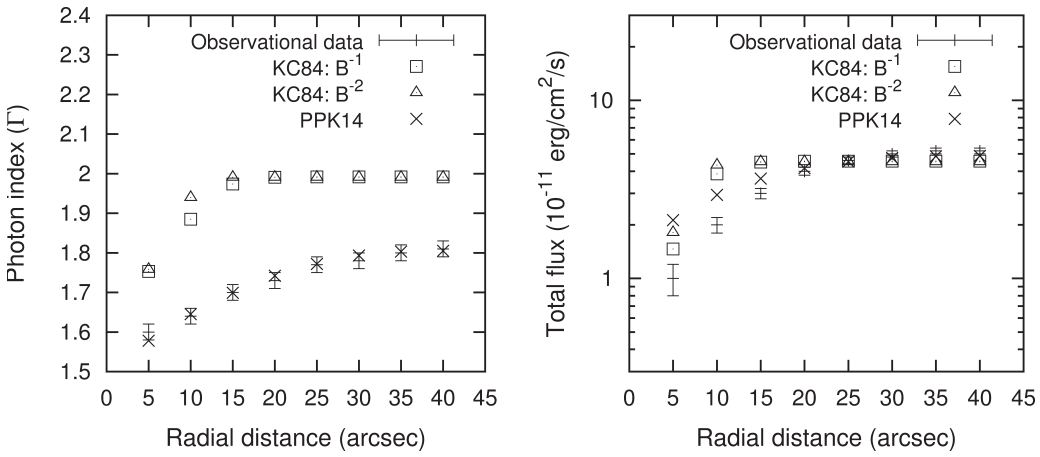

Figure 5.4: The left panel represents the radial profile of the X-ray photon index of G21.5-0.9 calculated with the diffusion–advection model of Porth et al. (2016). The right panel represents the cumulative flux for each radius. The points labeled KC84 are models using KC model for the calculation of advection. The points labeled PPK14 is a model using the simulation result of Porth et al. (2013) for the calculation of advection. KC84:B^{-1} is a model calculated with the diffusion coefficient D proportional to the inverse of the magnetic field B (i.e. $D \propto B^{-1}$). KC84:B^{-2} is the case for $D \propto B^{-2}$. The diffusion coefficient in PPK14 is obtained by performing the test particle simulation on the calculation result of Porth et al. (2014). The resultant averaged diffusion coefficients for KC84:B^{-1}, KC84:B^{-2} and PPK14 are 1.2×10^{26} cm^2 s^{-1}, 0.3×10^{26} cm^2 s^{-1} and 5.7×10^{26} cm^2 s^{-1}, respectively. Credit: Porth et al., MNRAS, 460, 4135, 2016, reproduced with permission ©OUP.

energy and momentum conservations with the diffusion effect. In Section 5.4, we demonstrate our 1–D steady state model and discuss the velocity and magnetic field profiles in the flow, photon spectrum, and the radial profile of the surface brightness especially for the model dependence on the diffusion coefficient. In Section 5.5, we apply our model to two observed sources 3C 58 and G21.5-0.9, which has been also discussed in Chapter 3. In Section 5.6, we summarize and discuss the results.

5.2 Pulsar Wind Model with particle diffusion

5.2.1 Central Idea

The concept of diffusion in PWNe is ambiguous. It is not possible to clearly distinguish the diffusion component from the background fluid. This may indicate that the fluid approximation itself is not suitable for the PWNe. However, the concept of fluid approximation is still useful for understanding the physics of PWNe. In this section, while maintaining the fluid picture, we formulate the fluid equation by considering the spatial diffusion of particles self-consistently. These equations are solved by combining with the advection diffusion equation of the energy distribution function of non-thermal particles.

We clarify the definitions of the diffusion and background fluid, then we present general formulation for the fluid equations describing the macroscopic motion of the non-thermal particles in Section 5.2.2, and the transport equation describing the evolution of the energy spectrum of the particles in Section 5.2.3. In Section 5.2.4, we adopt those general equations to a spherically

symmetric and steady system, and show our model to apply for PWNe. Note that, hereafter, the rest frame of the entire nebula is defined as reference frame K.

5.2.2 Fluid equations

In order to treat the diffusion in a one-component fluid, we assume a spatial diffusion coefficient with energy dependence, whereby the diffusion effect can be neglected for the lowest energy particles which make up the majority of the particle number. The fluid flow velocity approximately corresponds to the average velocity of such low energy particles. Note that energetically dominating particles, whose average energy is much higher than the lowest particle energy, can be affected by the diffusion significantly. Since the current to maintain the magnetic field in the fluid is also dominated by low energy particles, in this case the frozen-in condition in the ideal MHD will be held (See D for details).

The Boltzmann equation represented in the frame K is written as

$$\frac{\partial f_s}{\partial t} + \boldsymbol{v} \cdot \nabla f_s + q_s \left[\boldsymbol{E} + \frac{\boldsymbol{v}}{c} \times \boldsymbol{B} \right] \cdot \frac{\partial f_s}{\partial \boldsymbol{p}} = S_s \tag{5.1}$$

where f_s is the phase space distribution functions of particles, s is species (e=electron, p=positron), q is a charge of each particle, $\boldsymbol{v}$ is the velocity of each particle, $\boldsymbol{E}$ and $\boldsymbol{B}$ are the electric field and magnetic field in the frame K, and S is the collision term. In this calculation, we consider the Lorentz force as the force from the macroscopic ordered electromagnetic fields, and S as the contribution from the microscopic disturbed field. Since the mass of a electron is equal to the mass of a positron, the bulk flow velocity normalized by speed of light c is,

$$\boldsymbol{\beta} \equiv \frac{1}{c} \frac{\int \boldsymbol{v} \left(f_e + f_p \right) d^3 p}{\int \left(f_e + f_p \right) d^3 p}, \tag{5.2}$$

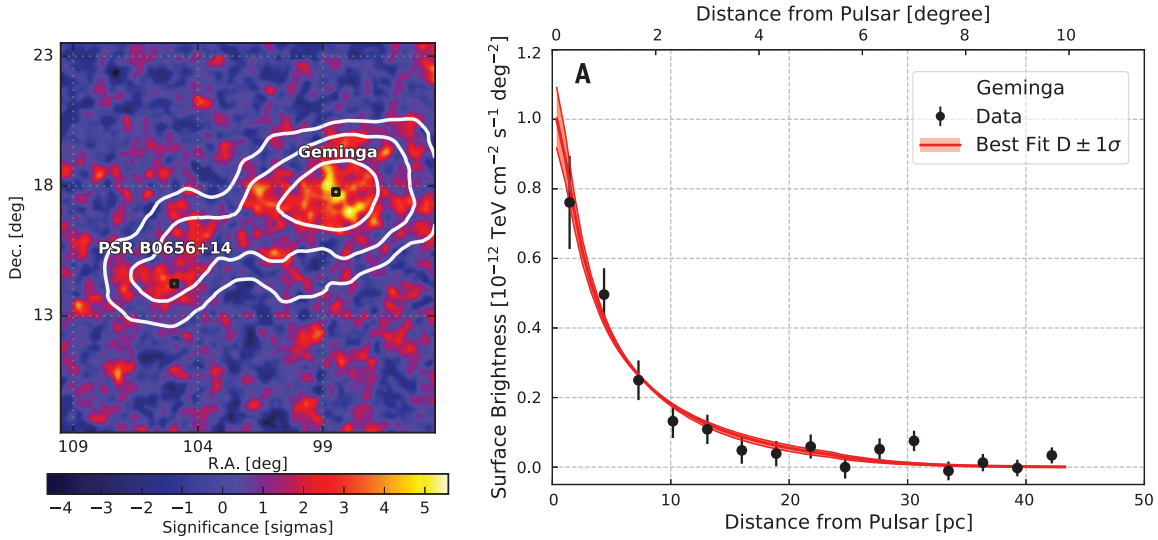

Figure 5.5: (Left) HAWC significance map for the Geminga and PSR B0656+14 at the γ-ray energy with 1-50 TeV. (Right) The surface brightness of the γ-rays from Geminga. The red line represents the pure diffusion model with the diffusion coefficient $D \sim 5.0 \times 10^{27}$ cm^2 s^{-1} for 100 TeV electrons. From Abeysekara et al. (2017b). Reprinted with permission from AAAS.

and the corresponding Lorentz factor is $\gamma = 1/\sqrt{1-\beta^2}$. The co-moving frame of the fluid K' is defined as the frame moving at velocity $\boldsymbol{\beta}$ with respect to the frame K. The collision term S_s, which expresses a stochastic process in a disturbed field (e.g., Blandford & Eichler, 1987), is defined in the frame K as

$$S_s \equiv \nabla \cdot (\kappa \nabla f_s)\,, \tag{5.3}$$

where κ is an energy-dependent diffusion coefficient[1].

Integrating equation (5.1) over the momentum space, we obtain two-component fluid equations for electrons and positrons. For the case of no diffusion, assuming that the wind is almost electrically neutral ($n_e \sim n_p$) and the convection current (which is generated by advection of true charge in the fluid) is much smaller than the conduction current, we can safely use the one-component fluid equation as used in KC model (Melatos & Melrose, 1996). Furthermore, even if there is a diffusion process, the ideal MHD condition,

$$\boldsymbol{E} + \boldsymbol{\beta} \times \boldsymbol{B} = 0, \tag{5.4}$$

still holds (see Appendix D for details). Thus, hereafter, we consider introducing the effect of the diffusion term on the one-component fluid equation.

The energy (momentum) transfer due to the spatial diffusion is obtained by integrating the product of the energy $E_\pm$ (the momentum $\boldsymbol{p}_\pm$) and the diffusion term (5.3) over the momentum space. Adding those diffusion terms, we obtain the energy conservation law,

$$\frac{1}{c}\frac{\partial}{\partial t}\left[\gamma^2(\epsilon + P) - P + \frac{E^2+B^2}{8\pi}\right] + \nabla\cdot\left[\gamma^2(\epsilon+P)\boldsymbol{\beta} + \frac{\boldsymbol{E}\times\boldsymbol{B}}{4\pi} - \nabla\left\{\left(\frac{4}{3}u^2+1\right)\delta\right\} + \left(\frac{4}{3}u^2+1\right)\boldsymbol{\theta}\right] = -\gamma\Lambda, \tag{5.5}$$

and the momentum conservation law,

$$\frac{1}{c}\frac{\partial}{\partial t}\left[\gamma^2(\epsilon+P)\boldsymbol{\beta} + \frac{\boldsymbol{E}\times\boldsymbol{B}}{4\pi}\right] + \nabla\cdot\left[\gamma^2(\epsilon+P)\boldsymbol{\beta}\boldsymbol{\beta} + P\boldsymbol{I} + \frac{\boldsymbol{E}\boldsymbol{E}+\boldsymbol{B}\boldsymbol{B}}{8\pi} - \nabla\left(\frac{4}{3}\gamma^2\boldsymbol{\beta}\delta\right) + \frac{4}{3}\gamma^2\boldsymbol{\beta}\boldsymbol{\theta}\right] = -\gamma\boldsymbol{\beta}\Lambda, \tag{5.6}$$

where ϵ and P are energy density and gas pressure in the frame K', respectively. Hereafter, we assume that non-thermal particles are ultra-relativistic ($E'_\pm \simeq cp' \gg m_e c^2$), which implies

$$P = \frac{1}{3}\epsilon. \tag{5.7}$$

The diffusion terms have been calculated with the fact that f_s and $d^3\boldsymbol{p}/E_\pm$ are Lorentz invariant and the assumption of the isotropic momentum distribution in the frame K'. In the usual formulation of the two-fluid equation, it is assumed that f_s is isotropic in the center-of-mass system of each component. However, since we are considering a situation where a one-component fluid equation holds, we assume that f_s is almost isotropic in the center-of-mass system of all particles. Thus, the values, δ and $\boldsymbol{\theta}$, in the diffusion terms are defined by

$$\delta \equiv \frac{1}{c}\int \kappa E'_\pm (f_e + f_p)\, d^3\boldsymbol{p}', \tag{5.8}$$

[1]The diffusion process is usually defined in the fluid rest frame K'. In a spherically symmetric steady flow, if we rewrite the collision term with the coordinate of the frame K, the diffusion coefficient for the radial direction is re-defined as an enlarged value by a factor of γ^2. The value κ in equation (5.3) is interpreted as such an effective value.

$$\boldsymbol{\theta} \equiv \frac{1}{c}\int (\nabla\kappa)\, E'_{\pm}\, (f_e + f_p)\, d^3\boldsymbol{p}', \tag{5.9}$$

respectively. The radiative cooling term is written with the cooling rate in the frame K' as

$$\Lambda \equiv \frac{1}{c}\int Q'_{\rm rad}\, (f_e + f_p)\, d^3\boldsymbol{p}', \tag{5.10}$$

where $Q'_{\rm rad}(E'_{\pm})$ is the energy radiative loss rate per particle. As shown in Tanaka & Takahara (2010), the radiative cooling by inverse Compton is negligibly inefficient compared to the synchrotron cooling so that

$$Q'_{\rm rad} = \frac{4}{3}\sigma_{\rm T} c \left(\frac{E'_{\pm}}{m_{\rm e}c^2}\right)^2 \frac{B'^2}{8\pi}. \tag{5.11}$$

The induction equation with the ideal MHD condition is

$$\frac{1}{c}\frac{\partial \boldsymbol{B}}{\partial t} = \nabla \times (\boldsymbol{\beta} \times \boldsymbol{B})\,. \tag{5.12}$$

If δ, $\boldsymbol{\theta}$, and Λ are given, the fluid quantities $\boldsymbol{\beta}$, ϵ, p, $\boldsymbol{E}$ and $\boldsymbol{B}$ can be calculated by solving equations (5.5), (5.6), (5.7), (5.12) and (5.4) (hereafter fluid equations). However, those quantities depending on the functional form of f are not given in advance.

5.2.3 Diffusion-Advection equation

In order to obtain δ, $\boldsymbol{\theta}$, and Λ, we also solve the advection–diffusion equation (hereafter AD equation, e.g., Ginzburg & Syrovatskii, 1964) written as

$$\frac{\partial n(\boldsymbol{x}, E'_{\pm})}{\partial t} + \nabla\cdot\left[c\boldsymbol{u}n(\boldsymbol{x}, E'_{\pm}) - \kappa\nabla n(\boldsymbol{x}, E'_{\pm})\right] - \frac{\partial}{\partial E'_{\pm}}\left[Q' n(\boldsymbol{x}, E'_{\pm})\right] = 0, \tag{5.13}$$

where $n(\boldsymbol{x}, E'_{\pm}) = 4\pi p'^2\, (f_e + f_p)\, /c$ is the energy spectrum of particles in the frame K', $\boldsymbol{u} = \gamma\boldsymbol{\beta}$ is the flow 4-velocity, and Q' is the energy loss rate due to the radiative and adiabatic cooling per particle. This equation can be solved if $\boldsymbol{u}$ and B' are given in advance, so that the fluid equations and the AD equation are complementary each other. We can solve the AD equation and the fluid equations alternately until the energy densities estimated from both the methods agree with each other.

5.2.4 Spherical steady nebulae

We impose the spherical symmetry and steady state to the fluid equations and the AD equation. Furthermore, we assume that the configuration of magnetic field is purely toroidal as the KC model assumed. Thus, the magnetic field in the frame K' is $B' = B/\gamma$, and the induction equation (5.12) leads to

$$r\beta B = \text{const.} \tag{5.14}$$

For simplicity, we assume that the diffusion coefficient is expressed by a separable form as

$$\kappa(r, E'_{\pm}) = \phi(r)\tilde{\kappa}(E'_{\pm}). \tag{5.15}$$

Then, the terms with δ and $\boldsymbol{\theta}$ in the fluid equations can be put together. Equations (5.5) and (5.6) are written as

$$\frac{1}{r^2}\frac{\partial}{\partial r}\left[r^2\left(\gamma^2\,(\epsilon + P)\,\beta + \frac{B^2}{4\pi}\beta - \phi(r)\frac{\partial}{\partial r}\left\{\left(\frac{4}{3}\gamma^2\beta^2 + 1\right)\tilde{\delta}(r)\right\}\right)\right] = -\gamma\Lambda(r), \tag{5.16}$$

and

$$\frac{1}{r^2}\frac{\partial}{\partial r}\left[r^2\left(\gamma^2\left(\epsilon+P\right)\beta^2+P+\frac{B^2}{8\pi}\left(1+\beta^2\right)-\phi(r)\frac{\partial}{\partial r}\left\{\frac{4}{3}\gamma^2\beta\tilde{\delta}(r)\right\}\right)\right]=\frac{2P}{r}-\gamma\beta\Lambda(r), \quad (5.17)$$

respectively, where $\tilde{\delta}$ is defined as

$$\tilde{\delta}(r)\equiv\frac{1}{c}\int\tilde{\kappa}E'_{\pm}n(r,E'_{\pm})dE'_{\pm}. \quad (5.18)$$

The AD equation (5.13) in a spherical steady system becomes

$$\frac{1}{r^2}\frac{\partial}{\partial r}\left[r^2\left(cu(r)n(r,E'_{\pm})-\kappa\frac{\partial n(r,E'_{\pm})}{\partial r}\right)\right]-\frac{\partial}{\partial E'_{\pm}}\left[Q'n(r,E'_{\pm})\right]=0, \quad (5.19)$$

where Q' expresses the radiative and adiabatic cooling effects as

$$Q'=Q'_{\rm rad}+\frac{E'_{\pm}}{3}\frac{c}{r^2}\frac{\partial}{\partial r}\left[r^2u(r)\right]. \quad (5.20)$$

We solve only the downstream of the termination shock at $r=r_{\rm s}$. Given $r_{\rm s}$, the energy injection rate (the spin-down luminosity) $L_{\rm sd}$, and the magnetization parameter σ, the Rankine–Hugoniot jump condition (for details see Kennel & Coroniti, 1984a) provides the boundary condition at $r=r_{\rm s}$ for the fluid equations.

As the inner boundary condition for the AD equation, we assume a broken power-law energy distribution as used in Section 3,

$$n(r_{\rm s},E'_{\pm})=\begin{cases}\dfrac{n_0}{E_{\rm b}}\left(\dfrac{E'_{\pm}}{E_{\rm b}}\right)^{-p_1} & \left(E_{\rm min}<E'_{\pm}<E_{\rm b}\right)\\ \dfrac{n_0}{E_{\rm b}}\left(\dfrac{E'_{\pm}}{E_{\rm b}}\right)^{-p_2} & \left(E_{\rm b}<E'_{\pm}<E_{\rm max}\right)\end{cases}, \quad (5.21)$$

where n_0 is a normalization factor which is adjusted to be consistent with the boundary condition of the fluid equations, $E_{\rm b}$ is the intrinsic break energy, $E_{\rm min}$ and $E_{\rm max}$ are the minimum and maximum energy, respectively, and p_1 and p_2 are power-law indices for low- and high-energy potion of the particle spectrum, respectively. Hereafter, we also assume $p_1<2<p_2$, which implies that particles with energy $\sim E_{\rm min}$ dominate in the number of particles, and particles with energy $\sim E_{\rm b}$ dominate in the energy density of particles.

The density at the edge of the nebula depends on the flow velocity and diffusion coefficient outside the nebula, which are not considered in this paper. If the diffusion coefficient outside the nebula is very smaller than the inner value, particles pile up around the edge of the nebula. However, the diffusion coefficient in the ISM is larger than the value adopted in this paper, so that the pile-up case may be unlikely. Here we assume that the contribution of the re-entering particles from ISM/SNR is not so large. As the simplest case, we take an outer boundary condition,

$$\frac{\partial^2}{\partial r^2}\left[r^2n(r,E'_{\pm})\right]_{r=r_{\rm N}}=0. \quad (5.22)$$

This condition makes the density profile smoothly connect to the outside profile of the steady solution without advection, $n(r,E'_{\pm})\propto r^{-1}$.

The diffusion process in PWNe is highly uncertain. For simplicity, we assume that the energy dependence of κ is Kolmogorov-like as

$$\tilde{\kappa}(E_{\pm})=\kappa_0\left(\frac{E_{\pm}}{E_{\rm b}}\right)^{1/3}, \quad (5.23)$$

where the parameter κ_0 is constant.

The parameters other than the diffusion coefficient are the same as those in Chapter 3. As in Chapter 3, we assume that the minimum energy is fixed as $E_{\rm min} = 10 m_{\rm e} c^2$, and that the maximum energy $E_{\rm max}$ is defined as Equation 3.15. The nebula size $r_{\rm N}$ and the energy release rate, which is the same as the spin down luminosity $L_{\rm sd}$, are obtained from observation. In summary, the parameters to be adjusted are six: $r_{\rm s}$, σ, $E_{\rm b}$, p_1, p_2 and κ_0.

5.3 Detailed Calculation Method

Since the AD equation is 2-dimensional elliptic equation, it is solved using the finite difference method and the SOR method (e.g., Press et al., 1992). The fluid equations are integrated using a 4-th order Runge–Kutta method. Until the outputs from the fluid equations and the AD equation become consistent with each other, we iterate the calculation. All of results shown in this paper satisfy an accuracy of $\mathcal{O}(1)$ % in the energy/momentum conservation.

As for the spatial dependence of κ, the simplest model is the homogeneous diffusion with $\phi(r) = 1$. However, in such a case, the diffusion can influence the shock jump condition. The diffusion effect on the termination shock is beyond the scope of this paper. To avoid a complicated situation with a modified jump condition by diffusion, we neglect the effect of the diffusion near the termination shock. We turn on the diffusion effect at a certain radius $r_{\rm diff} > r_{\rm s}$. However, a sudden onset of the diffusion effect induces numerical instability. We assume an artificial function form as

$$\phi(r) = \frac{1}{2}\left[1 + \tanh\left(\frac{r - r_{\rm diff}}{\Delta r}\right)\right], \tag{5.24}$$

where Δr is a transition scale of the smoothing. This function smoothly changes from zero (for $r_{\rm diff} - r \gg \Delta r$) to unity (for $r - r_{\rm diff} \gg \Delta r$). The equation (5.24) is introduced just to avoid the technical issue in numerical calculation. As we will see later, the diffusion effect in the inner part of the nebula is negligible. As long as we take significantly small $r_{\rm diff}$ and Δr, the diffusion can be regarded as almost homogeneous, and the result does not depend on the details of this artificial functional form. The very weak dependence on $r_{\rm diff}$ and Δr in our results has been checked.

5.4 Parameter Dependence: diffusion coefficient

In this section, we show example results with various values of κ_0, and fixed values of the other parameters ($L_{\rm sd}$, $E_{\rm b}$, p_1, p_2, $r_{\rm s}$, $r_{\rm N}$ and σ). Here, to help understand the dependence on the κ_0, we define the length scale $r_{\rm pe}$ where the diffusion process begins to become effective for the energetically dominating particles, whose energy is $E_{\rm b}$, by

$$r_{\rm pe} \equiv \frac{r_{\rm s}^2 c u_{\rm d}}{2\kappa_0} \sim 5.0 \times 10^{18} \left(\frac{r_{\rm s}}{0.1\ {\rm pc}}\right)^2 \left(\frac{\kappa_0}{10^{26}\ {\rm cm^2\ s^{-1}}}\right)^{-1}\ {\rm cm}, \tag{5.25}$$

where $u_{\rm d}$ is the four speed of the flow at just downstream of the termination shock and approximately equal to $1/\sqrt{8}$ for $\sigma \ll 1$. This radius corresponds to the location where the advection and diffusion timescales are the same. This is obtained from the analytical steady state solution of advection diffusion equation assuming that the flow is incompressible and radial, the diffusion coefficient is uniform in space, and the cooling process is negligible. In this case, the advection-diffusion equation can be written as:

$$\frac{1}{r^2}\frac{d}{dr}\left[r^2\left(V_r n - \kappa \frac{dn}{dr}\right)\right] = 0. \tag{5.26}$$

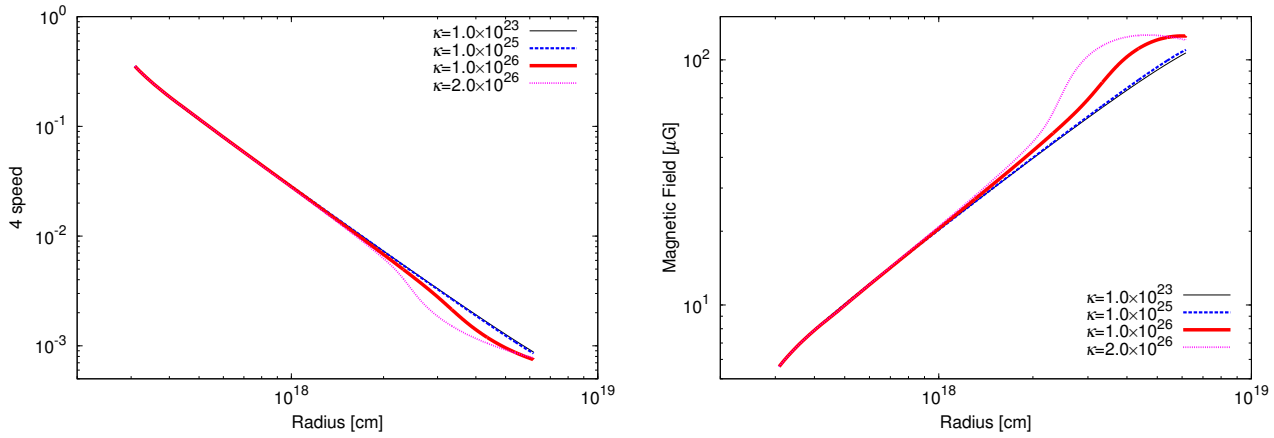

Figure 5.6: Radial profiles of 4-speed (Left) and magnetic field (Right) in the test calculations for various κ_0.

If we impose the boundary condition,

$$n(r = r_{\rm s}) = n_2 \quad , \quad n(r = \infty) = 0, \tag{5.27}$$

we can obtain the solution to the equation (5.26) as:

$$n(z) = n_2 \frac{1 - \exp\left(-P_e/z\right)}{1 - \exp\left(-P_e\right)} \tag{5.28}$$

where $z = r/r_{\rm s}$ and $P_e = r_s V_2/\kappa$ is Péclet number. From the derivative of Equation (5.28), it is shown that $r_{\rm pe}$ is the radius where the energy density of the pairs becomes decreasing.

In this section, the model of the inter stellar photon field is the same as for G21.5-0.9 (see Chapter 3). As an example, the parameter values other than κ_0 are set as $L_{\rm sd} = 10^{38}$ erg s^{-1}, $E_{\rm b} = 10^5 m_{\rm e}c^2$, $p_1 = 1.1$, $p_2 = 2.5$, $r_{\rm s} = 0.1$ pc, $r_{\rm N} = 2.0$ pc and $\sigma = 10^{-4}$. We test changing κ_0 as 10^{23}, 10^{25}, 10^{26}, and 2×10^{26} cm^2 s^{-1}. We also set the parameters in equation (25) as $r_{\rm diff} = 0.14$ pc and $\Delta r = 0.001$ pc.

The case of $\kappa_0 = 10^{23}$ cm^2 s^{-1} is almost the same as the KC model, in which the diffusion is negligible ($r_{\rm pe} \gg r_{\rm N}$). In Figure 5.6, it is shown that the wind is decelerated at outer region as κ_0 increases. Accordingly, the magnetic field is amplified conserving the value of $r\beta B$.

As the benchmark case, let us see the case of $\kappa_0 = 10^{26}$ cm^2 s^{-1} (red thick lines in Figure 5.6). The deviation from the lines for low κ_0 models is seen around $r = 3 \times 10^{18}$ cm. The radius of $r_{\rm pe}$ is consistent with this deceleration radius within a factor 2. As seen in Figure 5.7, at the deceleration radius the gas pressure also starts deviating from the KC model. Outside $r_{\rm pe}$ the gas pressure decreases steeper than the pressure profile in the KC model.

In spherically symmetric system, the particles basically diffuse outward, so that the diffusion flux brings out the fluid momentum outward. Since the fluid receives inward reaction force via particle diffusion, the fluid starts decelerating at $r = r_{\rm pe}$.

After the sudden deceleration by the diffusion, the deceleration the flow velocity is rather gradual. From the energy conservation law, we derive an analytically simple expression of the radial dependence of the velocity field and magnetic field in Figure 5.6. As shown in Figure 5.8, in the region of $r > 3 \times 10^{18}$ cm, the energy flux due to diffusion and the heat flux of the particles are

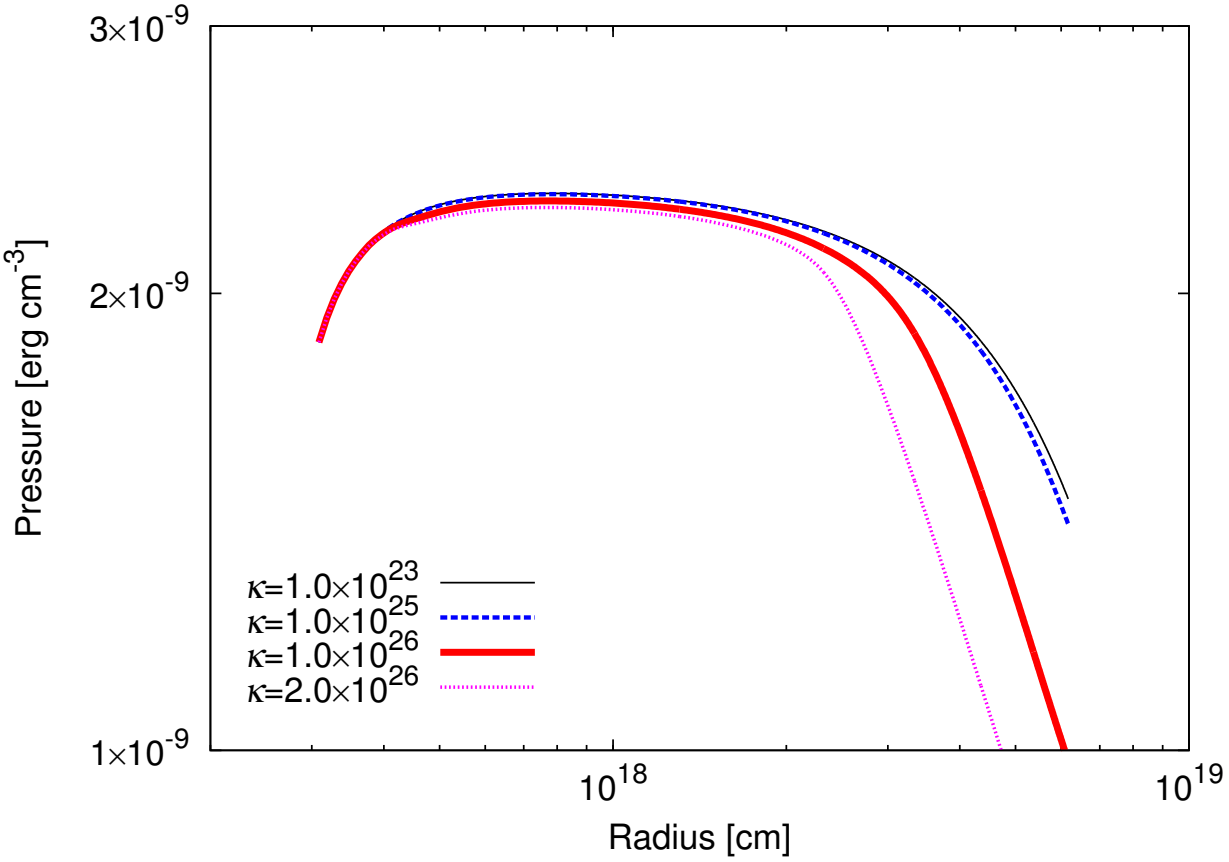

Figure 5.7: Radial profiles of gas pressure in the test calculations for various κ_0.

balanced, that is

$$\gamma^2 (\epsilon + P) \beta \sim \frac{\partial}{\partial r} \left[\left(\frac{4}{3} \gamma^2 \beta^2 + 1 \right) \tilde{\delta} \right]. \tag{5.29}$$

For r outside 3×10^{18} cm, as we can approximate $\beta \ll 1$, $\gamma \sim 1$ and $\delta \sim \kappa\epsilon$, thus $\beta \propto r^{-1}$ and $B \propto r^0$ are derived. This simple estimate is consistent with the behavior in our calculation result.

The energy spectrum of particles in the benchmark case is indicated by a red thick line in Figure 5.9. As we have expected, in the benchmark case, the spectral shapes show that the low-energy particles with $E'_\pm \sim E_{\rm min}$ are not affected by the diffusion, which modifies the spectrum above $E'_\pm \sim E_{\rm b}$. The black dotted line is the result of the KC model written for comparison. Since, in the KC model, all particles are moving with the fluid, they exhaust their energy all at once at the radius where the advection time equal to the cooling time. This results to appear as a cutoff shape in the spectrum in the KC model. In contrast, in the benchmark case, the energy spectrum does not show the cutoff shape like the KC model. This is because the time required getting to each radius from $r = r_{\rm s}$ is various due to the stochastic aspect of the diffusion. As shown in the line labeled $r = r_{\rm N}$ in Figure 5.9, particles with $E \sim 10^{13}$ eV exist in the benchmark case, while such particles can not exist at $r = r_{\rm N}$ in the KC model. In this calculation, since we impose the condition that particles stream out freely as a boundary condition at $r = r_{\rm N}$, particles with higher energy escape out the nebula more efficiently via the diffusion. As a result, the number of the high energy particles decrease, and so the energy spectrum of particles becomes soft. This behavior is consistent with the result of the time-dependent one-zone model constructed by Martín et al. (2012), which

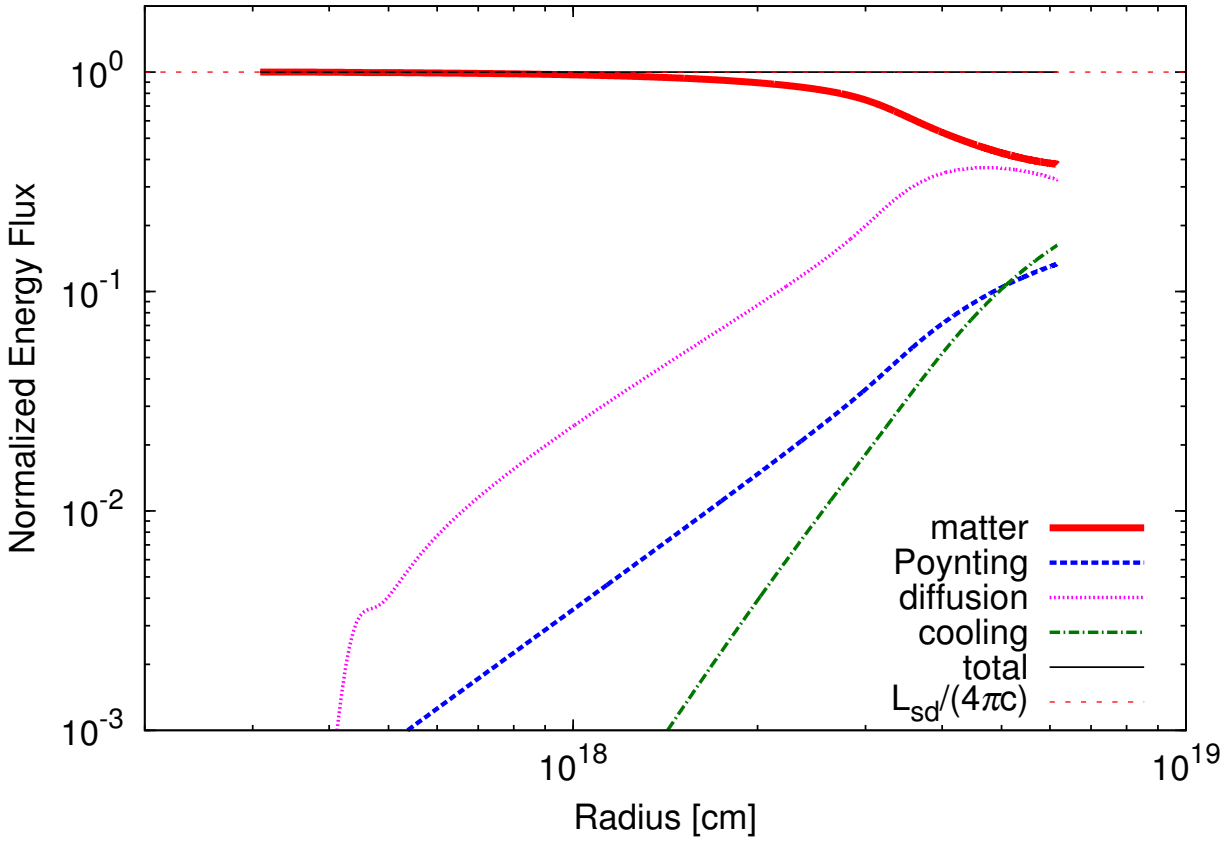

Figure 5.8: The radial profiles of the energy flow outward through the area of $4\pi r^2$ per unit time normalized by the value at the $r = r_s$ for the case of $\kappa_0 = 10^{26}\mathrm{cm}^2\ \mathrm{s}^{-1}$. The line labeled "cooling" is the total amount of synchrotron radiation per unit time emitted inside the radius r divided by $4\pi c$.

takes into account the diffusion effect as a particle escape from the nebula.

Figure 5.9 shows the evolution of the particle energy spectrum for the benchmark case comparing with the KC model. As we have expected, in the benchmark case, the spectral shapes show that the low-energy particles with $E'_{\pm} \sim E_{\mathrm{min}}$ are not affected by the diffusion, which modifies the spectrum above $E'_{\pm} \sim E_{\mathrm{b}}$. In the KC model, the sudden cooling cutoff of the spectrum shifts to lower energy with the radius. In contrast, in a model with diffusion, the energy spectrum does not show a clear cutoff shape. The energy dependence of the diffusion time eliminates the sharp cutoff feature. As shown in the line labeled $r = r_{\mathrm{N}}$ in Figure 5.9, particles with $E \sim 10^{13}$ eV, which are main population responsible for emitting X-rays, exist in the benchmark case, while such particles can not exist at $r = r_{\mathrm{N}}$ in the KC model. In our calculation, particles with higher energy escape through the boundary $r = r_{\mathrm{N}}$ more efficiently via the diffusion. As a result, given the radius r, the spectrum with the diffusion effect becomes softer than the KC model spectrum. This behavior is similar to the result of the time-dependent 1-zone model by Martín et al. (2012), which takes into account the diffusive escape from the nebula. The spectral softening due to particle diffusion is the same mechanism as that seen in the cosmic-ray spectrum in our galactic plane (e.g. see Strong & Moskalenko, 1998).

The amplification of the magnetic field by the back-reaction of the diffusion also affects the

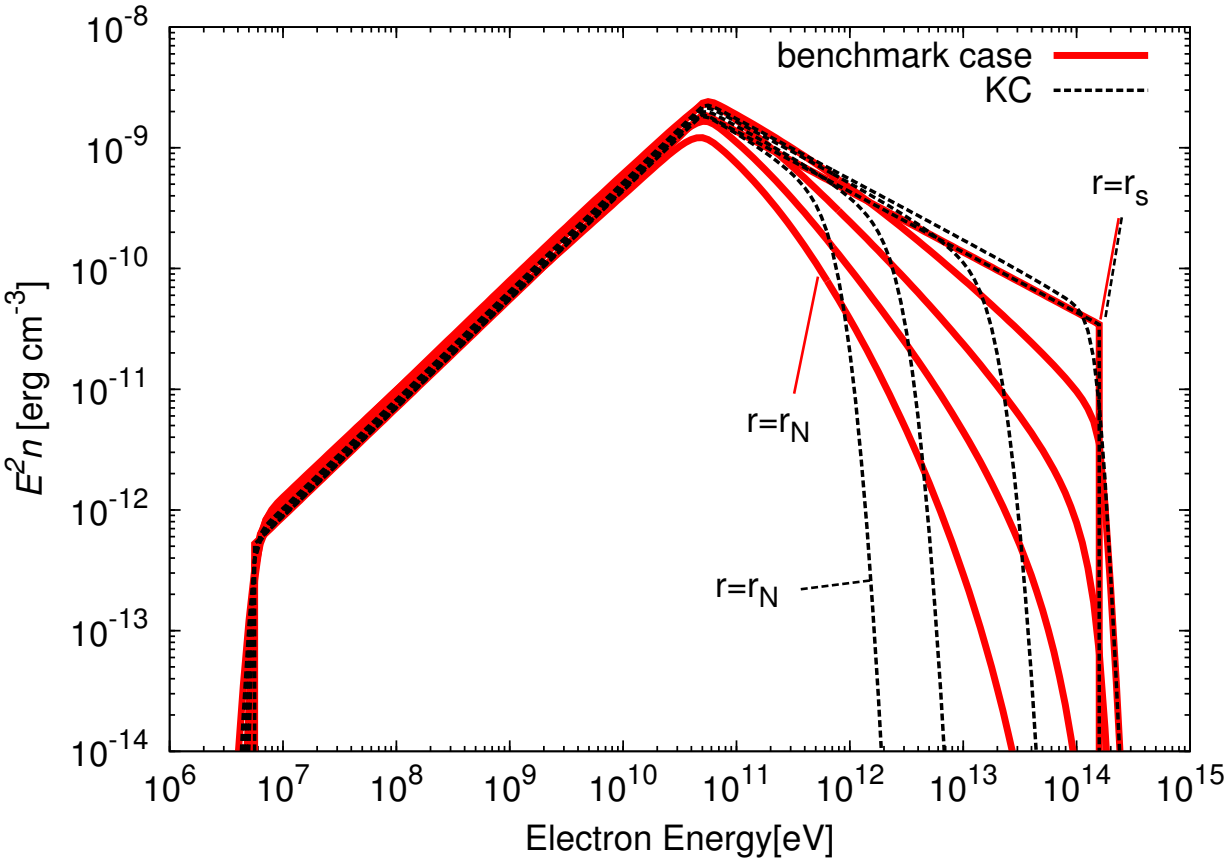

Figure 5.9: The energy spectrum of pairs at $r = r_{\rm s}$, $5r_{\rm s}$, $10r_{\rm s}$, $15r_{\rm s}$, and $r_{\rm N} = 20r_{\rm s}$. Red solid lines represent the model taking into account the diffusion, and black dashed line represent the KC model. The parameters are same as Fig. 5.8.

particle spectrum through the synchrotron cooling. As seen in Figure 5.6, in the benchmark case, the magnetic field is stronger than the KC model at any radius. Although the radiative cooling becomes more severe, the radius at which the particles are able to reach is not reduced. As the diffusion is more efficient for particles with higher energy, even if it receives the effect of strong radiative cooling, the particles are able to spread to outer side of the nebula. In addition, high energy particles are more likely to be distributed to the outer side of the nebula and emit synchrotron emission more efficiently, so that the spectrum of particles becomes more softer with increasing radius.

Based on the particle spectra shown in Figure 5.9 and the magnetic field shown in Figure 5.6, we can calculate the emission from the nebula. For the calculation of the emission, we adopt the same method in Chapter 3. We consider only synchrotron radiation and ICS including the Klein–Nishina effect. The model of the interstellar radiation field is taken from GALPROP v54.1 (Vladimirov et al., 2011, and references therein), in which the results of Porter & Strong (2005) are adopted.

Figure 5.10 shows entire spectra of the nebula for each κ_0, which calculated by using spectra of particles shown in Figure 5.9 and profiles of the magnetic field shown in Figure 5.6. In the case of $\kappa_0 = 10^{23}$ cm^2 s^{-1}, it is almost the same as the KC model. The entire spectrum of the benchmark case becomes harder than the KC model. As seen in Figure 5.9, the particle energy spectrum becomes softer with increasing radius. However, due to the strong magnetic field, synchrotron photons with the high frequency are efficiently emitted and the spectrum becomes hard. More

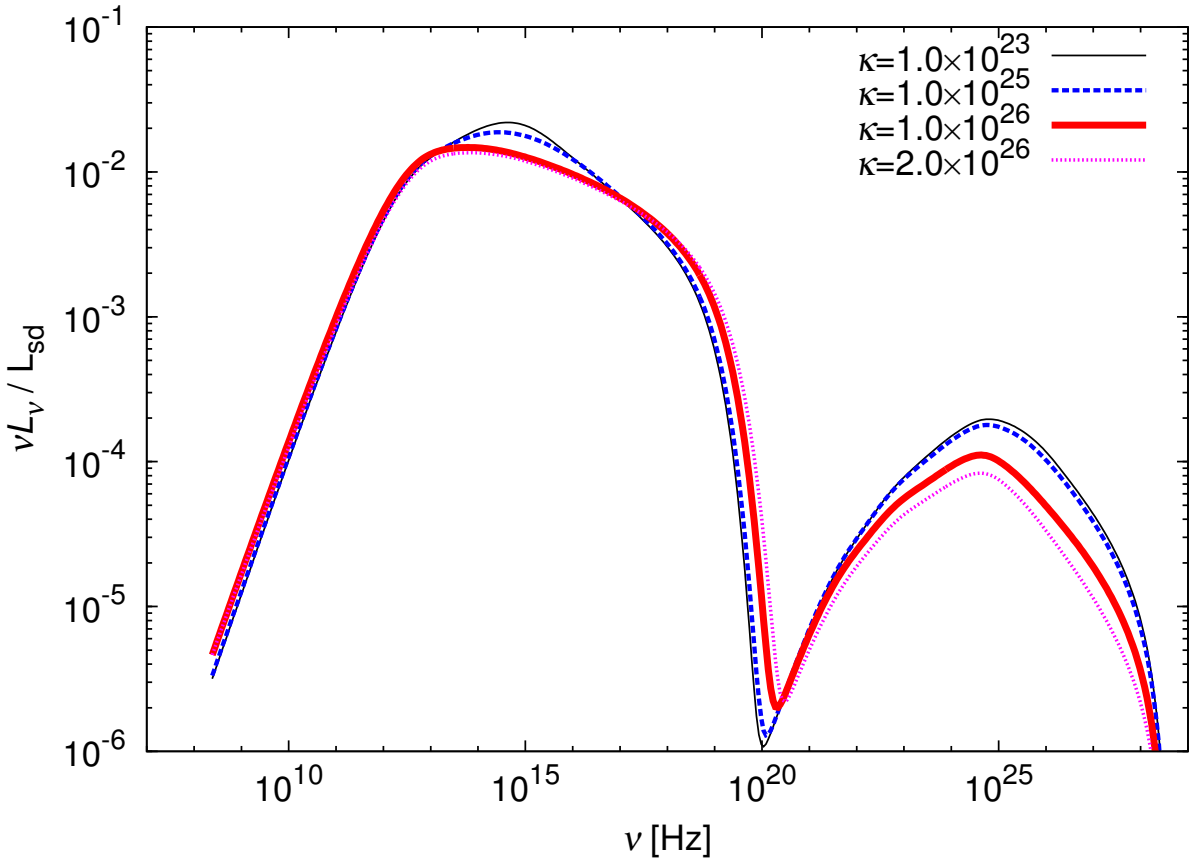

Figure 5.10: The entire photon spectrum calculated for various values of κ_0.

precisely, since the high energy particles are diffused to outside region, where the magnetic field is strong, high-energy synchrotron photons are efficiently emitted from the outer region. As a result, this mechanism hardens the integrated spectrum. On the other hand, the flux of the inverse Compton scattering monotonically decreases with increasing the diffusion coefficient κ_0. This is because as the diffusion coefficient increases, the particles escape efficiently. Here, we have neglected the emission outside the nebula so that the ICS flux decreases with κ_0.

In Figure 5.11, the X-ray surface brightness profile is shown. As expected, the size of X-ray emission region becomes larger with increasing κ_0. Although the case of $\kappa_0 = 10^{25}$ cm^2 s^{-1} almost agrees with the case of $\kappa_0 = 10^{23}$ cm^2 s^{-1} in Figure 5.6, clear differences are seen in the radial profile of X-rays. This is because the diffusion is starting to be effective for a part of particles having energy such as emitting X-rays for $\kappa_0 = 10^{25}$ cm^2 s^{-1} case. In the benchmark case, the emission region of X-rays extends to the edge of the nebula, where the magnetic field is strong. In the case of $\kappa_0 = 2 \times 10^{26}$ cm^2 s^{-1}, where diffusion is more effective than the benchmark case, a peak in the X-ray surface brightness is observed around 100". The peak radius roughly corresponds to the radius at which the magnetic field amplification is finished. Outside the peak radius, the effect of radiative cooling becomes efficient, so that it is considered that a peak-like structure in brightness profile can be formed. Additionally, the radial profile of the photon index in X-rays is also shown in Figure 5.12. For all the cases, the photon index shows a softening with increasing radius. The sudden softening in the radial profile of the X-ray photon index of the KC model, which is considered a problem with Reynolds (2003) or Slane et al. (2004), is improved by taking

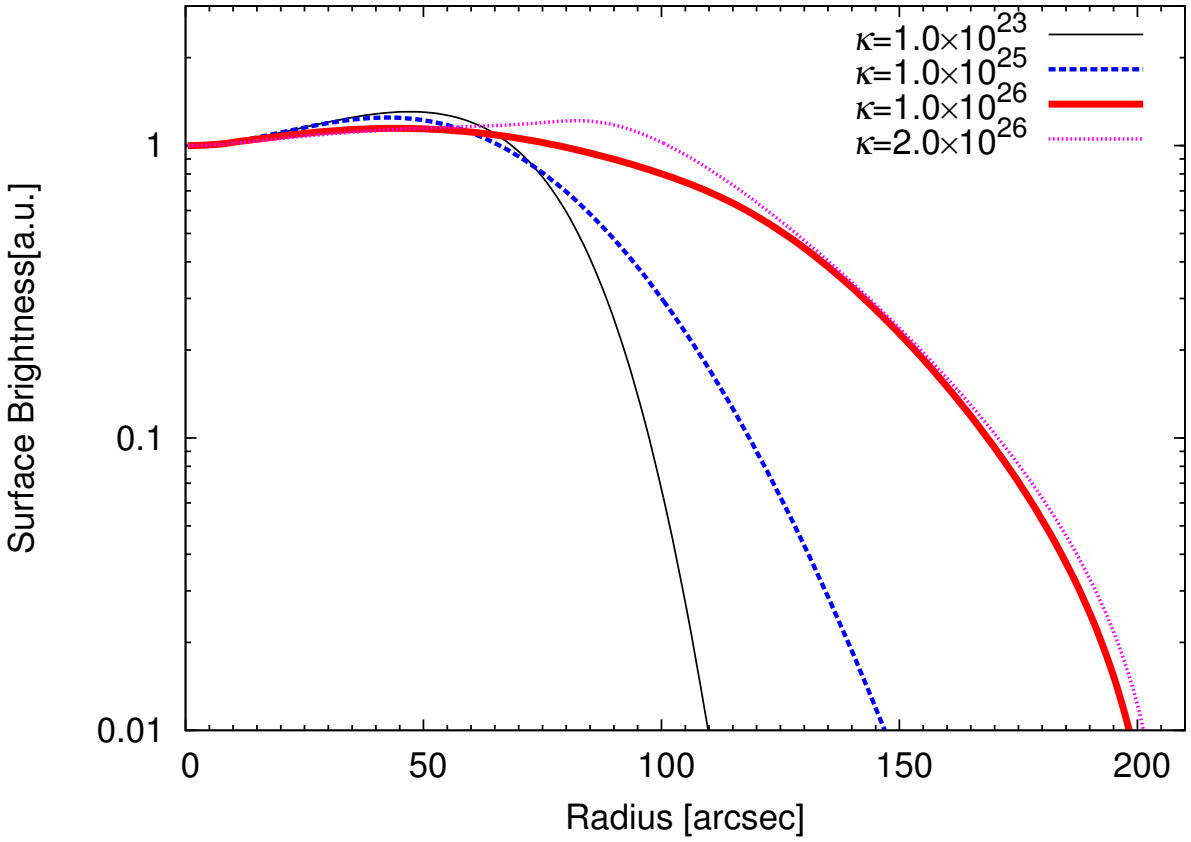

Figure 5.11: The dependence on the κ_0 of the X-ray surface brightness profile for 0.5-10 keV range. Here we assume that the distance to the nebula is 2 kpc. The edge of the nebula $r_{\rm N}$ is corresponding to 200″.

into account the spatial diffusion. Furthermore, the photon index is kept harder as κ_0 is larger. The sudden softening at a certain radius in the KC model (Reynolds, 2003; Slane et al., 2004) is not seen in our diffusion models.

Finally, in order to investigate how much the reaction of diffusion affects the emission of the nebula, we compare the calculations with and without the back reaction of diffusion to the fluid. The model without the back reaction is obtained solving the AD equation with $\kappa_0 = 10^{26}$ cm^2 s^{-1} for the given velocity field in the KC model. In this case, the energy and momentum conservations are not ensured. In Figure 5.13, the entire spectrum and the X-ray surface brightness are compared with those of the benchmark model and KC model ($\kappa_0 = 0$). If the back-reaction is not taken into consideration, since the magnetic field is not amplified, the synchrotron component is estimated about 2 times darker in the entire spectrum. Moreover, since the flow velocity is decelerated in the benchmark case, the advection time in the benchmark case is longer than that in the KC model. Due to the stronger magnetic field and the longer advection time, the spectral peak, which corresponds to the cooling break, appears at lower frequency than the case without the back reaction. On the other hand, there is not much difference in the X-ray surface brightness. Considering the back-reaction, the emission region concentrates only a little at the center, because the magnetic field amplifies and radiative cooling becomes efficient.

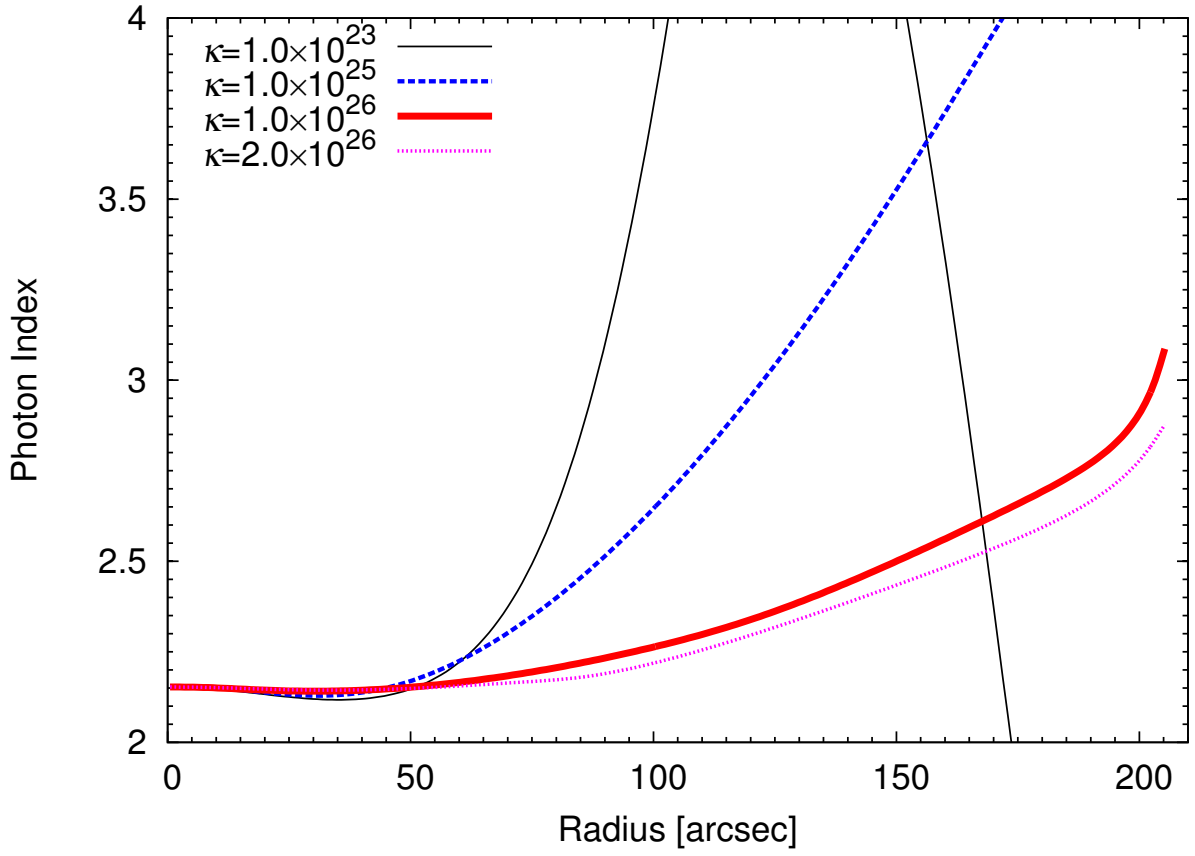

Figure 5.12: The dependence on the κ_0 of the photon index profile for 0.5-10 keV range. The distance and the nebula size are the same as those in Fig. 5.11

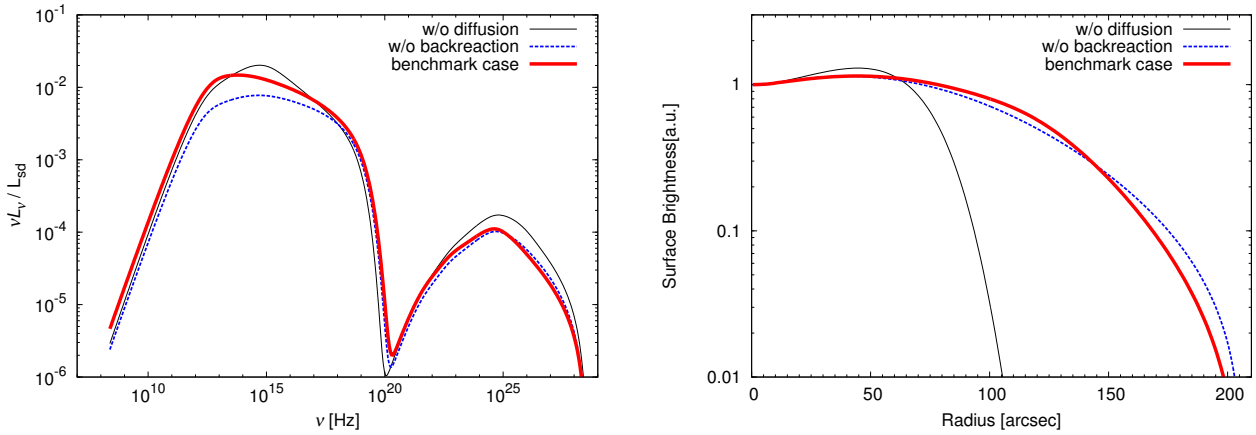

Figure 5.13: Comparison of the self-consistent model (benchmark model, red thick), the diffusion model without the back reaction (blue dashed), and the KC model (black thin).(Left) The entire spectra. (Right) The X-ray surface brightness for 0.5-10 keV range. The diffusion coefficient is commonly $\kappa_0 = 10^{26}$ cm^2 s^{-1} for the self-consistent model and the model without the back reaction.

Table 5.1: Parameters in our calculations.

		3C 58		G21.5-0.9	
Given Parameters	Symbol	KC[a]	DF	KC[a]	DF
Spin-down Luminosity (erg s^{-1})	L_{sd}	3.0×10^{37}		3.5×10^{37}	
Distance (kpc)	D	2.0[b]		4.8[c]	
Radius of the nebula (pc)	r_N	2.0		0.9	
Fitting Parameters					
Break Energy (eV)	E_b	4.1×10^{10}	3.0×10^{10}	2.6×10^{10}	6.0×10^{10}
Low-energy power-law index	p_1	1.26	1.08	1.1	1.2
High-energy power-law index	p_2	3.0	2.9	2.3	2.5
Radius of the termination shock (pc)	r_s	0.13	0.14	0.05	0.05
Magnetization parameter	σ	1.0×10^{-4}	2.0×10^{-4}	2.0×10^{-4}	6.0×10^{-4}
Diffusion coefficient at E_b (cm^2 s^{-1})	κ_0	-	1.0×10^{26}	-	1.0×10^{26}
Obtained Parameters					
Initial bulk Lorentz factor	γ_u	7.3×10^3	2.4×10^4	2.1×10^4	1.9×10^4
Pre-shock density (cm^{-3})	n_u	1.1×10^{-11}	2.7×10^{-12}	1.1×10^{-11}	1.3×10^{-11}
Pre-shock magnetic field (μG)	B_u	0.79	1.0	3.1	5.4
Maximum energy (eV)	E_{max}	9.5×10^{13}	1.3×10^{14}	1.4×10^{14}	2.5×10^{14}
Average magnetic field (μG)	B_{ave}	31	34	120	133
Advection time (year)	t_{adv}	1500	1300	800	630
Flow velocity at $r = r_N$ (km s^{-1})		490	540	460	720
Ratio of r_{pe} to r_N	r_{pe}/r_N	-	3.2	-	0.91

[a] The parameter of the broadband model shown in Chapter 3; [b] Kothes (2013); [c] Tian & Leahy (2008).

5.5 Application to the Observed Source

In this section, we apply our model to the two PWNe 3C58 and G21.5-0.9, for which we have rich observational data especially in X-rays. Observational properties of these PWNe are summarized in Table 5.1 (see Chapter 3 for detail). In these objects, for parameter sets that reproduce the entire spectra, the extent of X-rays in the KC model inconsistently becomes smaller than the observed extent.

As discussed in Chapter 3, the spectral indices of the observed spectra in X-rays can not be reproduced by the KC model. If parameters are adjusted to reconcile the X-ray spectral index, the IR/Opt and radio emission can not be reproduced. Below we discuss whether the diffusion effects can resolve those problems or not. Hereafter we call the model with diffusion the DF model.

The model parameters and results are summarized in Table 5.1. For comparison, we also show the result of "broadband model" in Chapter 3 (denoted "KC" in Table 5.1), in which the diffusion effect is not incorporated. For each object, despite the fact that the wind is more decelerating in the DF model, the advection time in the DF model is shorter than that in the KC model. This is because σ in the DF model is larger than that of the KC model. Furthermore, we also calculate the ratio of r_{pe} to r_N, which is a measure of the effectiveness of diffusion. For 3C 58, since $r_{pe}/r_N > 1$, the diffusion has not much effect on fluid motion. In contrast, in the case of G21.5-0.9, r_{pe}/r_N is smaller than unity, this indicates that diffusion is efficient with this parameter set. For the DF models, we adjusted the parameters in equation (5.24) as $|r_{diff} - r_s| \leq 0.03 r_N$ and $\Delta r \leq 0.008 r_N$. Those small values may not affect the results largely.

In Figure 5.14, the obtained radial profiles of 4-speed and the magnetic field are shown. As expected from the value of r_{pe}/r_N, $u(r)$ in 3C 58 shows an almost the same profile as the KC model profile.

In G21.5-0.9, a modification of $u(r)$ due to the diffusion is seen. For $r > 10^{18}$ cm, since the

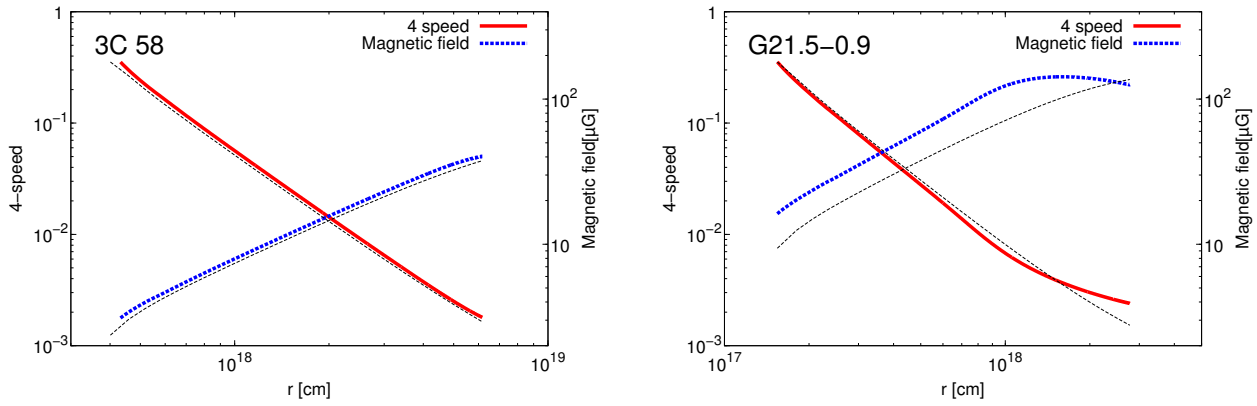

Figure 5.14: Radial profiles of the 4-speed $u(r)$ (left axis) and the magnetic field $B(r)$ (right axis) in the DF model (see Table 5.1) for 3C 58 (left panel) and G21.5-0.9 (right panel). The dashed black line represents the radial profiles for the KC model.

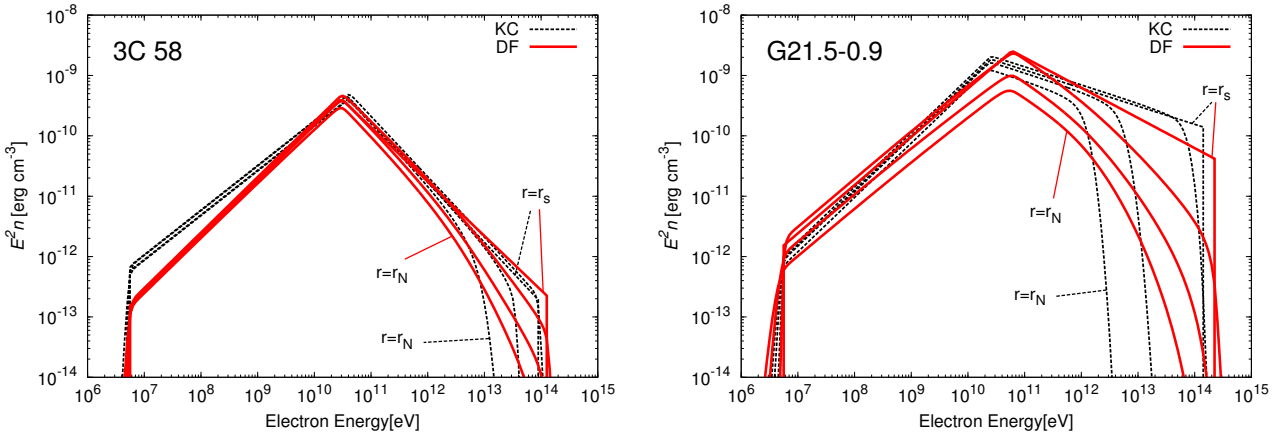

Figure 5.15: The particle energy spectra for 3C 58 (left panel) and G21.5-0.9 (right panel) in the DF (red solid) and KC (black dashed) models. The different lines show the hard-to-soft evolutions: $r = r_{\rm s}$, $5r_{\rm s}$, $10r_{\rm s}$, $r_{\rm N} \simeq 15r_{\rm s}$ for 3C 58, and $r = r_{\rm s}$, $6r_{\rm s}$, $12r_{\rm s}$, $r_{\rm N} = 18r_{\rm s}$ for G21.5-0.9.

magnetic pressure is large, the deceleration and amplification of the magnetic field are almost saturated. Despite the high-σ and amplification of the magnetic field, the magnitude of the average magnetic field is not so different between the DF model and the KC model, because the volume-averaged magnetic field is largely controlled by the field near the edge of the nebula, which are almost the same in the two models.

For the DF model, obtained flow velocity at the edge of the nebula is 540 km s^{-1} and 720 km s^{-1} for 3C 58 and G21.5-0.9, respectively. These value are roughly consistent with the observed expansion speed 400 km s^{-1} and 870 km s^{-1} for 3C 58 (Bietenholz, 2006) and G21.5-0.9 (Bietenholz & Bartel, 2008), respectively.

Figure 5.15 shows energy spectra of pairs for 3C 58 and G21.5-0.9, and Figure 5.16 shows the

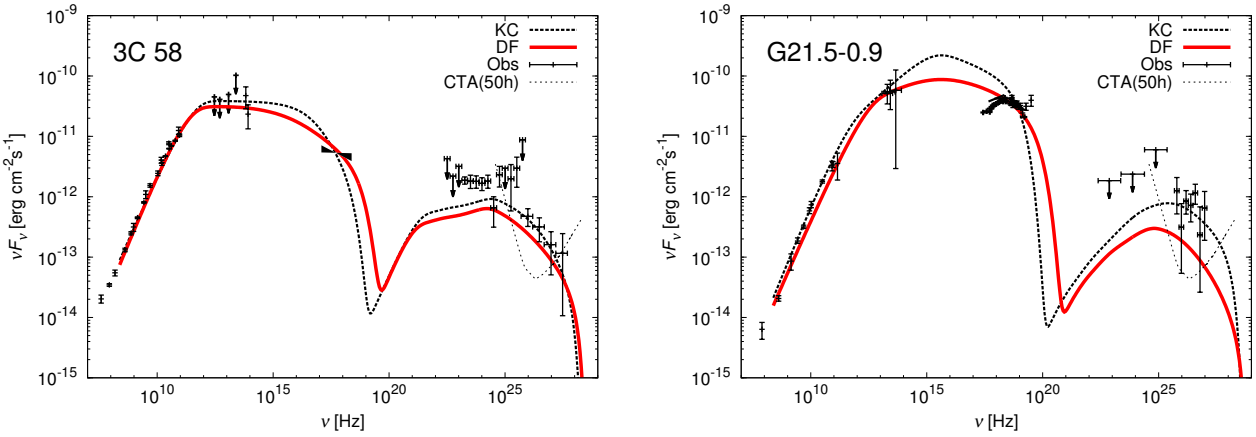

Figure 5.16: Entire photon spectra for 3C 58 (left panel) and G21.5-0.9 (right panel). The red line represents the DF model, and the black line represents the KC model calculated with the "broadband model" parameter in Chapter 3. The data points are taken from Weiland et al. (2011) (radio), Green (1994), Slane et al. (2008) (IR), Torii et al. (2000) (X), Li et al. (2018) (GeV), and Aleksić et al. (2014) (TeV) for 3C 58, and Salter et al. (1989) (Radio), Gallant & Tuffs (1998) (IR), Tsujimoto et al. (2011), Nynka et al. (2014), de Rosa et al. (2009), Hitomi Collaboration et al. (2018) (X), Ackermann et al. (2011) (GeV), and Djannati-Ataï et al. (2008) (TeV) for G21.5-0.9.

entire spectra obtained from these particle spectra. First, for both the cases, the diffusion is not effective for particles at $E'_\pm \sim E_{\rm min}$, so the treatment with the fluid picture, as mentioned in Section 5.2, is justified. In 3C 58, although the diffusion is not effective for particles with $E'_\pm \sim E_{\rm b}$, the particle spectrum above 10^{13} eV is significantly modified by diffusion. Thus, the cutoff shape in the energy spectrum like the KC model does not appear in the DF model, rather it becomes a shape that softens smoothly with the radius. In the DF model, since high energy particles are exist also in the strong magnetic field region where such particles can not exist due to radiative cooling in the KC model, so the DF model produces a harder entire spectrum. As a result, despite the fact that the injection spectrum of particle changed little, the hard spectrum observed in X-ray is able to reproduced. Thus, just considering the weak diffusion that does not affect the fluid motion, the entire spectrum changes greatly from the KC model.

In the DF model of G21.5-0.9, which is the case where diffusion is more effective than the case of 3C 58, not only the effect of diffusion seen in 3C 58 case but also the effect of changing the profile of the fluid can be seen. As shown in Figure 5.14, the velocity field decelerates more shallowly than r^{-2} outside $r \sim 10^{18}$ cm, so the adiabatic cooling becomes efficient. As a result, the energy spectrum of particles shows an evolution that all particles lose energy simultaneously with increasing radius. Moreover, the spectrum of the synchrotron radiation shifts to the higher frequency side due to the amplification of the magnetic field. The highest frequency X-ray of synchrotron radiation is emitted at the place where the magnetic field is most amplified, while the IR/Optical emission is most strongly emitted around the edge of the nebula. Although particles near the edge of the nebula lose energy with adiabatic cooling, whereas particles near the radius where the magnetic field is most amplified do not lose much energy by adiabatic cooling. Therefore the IR/Optical emission emitted inefficiently, so that the resulting entire spectrum being hard.

In the DF model, the fluxes of γ-rays in both objects are several times lower than the observation. However, considering the following two points, this discrepancy can be solved. The first is the

uncertainty of the interstellar photon field. The γ-rays are emitted mainly via the ICS with the infrared photon from the interstellar dust. Since the flux of the ICS is roughly proportional to the energy density of the seed photons, the γ-ray flux in our model is largely affected by the uncertainty of the inter stellar radiation field (e.g., Torres et al., 2013). In addition, the photon field model used in our calculations is a value in ordinary interstellar space, but the supernova remnants may be the site of dust formation (Kozasa et al., 2009), so that the intensity of the dust radiation may be different from ordinary interstellar space.

The second point is γ-ray emission from particles escaped out of the nebula. Recently, Abeysekara et al. (2017a) (HAWC) reported that around the Geminga there is a much larger γ-ray halo than the X-ray PWN. Even for MSH 15-52, whose age is comparable to that for G21.5-0.9 and 3C 58, diffuse γ-ray emission extending beyond X-rays was detected (Tsirou et al., 2017). Those facts suggest that electrons and positrons escape out of the PWN to the ISM. For example, an electron and a positron with energy $E_{\rm VHE} = 1.5 \times 10^{13}$ eV product γ-rays of ~ 1 TeV via the ICS with the CMB photons ($\sim 10^{-3}$ eV). For both fitting results, diffusion is more effective for such particles than advection. If such particles continuously escape out of the nebula by diffusion,[2] during the age of the nebula $\sim t_{\rm adv}$, the number of escaped particles is $N_{\rm esc} \sim 4\pi r_{\rm N}^2 (\kappa(E_{\rm VHE})/r_{\rm N}) E_{\rm VHE} n(r_{\rm N}, E_{\rm VHE}) t_{\rm adv}$. Roughly adopting $E_{\rm VHE}^2 n = 10^{-13}$ erg cm^{-3} (10^{-12} erg cm^{-3}) for 3C 58 (G21.5-0.9), the number is estimated as $N_{\rm esc} \sim 10^{43}$ for both PWNe. The energy release rate via ICS with the CMB photons is $\sim 10^{-11}$ erg s^{-1} per particle. Then, the γ-ray flux from escaped particles is estimated as comparable to the flux inside the nebula for both the cases. The observed gamma-ray fluxes in Figure 5.16 may include both the components inside and outside the nebula. Assuming the same diffusion coefficient inside and outside the nebula (see section 5.6), the extent of γ-rays is estimated as $\sim r_{\rm N} + \sqrt{\kappa t_{\rm adv}}$, which is ~ 4 pc ($400''$) for 3C 58, and ~ 2 pc ($90''$) for G21.5-0.9, respectively.

In G21.5-0.9, a spectral break around a few keV is reported by Nynka et al. (2014) (NuSTAR) and Hitomi Collaboration et al. (2018). Moreover, by using the time-dependent 1-zone model, Hitomi Collaboration et al. (2018) concluded that the spectral break is not reproduced under the conventional assumption of the particle injection and the energy loss processes. Also, if we try to explain this spectral break with a cooling break of a 1–D steady model, we need to take parameters like the "alternative model" shown in Chapter 3, then it is inconsistent with observation fact of the entire spectrum in radio and optical band and of the age of the nebula. Our model considers the diffusion process in addition to the spatial structure, but it was not eventually possible to reproduce this spectral break. Rather, the cooling break becomes smoother due to the diffusion process, so that it would be difficult to explain such a sharp break simply by considering the spatial diffusion process. If we seriously accept this spectral break, the alternative model without the diffusion in Chapter 3 would be better than the diffusion model.

The radial profile of the X-ray surface brightness is shown in red-thick line in Figure 5.17. All curves of the surface brightness of the model in the figure are normalized to be 1 at the center. Since the absolute value of the flux can be fitted in the entire spectrum, the observed value in Figure 5.17 is plotted by multiplying a constant multiple so that the result of integrating the surface brightness profile in the radial direction matches the observed value with the model line. Furthermore, as there is a possibility of contribution from the central pulsar, the observed values at the center of the surface brightness of both objects are excluded from the calculation. In both objects, since the X-rays extent to the edge of nebulae, it can be said that the observed data could be reproduced qualitatively. The observed X-ray profile of G21.5-0.9 is well reproduced quantitatively, but for 3C 58, it is not done well. The reason why the surface brightness of 3C 58 does not be quantitatively

[2] While higher energy particles can escape from the nebula, almost all (low-energy) particles are still confined inside the nebula.

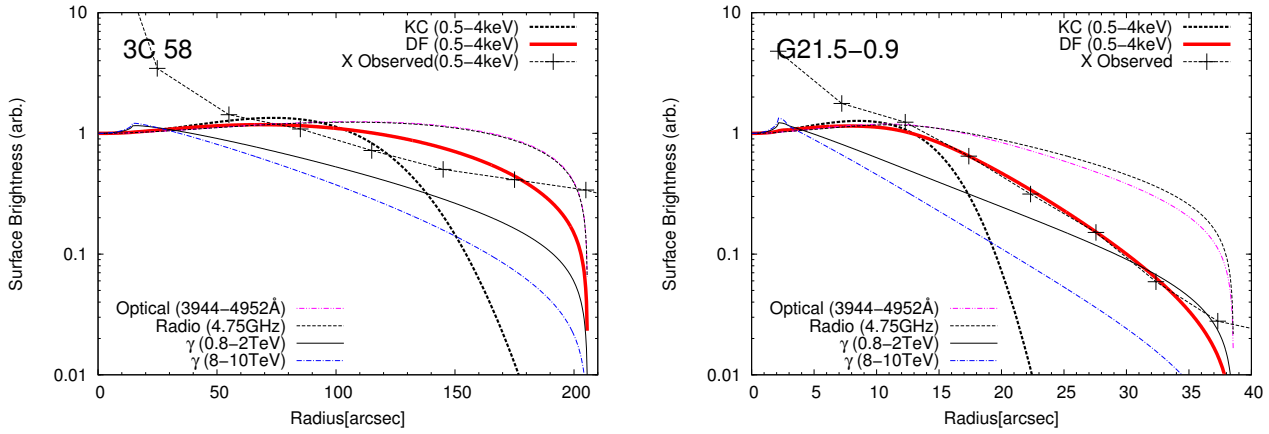

Figure 5.17: Radial profiles of the surface brightness of X-rays (3-5 keV; bold), radio (4.75GHz; dashed), optical (3944-4952Å; dashed double-dotted), 0.8-2 TeV γ-rays (thin) and 8-10 TeV γ-rays (dashed dotted). The red lines represent the DF model, and the thin black solid line represent the X-ray profile of the KC model. All curves are normalized as unity at the center. The data points are taken from Slane et al. (2004) (X) for 3C 58, and Bock et al. (2001) (radio) and Matheson & Safi-Harb (2005) (X) for G21.5-0.9.

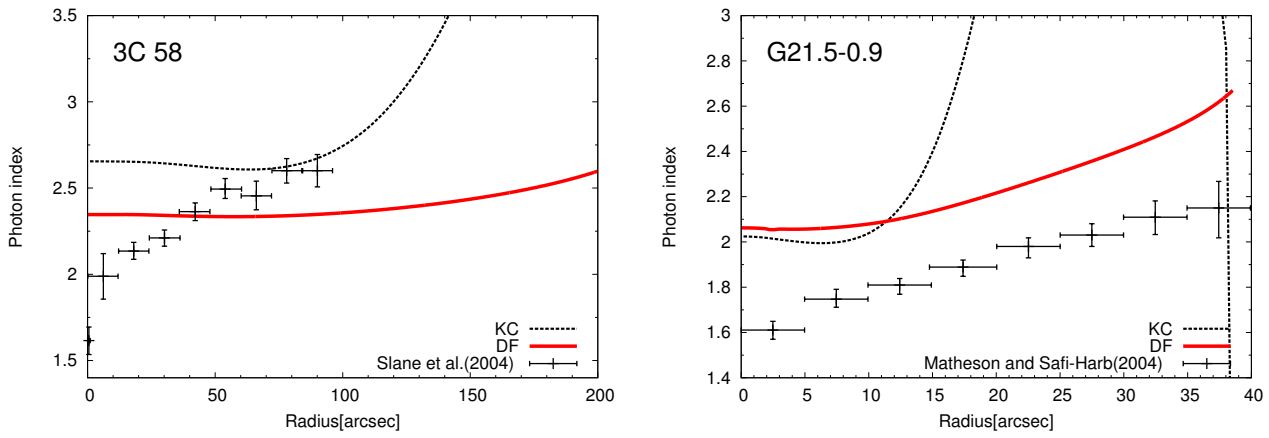

Figure 5.18: Radial profiles of the photon indices in 0.5-10.0 keV range in the DF model (red), and the KC model (black). The data points are taken from Slane et al. (2004) and Matheson & Safi-Harb (2005) for 3C 58 and G21.5-0.9, respectively.

reproduced is considered to be due to the possibility of contamination of X-rays from SNR and that spherical symmetric approximation is not appropriate. Note that, we also plot the surface brightness in radio (4.75 GHz), optical (3944-4952 Å), and γ-rays (0.8–2 TeV and 8–10 TeV). For radio and optical band, the surface brightness profile is almost spatially uniform and shows a profile that it becomes dim rapidly at the edge. For γ-rays, the width at half maximum of the size of the γ-ray emission region becomes the smaller with increasing energy of the observing γ-ray.

In Figure 5.18, the radial profile of photon index is shown. Although sudden softening in KC

model was solved, the observed values are not well reproduced quantitatively even with DF model. For 3C 58, the fact that the radial dependence of the photon index is not reproduced may be due to the same reason as in the case of the surface brightness that the shape is deviated from the spherical symmetry. On the other hand, for G21.5 - 0.9, the degree of softening in the radial direction is similar to the observation, but the absolute value is deviated.

5.6 Discussion

The escaped particles from the nebula also emit gamma-rays as detected from Geminga (Abeysekara et al., 2017a), where the diffusion coefficient outside the nebula is estimated as $\kappa(E = 100\ \mathrm{TeV}) \sim 2 \times 10^{27}\ \mathrm{cm}^2\ \mathrm{s}^{-1}$. This value is close to the values inside the nebulae in our model. Adopting the same diffusion coefficient outside the nebulae, our model yields the gamma-ray halo of $400''$ for 3C 58, and $90''$ for G21.5-0.9, respectively. The contribution from the halo emission may improve the dim gamma-ray fluxes in our model. We expect that a better angular resolution of CTA (Bernlöhr et al., 2013) will confirm an extended component around G21.5-0.9 and 3C 58.

The diffusion coefficients at $E_{\pm} \sim 10^{14}$ eV in our model for G21.5-0.9 and 3C 58 are consistent with the previous values in Porth et al. (2016) and Tang & Chevalier (2012). In other words, the effect of the back-reaction of the diffusion does not affect the parameter estimate so much in those objects ($r_{\mathrm{pe}}/r_{\mathrm{N}} \gtrsim 1$). However, it is not trivial whether the back-reaction affects significantly or not, in other cases.

Estimating the mean free path λ of a particle using $D = \lambda c/3$, it is about 0.05 pc in both objects. In the setting of this paper, since the diffusion of particles is perpendicular to the global magnetic field, the mean free path is given by $\lambda \sim r_{\mathrm{L}}(\delta B/B)^2$ within the framework of the quasi-linear theory of the resonant scattering (e.g., Blandford & Eichler, 1987), where r_{L} is the gyro radius of the particle and δB is the turbulence amplitude at the scale of $\sim r_{\mathrm{L}}$.. Our model parameter set implies $r_{\mathrm{L}} \sim 10^{-3}$ pc so that $\delta B/B > 1$ is required to achieve the value $\kappa \sim 10^{27}\ \mathrm{cm}^2\ \mathrm{s}^{-1}$ at 10^{14} eV, which indicates that the simple picture of the quasi-linear theory is no longer valid (cf. in the typical interstellar space, $\delta B/B \sim O(10^{-2})$ [3]). As discussed in Tang & Chevalier (2012), if the direction of the magnetic field deforms in the radial direction as seen in the Rayleigh–Taylor finger, the particles can diffuse efficiently in the radial direction. On the other hand, as proposed in Porth et al. (2016), the transport of particles due to the global vortex motion is also a candidate of an effective diffusion process. In this case, the energy dependence of the diffusion coefficient is very weak, such a model is different from ours. In this model, further assumptions are needed to consider the escape of particles from the nebula. Therefore, the value of the diffusion coefficient suggested by our model is not trivial. Besides diffusion, there may be other options for modifying the KC model.

As shown in Figure 5.18, the radial profile of the photon index in the DF model of G21.5-0.9 has deviated from the observed value in absolute value, but the degree of softening in the radial direction has been consistent with observation. The deviation of the absolute value suggests that the index of injection spectrum is different in the first place. It also supports this that the spectral index of soft X-ray of the entire spectrum is not explained. As we discussed in Section **??**, it is difficult to reproduce the observed spectral break of several keV with only the effects of cooling and diffusion, which suggests that there is a more complex structure in the injection spectrum. As one possibility to explain this, there are ideas that particles emitting radio and IR/optical and particles emitting X-rays have different origins, as proposed by Tanaka & Asano (2017) (and also proposed in Chapter 3.). An observation focusing on the morphology coincidence in radio and IR/optical will

[3] This is estimated assuming the parallel diffusion (e.g., Strong et al., 2007).

be a clue as to which frequencies of the entire spectrum are emitted from the same component.

In this model, for simplicity, we have adopted a uniform diffusion coefficient. If we consider the spatial dependence of the diffusion coefficient, a more sophisticated model to explain the observed properties may be possible. In order to establish such a model, study for both the microscopic plasma waves and hydrodynamic turbulence should be promoted. Furthermore, a detailed investigation of the escape process from the nebula is also required. Since particles escape through the contact discontinuity to the SNR, the turbulence near $r = r_{\rm N}$ as the result of the interaction between the SNR and the PWN is important.

5.7 Conclusion

In this work, in order to consider the spatial diffusion process in the 1–D steady model of PWNe, we have formulated the transport equation of non-thermal pairs and the fluid equations. In the model of PWNe, since the random-walking non-thermal particles also constitute the "background fluid" that is the reference of the diffusion, we have made the definition of the fluid frame clear and derived the fluid equations with careful treatment of the diffusion. Furthermore, we have numerically calculated these equations for 1–D steady PWNe, and investigated the dependence on the diffusion coefficient of the fluid structure (the velocity field and the magnetic field), the entire spectrum and the radial profile of the surface brightness in X-ray. With increasing the diffusion coefficient, the entire spectrum becomes harder, and the X-ray surface brightness extents larger. For the fluid structure, we have found that the diffusion process causes the deceleration of the flow by the back reaction of diffusion. The deceleration leads to amplification of the magnetic field, and influences the energy distribution of particles through radiation cooling nonlinearly.

We have applied this model to 3C 58 and G21.5-0.9, which had been pointed out that the observed entire spectra and X-ray profiles can not be reproduced simultaneously by KC model. For these objects, entire spectra and X-ray surface brightness have been almost reproduced simultaneously. This is the first attempt to reproduce both entire spectra and X-ray surface brightness with diffusion effect. Roughly speaking, we have succeeded in reproducing them. However the γ-ray fluxes of entire spectra are the two times darker than the observed ones, and radial profiles of the photon index are slightly deviated from the observed data.

Chapter 6

Summary and Future Prospects

The rotation powered pulsar releases their rotation energy as a relativistic wind of electrons and positrons, called the pulsar wind. This relativistic outflow forms a shock structure via the interaction with the surrounding medium. Such a shocked wind spread around the pulsar is called the pulsar wind nebula.

The observed radial profiles of the X-ray emission from Pulsar Wind Nebulae (PWNe) have been claimed to conflict with the standard one-dimensional (1-D) steady model, called the KC model. However, the KC model has not been tested to reproduce both the volume-integrated spectrum and the radial profile of the surface brightness, simultaneously. Our aim is to construct a consistent model of the radial profile and emission in PWNe.

We revisited the 1-D steady model and apply it to the Crab nebula, 3C 58 and G21.5-0.9. We found that the parameters of the pulsar wind, the radius of the termination shock $r_{\rm s}$ and magnetization σ, greatly affect both the photon spectrum and radial profile of the emission. We had shown that the parameters constrained by the entire spectrum lead to a smaller X-ray nebula than observed one. We had also tested the case that reproduces only the observations in X and gamma-rays, ignoring the radio and optical components. In this case, there are parameter sets that reproduce both the spectrum and emission profile, but the advection time to the edge of the nebula becomes much smaller than the age. Our detailed discussion clarified that the KC model has severe difficulty to reproduce both the volume-integrated spectrum and the surface brightness simultaneously. This implies that the model should be improved by taking into account extra physical processes such as temporal evolution of the nebula or spatial diffusion of particles. Additionally, we calculated the surface brightness profile of the radio, optical and TeV gamma-rays. The future observations in these wavelengths are also important to probe the spatial distributions of the relativistic plasma and the magnetic field of PWNe.

Since we found that the KC model has difficulty in reproducing the entire spectrum and the X-ray surface brightness simultaneously, we discuss improvement of the KC model. The main assumptions in the KC model are steady state, spherical symmetry and toroidal magnetic field configuration. In Chapter 4, we investigated the validity of the steady-state approximation of the nebula. We solved the time-dependent and spherical symmetric MHD equations taking into account the effect of the spin-down evolution of the central pulsar and the surrounding SNR. Although the steady KC model ignores the time-dependent effect, it showed a very good agreement on both the fluid structure and the emission calculated in the time-dependent 1-D model.

Therefore, we next considered a model that changed the assumption of toroidal magnetic field configuration from the KC model. Namely, in addition to the ordered toroidal field, we considered a turbulent magnetic field to be present, and constructed a model that includes the diffusion process, which is not considered in the KC model in the particle transport process. The previous studies

adopted a large diffusion coefficient that makes diffusion more efficient than advection in order to reproduce the large extent of the X-ray. In such a case, since the pressure profile of the fluid changes significantly, the hydrodynamic structure in the PWN may change. In Chapter 5, we presented a PWN model solving both advection and diffusion of non-thermal particles in a self-consistent way to satisfy the momentum and energy conservation laws. Assuming spherically symmetric (1–D) steady outflow, we calculated the emission spectrum integrating over the entire nebula and the radial profile of the surface brightness. We found that the back reaction of the particle diffusion modifies the flow profile. The photon spectrum and the surface brightness profile are different from the model calculations without the back reaction of the particle diffusion. Our model had been applied to the two well-studied PWNe 3C 58 and G21.5-0.9. By fitting the spectra of these PWNe, we determined the parameter sets and calculate the radial profiles of X-ray surface brightness. For both the objects, obtained profiles of X-ray surface brightness and photon index are well consistent with observations. Our model suggests that particles escaped from the nebula significantly contribute to the gamma-ray flux. A γ-ray halo larger than the radio nebula has been predicted in our model.

The extent of the X-ray emission region is as large as that of the radio in 3C 58 and G21.5-0.9, which can not be explained by KC model. Therefore the spatial diffusion seems indispensable to reproduce the X-ray extent. The time-dependent effect is not important for solving the problem of X-ray extent, but is important for the middle and old aged PWNe due to the interaction between the PWN and the SNR reverse shock.

Spatially resolved observation with very high energy γ-rays is important for verifying the diffusion model. CTA telescope currently under construction is expected to achieve a better angular resolution ($\sim \mathcal{O}(10)''$), which is sufficient to confirm the presence or absence of a predicted γ-ray halo predicted by the diffusion model. Furthermore, for the case of 3C 58, CTA might be spatially resolve. The surface brightness in the synchrotron band, the information of the energy density of the particle and the magnetic field strength are degenerate, whereas the surface brightness of the γ-ray is not related to the magnetic field. Thus, measuring the surface brightness of γ-ray emission in detail is very important for unlocking degeneracy. Also, unlike the Cherenkov telescope, HAWC is good at detecting largely extended sources. For several old pulsar wind nebulae including Geminga, γ-ray halos have been detected. If this is also found about young objects, pulsars efficiently emit electrons and positrons into the interstellar space, which also have an impact on the research of cosmic-rays.

Observation by hard X-ray and soft γ-ray are also important in the sense of observing emission from the highest energy electrons in the nebula. The observation of SED in such energy band corresponds to examining the acceleration limit of the particle. Since this is linked to the strength of the magnetic field at the termination shock, we can constrain the sigma parameter better. If the SED does not show a cutoff shape with higher energy than the energy determined from fitted SED suggested by σ, this will also pose a new problem for the PWNe model. It is also important to observe spatially resolved observations, especially energy-dependent morphologies. For particles with higher energy, both radiative cooling and the diffusion effect become more efficient, so that we can verify the propagation process of particles in the PWNe more severely.

The specific physical process indicated by the value of diffusion coefficient obtained by us is still unclear. The obtained diffusion coefficient is a parameter that can not be treated in the quasi-linear approximation, so that it is significantly different from the naive understanding in cosmic-ray diffusion. This large diffusion may be caused by the global eddy motion of the fluid or the deformation of the magnetic field structure due to the filament extending from the SNR. In order to take these effects into consideration precisely, 2D or 3D calculations are necessary. However, computational cost in 2D or 3D makes it difficult to find model parameters. So a 1-D model is still valuable to survey the model parameters, as Tanaka et al. (2018) have modeled phenomenologically

the multi dimensional effects into a 1-D model.

By considering a 1-D model that treats the eddy motion as an eddy viscosity, it would be interesting to discuss the kinematic mixing by eddy motion. There is still much room for discussion on the diffusion of particles escaping outside the nebula. By incorporating the effect of the spatial diffusion into the time-dependent 1-D model, if we construct a transport model of particles from the PWN to the interstellar space, we can quantitatively discuss the amount of leptonic cosmic-rays from the pulsar. No matter how nebula shows complex structure, the study with simple modeling of pulsar wind nebulae is still important.

Appendix A

Detail Review of a 1–D steady MHD flow

A.1 Relativistic MHD Equations

A.1.1 Conservation laws in relativistic MHD

The covariant expression of the particle number flux is

$$n^\mu \equiv nu^\mu = (nc\gamma, n\gamma \boldsymbol{v}), \tag{A.1}$$

where n is the number density measured in the **fluid rest frame** and the u^μ is the four speed of the fluid. The conservation law of the number is written as:

$$\partial_\mu n^\mu = 0. \tag{A.2}$$

The conservation law of energy and momentum combining matter and electromagnetic field is

$$\partial_\nu \left(T^{\mu\nu}_{\mathrm{M}} + T^{\mu\nu}_{\mathrm{EM}}\right) = 0. \tag{A.3}$$

The energy momentum tensor of the perfect fluid $T^{\mu\nu}$ is written as

$$T^{\mu\nu}_{\mathrm{M}} = \frac{\epsilon + P}{c^2} u^\mu u^\nu + p\eta^{\mu\nu}, \tag{A.4}$$

where ϵ is the internal density of the fluid including the rest mass energy, P is the gas pressure of the fluid, u is the four velocity of the fluid and $\eta^{\mu\nu}$ is the Minkowski metric. The energy momentum tensor of the electromagnetic field $T^{\mu\nu}_{\mathrm{EM}}$ is

$$T^{\mu\nu}_{EM} = \frac{1}{4\pi}\left(F^{\mu\nu}F^{\nu}_{\lambda} - \frac{1}{4}\eta^{\mu\nu}F^{\lambda\rho}F_{\lambda\rho}\right), \tag{A.5}$$

where $F_{\mu\nu} = \partial_\mu A^\nu - \partial_\nu A^\mu$ is the electromagnetic tensor. The energy momentum tensor of the entire system $T^{\mu\nu} = T^{\mu\nu}_{\mathrm{M}} + T^{\mu\nu}_{\mathrm{EM}}$ in matrix form is

$$T^{\mu\nu} = \begin{pmatrix} (\epsilon + P)\gamma^2 - P + \frac{E^2+B^2}{8\pi} & (\epsilon + P)\gamma^2\boldsymbol{\beta} + \frac{1}{4\pi}(\boldsymbol{E}\times\boldsymbol{B}) \\ (\epsilon + P)\gamma^2\boldsymbol{\beta} + \frac{1}{4\pi}(\boldsymbol{E}\times\boldsymbol{B}) & (\epsilon + P)\gamma^2\boldsymbol{\beta}\otimes\boldsymbol{\beta} - \frac{1}{4\pi}(\boldsymbol{E}\otimes\boldsymbol{E} + \boldsymbol{B}\otimes\boldsymbol{B}) + (P + \frac{E^2+B^2}{8\pi})\overleftrightarrow{I} \end{pmatrix} \tag{A.6}$$

where E and B is the electric field measured in the **reference frame**. Therefore, in relativistic MHD, the energy conservation law is written as

$$\frac{\partial}{\partial t}\left[(\epsilon+P)\gamma^2 - P + \frac{1}{8\pi}\left(E^2+B^2\right)\right] + \nabla\cdot\left[(\epsilon+P)\gamma^2\boldsymbol{v} + \frac{c}{4\pi}(\boldsymbol{E}\times\boldsymbol{B})\right] = 0, \tag{A.7}$$

and the momentum conservation law is written as

$$\begin{aligned}\frac{\partial}{\partial t}&\left[(\epsilon+P)\gamma^2\boldsymbol{v} + \frac{c}{4\pi}(\boldsymbol{E}\times\boldsymbol{B})\right] \\ &+ \nabla\cdot\left[(\epsilon+P)\gamma^2\boldsymbol{v}\otimes\boldsymbol{v} - \frac{c^2}{4\pi}(\boldsymbol{E}\otimes\boldsymbol{E}+\boldsymbol{B}\otimes\boldsymbol{B})\right] + c^2\nabla\left[P+\frac{E^2+B^2}{8\pi}\right] = 0.\end{aligned} \tag{A.8}$$

A.1.2 MHD Systems

In the relativistic MHD equation, the charge density and the current density are not regarded as dynamics variables. Since these are linked to an electromagnetic field by the Maxwell equation, they are considered to be dependent variables determined from the electromagnetic field. This corresponds to the assumption that the Ohm's law for electric current is applicable. At the limit of the ideal MHD where the electrical conductivity is infinite, this results in an ideal MHD condition [1]

$$\boldsymbol{E} + \frac{1}{c}\boldsymbol{v}\times\boldsymbol{B} = 0. \tag{A.9}$$

From this condition and the Maxwell equation, we obtain:

$$\frac{\partial \boldsymbol{B}}{\partial t} = \nabla\times(\boldsymbol{v}\times\boldsymbol{B}). \tag{A.10}$$

This is called the induction equation. The induction equation is exactly same as its form in the non-relativistic MHD. Consequently, the Alfvén theorem (i.e. the magnetic field lines are frozen into the fluid) still holds in relativistic MHD equations.

In summary, in the relativistic MHD, the number of the dynamical variables are nine, namely fluid velocity, energy density, pressure, number density and magnetic field. On the other hand, the equations of MHD system are: the energy momentum conservation (A.7) and (A.8), particle number conservation (A.2), induction equation (A.10) and equation of state. These equations become the basic equation system of relativistic MHD.

A.2 Rankine–Hugoniot Condition in Relativistic MHD

A.2.1 Assumptions

Assumption 0 Ideal MHD

Assumption 1 A magnetic field is purely toroidal.

Assumption 2 A flow is purely radial.

Assumption 3 Ignoring the gas pressure of the unshocked pulsar wind.

[1] As can be seen from this condition, the electric field is also a dependent variable.

Assumption 4 The unshocked pulsar wind is ultra-relativistic.

Assumption 5 The termination shock is stable.

Assumption 6 Physical quantities vary only along the radial direction.

Assumption 7 The adiabatic index of the shocked pulsar wind is 4/3. [2]

Assumption 8 The flow is adiabatic.

In deriving the Rankine-Hugoniot condition, we choose **the reference frame as the system where the shock wave rests**. According to Assumption 2, the shock wave is a perpendicular shock, and from Assumption 1, the direction of the magnetic field is parallel to the wave front. In the following description, the subscript 1 represents the upstream value, and the subscript 2 represents the downstream value. Also, we take the direction of flow x axis positively and take the magnetic field to the positive direction of z. Therefore, the direction of the electric field is positive in the y direction [3].

A.2.2 Number Conservation

Since the system is steady (Assumption 5) and the change in the physical quantity is only in the x direction (Assumption 6), equation (A.2) is written as

$$\frac{\partial}{\partial x}\left[nu\right] = 0. \quad \Longrightarrow \quad n_1 u_1 = n_2 u_2. \tag{A.11}$$

A.2.3 Magnetic Flux Conservation

The induction equation (A.10) is

$$\frac{\partial \boldsymbol{B}}{\partial t} = \nabla \times \left(\boldsymbol{v} \times \boldsymbol{B}\right).$$

Since $\boldsymbol{v} \parallel \hat{\boldsymbol{x}}$ (Assumption 2) and $\boldsymbol{B} \parallel \hat{\boldsymbol{z}}$ (Assumption 1), $\boldsymbol{v} \times \boldsymbol{B} \parallel \hat{\boldsymbol{y}}$. Using the steady state assumption (Assumption 5), we obtain

$$\frac{\partial B_y}{\partial x} = 0. \quad \Longrightarrow \quad \frac{\partial}{\partial x}\left[vB\right] = 0 \tag{A.12}$$

According to the ideal MHD condition (Assumption 0), finally the induction equation (A.10) is written as:

$$\boldsymbol{E} = \frac{\boldsymbol{B} \times \boldsymbol{v}}{c} \quad \Longrightarrow \quad \boldsymbol{E} = \frac{vB}{c}\hat{\boldsymbol{y}}. \tag{A.13}$$

Using $u = \gamma\beta$, we obtain

$$E = \frac{u_1 B_1}{\gamma_1} = \frac{u_2 B_2}{\gamma_2}. \tag{A.14}$$

Note that this is also the condition that the normal component of the electric field is continuous on the discontinuous surface.

[2] Equivalently, the shocked wind has enough relativistic temperature.
[3] Because the ideal MHD condition (A.9) holds according to Assumption 0.

A.2.4 Energy and Momentum Conservation

The energy conservation law (A.7) is

$$\frac{\partial}{\partial t}\left[(\epsilon+P)\,\gamma^2 - P + \frac{1}{8\pi}\left(E^2+B^2\right)\right] + \nabla\cdot\left[(\epsilon+P)\,\gamma^2\boldsymbol{v} + \frac{c}{4\pi}\left(\boldsymbol{E}\times\boldsymbol{B}\right)\right] = 0.$$

Using Assumption 0 and 1, we obtain

$$\frac{\partial}{\partial x}\left[w\gamma^2 v + \frac{c}{4\pi}EB\right] = 0 \tag{A.15}$$

where $w = \epsilon + p$ is the enthalpy density. By introducing the specific enthalpy $\mu = w/n$, we have

$$\frac{\partial}{\partial x}\left[nu\left(\mu\gamma + \frac{B^2}{4\pi nu}\right)\right] = 0 \quad\Longrightarrow\quad \mu_1\gamma_1 + \frac{B_1^2}{4\pi n_1 u_1} = \mu_2\gamma_2 + \frac{B_2^2}{4\pi n_1 u_1}. \tag{A.16}$$

Here, we used the number conservation law (A.11) and the magnetic flux conservation (A.14).

The momentum conservation (A.8) is

$$\frac{\partial}{\partial t}\left[(\epsilon+P)\,\gamma^2\boldsymbol{v}\right] + \nabla\cdot\left[(\epsilon+P)\,\gamma^2\boldsymbol{v}\otimes\boldsymbol{v} - \frac{c^2}{4\pi}\left(\boldsymbol{E}\otimes\boldsymbol{E}+\boldsymbol{B}\otimes\boldsymbol{B}\right)\right] + c^2\nabla\left[P + \frac{E^2+B^2}{8\pi}\right] = 0$$

According to Assumption 0 and 1, the x-component of equation (A.8) gives

$$\nabla\cdot\left[w\gamma^2\boldsymbol{v}v_x - \frac{c^2}{4\pi}\left(\boldsymbol{E}E_x + \boldsymbol{B}B_x\right)\right] + c^2\frac{\partial}{\partial x}\left[p + \frac{E^2+B^2}{8\pi}\right] = 0 \tag{A.17}$$

and y and z component give trivial equations. Since $\boldsymbol{B}\parallel\hat{\boldsymbol{z}}$ and $\boldsymbol{E}\parallel\hat{\boldsymbol{y}}$, $E_x = B_x = 0$. Now using $\boldsymbol{v}\parallel\hat{\boldsymbol{x}}$ we obtain

$$\frac{\partial}{\partial x}\left[w\gamma^2 v^2 + c^2 P + \frac{c^2}{8\pi}\left(E^2+B^2\right)\right] = 0 \tag{A.18}$$

Furthermore, using the equation (A.11) and (A.14), we have

$$\mu_1 u_1 + \frac{P_1}{n_1 u_1} + \frac{B_1^2}{8\pi n_1 u_1} = \mu_2 u_2 + \frac{P_2}{n_1 u_1} + \frac{B_2^2}{8\pi n_1 u_1}. \tag{A.19}$$

A.2.5 Equation of State

Since the fluid is the ideal gas (Assumption 7) and is adiabatic (Assumption 8), equation of state is

$$P = (\Gamma-1)\left(\epsilon - nmc^2\right), \tag{A.20}$$

where Γ is the adiabatic index. This is equivalent with the Poisson's law

$$P \propto n^{\Gamma}. \tag{A.21}$$

Using $w = n\mu = \epsilon + P$, we obtain

$$\mu = mc^2 + \frac{\Gamma}{\Gamma-1}\left(\frac{P}{n}\right). \tag{A.22}$$

A.2.6 Compression Ratio

Using the number density measured in the reference frame $N = n\gamma$, we define the compression ratio Y as

$$Y \equiv \frac{N_2}{N_1} = \frac{\gamma_2 n_2}{\gamma_1 n_1}. \tag{A.23}$$

Using equation (A.11), we have

$$Y = \frac{\gamma_2 u_1}{\gamma_1 u_2}. \tag{A.24}$$

Furthermore, using (A.14), we obtain

$$Y = \frac{B_2}{B_1}. \tag{A.25}$$

Note that equation (A.25) is a natural result expected from the flux freezing.

Let us derive an equation of Y. First, solve the energy conservation law (A.16) for μ_2. Then,

$$\mu_2 = \frac{1}{\gamma_2}\left(\gamma_1\mu_1 + \frac{EB_1}{4\pi n_1 u_1}(1-Y)\right). \tag{A.26}$$

Since the downstream is the relativistic temperature (Assumption 7), $\Gamma_2 = \frac{4}{3}$, so the equation of state (A.22) is written as

$$\frac{4p_2}{n_2} = \mu_2 - mc^2. \tag{A.27}$$

Substitute these into equation (A.19), we obtain

$$\mu_1 u_1 + \frac{p_1}{n_1 u_1} + \frac{B_1^2}{8\pi n_1 u_1} = \mu_2 u_2 + \frac{p_2}{n_1 u_1} + \frac{B_2^2}{8\pi n_1 u_1}.$$

Writing the second term on the right hand side with μ_2 (A.27) and the third term on the right side using Y, we have

$$\mu_1 u_1 + \frac{p_1}{n_1 u_1} + \frac{B_1^2}{8\pi n_1 u_1} = \mu_2 u_2 + \frac{\mu_2}{4u_2} - \frac{mc^2}{4u_2} + \frac{B_1^2}{8\pi n_1 u_1}Y^2. \tag{A.28}$$

By using equation (A.27), we obtain

$$\mu_1 u_1 + \frac{p_1}{n_1 u_1} + \frac{B_1^2}{8\pi n_1 u_1} = \frac{1}{\gamma_2 u_2}\left(u_2^2 + \frac{1}{4}\right)\left(\gamma_1\mu_1 + \frac{B_1^2}{8\pi n_1 u_1} \times 2(1-Y)\frac{u_1}{\gamma_1}\right) - \frac{mc^2}{4u_2} + \frac{B_1^2}{8\pi n_1 u_1}Y^2. \tag{A.29}$$

Here we used the equation (A.14). Collecting all the terms on the right side, arranging them in descending order, and dividing both sides by the coefficient of Y^2, we obtain

$$Y^2 - Y\left[\frac{2}{\gamma_2 u_2}\left(u_2^2 + \frac{1}{4}\right)\frac{u_1}{\gamma_1}\right] + \left[\frac{2}{\gamma_2 u_2}\left(u_2^2 + \frac{1}{4}\right)\left(\frac{4\pi n_1 u_1 \gamma_1 \mu_1}{B_1^2} + \frac{u_1}{\gamma_1}\right)\right] - \frac{2\pi n_1 u_1 mc^2}{B_1^2}\frac{u_2}{u_1} - \left(1 + \frac{8\pi n_1 u_1^2 \mu_1 + 8\pi p_1}{B_1^2}\right) = 0. \tag{A.30}$$

A.2.7 Flow Velocity at the Downstream

Ignoring the pressure p_1 of the upstream pulsar wind (Assumption 3), $\mu_1 \sim mc^2$ can be said from equation (A.22). Furthermore, considering the limit of a strong shock, we have $u_2 \ll u_1$. Since upstream is highly relativistic (Assumption 4), $u_1 \sim \gamma_1$. Substituting these to equation (A.30), we obtain

$$Y^2 - Y\left[\frac{2}{\gamma_2 u_2}\left(u_2^2+\frac{1}{4}\right)\right] + \left[\frac{2}{\gamma_2 u_2}\left(u_2^2+\frac{1}{4}\right)\left(\frac{4\pi n_1 u_1 \gamma_1 \mu_1}{B_1^2}+1\right)\right] - \left(1+\frac{8\pi n_1 u_1^2 \mu_1}{B_1^2}\right) = 0. \quad \text{(A.31)}$$

Here, introducing the magnetization parameter σ

$$\sigma \equiv \frac{B_1^2}{4\pi n_1 u_1 \gamma_1 mc^2}, \quad \text{(A.32)}$$

and substituting this to the equation of Y, we have

$$Y^2 - Y\left[\frac{2}{\gamma_2 u_2}\left(u_2^2+\frac{1}{4}\right)\right] + \left[\frac{2}{\gamma_2 u_2}\left(u_2^2+\frac{1}{4}\right)\left(\frac{1}{\sigma}+1\right)\right] - \left(1+\frac{2}{\sigma}\right) = 0. \quad \text{(A.33)}$$

Substituting equation (eq:Ygam) and multiplying u_2^2 both sides, we have

$$\gamma_2^2 - 2\left(u_2^2+\frac{1}{4}\right) + \frac{2u_2}{\gamma_2}\left(u_2^2+\frac{1}{4}\right)\left(1+\frac{1}{\sigma}\right) - u_2^2\left(1+\frac{2}{\sigma}\right) = 0. \quad \text{(A.34)}$$

Using $\gamma_2^2 = 1+u_2^2$, we have

$$u_2\left(u_2^2+\frac{1}{4}\right) = \gamma_2\left(u_2^2 - \frac{1}{4}\frac{\sigma}{\sigma+1}\right). \quad \text{(A.35)}$$

Squaring both sides, we obtain

$$u_2^2\left(u_2^2+\frac{1}{4}\right)^2 = \left(1+u_2^2\right)\left(u_2^2 - \frac{1}{4}\frac{\sigma}{\sigma+1}\right)^2. \quad \text{(A.36)}$$

This is a bi-quadratic equation for u_2, so it can be easily solved and the solution is as follows:

$$u_2^2 = \frac{8\sigma^2+10\sigma+1}{16(\sigma+1)} \pm \frac{\sqrt{64\sigma^2(\sigma+1)^2+20\sigma(\sigma+1)+1}}{16(\sigma+1)} \quad \text{(A.37)}$$

Since σ is determined by only upstream physical quantity, equation (A.37) means that the downstream speed is represented by the upstream quantities.

A.2.8 Downstream Magnetic Field and Number Density

If we know Y, the downstream magnetic field and the number density can be obtained, because the compression ratio in reference frame is

$$Y = \frac{\gamma_2 u_1}{\gamma_1 u_2} = \frac{B_2}{B_1} = \frac{N_2}{N_1}. \quad \text{(A.38)}$$

Since $u_1 \sim \gamma_1$ and $\gamma^2 = 1+u^2$, $Y \sim \frac{\sqrt{1+u_2^2}}{u_2}$. As seen in equation (A.37), u_2 is already written by the downstream quantities, thus we have finished writing the downstream magnetic field and number density by upstream quantities.

A.2.9 Downstream Pressure and Temperature

Let us solve equation (A.16). Using equation (A.14), we write equation (A.16) as

$$\gamma_1\mu_1 + \frac{u_1 B_1^2}{4\pi n_1 u_1 \gamma_1} = \gamma_2\mu_2 + \frac{u_1 B_1^2}{4\pi n_1 u_1 \gamma_1}\frac{B_2}{B_1}. \tag{A.39}$$

According to Assumption 3 ($p_1 \ll n_1 mc^2$), $\mu_1 \sim mc^2$. Using σ, we have

$$\gamma_1 mc^2 + \sigma mc^2 u_1 = \gamma_2\mu_2 + \sigma mc^2 u_1 Y. \tag{A.40}$$

Since $p_2 \gg n_2 mc^2$, $\mu_2 \sim \frac{4p_2}{n_2}$ (Assumption 7), so

$$\gamma_1 mc^2 + \sigma mc^2 u_1 = \gamma_2\frac{4p_2}{n_2} + \sigma mc^2 u_1 Y. \tag{A.41}$$

Using $u_1 \sim \gamma_1$ (Assumption 4) and $Y \sim \frac{\gamma_2}{u_2}$, we obtain

$$\frac{p_2}{n_1 mc^2 u_1^2} = \frac{1}{4\gamma_2 u_2}\left[1 + \sigma\left(1 - \frac{\gamma_2}{u_2}\right)\right]. \tag{A.42}$$

The left hand side of this equation is the pressure normalized by the upstream dynamic pressure. If the sign of u_2^2 in the equation (A.37) is taken the pressure takes a negative value for a small σ. Therefore, the physical solution of (A.37) is limited to positive sign. Since $T_2 = \frac{p_2}{n_2}$, the downstream temperature is

$$\frac{T_2}{u_1 mc^2} = \frac{p_2}{n_2 u_1 mc^2} = \frac{1}{4\gamma_2}\left[1 + \sigma\left(1 - \frac{\gamma_2}{u_2}\right)\right]. \tag{A.43}$$

Here we used the number conservation law (A.11)

A.2.10 Dependence on σ

With the above discussion, all physical quantities in the downstream are represented by upstream physical quantities. In summary, we have

$$\begin{aligned}
u_2^2 &= \frac{8\sigma^2 + 10\sigma + 1}{16(\sigma+1)} + \frac{\sqrt{64\sigma^2(\sigma+1)^2 + 20\sigma(\sigma+1) + 1}}{16(\sigma+1)} \\
Y &= \frac{\gamma_2}{u_2} \\
\frac{p_2}{n_1 mc^2 u_1^2} &= \frac{1}{4\gamma_2 u_2}\left[1 + \sigma\left(1 - \frac{\gamma_2}{u_2}\right)\right] \\
\frac{T_2}{u_1 mc^2} &= \frac{p_2}{n_2 u_1 mc^2} = \frac{1}{4\gamma_2}\left[1 + \sigma\left(1 - \frac{\gamma_2}{u_2}\right)\right].
\end{aligned}$$

In Figure A.1, the dependence of the 4-speed and the compression ratio on σ. The σ dependence of the pressure is shown in Figure A.2.

High σ Limit

Expanding equation (A.37) with a power of $1/\sigma$ results in the following:

$$u_2^2 = \sigma + \frac{1}{8} + \frac{1}{64}\frac{1}{\sigma} - \frac{1}{64}\frac{1}{\sigma^2} + O\left(\frac{1}{\sigma^3}\right). \tag{A.44}$$

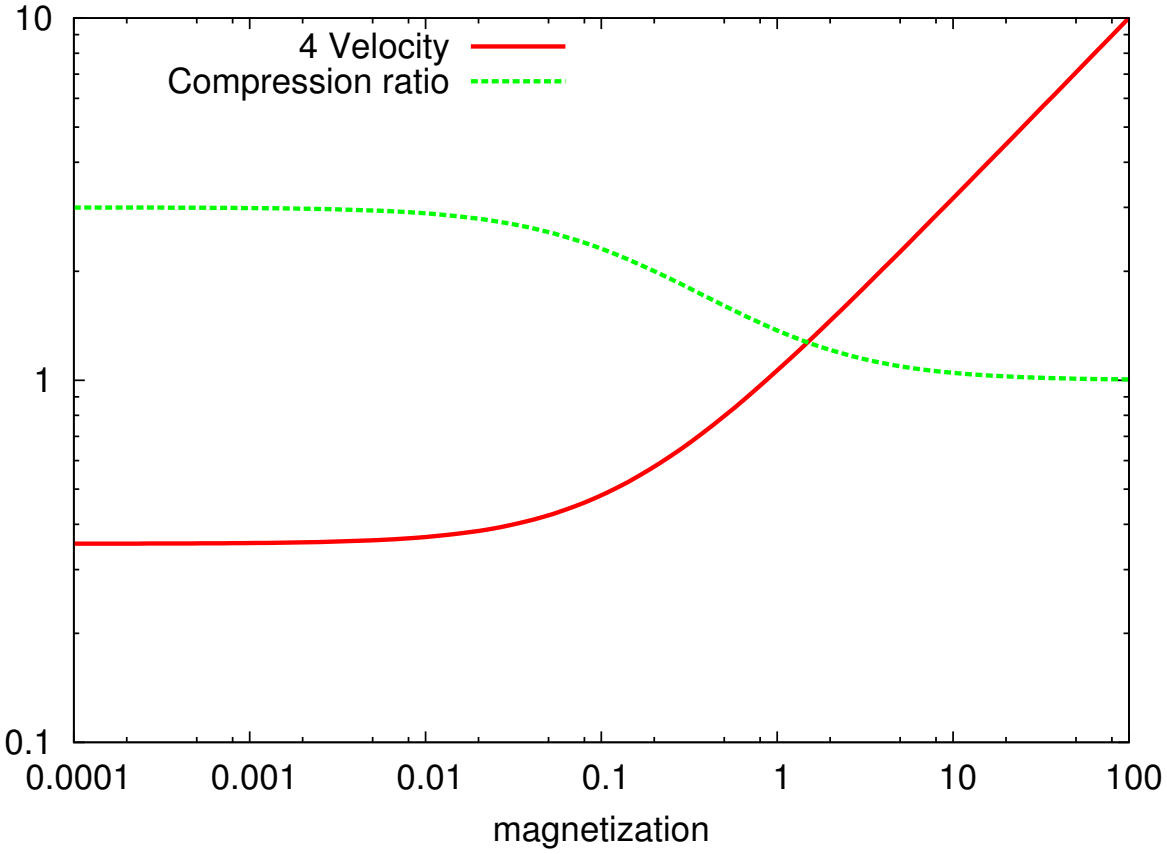

Figure A.1: The dependence on σ of the 4 velocity and the compression ratio in reference frame.

Then we obtain

$$u_2^2 = \sigma + \frac{1}{8} + \frac{1}{64}\frac{1}{\sigma} + \cdots \tag{A.45a}$$

$$\gamma_2^2 = \sigma + \frac{9}{8} + \frac{1}{64}\frac{1}{\sigma} + \cdots \tag{A.45b}$$

$$Y = \frac{B_2}{B_1} = \frac{N_2}{N_1} = 1 + \frac{1}{2}\frac{1}{\sigma} + \cdots \tag{A.45c}$$

$$\frac{T_2}{u_1 mc^2} = \frac{1}{8\sqrt{\sigma}}\left(1 - \frac{19}{64}\frac{1}{\sigma}\right) + \cdots . \tag{A.45d}$$

Note that these are solutions assuming that the downstream temperature is sufficiently high. In order for the temperature expression to be valid, it is necessary to be $u_1 \gg 8\sqrt{\sigma}$. Furthermore, as σ increases, the downstream temperature decreases and the compression ratio also approaches 1. From these results, it is found that when σ is large, that is, when the energy of the magnetic field is large, the shock wave effectively weakens.

Low σ Limit

Expanding equation (A.37) with a power of σ results in the following:

$$u_2^2 = \frac{1}{8} + \frac{9}{8}\sigma - \frac{9}{8}\sigma^2 + O\left(\sigma^3\right) \tag{A.46}$$

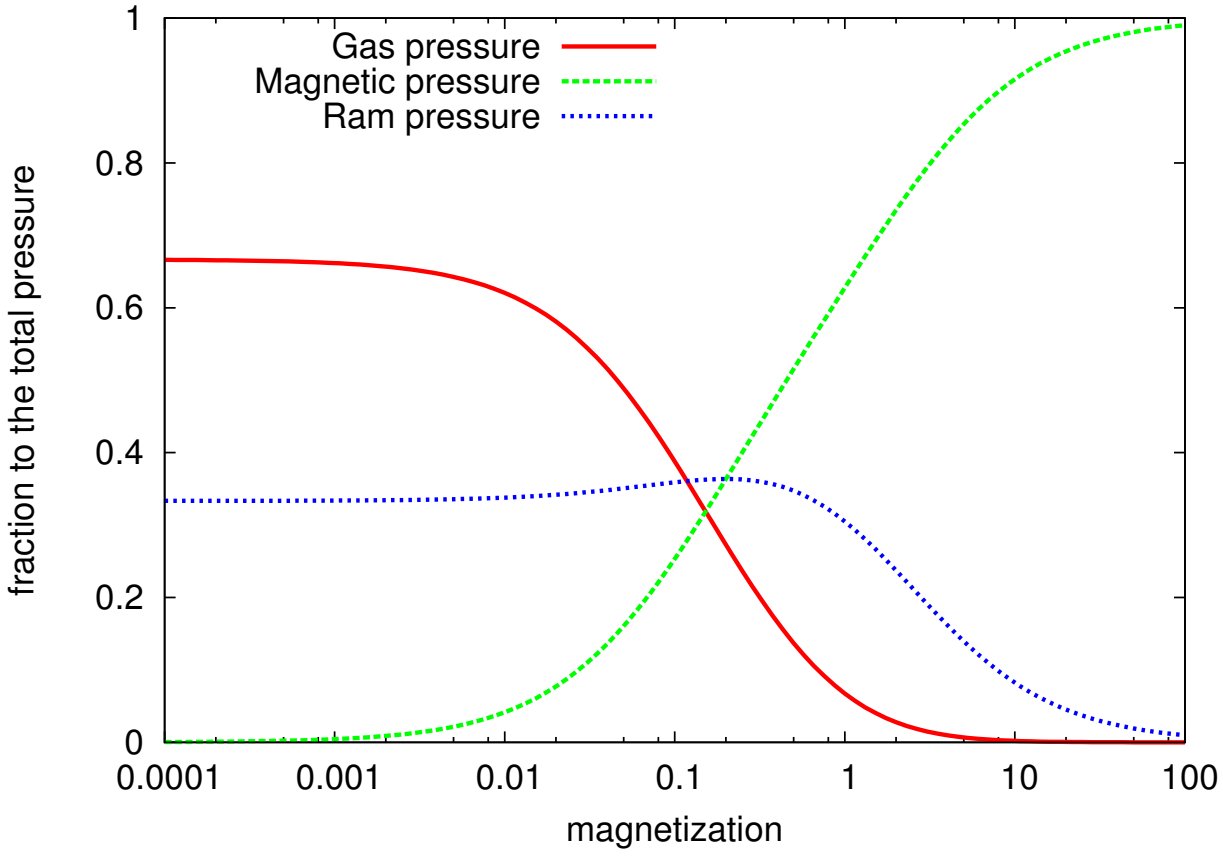

Figure A.2: The dependence on σ of the gas, magnetic and ram pressure.

Then we obtain

$$u_2^2 = \frac{1+9\sigma}{8} + \cdots \tag{A.47a}$$

$$\gamma_2^2 = \frac{9+9\sigma}{8} + \cdots \tag{A.47b}$$

$$Y = \frac{B_2}{B_1} = \frac{N_2}{N_1} = 3(1-4\sigma)\cdots \tag{A.47c}$$

$$\frac{T_2}{u_1 mc^2} = \frac{1}{\sqrt{18}}(1-2\sigma) + \cdots . \tag{A.47d}$$

These expressions are valid for $\sigma \lesssim 0.1$.

Furthermore, taking the limit $\sigma \to 0$, we obtain the downstream 3-speed

$$\beta_2 = \frac{u_2}{\gamma_2} \to \frac{1}{3}, \tag{A.48}$$

which recovers the result of the non-magnetized hydrodynamics.

A.3 Steady Solution to the Relaticistic 1–D MHD equations

In this section, we find a spherically symmetric steady flow with the physical quantity obtained according to Rankine-Hugoniot condition as the boundary condition. We continue to use the as-

sumptions in Section A.2. We set the direction of flow in the radial direction ($\hat{\boldsymbol{r}}$ direction), the direction of the magnetic field in the azimuth direction ($\hat{\boldsymbol{\phi}}$ direction) and the direction of the electric field in the zenith direction ($\hat{\boldsymbol{\theta}}$ direction).

A.3.1 Basic equations

Number Conservation

From the number conservation law (A.2),

$$\partial_\mu u^\mu = 0,$$

and the Assumptions 2,5, and 6, we have

$$\nabla_r \cdot [nu] = 0 \quad \Longrightarrow \quad \frac{1}{r^2}\frac{d}{dr}\left[nur^2\right] = 0. \tag{A.49}$$

Magnetic Flux Conservation

Let us reduce the induction equation (A.10),

$$\frac{\partial \boldsymbol{B}}{\partial t} = \nabla \times (\boldsymbol{v} \times \boldsymbol{B}),$$

for spherical symmetrical configuration. Since $\boldsymbol{B} \parallel \hat{\boldsymbol{\phi}}$ (Auumption 1), $\boldsymbol{v} \parallel \hat{\boldsymbol{r}}$ (Assumption 2), $\boldsymbol{B} \times \boldsymbol{v} \parallel \hat{\theta}$, and the fact that the physical quantity has only the radial dependence (Assumption 6) hold, so non-trivial equation from $\nabla \times \boldsymbol{v} \times \boldsymbol{B}$ is obtained from only *theta* component. Thus, we obtain

$$\left[\nabla \times (\boldsymbol{v} \times \boldsymbol{B})\right]_\phi = 0 \quad \Longrightarrow \quad \frac{d}{dr}\left[\frac{ruB}{\gamma}\right] = 0. \tag{A.50}$$

Energy Equation

Since the fluid motion is adiabatic (Assumption 8), the first law of thermodynamics is written as:

$$dE = -PdV \quad \Longrightarrow \quad \frac{d}{dr}\left(ur^2 ne\right) + P\frac{d}{dr}\left(ur^2\right) = 0. \tag{A.51}$$

where $e = \epsilon/n$ is specific energy. In the 1–D configuration, this equation is equivalent with the momentum conservation law.

Energy Conservation

The energy conservation law (A.7) is

$$\frac{\partial}{\partial t}\left[(\epsilon + P)\gamma^2 - P + \frac{1}{8\pi}\left(E^2 + B^2\right)\right] + \nabla \cdot \left[(\epsilon + P)\gamma^2 \boldsymbol{v} + \frac{c}{4\pi}(\boldsymbol{E} \times \boldsymbol{B})\right] = 0.$$

Using Assumption 5 and 6, $\boldsymbol{E} \parallel \hat{\boldsymbol{\theta}}$ and $\boldsymbol{B} \parallel \hat{\boldsymbol{\phi}}$, we obtain

$$\nabla_r \cdot \left[(\epsilon + P)\gamma^2 \boldsymbol{v} + \frac{c}{4\pi}(\boldsymbol{E} \times \boldsymbol{B})\right] = 0 \quad \Longrightarrow \quad \frac{1}{r^2}\frac{d}{dr}\left[r^2\left\{(\epsilon + P)\gamma^2 v + \frac{cuB^2}{4\pi\gamma}\right\}\right] = 0. \tag{A.52}$$

Furthermore, using $w = n\mu = \epsilon + P$ and the number conservation law (A.49), we obtain

$$nur^2 \frac{d}{dr}\left[\gamma\mu + \frac{B^2}{4\pi n\gamma}\right] = 0. \tag{A.53}$$

Equation of State

From equation of state (A.22),

$$\mu = mc^2 + \frac{\Gamma}{\Gamma - 1}\left(\frac{p}{n}\right),$$

and $\Gamma = \frac{4}{3}$ (Assumption 7) and $\mu = (\epsilon + P)/n = e + p/n$, we obtain

$$3p + nmc^2 = ne. \tag{A.54}$$

Substituting this to the energy equation (A.51) and (A.49), we have

$$4p\frac{d}{dr}\left(ur^2\right) + 3ur^2\frac{d}{dr}\left(p\right) = 0. \tag{A.55}$$

Dividing both sides by $3r^2u$ and using equation (A.49), we obtain

$$\frac{d}{dr}\ln p - \frac{4}{3}\frac{d}{dr}\ln n = 0 \quad \Longrightarrow \quad \frac{d}{dr}\ln\left(\frac{p}{n^{4/3}}\right) = 0. \tag{A.56}$$

Momentum Conservation (Not used)

Although not used in the subsequent discussion, we derive the equation of momentum conservation in steady and spherical systems. The divergence of the tensor T has a term due to the basis differentiation, so it is necessary to calculate as follows:

$$(\nabla \cdot \boldsymbol{T})^r = \frac{1}{r^2}\frac{\partial}{\partial r}\left(r^2 T^{rr}\right) + \frac{1}{r\sin\theta}\left[\frac{\partial}{\partial\theta}\left(\sin\theta T^{r\theta}\right) + \frac{\partial T^{r\phi}}{\partial\phi}\right] - \frac{1}{r}\left(T^{\theta\theta} + T^{\phi\phi}\right) \tag{A.57}$$

Let T be

$$\boldsymbol{T} \equiv (\epsilon + p)\gamma^2\boldsymbol{v}\otimes\boldsymbol{v} - \frac{c^2}{4\pi}\left(\boldsymbol{E}\otimes\boldsymbol{E} + \boldsymbol{B}\otimes\boldsymbol{B}\right) + c^2\left(p + \frac{E^2+B^2}{8\pi}\right)\overleftrightarrow{I}, \tag{A.58}$$

then we have:

$$T^{rr} = (\epsilon + p)\gamma^2 v_r v_r - \frac{c^2}{4\pi}\left(E_r E_r + B_r B_r\right) + c^2\left(p + \frac{E^2+B^2}{8\pi}\right) = (\epsilon + p)u^2 + c^2\left(p + \frac{E^2+B^2}{8\pi}\right), \tag{A.59}$$

$$T^{r\theta} = (\epsilon + p)\gamma^2 v_r v_\theta - \frac{c^2}{4\pi}\left(E_r E_\theta + B_r B_\theta\right) = 0, \tag{A.60}$$

$$T^{r\phi} = (\epsilon + p)\gamma^2 v_r v_\phi - \frac{c^2}{4\pi}\left(E_r E_\phi + B_r B_\phi\right) = 0, \tag{A.61}$$

$$T^{\theta\theta} = (\epsilon + p)\gamma^2 v_\theta v_\theta - \frac{c^2}{4\pi}\left(E_\theta E_\theta + B_\theta B_\theta\right) + c^2\left(p + \frac{E^2+B^2}{8\pi}\right) = -c^2\left(\frac{E_\theta^2}{4\pi} + c^2 p + c^2\frac{E^2+B^2}{8\pi}\right), \tag{A.62}$$

and

$$T^{\phi\phi} = (\epsilon + p)\gamma^2 v_\phi v_\phi - \frac{c^2}{4\pi}\left(E_\phi E_\phi + B_\phi B_\phi\right) + c^2\left(p + \frac{E^2+B^2}{8\pi}\right) = -c^2\left(\frac{B_\phi^2}{4\pi} + p + \frac{E^2+B^2}{8\pi}\right). \tag{A.63}$$

Here we used $v_\theta = v_\phi = 0$, $\boldsymbol{v}^2 = v_r^2$, $\boldsymbol{E} = E_\theta\boldsymbol{e}_\theta$ and $\boldsymbol{B} = B_\phi\boldsymbol{e}_\phi$. All components not shown here are equal to zero. Using this to calculate the divergence of the tensor T, we obtain

$$\frac{1}{r^2}\frac{d}{dr}\left[r^2\left((\epsilon + p)\gamma^2\beta^2 + p + \frac{E^2+B^2}{8\pi}\right)\right] - \frac{2p}{r} = 0. \tag{A.64}$$

A.3.2 Derivation of 1–D Steady Flow Solution

In the shock wave, since the boundary condition is given as the value of the shock just downstream, the solution is set to one. Namely, from the number conservation law (A.49), we have

$$nur^2 = n_2 u_2 r_s^2 = \text{const.}$$

From the magnetic flux conservation (A.50), we have

$$\frac{ruB}{\gamma} = \frac{r_s u_2 B_2}{\gamma_2} = \text{const.}$$

From equation of state (A.56), we have

$$\frac{p}{n^{4/3}} = \frac{p_2}{n_2^{4/3}} = \text{const.}$$

Bernoulli Equation of Velocity Field

The equation of state (A.22) is written as:

$$4p = n\left(\mu - mc^2\right). \tag{A.65}$$

From the energy conservation law (A.53), we obtain

$$\gamma\left(\mu + \frac{B^2}{4\pi n\gamma^2}\right) = \text{const.}$$

Using the equation (A.65), we obtain

$$\begin{aligned}\gamma\left(\mu + \frac{B^2}{4\pi n\gamma^2}\right) &= \gamma\left(\mu - mc^2 + mc^2 + \frac{B^2}{4\pi n\gamma^2}\right) \\ &= \gamma\left(\frac{4p}{n} + mc^2 + \frac{B^2}{4\pi n\gamma^2}\right) = \text{const.}\end{aligned} \tag{A.66}$$

Furthermore, using the boundary condition, we obtain

$$\begin{aligned}\gamma\left(\mu + \frac{B^2}{4\pi n\gamma^2}\right) &= \gamma\left(\frac{4p}{n} + mc^2 + \frac{B^2}{4\pi n\gamma^2}\right) \\ &= \gamma\left(\frac{4p_2}{n_2} \times \left(\frac{u}{u_2}\frac{r^2}{r_s^2}\right)^{-1/3} + mc^2 + \frac{B_2^2}{4\pi n_2\gamma_2^2}\left(\frac{u}{u_2}\right)^{-1}\right) \\ &= \frac{B_2^2}{4\pi n_2\gamma_2^2}\gamma\left(\frac{16\pi p_2\gamma_2^2}{B_2^2} \times \left(vz^2\right)^{-1/3} + \frac{4\pi n_2\gamma_2 mc^2}{B_2^2} + \frac{1}{v}\right) = \text{const},\end{aligned}$$

where $v \equiv u/u_2$ and $z \equiv r/r_s$. Here, introducing Δ and δ, which defined as

$$\Delta \equiv \frac{16\pi p_2\gamma_2^2}{B_2^2} \quad , \quad \delta \equiv \frac{4\pi n_2\gamma_2 mc^2}{B_2^2}, \tag{A.67}$$

then we obtain the Bernoulli equation

$$\left(1 + u_2^2 v^2\right)^{\frac{1}{2}}\left(\delta + \Delta\left(vz^2\right)^{-1/3} + \frac{1}{v}\right) = \gamma_2\left(\delta + \Delta + 1\right). \tag{A.68}$$

The quantities δ and Δ are written to more simplified forms as:

$$\begin{aligned}\delta = \frac{4\pi n_2\gamma_2 mc^2}{B_2^2} &= \frac{4\pi n_1 u_1\gamma_1 mc^2}{B_1^2}\times\frac{B_1^2}{B_2^2}\times\frac{n_2\gamma_2^2}{n_1 u_1\gamma_1}\\ &= \frac{\gamma_1}{u_1}\times\frac{u_2}{\sigma u_1}\sim\frac{u_2}{\sigma u_1}\end{aligned} \tag{A.69}$$

and

$$\begin{aligned}\Delta \equiv \frac{16\pi p_2\gamma_2^2}{B_2^2} &= \frac{p_2}{n_1 mc^2 u_1^2}\times\frac{4\pi n_1 u_1^2 mc^2}{B_1^2}\times\frac{4\gamma_2^2 B_1^2}{B_2^2}\\ &= \frac{1}{4u_2\gamma_2}\left[1+\sigma\left(1-\frac{\gamma_2}{u_2}\right)\right]\times\frac{4\gamma_2^2 B_1^2}{\sigma B_2^2}\\ &= \left(\frac{1+\sigma}{\sigma}\right)\frac{u_2}{\gamma_2}-1.\end{aligned} \tag{A.70}$$

Equation (A.36) is rewritten by using Δ as

$$u_2\left(u_2^2+\frac{1}{4}\right) = u_2\gamma_2\left(u_2-\frac{1}{4\gamma_2}\frac{1}{\Delta+1}\right).$$

Multiplying $\dfrac{\Delta+1}{u_2}$ both sides of this equation, we obtain

$$\begin{aligned}(\Delta+1)\left(u_2^2+\frac{1}{4}\right) &= \gamma_2 u_2\left(1+\Delta\right)-\frac{1}{4}\\ &= \frac{u_2^2}{\sigma}+u_2^2-\frac{1}{4}.\end{aligned}$$

Solving this for Δ, we have

$$\Delta = \frac{\left(u_2^2/\sigma\right)-\frac{1}{2}}{u_2^2+\frac{1}{4}}. \tag{A.71}$$

Let us check the dependence of δ and Δ on σ. For $\sigma\gg 1$, $\delta\sim 1/\left(u_1\sqrt{\sigma}\right)$ enough smaller than unity. Contrary, for $\sigma\ll 1$, depending on the value of u_1, δ is not always small. However, we assume that u_1 is enough large so that $u_1\sigma$ is sufficiently large and then consider δ to be small. Since Δ depends only on σ, its behavior is simple. Considering the large limit of σ from the expression (A.71), by using $u_2^2\sim\sigma$ we obtain

$$\Delta = \frac{\left(u_2^2/\sigma\right)-\frac{1}{2}}{u_2^2+\frac{1}{4}}\sim\frac{1}{2\sigma}. \tag{A.72}$$

For small σ, since $u_2^2\sim\frac{1}{8}$, we obtain

$$\Delta\sim\frac{\frac{1}{8\sigma}-\frac{1}{2}}{\frac{1}{8}+\frac{1}{4}}\sim\frac{1}{3\sigma}. \tag{A.73}$$

A.3.3 Asymptotic Value

Let us find the flow velocity at very far. Taking the limit $z \to \infty$ of the Bernoulli equation (A.68) and ignoring δ, we obtain

$$\left(1 + u_2^2 v_\infty^2\right)^{\frac{1}{2}} \frac{1}{v_\infty} = \gamma_2 \left(\Delta + 1\right).$$

Solving for v_∞, we have

$$v_\infty = \left[\gamma_2^2 \left(1 + \Delta\right)^2 - u_2^2\right]^{-\frac{1}{2}}. \tag{A.74}$$

Thus, we obtain

$$u_\infty \equiv u_2 v_\infty = \left(\sqrt{\frac{(1+\sigma)^2}{\sigma^2} - 1}\right)^{-1} = \left(\frac{\sigma^2}{1+2\sigma}\right)^{\frac{1}{2}} \tag{A.75}$$

$$\beta_\infty \equiv \frac{u_\infty}{\gamma_\infty} = \sqrt{\frac{1}{1 + \frac{1+2\sigma}{\sigma^2}}} = \frac{\sigma}{1+\sigma}. \tag{A.76}$$

As this equation shows, when σ is large, the flow velocity has a finite value even at infinite point.

A.3.4 Other Quantities

By solving the Bernoulli equation (A.68), we can obtain the velocity field $u(r)$ in the nebula. In section, if $u(r)$ is given, we explicitly write down how other physical quantities are obtained.

Number Density

From the number conservation (A.49), we obtain

$$nur^2 = n_2 u_2 r_s^2. \tag{A.77}$$

Using the boundary condition, we obtain

$$n = n_2 \left(vz^2\right)^{-1}. \tag{A.78}$$

Magnetic Field

From the magnetic flux conservation (A.50), we have

$$\frac{ruB}{\gamma} = \frac{r_s u_2 B_2}{\gamma_2}.$$

Using the boundary condition, we obtain

$$\begin{aligned} B &= B_1 \frac{r_s u_2 \gamma B_2}{ru\gamma_2 B_1} \\ &= B_2 \frac{\gamma}{\gamma_2} \frac{1}{zv}. \end{aligned} \tag{A.79}$$

Pressure and Temperature

From the equation (A.21) and (A.49), we obtain

$$\frac{p}{n^{4/3}} = \frac{p_2}{n_2^{4/3}} \quad , \quad nur^2 = n_2 u_2 r_s^2$$

Furthermore, using equation (A.42), we have

$$\frac{p_2}{n_1 mc^2 u_1} = \frac{1}{4\gamma_2 u_2}\left[1 + \sigma\left(1 - \frac{\gamma_2}{u_2}\right)\right].$$

Thus, we obtain

$$\frac{p}{n_1 mc^2 u_1^2} = \frac{1}{4\gamma_2 u_2}\left[1 + \sigma\left(1 - \frac{\gamma_2}{u_2}\right)\right] \times \frac{1}{(z^2 v)^{4/3}}. \tag{A.80}$$

The temperature is obtained by same way, namely

$$\frac{T}{mc^2 u_1} = \frac{1}{4\gamma_2}\left[1 + \sigma\left(1 - \frac{\gamma_2}{u_2}\right)\right] \times \frac{1}{(z^2 v)^{1/3}}. \tag{A.81}$$

Appendix B

Leptonic Emission

In this chapter, we briefly review the emission from the relativistic electrons (and positrons).

B.1 Synchrotron radiation

Electromagnetic radiation from a particle which gyrates with a relativistic velocity is called the synchrotron radiation. The equation of motion of a particle under a uniform magnetic field is

$$m\gamma\frac{d\boldsymbol{v}}{dt} = \frac{e}{v}\boldsymbol{v}\times\boldsymbol{B}. \tag{B.1}$$

The solution of this equation is the gyro-motion, namely

$$\boldsymbol{v}_{\parallel} = \text{const}, \quad |\boldsymbol{v}_{\perp}| = \text{const}, \tag{B.2}$$

the gyro frequency of the uniform circular motion is ω_B/γ, where ω_B is the cyclotron frequency

$$\omega_B = \frac{eB}{mc}. \tag{B.3}$$

The total emitted power from the accelerated particle is given by (see Rybicki & Lightman, 1979, for detail)

$$P = \frac{2e^2}{3c^3}\gamma^4\left(a_{\perp}^2 + \gamma^2 a_{\parallel}^2\right), \tag{B.4}$$

where a is the acceleration of the particle. Thus, the total emitted power averaged over all pitch angles is calculate as:

$$P_{\rm syn} = \frac{4}{3}\sigma_{\rm T}c\beta^2\gamma^2 U_{\rm B}, \tag{B.5}$$

where $U_{\rm B} = B^2/8\pi$ is the energy density of the magnetic field.

As can be seen from Figure B.1, the duration of radiation Δt in the reference frame can be written as:

$$\Delta t \sim \frac{2}{\omega_B \sin\alpha}, \tag{B.6}$$

where α is a pitch angle of the charged particle. Since the charged particle moves against us, the "received" duration $\Delta t_{\rm A}$ is different from Δt, namely

$$\Delta t_{\rm A} = \frac{2}{\omega_c \sin\alpha}\left(1 - \frac{v}{c}\right) \sim \frac{2}{\gamma^2\omega_B \sin\alpha}. \tag{B.7}$$

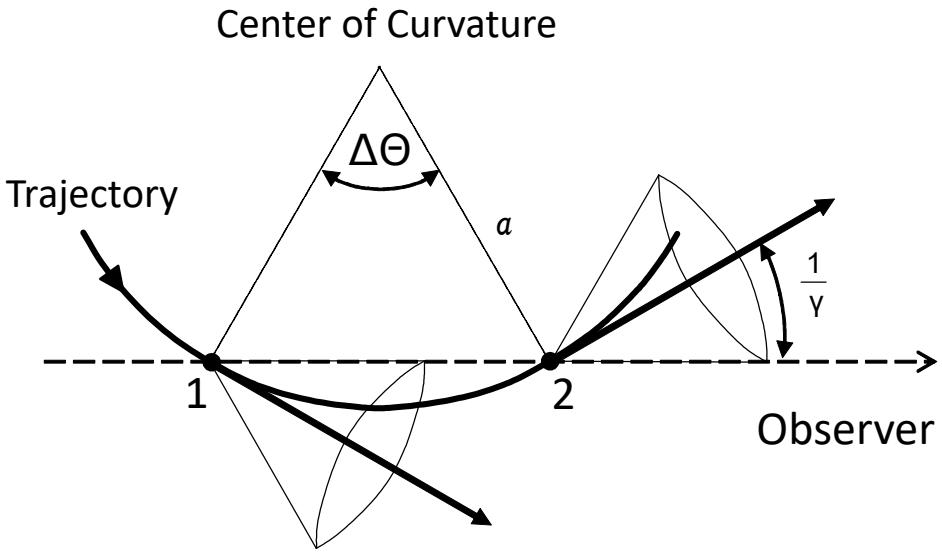

Figure B.1: The trajectory of a charged particle looking down from the direction of the magnetic field. Note that the curvature radius of the trajectory is not $\frac{\gamma c}{\omega_B}$, but $a = \frac{\gamma c}{\omega_B \sin\alpha}$, because the trajectory is tilted by the pitch angle α. Due to the relativistic beaming effect, the electromagnetic wave emitted from a relativistic particle is concentrated into the range of angles on $\sim 1/\gamma$ from the direction of motion. As a result, the emission that the observer receives is limited to that emitted while the particles move from 1 to 2.

Therefore, the typical frequency of the emission is written as:

$$\omega_c = \frac{3}{2}\gamma^2 \omega_B \sin\alpha. \tag{B.8}$$

The detailed spectrum is obtained by integrating:

$$\frac{dW}{d\omega d\Omega} = \frac{e^2\omega^2}{4\pi^2 c}\left[\int \boldsymbol{n}\times(\boldsymbol{n}\times\boldsymbol{\beta})\exp\left[i\omega\left(t_0 - \boldsymbol{n}\cdot r_0(t_0)/c\right)\right]dt_0\right]^2, \tag{B.9}$$

where $\boldsymbol{n}$ is a unit vector pointing to the observer and r_0 is the trajectory of the particle. After some calculation, the emitted power per frequency $P_{\rm syn}(\omega)$ is obtained as (see Rybicki & Lightman, 1979, for details):

$$P_{\rm syn}(\omega) = \frac{\sqrt{3}e^2 B\sin\alpha}{2\pi m c^2} F(x), \tag{B.10}$$

where $x = \omega/\omega_c$,

$$F(x) = x\int_x^\infty K_{\frac{5}{3}}(\xi)d\xi, \tag{B.11}$$

and K_ν is the modified Bessel function of ν-th order. Note that $P_{\rm syn}(\omega)$ takes its maximum value at $0.29\omega_c$ rather than ω_c.

For electrons which follow a power-law distribution, namely

$$\frac{dN}{d\gamma} = N_0\gamma^{-p}, \tag{B.12}$$

the total spectrum of the synchrotron emission is calculated as:

$$P_{\mathrm{tot,syn}}(\omega) = \frac{\sqrt{3}e^3 N_0 B \sin\alpha}{2\pi mc^2\,(p+1)}\Gamma\left(\frac{p}{4}+\frac{19}{12}\right)\Gamma\left(\frac{p}{4}-\frac{1}{12}\right)\left(\frac{mc\omega}{3eB\sin\alpha}\right)^{-(p-1)/2} \propto \omega^{-(p-1)/2}. \quad \text{(B.13)}$$

B.2 Inverse Compton scattering

The elastic collision of an electron and a photon, which takes into consideration the recoil of an electron, is called the Compton scattering. Let us consider the situation where a photon of energy ϵ is incident on a stationary electron as shown in Figure B.2. The conservation law of the 4-momentum P^μ is written as:

$$P^m_\gamma u + P^\mu_e = P^m_{\gamma,1} u + P^\mu_{e,1}. \quad \text{(B.14)}$$

By solving equation (B.14) for the energy of the photon after collision ϵ_1, we have

$$\epsilon_1 = \frac{\epsilon}{1+\frac{\epsilon}{mc^2}\,(1-\cos\theta)}. \quad \text{(B.15)}$$

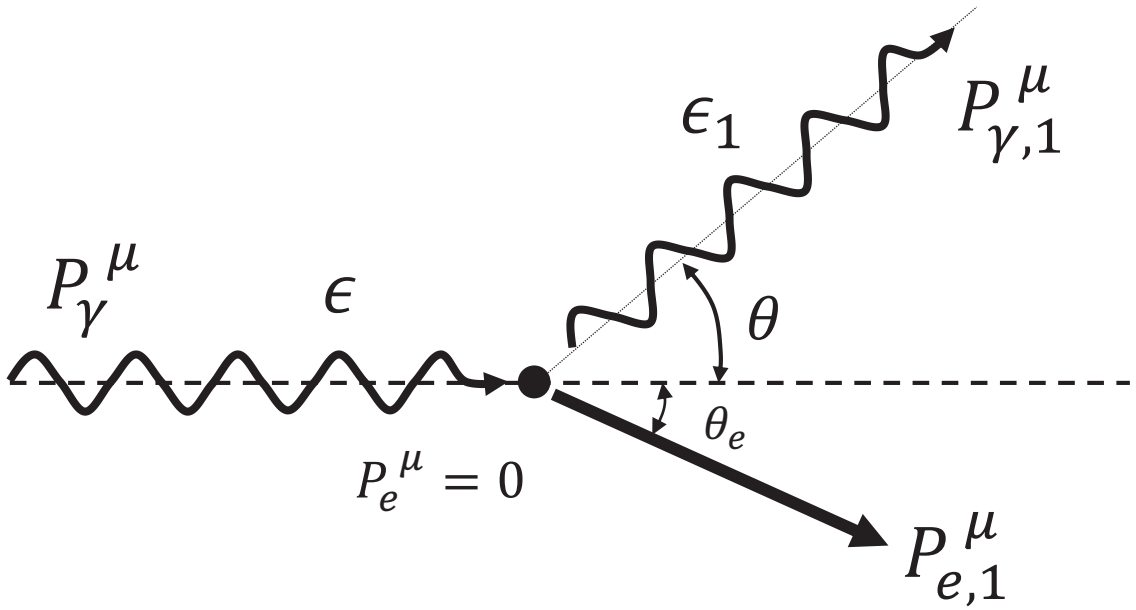

Figure B.2: The geometry of the Compton scattering.

The differential cross section is given by the Klein–Nishina formula, namely

$$\frac{d\sigma_{\mathrm{KN}}}{d\Omega} = \frac{r_0^2}{2}\frac{\epsilon_1^2}{\epsilon^2}\left(\frac{\epsilon}{\epsilon_1}+\frac{\epsilon_1}{\epsilon}-\sin^2\theta\right). \quad \text{(B.16)}$$

The total cross section is

$$\sigma_{\mathrm{KN}} = \sigma_{\mathrm{T}}\cdot\frac{3}{4}\left[\frac{1+x}{x^3}\left\{\frac{2x\,(1+x)}{1+2x}-\ln\left(1+2x\right)\right\}+\frac{1}{2x}\ln\left(1+2x\right)-\frac{1+3x}{(1+2x)^2}\right] \quad \text{(B.17)}$$

where $x = \epsilon/mc^2$. For the non-relativistic limit ($x \ll 1$), we obtain the Thomson cross section

$$\sigma_{\mathrm{KN}} \sim \sigma_{\mathrm{T}}, \quad \text{(B.18)}$$

and, for the ultra-relativistic limit ($x \gg 1$), we have

$$\sigma_{\rm KN} \sim \frac{3}{8}\sigma_{\rm T} x^{-1}\left[\ln 2x + \frac{1}{2}\right]. \tag{B.19}$$

Next, we consider the situation where the electron is moving (see Figure B.3). From the Lorentz transform, we have

$$\epsilon' = \epsilon\gamma\left(1 - \beta\cos\theta\right), \tag{B.20}$$

and

$$\epsilon_1 = \epsilon_1'\gamma\left(1 - \beta\cos\theta_1'\right). \tag{B.21}$$

Assuming that $x \ll 1$ at the rest frame of the electron, we have

$$\epsilon_1' \sim \epsilon'\left[1 - \frac{\epsilon'}{mc^2}\left(1 - \cos\Theta\right)\right], \tag{B.22}$$

and

$$\cos\Theta = \cos\theta_1'\cos\theta' + \sin\theta'\sin\theta_1'\cos\left(\phi' - \phi_1'\right). \tag{B.23}$$

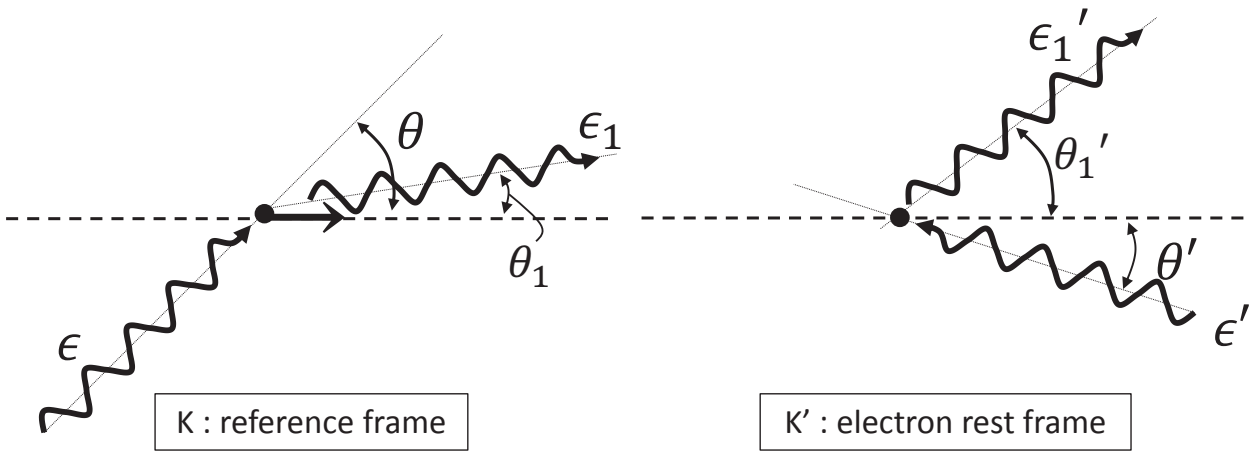

Figure B.3: Geometries of the inverse Compton scattering. The left represents the geometry in a frame in which the electron moves rightward. The right is the geometry in the rest frame of the electron.

For the case $\gamma^2 \gg h\nu/mc^2$, we have

$$\epsilon : \epsilon' : \epsilon_1 \sim 1 : \gamma : \gamma^2. \tag{B.24}$$

For example, when an electron with $\gamma \sim 10^6$ scatters a photon with $\epsilon \sim 10^{-3}$ eV, the scattered photon has energy $\epsilon_1 \sim \times 1$ GeV. However, when an electron with $\gamma \sim 10^6$ scatters a photon with $\epsilon \sim 10$ eV, the approximation $x \ll 1$ is invalid because the photon energy at K' frame is $\epsilon' \sim 10^7$ eV $> m_e c^2$. In such a case, the electron is recoiled, and consequently the energy of the scattered photon becomes about $\epsilon_1 \sim \gamma mc^2$. In contrast to the Compton scattering, since the photons gain energy by the scattering, this process is called the "inverse" Compton scattering.

Assuming that the incident photon distribution is isotropic and the recoil of the electron is negligible (equivalently $\epsilon' \sim \epsilon_1'$), the total emitted (i.e., scattered) power is calculated as:

$$P_{\rm IC} = \frac{4}{3}\sigma_T c\gamma^2\beta^2 U_{\rm ph}, \tag{B.25}$$

where $U_{\rm ph}$ is the energy density of the incident photons. The ratio of the equation (B.25) to (B.25) is

$$\frac{P_{\rm syn}}{P_{\rm IC}} = \frac{U_B}{U_{\rm ph}}. \tag{B.26}$$

This means that the ratio of the power of the synchrotron radiation and the power of the inverse Compton scattering emitted by single electron is equal to the ratio of the energy density of the magnetic field and the energy density of the photon. Note that above relations are only valid for $x \ll 1$.

The power per scattered photon energy from the isotropic electrons is obtained from (see Blumenthal & Gould (1970) for details):

$$P_{\rm tot,IC}\left(E_\gamma\right) = cE_\gamma \int d\gamma N(\gamma) \int d\epsilon n_{ph}(\epsilon)\sigma_{KN}\left(E_\gamma, \epsilon; \gamma\right), \tag{B.27}$$

where

$$\sigma_{KN}\left(E_\gamma, \epsilon; \gamma\right) = \frac{3\sigma_T}{4\epsilon\gamma^2} G\left(q, \eta_\epsilon\right), \tag{B.28}$$

$$G\left(q, \eta_\epsilon\right) = 2q\ln q + (1+2q)(1-q) + 2\eta_\epsilon q(1-q),. \tag{B.29}$$

$$q = \frac{E_\gamma}{\Gamma_\epsilon(\gamma m_e c^2 - E_\gamma)}, \qquad \Gamma_\epsilon = \frac{4\epsilon\gamma}{m_e c^2}, \qquad \eta_\epsilon = \frac{\epsilon E_\gamma}{(m_e c^2)^2}. \tag{B.30}$$

For the electrons which follow the power-law distribution (equation (B.12)), the spectral index of the scattered photon $P_{\rm tot,IC} \propto E_\gamma^{-s}$ in the band where $x \ll 1$ holds is (see Rybicki & Lightman, 1979, for details)

$$s = \frac{p-1}{2}, \tag{B.31}$$

which is the same as the case of the synchrotron radiation (equation (B.13)).

Appendix C

Particle Acceleration

C.1 Diffusive shock acceleration

Shocks in the context of astrophysics are often collisionless shocks. In a collisionless shock, particles are able to cross the shock plane. Particles are advected together with the fluid from the shock upstream to the downstream, but particles with some pitch angles may return to the upstream of the shock waves. Such particles are again trapped in the fluid upstream and return to the downstream again. Since the macroscopic fluid has much larger momentum than one microscopic particle, so this process is equivalent to the elastic reflection of the particle. This means that a particle with energy ϵ gets energy approximately $\epsilon \Delta u/c$ once every round-trip of the shock wave surface of velocity difference Δu. The probability of particles returning to the upstream is determined mainly by the pitch angle of the particles and the velocity of the downstream fluid, not depending on the energy. Therefore, in this process, particles with higher energy are more likely to obtain energy. As a result, a non-thermal energy distribution extending to the higher energy than the Maxwellian distribution is formed. This process is known as the Diffusive Shock Acceleration (DSA) (or First-order Fermi acceleration).

In order to treat this process more quantitatively, it is appropriate to solve the advection–diffusion equation of non-thermal particles on the background fluid profile. Let us derive the distribution function of non-thermal particles formed by DSA following Blandford & Eichler (1987). The advection diffusion equation of non-thermal particles can be written as

$$\frac{\partial f}{\partial r} + (\boldsymbol{u} \cdot \nabla) f - \nabla \cdot [\boldsymbol{n} D (\boldsymbol{n} \cdot \nabla) f] = \frac{1}{3} (\nabla \cdot \boldsymbol{u}) p \frac{\partial f}{\partial p} \tag{C.1}$$

where $\boldsymbol{n}$ is a unit vector pararell to the local magnetic field of the background fluid. This equation is derived with an assumption that particles are almost isotropic in the momentum space, upstream and downstream. To be accurate, it is an equation that considers up to the second order of minute displacement from fluid approximation. Let us solve this equation under $\partial_t = \partial_y = \partial_z = 0$, $\boldsymbol{n} \parallel \boldsymbol{e_x}$ and the following fluid velocity u profile

$$u = \begin{cases} u_- & \text{for } x < 0 \\ u_+ & \text{for } x > 0 \end{cases}, \tag{C.2}$$

where subscript $-$ and $+$ represent physical quantities at the upstream and the downstream of the shock wave, respectively. As a fluid profile, we consider a non-relativistic fluid. From the Rankine-Hugoniot condition, the compression ratio is obtained as

$$\frac{1}{r_a} = \frac{u_-}{u_+} = \frac{\Gamma_a - 1}{\Gamma_a + 1} + \frac{2}{(\Gamma_a + 1) M^2} \tag{C.3}$$

where Γ_a is the adiabatic index, and M is the Mach number of the shock wave. For $Gamma_a = 5/3$ and the strong shock limit (i.e. $M \gg 1$), it is approximately $r_a \sim 4$.

Now, the advection-diffusion equation to be solved is as

$$\frac{\partial}{\partial x}\left[uf - D\frac{\partial f}{\partial x}\right] = \frac{1}{3}\left(u_+ - u_-\right)\delta(x)p\frac{\partial f}{\partial p}. \tag{C.4}$$

As a boundary condition, it is assumed that the phase space distribution becomes constant at sufficiently downstream, namely $f\left(-\infty, p\right) = f_-\left(p\right)$. For $x \neq 0$, the solution to the equation is:

$$f\left(x,p\right) = \begin{cases} f_-(p) + \left(f_+(p) - f_-(p)\right)\exp\left[\int_0^x \frac{u_- dx}{D(x,p)}\right] & x < 0 \\ f_+(p) & x > 0 \end{cases} \tag{C.5}$$

The solution of $x = 0$ is derived from the continuity condition of equation (C.5). By integrating with $-\epsilon < x < \epsilon$ and taking the limit of $\epsilon \to 0$, we obtain:

$$\frac{df_+}{d\left(\ln p\right)} = \frac{3r_a}{r_a - 1}\left(f_- - f_+\right). \tag{C.6}$$

Solve for f_+, we get:

$$f_+ = qp^{-q}\int_0^p f_-\left(p_0\right)p_0^{q-1}dp_0, \tag{C.7}$$

where $q = 3r_a/(r_a - 1)$. When f_- is a distribution where the number of high energy particles decreases (e.g. the Maxwell distribution), this equation means $f_+ \propto p^{-q}$ for sufficiently large p. Thus, in DSA, it can be seen that a power-law distribution function can be formed at higher energy than the thermal distribution. For $M \gg 1$ (i.e. $r_a \sim 4$), $q = 4$. The energy spectrum of the particle $dN/dE \propto p^2 f$, that is, the number per unit energy, is $dN/dE \propto E^{-2}$.

C.2 DSA in Relativistic shock

When the velocity of the background fluid becomes relativistic, the approximation that the distribution function of the particles is almost isotropic breaks. Therefore, analysis by equation (C.1) is incorrect. In such a case, analysis by the numerical simulation is carried out. Since it is necessary to calculate the particle acceleration for the particle deviated from the fluid approximation, it is appropriate to use the PIC simulation. Sironi et al. (2013) investigated the particle acceleration in relativistic perpendicular shock by PIC simulation. Figure C.1 shows the temporal evolution of energy spectrum with $\sigma = 0$ (unmagnetized case). In a relativistic shock wave, it is believed that a power-law spectrum with index about $p^{-2.4}$ is formed. They also investigated how particle acceleration process depend on the upstream magnetic field. Figure C.2 shows the σ dependence of ϵ_B, which is the ratio to the kinetic energy of the up-stream plasma flow, and the phase space $x - \gamma v_x$. When the magnetic field is weak, turbulent magnetic field is generated by the Weibel instability both the upstream and downstream of the shock. This turbulent magnetic field becomes a scatterer and the DSA mechanism works. Contraly, when the magnetic field is strong, a turbulent magnetic field is not formed upstream and particles are not much returned. Thus, it is known that particle acceleration process becomes inefficient in shock with a strong magnetic field. Note that this is also one example of the sigma problem.

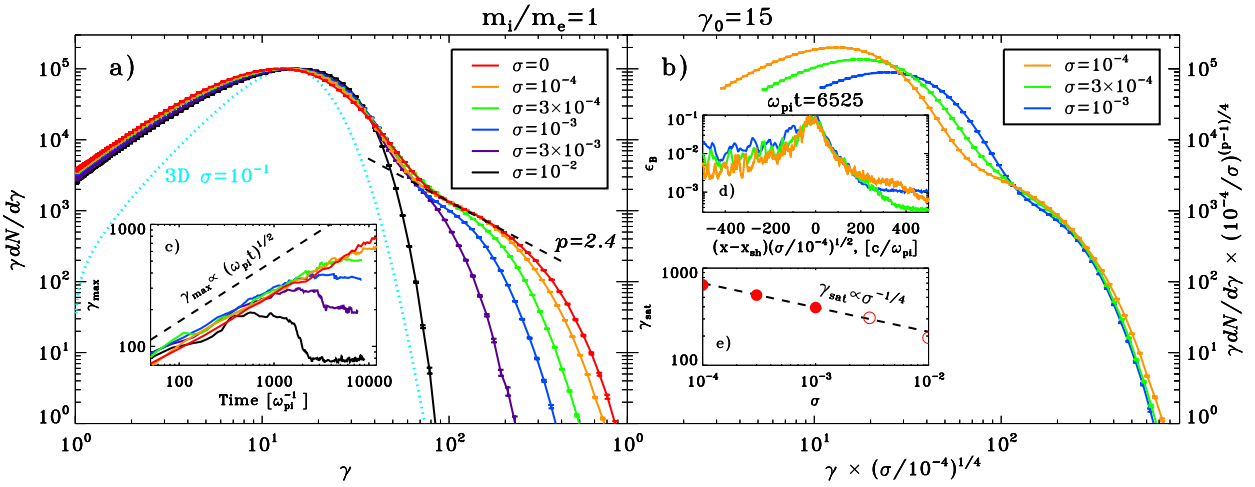

Figure C.1: (Left) The temporal evolution of energy spectrum with $\sigma = 0$ (unmagnetized case). (Right) Shifted energy spectrum to show that the exponential cutoff scale in $t^{1/2}$. The figure from Sironi et al. (2013). ©AAS. Reproduced with permission.

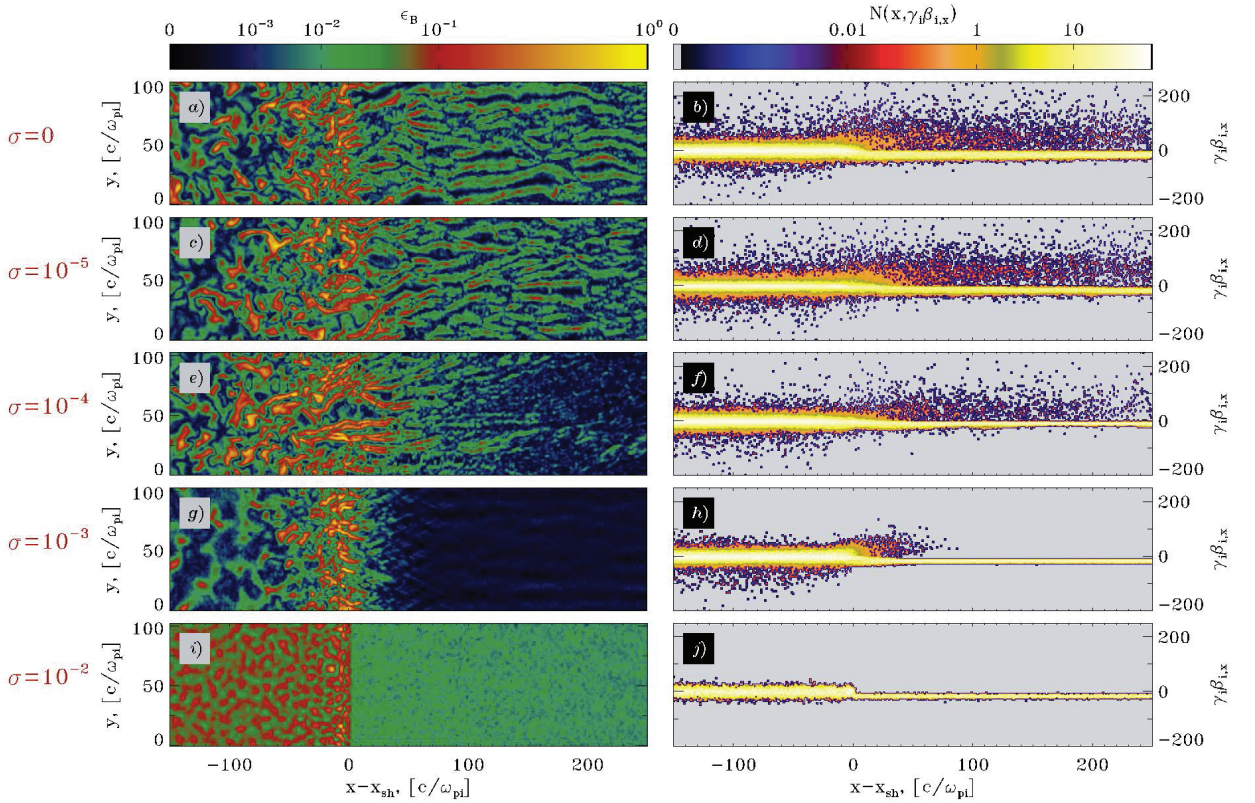

Figure C.2: Structure of the shock with varying σ. The left panels show the magnetic energy fraction of the up-stream kinetic energy. The right panels show the phase space $x - \gamma v_x$. The figure from Sironi et al. (2013). ©AAS. Reproduced with permission.

Appendix D

Notes on the Ideal MHD Condition in the Diffusion Model

In this Chapter, we explain that the current generated by the diffusion process can be neglected in generalized Ohm's law. For simplicity, we discuss a non-relativistic case. The Boltzmann equation of electrons and positrons is given by:

$$\frac{\partial f_s}{\partial t} + \boldsymbol{v} \cdot \nabla f_s + q_s \left[\boldsymbol{E} + \frac{\boldsymbol{v}}{c} \times \boldsymbol{B} \right] \cdot \frac{\partial f_s}{\partial \boldsymbol{p}} = S_s \tag{D.1}$$

where f_s is the phase space distribution functions of particles, s is species (e=electron, p=positron), $\boldsymbol{E}$ and $\boldsymbol{B}$ are the electric and magnetic field in the frame K, $\boldsymbol{v}$ is the velocity of each particle, and S is the collision term.

In order to obtain the generalized Ohm's law, we first derive the equation of motion. To prepare for that, we define several moment amounts. The number density is calculated as:

$$n_s \equiv \int f_s d^3p. \tag{D.2}$$

The flow velocity is

$$\boldsymbol{V_s} \equiv \frac{1}{n_s} \int \boldsymbol{v} f_s d^3p. \tag{D.3}$$

The gas pressure is

$$P_s \equiv \int (\boldsymbol{v} - \boldsymbol{V_s}) (\boldsymbol{v} - \boldsymbol{V_s}) f_s d^3p. \tag{D.4}$$

Multiplying a momentum of a particle $m_s \boldsymbol{V_s}$ to equation (D.1) and integrating over the momentum space, we obtain the equation of motion,

$$\frac{\partial}{\partial t} (m_s n_s \boldsymbol{V_s}) + \nabla \cdot (m_s n_s \boldsymbol{V_s} \boldsymbol{V_s}) = -\nabla P_s + q_s n_s \left(\boldsymbol{E} + \frac{\boldsymbol{V_s}}{c} \times \boldsymbol{B} \right) + \int m_s \boldsymbol{v} S_s d^3p, \tag{D.5}$$

where m_s is the mass of a particle. Here we assume that the pressure is isotropic. Multiplying a q_s/m_s to equation (D.5) and summing over $s = e, p$, we obtain,

$$\frac{\partial \boldsymbol{J}}{\partial t} + \nabla \cdot [e (n_p \boldsymbol{V_p} \boldsymbol{V_p} - n_e \boldsymbol{V_e} \boldsymbol{V_e})] = \frac{e}{m} \nabla (P_e - P_p) + \frac{e^2}{m} n \left(\boldsymbol{E} + \frac{\boldsymbol{V}}{c} \times \boldsymbol{B} \right) + e \int \boldsymbol{v} (S_p - S_e) d^3p, \tag{D.6}$$

where $\boldsymbol{J}$ is a total current,

$$\boldsymbol{J} = e (n_p \boldsymbol{V_p} - n_e \boldsymbol{V_e}), \tag{D.7}$$

n is total density,

$$n = n_e + n_p \tag{D.8}$$

and $\boldsymbol{V}$ is total bulk flow velocity,

$$\boldsymbol{V} = \frac{1}{n}\left(n_p V_p + n_e V_e\right). \tag{D.9}$$

Assuming that the charge neutrality $n_p = n_e$, we obtain the generalized Ohm's law,

$$\frac{\partial \boldsymbol{J}}{\partial t} + \nabla \cdot [\boldsymbol{J}\boldsymbol{V} + \boldsymbol{V}\boldsymbol{J}] = \frac{e}{m}\nabla\left(P_e - P_p\right) + \frac{e^2}{m} n \left(\boldsymbol{E} + \frac{\boldsymbol{V}}{c} \times \boldsymbol{B}\right) + e \int \boldsymbol{v}\left(S_p - S_e\right) d^3p. \tag{D.10}$$

Since we consider the radiative loss rate of electron and positron are almost same, $P_e \sim P_p$ is hold, so we neglect the first term of the right hand side. Furthermore, since we consider the long time scale, we can neglect the left hand side [1]. Note that the absence of the Joule dissipation term is caused by neglecting the energy transfer between electrons and positrons. This corresponds to the assuming that the fluid is a perfect conductor. The absence of the Hall term is caused by the equality of the mass of electrons and positrons.

The purpose in this Chapter is to confirm that the contribution of the diffusion process in Ohm's Law is negligibly small. Let us estimate the diffusion term of equation (D.10). Adopting the equation (5.3), we can proceed the calculation in the last term of equation (D.10) becomes

$$e \int \boldsymbol{v}\left(S_p - S_e\right) d^3p = \int e\boldsymbol{v} \nabla \cdot \left[\kappa \nabla \left(f_p - f_s\right)\right] d^3p. \tag{D.11}$$

Thus, the current $\boldsymbol{J}_{\rm diff}$ generated by diffusion process is written by

$$\boldsymbol{J}_{\rm diff} = \int e\kappa \nabla \left[f_p - f_s\right] d^3p. \tag{D.12}$$

By using the typical scale L of the system, we estimate $J_{\rm diff}$ as:

$$J_{\rm diff} \sim \frac{e\kappa}{L} \Delta n_{\pm}, \tag{D.13}$$

where $\Delta n_{\pm} = \int \left[f_p - f_s\right] d^3p$ is the local deference the number density between electrons and positrons. On the other hand, the conduction current $\boldsymbol{J}$ can be estimated by using the Maxwell equation:

$$J \sim \frac{c}{4\pi L} B \sim \frac{c}{4\pi L} \frac{c}{V} E. \tag{D.14}$$

The local difference $\Delta n_{\pm}$ yields charge density, so that from Gauss' law, we get:

$$J \sim \frac{ec^2 \Delta n_{\pm}}{V}. \tag{D.15}$$

Calculating the ratio of $J_{\rm diff}$ to J, we obtain

$$\frac{J_{\rm diff}}{J} \sim \frac{V}{c} \frac{\kappa}{Lc}. \tag{D.16}$$

Even if we estimate the most pessimistic case, namely $V \sim c/3$, $L \sim 10^{17}$ cm and $\kappa \sim 10^{27}$ cm^2 s^{-1}, this value is 1 or less. In particular, $\kappa \sim 10^{27}$ cm^2 s^{-1} is an exaggerated value, and such a large value of the diffusion coefficient is only realized for the highest energy particles, which is the group with the smallest number of particles. For the particles dominated in number, since the value of κ is about two orders of magnitude lower, we can safely neglect the contribution of $J_{\rm diff}$. Thus, we finally obtain the ideal MHD condition $\boldsymbol{E} + \boldsymbol{V} \times \boldsymbol{B}/c = 0$ from equation (D.10).

[1] Using the scale length L, we can estimate the value of $\left(\partial_t \boldsymbol{J}\right) / \left(e^2 n \boldsymbol{V} \times \boldsymbol{B}/mc\right) \sim 1/\left(4\pi L^2 r_e n\right)$, where r_e is the classical electron radius. Substituting the typical value of PWNe, we can conclude that the right hand side is much smaller than the Lorentz term. J/T/enV*Tc=(rho/en)*(Tc/T)

Acknowledgements

First of all, I sincerely acknowledge Prof. Katsuaki Asano for all his support and encouragement throughout 5 years. I learned from him the importance of accumulating knowledge itself, how to think logically and what a professional physicist is. I also appreciate Prof. Toshio Terasawa for supervising the master course. His deep and wide knowledge and amazing activity greatly influenced my future vision as a physicist. I am very grateful to Prof. Yoshikoshi for accepting to be a teacher in charge for 2 years.

I would like to express my sincere gratitude to: Dr. Shuta Tanaka for his guidance, advice and discussion on many topics not only about the modeling of pulsar wind nebulae. Dr. Kyohei Kawaguchi, for his insight backed by experience and knowledge about the numerical simulation. Mr. Kento Sasaki, for providing an easy-to-read code for numerical calculation.

I would also thank the fellow scientists and graduate students in Institute for Cosmic Ray Research (ICRR). I am grateful to Dr. Tomoya Kinugawa, Dr. Ryo Mikami, Mr. Sho To and Ms. Nagisa Hiroshima at the High Energy Astrophysics group in ICRR for useful discussion. I am also grateful to Mr. Tsutomu Nagayoshi for frank discussion about the research of SNRs. To Mr. Satoshi Fukami, Mr. Tomohiro Inada, Ms. Yuki Iwamura, Mr. Shunsuke Sakurai, Mr. Hayato Kuroda , Mr. Taku Kumon, Mr. Yukiho Kobayashi and Mr. Yoshiki Ohtani at Cherenkov Cosmic Gamma Ray group in ICRR and Mr. Yuma Sugahara at Observational Cosmology Group in ICRR, I would also thank them for fruitful discussion and cooperation for study session of astrophysics.

Bibliography

Abdo, A. A., Ackermann, M., Ajello, M., et al. 2010a, ApJ, 708, 1254, doi: 10.1088/0004-637X/708/2/1254

—. 2010b, ApJ, 720, 272, doi: 10.1088/0004-637X/720/1/272

Abdo, A. A., Ajello, M., Antolini, E., et al. 2010c, ApJ, 720, 26, doi: 10.1088/0004-637X/720/1/26

Abdo, A. A., Ajello, M., Allafort, A., et al. 2013, ApJS, 208, 17, doi: 10.1088/0067-0049/208/2/17

Abdollahi, S., Ackermann, M., Ajello, M., et al. 2017, Phys. Rev. D, 95, 082007, doi: 10.1103/PhysRevD.95.082007

Abeysekara, A. U., Albert, A., Alfaro, R., et al. 2017a, ApJ, 843, 40, doi: 10.3847/1538-4357/aa7556

—. 2017b, Science, 358, 911, doi: 10.1126/science.aan4880

Acharya, B. S., Actis, M., Aghajani, T., et al. 2013, Astroparticle Physics, 43, 3, doi: 10.1016/j.astropartphys.2013.01.007

Ackermann, M., Ajello, M., Baldini, L., et al. 2011, ApJ, 726, 35, doi: 10.1088/0004-637X/726/1/35

Adriani, O., Akaike, Y., Asano, K., et al. 2018a, Physical Review Letters, 120, 261102, doi: 10.1103/PhysRevLett.120.261102

Adriani, O., Barbarino, G. C., Bazilevskaya, G. A., et al. 2018b, ArXiv e-prints. https://arxiv.org/abs/1801.10310

Aguilar, M., Alberti, G., Alpat, B., et al. 2013, Physical Review Letters, 110, 141102, doi: 10.1103/PhysRevLett.110.141102

Aharonian, F., Akhperjanian, A., Beilicke, M., et al. 2004, ApJ, 614, 897, doi: 10.1086/423931

Aharonian, F., Akhperjanian, A. G., Bazer-Bachi, A. R., et al. 2006, A&A, 457, 899, doi: 10.1051/0004-6361:20065351

Aharonian, F., Akhperjanian, A. G., Anton, G., et al. 2009, A&A, 508, 561, doi: 10.1051/0004-6361/200913323

Akgün, T., Cerdá-Durán, P., Miralles, J. A., & Pons, J. A. 2018, MNRAS, 474, 625, doi: 10.1093/mnras/stx2814

Aleksić, J., Ansoldi, S., Antonelli, L. A., et al. 2014, A&A, 567, L8, doi: 10.1051/0004-6361/201424261

—. 2015, Journal of High Energy Astrophysics, 5, 30, doi: 10.1016/j.jheap.2015.01.002

Amato, E., Salvati, M., Bandiera, R., Pacini, F., & Woltjer, L. 2000, A&A, 359, 1107

Asano, K., & Mészáros, P. 2011, ApJ, 739, 103, doi: 10.1088/0004-637X/739/2/103

—. 2012, ApJ, 757, 115, doi: 10.1088/0004-637X/757/2/115

Atoyan, A. M., & Aharonian, F. A. 1996, MNRAS, 278, 525, doi: 10.1093/mnras/278.2.525

Baars, J. W. M., Genzel, R., Pauliny-Toth, I. I. K., & Witzel, A. 1977, A&A, 61, 99

Bai, X.-N., & Spitkovsky, A. 2010, ApJ, 715, 1282, doi: 10.1088/0004-637X/715/2/1282

Bednarek, W., & Bartosik, M. 2003, A&A, 405, 689, doi: 10.1051/0004-6361:20030593

Begelman, M. C., & Li, Z.-Y. 1994, ApJ, 426, 269, doi: 10.1086/174061

Berestetskii, V., Landau, L., Lifshitz, E., Pitaevskii, L., & Sykes, J. 1982, Quantum Electrodynamics, Course of theoretical physics (Elsevier Science). https://books.google.co.jp/books?id=URL5NKX8vbAC

Bernlöhr, K., Barnacka, A., Becherini, Y., et al. 2013, Astroparticle Physics, 43, 171, doi: 10.1016/j.astropartphys.2012.10.002

Beskin, V. S. 1999, Usp. Fiz. Nauk, 169, 1169, doi: 10.3367/UFNr.0169.199911a.1169

Beskin, V. S. 2009, MHD Flows in Compact Astrophysical Objects: Accretion, Winds and Jets

Bietenholz, M. F. 2006, ApJ, 645, 1180, doi: 10.1086/504584

Bietenholz, M. F., & Bartel, N. 2008, MNRAS, 386, 1411, doi: 10.1111/j.1365-2966.2008.13058.x

Bietenholz, M. F., Kassim, N., Frail, D. A., et al. 1997, ApJ, 490, 291

Bietenholz, M. F., Kondratiev, V., Ransom, S., et al. 2013, MNRAS, 431, 2590, doi: 10.1093/mnras/stt353

Blandford, R., & Eichler, D. 1987, Phys. Rep., 154, 1, doi: 10.1016/0370-1573(87)90134-7

Blumenthal, G. R., & Gould, R. J. 1970, Reviews of Modern Physics, 42, 237, doi: 10.1103/RevModPhys.42.237

Bocchino, F., & Bykov, A. M. 2001, A&A, 376, 248, doi: 10.1051/0004-6361:20010882

Bock, D. C.-J., Wright, M. C. H., & Dickel, J. R. 2001, ApJ, 561, L203, doi: 10.1086/324703

Bogovalov, S. V. 2001, A&A, 371, 1155, doi: 10.1051/0004-6361:20010201

Bucciantini, N., Arons, J., & Amato, E. 2011, MNRAS, 410, 381, doi: 10.1111/j.1365-2966.2010.17449.x

Bucciantini, N., Bandiera, R., Blondin, J. M., Amato, E., & Del Zanna, L. 2004, A&A, 422, 609, doi: 10.1051/0004-6361:20034400

Bucciantini, N., Blondin, J. M., Del Zanna, L., & Amato, E. 2003, A&A, 405, 617, doi: 10.1051/0004-6361:20030624

Bühler, R., & Blandford, R. 2014, Reports on Progress in Physics, 77, 066901, doi: 10.1088/0034-4885/77/6/066901

Camilo, F., Ransom, S. M., Gaensler, B. M., et al. 2006, ApJ, 637, 456, doi: 10.1086/498386

Camilo, F., Stairs, I. H., Lorimer, D. R., et al. 2002, ApJ, 571, L41, doi: 10.1086/341178

Cheng, K. S., Ho, C., & Ruderman, M. 1986, ApJ, 300, 500, doi: 10.1086/163829

Chevalier, R. A. 2005, ApJ, 619, 839, doi: 10.1086/426584

Contopoulos, I., Kazanas, D., & Fendt, C. 1999, ApJ, 511, 351, doi: 10.1086/306652

DAMPE Collaboration, Ambrosi, G., An, Q., et al. 2017, Nature, 552, 63, doi: 10.1038/nature24475

Daugherty, J. K., & Harding, A. K. 1996, ApJ, 458, 278, doi: 10.1086/176811

de Jager, O. C., & Djannati-Ataï, A. 2009, in Astrophysics and Space Science Library, Vol. 357, Astrophysics and Space Science Library, ed. W. Becker, 451

de Jager, O. C., & Harding, A. K. 1992, ApJ, 396, 161, doi: 10.1086/171706

de Jager, O. C., Harding, A. K., Michelson, P. F., et al. 1996, ApJ, 457, 253, doi: 10.1086/176726

de Rosa, A., Ubertini, P., Campana, R., et al. 2009, MNRAS, 393, 527, doi: 10.1111/j.1365-2966.2008.14160.x

Djannati-Ataï, A., deJager, O. C., Terrier, R., Gallant, Y. A., & Hoppe, S. 2008, International Cosmic Ray Conference, 2, 823. https://arxiv.org/abs/0710.2247

Eilek, J. A., & Hankins, T. H. 2016, Journal of Plasma Physics, 82, 635820302, doi: 10.1017/S002237781600043X

Ferraro, V. C. A. 1937, Monthly Notices of the Royal Astronomical Society, 97, 458, doi: 10.1093/mnras/97.6.458

Gaensler, B. M., & Slane, P. O. 2006, ARA&A, 44, 17, doi: 10.1146/annurev.astro.44.051905.092528

Gallant, Y. A., & Tuffs, R. J. 1998, Mem. Soc. Astron. Italiana, 69, 963

Ginzburg, V. L., & Syrovatskii, S. I. 1964, The Origin of Cosmic Rays

Gold, T. 1969, Nature, 221, 25, doi: 10.1038/221025a0

Goldreich, P., & Julian, W. H. 1969, ApJ, 157, 869, doi: 10.1086/150119

Grad, H. 1960, Reviews of Modern Physics, 32, 830, doi: 10.1103/RevModPhys.32.830

Grasdalen, G. L. 1979, PASP, 91, 436, doi: 10.1086/130516

Green, D. A. 1994, ApJS, 90, 817, doi: 10.1086/191908

Gupta, Y., Mitra, D., Green, D. A., & Acharyya, A. 2005, Current Science, 89, 853

Helfand, D. J., Gotthelf, E. V., & Halpern, J. P. 2001, ApJ, 556, 380, doi: 10.1086/321533

Hester, J. J. 2008, ARA&A, 46, 127, doi: 10.1146/annurev.astro.45.051806.110608

Hewish, A., Bell, S. J., Pilkington, J. D. H., Scott, P. F., & Collins, R. A. 1968, Nature, 217, 709, doi: 10.1038/217709a0

Hirotani, K. 2006, ApJ, 652, 1475, doi: 10.1086/508317

Hitomi Collaboration, Aharonian, F., Akamatsu, H., et al. 2018, Publications of the Astronomical Society of Japan, psy027, doi: 10.1093/pasj/psy027

Holler, M., Schöck, F. M., Eger, P., et al. 2012, A&A, 539, A24, doi: 10.1051/0004-6361/201118121

Huang, Z.-Q., Fang, K., Liu, R.-Y., & Wang, X.-Y. 2018, ApJ, 866, 143, doi: 10.3847/1538-4357/aadfed

Ioka, K. 2010, Progress of Theoretical Physics, 123, 743, doi: 10.1143/PTP.123.743

Ishizaki, W., Asano, K., & Kawaguchi, K. 2018, ApJ, 867, 141, doi: 10.3847/1538-4357/aae389

Ishizaki, W., Tanaka, S. J., Asano, K., & Terasawa, T. 2017, ApJ, 838, 142, doi: 10.3847/1538-4357/aa679b

Kargaltsev, O., Rangelov, B., & Pavlov, G. G. 2013, ArXiv e-prints. https://arxiv.org/abs/1305.2552

Kennel, C. F., & Coroniti, F. V. 1984a, ApJ, 283, 694, doi: 10.1086/162356

—. 1984b, ApJ, 283, 710, doi: 10.1086/162357

Komissarov, S. S. 2006, MNRAS, 367, 19, doi: 10.1111/j.1365-2966.2005.09932.x

Kothes, R. 2013, A&A, 560, A18, doi: 10.1051/0004-6361/201219839

Kozasa, T., Nozawa, T., Tominaga, N., et al. 2009, in Astronomical Society of the Pacific Conference Series, Vol. 414, Cosmic Dust - Near and Far, ed. T. Henning, E. Grün, & J. Steinacker, 43

Kuiper, L., Hermsen, W., Cusumano, G., et al. 2001, A&A, 378, 918, doi: 10.1051/0004-6361:20011256

Leung, G. C. K., Takata, J., Ng, C. W., et al. 2014, ApJ, 797, L13, doi: 10.1088/2041-8205/797/2/L13

Li, J., Spitkovsky, A., & Tchekhovskoy, A. 2012, ApJ, 746, 60, doi: 10.1088/0004-637X/746/1/60

Li, J., Torres, D. F., Lin, T. T., et al. 2018, ApJ, 858, 84, doi: 10.3847/1538-4357/aabac9

Livingstone, M. A., Kaspi, V. M., Gavriil, F. P., et al. 2007, Ap&SS, 308, 317, doi: 10.1007/s10509-007-9320-3

Livingstone, M. A., Ransom, S. M., Camilo, F., et al. 2009, ApJ, 706, 1163, doi: 10.1088/0004-637X/706/2/1163

Lorimer, D. R., & Kramer, M. 2004, Handbook of Pulsar Astronomy

Lu, F.-W., Gao, Q.-G., Zhu, B.-T., & Zhang, L. 2017, MNRAS, 472, 2926, doi: 10.1093/mnras/stx2223

Lyne, A. G., Jordan, C. A., Graham-Smith, F., et al. 2015, MNRAS, 446, 857, doi: 10.1093/mnras/stu2118

Lyne, A. G., Pritchard, R. S., Graham-Smith, F., & Camilo, F. 1996, Nature, 381, 497, doi: 10.1038/381497a0

Macías-Pérez, J. F., Mayet, F., Aumont, J., & Désert, F.-X. 2010, ApJ, 711, 417, doi: 10.1088/0004-637X/711/1/417

Madsen, K. K., Reynolds, S., Harrison, F., et al. 2015, ApJ, 801, 66, doi: 10.1088/0004-637X/801/1/66

Martín, J., Torres, D. F., & Rea, N. 2012, MNRAS, 427, 415, doi: 10.1111/j.1365-2966.2012.22014.x

Matheson, H., & Safi-Harb, S. 2005, Advances in Space Research, 35, 1099, doi: 10.1016/j.asr.2005.04.050

—. 2010, ApJ, 724, 572, doi: 10.1088/0004-637X/724/1/572

Melatos, A., & Melrose, D. B. 1996, MNRAS, 279, 1168, doi: 10.1093/mnras/279.4.1168

Melrose, D. B., & Rafat, M. Z. 2017, in Journal of Physics Conference Series, Vol. 932, Journal of Physics Conference Series, 012011

Meyer, M., Horns, D., & Zechlin, H. S. 2010, A&A, 523, A2, doi: 10.1051/0004-6361/201014108

Moskalenko, I. V., & Strong, A. W. 1998, ApJ, 493, 694, doi: 10.1086/305152

Murray, S. S., Slane, P. O., Seward, F. D., Ransom, S. M., & Gaensler, B. M. 2002, ApJ, 568, 226, doi: 10.1086/338766

Ney, E. P., & Stein, W. A. 1968, ApJ, 152, L21, doi: 10.1086/180170

Nomoto, K., Sparks, W. M., Fesen, R. A., et al. 1982, Nature, 299, 803, doi: 10.1038/299803a0

Nynka, M., Hailey, C. J., Reynolds, S. P., et al. 2014, ApJ, 789, 72, doi: 10.1088/0004-637X/789/1/72

Okamoto, I., & Sigalo, F. B. 2006, PASJ, 58, 987, doi: 10.1093/pasj/58.6.987

Olmi, B., Del Zanna, L., Amato, E., Bandiera, R., & Bucciantini, N. 2014, MNRAS, 438, 1518, doi: 10.1093/mnras/stt2308

Olmi, B., Del Zanna, L., Amato, E., & Bucciantini, N. 2015, MNRAS, 449, 3149, doi: 10.1093/mnras/stv498

Owen, P. J., & Barlow, M. J. 2015, ApJ, 801, 141, doi: 10.1088/0004-637X/801/2/141

Pacini, F. 1967, Nature, 216, 567, doi: 10.1038/216567a0

Parker, E. N. 1965, Planet. Space Sci., 13, 9, doi: 10.1016/0032-0633(65)90131-5

Pétri, J. 2016, MNRAS, 455, 3779, doi: 10.1093/mnras/stv2613

Philippov, A. A., & Spitkovsky, A. 2018, ApJ, 855, 94, doi: 10.3847/1538-4357/aaabbc

Pietka, M., Fender, R. P., & Keane, E. F. 2015, MNRAS, 446, 3687, doi: 10.1093/mnras/stu2335

Porter, T. A., & Strong, A. W. 2005, International Cosmic Ray Conference, 4, 77

Porth, O., Komissarov, S. S., & Keppens, R. 2013, MNRAS, 431, L48, doi: 10.1093/mnrasl/slt006

—. 2014, MNRAS, 438, 278, doi: 10.1093/mnras/stt2176

Porth, O., Vorster, M. J., Lyutikov, M., & Engelbrecht, N. E. 2016, MNRAS, 460, 4135, doi: 10.1093/mnras/stw1152

Press, W. H., Teukolsky, S. A., Vetterling, W. T., & Flannery, B. P. 1992, Numerical recipes in FORTRAN. The art of scientific computing

Rees, M. J., & Gunn, J. E. 1974, MNRAS, 167, 1, doi: 10.1093/mnras/167.1.1

Reynolds, S. P. 2003, ArXiv Astrophysics e-prints

—. 2009, ApJ, 703, 662, doi: 10.1088/0004-637X/703/1/662

Reynolds, S. P., & Aller, H. D. 1988, ApJ, 327, 845, doi: 10.1086/166242

Roy, J., Gupta, Y., & Lewandowski, W. 2012a, MNRAS, 424, 2213, doi: 10.1111/j.1365-2966.2012.21380.x

—. 2012b, MNRAS, 424, 2213, doi: 10.1111/j.1365-2966.2012.21380.x

Ruderman, M. A., & Sutherland, P. G. 1975, ApJ, 196, 51, doi: 10.1086/153393

Rybicki, G. B., & Lightman, A. P. 1979, Radiative processes in astrophysics

Sakurai, T. 1985, A&A, 152, 121

Salter, C. J., Reynolds, S. P., Hogg, D. E., Payne, J. M., & Rhodes, P. J. 1989, ApJ, 338, 171, doi: 10.1086/167191

Sasaki, K., Asano, K., & Terasawa, T. 2015, ApJ, 814, 93, doi: 10.1088/0004-637X/814/2/93

Schöck, F. M., Büsching, I., de Jager, O. C., Eger, P., & Vorster, M. J. 2010, A&A, 515, A109, doi: 10.1051/0004-6361/201014151

Schweizer, T., Bucciantini, N., Idec, W., et al. 2013, MNRAS, 433, 3325, doi: 10.1093/mnras/stt995

Shafranov, V. D. 1958, Soviet Journal of Experimental and Theoretical Physics, 6, 545

Shibata, S., Tomatsuri, H., Shimanuki, M., Saito, K., & Mori, K. 2003, MNRAS, 346, 841, doi: 10.1111/j.1365-2966.2003.07131.x

Sironi, L., Spitkovsky, A., & Arons, J. 2013, ApJ, 771, 54, doi: 10.1088/0004-637X/771/1/54

Slane, P., Helfand, D. J., Reynolds, S. P., et al. 2008, ApJ, 676, L33, doi: 10.1086/587031

Slane, P., Helfand, D. J., van der Swaluw, E., & Murray, S. S. 2004, ApJ, 616, 403, doi: 10.1086/424814

Spitkovsky, A. 2006, ApJ, 648, L51, doi: 10.1086/507518

—. 2008, ApJ, 682, L5, doi: 10.1086/590248

Stephenson, F. R. 1971, QJRAS, 12, 10

Strong, A. W., & Moskalenko, I. V. 1998, ApJ, 509, 212, doi: 10.1086/306470

Strong, A. W., Moskalenko, I. V., & Ptuskin, V. S. 2007, Annual Review of Nuclear and Particle Science, 57, 285, doi: 10.1146/annurev.nucl.57.090506.123011

Sturrock, P. A. 1971, ApJ, 164, 529, doi: 10.1086/150865

Szary, A., Zhang, B., Melikidze, G. I., Gil, J., & Xu, R.-X. 2014, ApJ, 784, 59, doi: 10.1088/0004-637X/784/1/59

Takahashi, M., & Shibata, S. 1998, PASJ, 50, 271, doi: 10.1093/pasj/50.2.271

Takata, J., & Chang, H. K. 2007, ApJ, 670, 677, doi: 10.1086/521785

Tanaka, S. J., & Asano, K. 2017, ApJ, 841, 78, doi: 10.3847/1538-4357/aa6f13

Tanaka, S. J., & Takahara, F. 2010, ApJ, 715, 1248, doi: 10.1088/0004-637X/715/2/1248

—. 2011, ApJ, 741, 40, doi: 10.1088/0004-637X/741/1/40

—. 2013a, MNRAS, 429, 2945, doi: 10.1093/mnras/sts528

—. 2013b, Progress of Theoretical and Experimental Physics, 12. https://arxiv.org/abs/1311.5337

Tanaka, S. J., Toma, K., & Tominaga, N. 2018, MNRAS, 478, 4622, doi: 10.1093/mnras/sty1356

Tang, X., & Chevalier, R. A. 2012, ApJ, 752, 83, doi: 10.1088/0004-637X/752/2/83

Temim, T., Gehrz, R. D., Woodward, C. E., et al. 2006, AJ, 132, 1610, doi: 10.1086/507076

Tian, W. W., & Leahy, D. A. 2008, MNRAS, 391, L54, doi: 10.1111/j.1745-3933.2008.00557.x

Timokhin, A. N., & Harding, A. K. 2015, ApJ, 810, 144, doi: 10.1088/0004-637X/810/2/144

—. 2018, ArXiv e-prints. https://arxiv.org/abs/1803.08924

Toma, K., & Takahara, F. 2013, Progress of Theoretical and Experimental Physics, 2013, 083E02, doi: 10.1093/ptep/ptt058

Torii, K., Slane, P. O., Kinugasa, K., Hashimotodani, K., & Tsunemi, H. 2000, PASJ, 52, 875, doi: 10.1093/pasj/52.5.875

Torres, D. F., Cillis, A., Martín, J., & de Oña Wilhelmi, E. 2014, Journal of High Energy Astrophysics, 1, 31, doi: 10.1016/j.jheap.2014.02.001

Torres, D. F., Cillis, A. N., & Martín Rodriguez, J. 2013, ApJ, 763, L4, doi: 10.1088/2041-8205/763/1/L4

Tsirou, M., Gallant, Y., Zanin, R., Terrier, R., & for the H. E. S. S. Collaboration. 2017, ArXiv e-prints. https://arxiv.org/abs/1709.01422

Tsujimoto, M., Guainazzi, M., Plucinsky, P. P., et al. 2011, A&A, 525, A25, doi: 10.1051/0004-6361/201015597

van der Swaluw, E., Achterberg, A., Gallant, Y. A., & Tóth, G. 2001, A&A, 380, 309, doi: 10.1051/0004-6361:20011437

Venter, C. 2016, in Proceedings of the 4th Annual Conference on High Energy Astrophysics in Southern Africa (HEASA 2016). 25-26 August, 40

Vladimirov, A. E., Digel, S. W., Jóhannesson, G., et al. 2011, Computer Physics Communications, 182, 1156, doi: 10.1016/j.cpc.2011.01.017

Vlahakis, N. 2004, ApJ, 600, 324, doi: 10.1086/379701

Vorster, M. J., Ferreira, S. E. S., de Jager, O. C., & Djannati-Ataï, A. 2013a, A&A, 551, A127, doi: 10.1051/0004-6361/201220276

Vorster, M. J., Tibolla, O., Ferreira, S. E. S., & Kaufmann, S. 2013b, ApJ, 773, 139, doi: 10.1088/0004-637X/773/2/139

Wang, Z. R., Li, M., & Zhao, Y. 2006, Chin. J. Astron. Astrophys., 6, 625, doi: 10.1088/1009-9271/6/5/15

Weiland, J. L., Odegard, N., Hill, R. S., et al. 2011, ApJS, 192, 19, doi: 10.1088/0067-0049/192/2/19

Weiler, K. W., & Panagia, N. 1978, A&A, 70, 419

Yatsu, Y., Kawai, N., Shibata, S., & Brinkmann, W. 2009, PASJ, 61, 129, doi: 10.1093/pasj/61.1.129